Technische Universität München
TUM School of Engineering and Design

Model Reduction for Biomedical Models in Vascular and Cardiac Mechanics

Alexander Schein

Vollständiger Abdruck der von der TUM School of Engineering and Design der Technischen Universität München zur Erlangung eines

Doktors der Ingenieurwissenschaften (Dr.-Ing.)

genehmigten Dissertation.

Vorsitz: Prof. Dr.-Ing. Boris Lohmann

Prüfer*innen der Dissertation:

1 Prof. Dr.-Ing. Michael W. Gee

2 Prof. Matthew J. Zahr, Ph.D.

3 Prof. Dr.-Ing. Alexander Popp

Die Dissertation wurde am 20.06.2022 bei der Technischen Universität München eingereicht und durch die TUM School of Engineering and Design am 17.01.2023 angenommen.

Abstract

In recent decades, scientists and engineers have benefited greatly from advances in computational mechanics. A key ingredient for the success of computational methods is the steadily increasing computing power as well as the development of algorithms capable of exploiting it. The simulation of complex mechanical systems' behavior is currently possible with great accuracy, which is especially valuable for systems hardly accessible by prototyping or experiments. The need for larger computing power is also the motivation for rising computing power, this seems to be a trivial statement. In other words however the statement reads: To date, the available computing power has never been sufficient to address the complexity of all prevailing questions to full satisfaction. As a result, approaches to generate approximate solutions to computationally unaffordable models have increasingly gained attention in computational science and established the field of *reduced order modeling*.

Starting from a full-order model (FOM), the so-called projection-based model order reduction (MOR) generates a reduced-order model (ROM) by searching an approximation to the FOM solution in a low-dimensional subspace. As a result, arising systems of equations throughout the iterative solution process can contain several orders of magnitude fewer unknowns than the high-dimensional FOM. A natural application of projection-based MOR arises for parametrized models, which have to be solved for a large number of parameter variations in a *many query* context, e.g. arising in uncertainty quantification or optimization. Although individual model evaluations might be affordable, the computational burden here results from the combination of large models and large number of requested model evaluations. Examples of such parametrized systems arise in biomedical applications. Complex geometries and pronounced nonlinearities require high spatial resolution. At the same time, uncertainties in model parameters due to imprecise data on the object of interest as part of the (human) body require e.g. statistical analysis or model calibration and establish the aforementioned many query context.

In this thesis, two biomedical models are investigated. The abdominal aortic aneurysm (AAA) is a pathological dilatation of the abdominal aorta, which is prone to spontaneous rupture with frequently a lethal outcome for the patient. The first computational model at hand returns a spatially resolved state of the aortic stress and can serve to examine critical conditions, e.g. if rupture is identified with material failure. Secondly, a cardiac mechanics model is investigated. This model returns, besides material deformation throughout heart beats, temporally resolved data on parameters related to cardiac performance such as ventricular pressures and volumes. Consequently, the model can be used to investigate critical conditions for heart failure. The application and adaption of projection-based MOR to these biomedical models is the subject of this thesis. Recalling the many query context, reduced subspaces are constructed in a data-driven approach from selected samples of the FOMs. Upon that, a so-called *hyper reduction* is performed for fast assembly of nonlinear system components. Prestressing, multidimensional parametrization, multiple nonlinear system components, large deformations and highly nonlinear material behavior are examples of arising challenges in the aforementioned context.

Zusammenfassung

Wissenschaftler und Ingenieure haben in den letzten Jahrzehnten in starker Ausprägung von Fortschritten in der numerischen Mechanik profitiert. Wichtige Voraussetzungen dieses Erfolgs waren die Verfügbarkeit stetig wachsender Rechenleistung sowie die Entwicklung von parallelisierten Algorithmen, welche diese Rechenleistung ausnutzen können. Die akkurate Simulation komplexer mechanischer Systeme ist derzeit möglich, was von besonders hohem Wert ist, wenn das betrachtete System nur schwer oder gar nicht durch Prototypisierung oder Experimente zugänglich ist. Die stetig wachsende Verfügbarkeit an Rechenleistung wird angetrieben durch den stetig wachsenden Bedarf an Rechenleistung, diese Aussage scheint trivial. Mit anderen Worten jedoch heißt das: Die verfügbare Rechenleistung war bisher nie ausreichend, um alle numerischen Probleme zur vollen Zufriedenheit behandeln zu können. Als Folge haben Ansätze zur Approximation von Lösungen komplexer Modelle zunehmend Aufmerksamkeit gewonnen und den Wissenschaftsbereich der *Modellordnungsreduktion* (MOR) begründet.

Ausgehend von einem hochdimensionalen Modell (FOM, Abkürzung für englischen Begriff "full-order model") wird in der sogenannten *projektionsbasierten* MOR ein reduziertes Modell (ROM, Abkürzung für englischen Begriff "reduced-order model") durch Suche einer Approximation der FOM Lösung in einem niedrigdimensionalen Lösungsraum erzeugt. Folglich können auftretende Gleichungssysteme im iterativen Lösungsprozess um Größenordnungen weniger Unbekannte enthalten als das FOM. Ein natürliches Anwendungsgebiet für projektionsbasierte MOR entspringt parametrisierten Systemen, welche für eine große Anzahl an Parametervariationen ausgewertet werden müssen. Ein solcher Kontext ergibt sich z.B. bei der Quantifizierung von Unsicherheiten oder der Optimierung. Auch wenn individuelle Modellauswertungen bezahlbar sein können, wird die verfügbare Rechenleistung zum Flaschenhals aufgrund der Kombination von hochaufgelöstem Modell und der Anzahl an auszuführenden Modellauswertungen. Zahlreiche Beispiele solcher parametrisierter Systeme ergeben sich aus der Biomechanik. Komplexe Geometrien und ausgeprägte Nichtlinearitäten setzen eine hohe räumliche Auflösung voraus. Gleichzeitig erfordern Unsicherheiten in Modellparametern aufgrund einer Unschärfe der Datenlage und bedingtem Zugang zum Objekt als Teil des (menschlichen) Körpers die Anwendung statistischer Analyse oder Modellkalibrierung und begründen daher den oben genannten Kontext vieler Modellauswertungen.

Im Fokus dieser Arbeit liegen zwei biomechanische Modelle. Das abdominale Aortenaneurysma ist eine pathologische Aufweitung der abdominalen Aorta. Das erkrankte Aortensegment kann spontan rupturieren, was in den meisten Fällen für den betroffenen Patienten tödlich endet. Das erste biomechanische Modell liefert einen räumlich aufgelösten Zustand der Aneurysmenwandspannungen und kann zur Untersuchung kritischer Bedingungen herangezogen werden, wenn Ruptur als mechanisches Materialversagen interpretiert wird. Das zweite biomechanische Modell beschreibt die Mechanik des schlagenden Herzens. Dieses Modell liefert, neben der Materialverformung während eines Herzschlags, zeitlich aufgelöste Daten (z.B. ventrikuläre Drücke und Volumen) im Zusammenhang mit der Herzperformanz. Folglich kann dieses Modell

für die Untersuchung kritischer Bedingungen mit Auswirkung auf Herzinsuffizienz herangezogen werden. Zielstellung der vorliegenden Arbeit ist die Adaption und Anwendung projektionsbasierter MOR auf die beschriebenen biomechanischen Modelle. Im oben erwähnten Kontext vieler Modellauswertungen werden niedrigdimensionale Lösungsräume datengetrieben aus Lösungen ausgewählter Parametersamples erzeugt. Zudem wird die sogenannte *Hyperreduktion* für schnelle Assemblierung nichtlinearer Systemkomponenten verwendet. Vorgespannte Geometrien, mehrdimensionale Parametrisierungen, mehrere nichtlineare Systemkomponenten, große Deformationen und hochgradig nichtlineares Materialverhalten sind Beispiele sich ergebender Herausforderungen im beschriebenen Kontext.

Contents

List of Figures

List of Tables

Acronyms

AAA	abdominal aortic aneurysm
CER	cycle error criterion
CT	computed tomography
DEIM	discrete empirical interpolation method
DHROM	dimensionally reduced as well as hyper reduced order model
DOE	design of (computer) experiments
DOF	degree of freedom
DROM	dimensionally reduced order model
ECM	empirical cubature method
ECSW	energy-conserving mesh sampling and weighting
EDV	end-diastolic ventricular volume
ESV	end-systolic ventricular volume
EVAR	endovascular aneurysm repair
FOM	full-order model
gen-α	generalized-α
GMmD	greedy maximin distance design
GNAT	Gauss-Newton with approximated tensors
ILT	intraluminal thrombus
MmD	maximin distance design
mMD	minimax distance design
MOR	model order reduction
MRI	magnetic resonance imaging
MULF	modified updated Lagrangian formulation
ODE	ordinary differential equation
OSR	open surgical repair
OST	one-step-θ
POD	proper-orthogonal decomposition

PTC	pseudo-transient continuation
PVW	principle of virtual work
QOI	quantity of interest
ROB	reduced-order basis
ROM	reduced-order model
SAD	subspace angle distance
SNNLS	sparse non-negative least-squares
SVD	singular value decomposition

Nomenclature

Subscripts and superscripts

$(\bullet)_{\mathrm{in}}$	inlet quantity
$(\bullet)_{\mathrm{out}}$	outlet quantity
$(\bullet)_{\mathrm{int}}$	internal quantity
$(\bullet)_{\mathrm{ext}}$	external quantity
$(\bullet)_{\mathrm{iso}}$	isochoric contribution
$(\bullet)_{\mathrm{vol}}$	volumetric contribution
$(\bullet)_{\mathrm{lid}}$	quantity related to artificial lids in heart model
$(\bullet)_{p}$	prestressing stage quantity
$(\bullet)_{d}$	deformation stage quantity
$(\bullet)_{\mathrm{ar}}$	arterial circulation quantity
$(\bullet)_{\mathrm{ven}}$	venous circulation quantity
$(\bullet)_{\mathrm{v}}$	ventricular quantity
$(\bullet)_{\mathrm{at}}$	atrial quantity
$(\bullet)_{\mathrm{min}}$	minimum quantity
$(\bullet)_{\mathrm{max}}$	maximum quantity
$(\bullet)_{\mathrm{sf}}$	structural and 0D flow network quantity
$(\bullet)^{(e)}$	quantity on finite element e
$(\bullet)^{\mathrm{ILT}}$	ILT quantity
$(\bullet)^{\mathrm{wall}}$	AAA wall quantity
$(\bullet)^{\ell}$	left heart quantity
$(\bullet)^{r}$	right heart quantity
$(\bullet)^{\mathrm{sys}}$	systemic circulation quantity
$(\bullet)^{\mathrm{pul}}$	pulmonary circulation quantity

Domains and surfaces

Ω_0	reference configuration domain
Ω	current configuration domain
$\partial\Omega$	surface of current configuration domain
Γ_l	luminal ILT surface
Γ_c	proximal and distal cut faces of AAA
Γ_b	heart base surface
Γ_e	epicardial surface
Γ_{lid}	abluminal surface of covering heart lids
$\Gamma_{\mathrm{v}}^{\ell}$	left ventricular surface
Γ_{v}^{r}	right ventricular surface

Continuum mechanics quantities

$\boldsymbol{\varphi}$	deformation map
$\boldsymbol{x}_0$	position vector of reference configuration material element
$\boldsymbol{x}$	position vector of current configuration material element
$\boldsymbol{u}$	material displacement field
$\boldsymbol{v}$	material velocity field
$\boldsymbol{a}$	material acceleration field
t	time
$\boldsymbol{F}$	deformation gradient
$d\boldsymbol{a}_0$	reference configuration material element surface
$d\boldsymbol{a}$	current configuration material element surface
J	determinant of deformation gradient
dv_0	reference configuration material element volume
dv	current configuration material element volume
$\boldsymbol{C}$	right Cauchy-Green tensor
$\boldsymbol{n}_0$	normed direction in reference configuration
$\boldsymbol{n}$	normed direction in current configuration
λ	stretch
$\varepsilon^{\mathrm{GL}}$	Green-Lagrange strain
$\varepsilon^{\mathrm{EA}}$	Euler-Almansi strain
$\boldsymbol{E}$	Green-Lagrange strain tensor
$\boldsymbol{e}$	Euler-Almansi strain tensor
$d\boldsymbol{f}$	force acting on material element
$\boldsymbol{t}_0$	first Piola-Kirchhoff traction
$\boldsymbol{P}$	first Piola-Kirchhoff stress tensor
$\boldsymbol{S}$	second Piola-Kirchhoff stress tensor
$\boldsymbol{\sigma}$	Cauchy stress tensor
Ψ	strain energy density function
I_1, I_2, I_3	principal invariants of right Cauchy-Green tensor
ρ_0	reference configuration mass density
ρ	current configuration mass density
dm	mass of material element
$\boldsymbol{f}_{\mathrm{vol},0}$	force per undeformed volume
$\boldsymbol{f}_{\mathrm{vol}}$	force per deformed volume
p	pressure
ν_{dyn}	dynamic viscosity
$\boldsymbol{\tau}$	symmetric part of spatial velocity gradient
E	elastic modulus
ν	Poisson's ratio
$\bar{\boldsymbol{C}}$	modified right Cauchy-Green tensor
$\bar{I}_1, \bar{I}_2$	principle invariants of modified right Cauchy-Green tensor
α, β	stiffness related material parameters of AAA wall

κ	bulk modulus
c	stiffness related material parameter of ILT
$\boldsymbol{P}_F$	first Piola-Kirchhoff stress tensor field as function of the deformation gradient
$\boldsymbol{P}_u$	first Piola-Kirchhoff stress tensor field as function of the displacement
$\boldsymbol{P}_{u,F}$	mixed representation of first Piola-Kirchhoff stress tensor field as function of the displacement and deformation gradient
p_{sys}	systolic blood pressure
p_{dia}	diastolic blood pressure
t_w	AAA wall thickness
$\boldsymbol{\sigma}_{\text{vM}}$	von Mises stress field
$\boldsymbol{e}_{\text{vM}}$	von Mises strain field
$\boldsymbol{f}_0$	fiber direction in heart model
$\boldsymbol{s}_0$	sheet direction in heart model
σ_0	contractility
α_{max}	active contraction upstroke rate
α_{min}	active contraction relaxation rate
t_{contr}	initialization time of active stress
t_{relax}	relaxation time of active stress
$k_{i,\perp}$	spring stiffness per reference surface area, $i \in \{b, e, \text{lid}\}$
$c_{i,\perp}$	dashpot stiffness per reference surface area, $i \in \{b, e, \text{lid}\}$

Dimensionally reduced flow network quantities

p	pressure
q	flow rate
R	resistance
C	capacitance
L	inertance
$\tilde{R}$	valve resistance
E_{at}	atrial elastance
$\Delta t_{\text{at,act}}$	duration of atrial activation
$\boldsymbol{q}$	0D flow state variables
$\boldsymbol{g}$	0D flow residual

Symbols related to finite element discretization

N_e	number of full mesh elements
N	number of global DOFs
n_e	number of element DOFs
n_n	number of element nodes
$\boldsymbol{\Phi}$	shape function matrix
$\boldsymbol{d}$	displacement DOFs
$\delta\boldsymbol{d}$	virtual displacement DOFs
N_i	shape functions, with $i \in \{0, \dots, n_n - 1\}$

$\boldsymbol{M}$	assembled mass matrix
$\boldsymbol{f}$	assembled force vector
$\boldsymbol{D}$	assembled Rayleigh damping matrix
c_M	mass scaling in Rayleigh damping
c_f	stiffness scaling in Rayleigh damping
$\boldsymbol{r}$	assembled solid mechanics residual
$\boldsymbol{J}_r$	assembled solid mechanics residual Jacobian
ε_r	residual convergence tolerance
ε_d	solution increment convergence tolerance
k^{PTC}	scaling in pseudo-transient continuation
$\Delta\boldsymbol{d}$	displacement DOFs increment
$\boldsymbol{L}^{(e)}$	assembly operator of element e towards global system
$\mathcal{E}$	index set of full mesh elements

Symbols related to temporal discretization

N_T	number of time steps
n	time step count
Δt	time step size
θ	parameter in one-step-θ scheme
α_m, α_f	residual interpolation factors in generalized-α scheme
β, γ	velocity and acceleration reconstruction factors in generalized-α scheme
ρ_∞	numerical dissipation controlling parameter in generalized-α scheme

Symbols in dimensional reduction and hyper reduction

$\boldsymbol{V}$	reduced-order basis
$\mathcal{P}$	discrete projection operator
$\tilde{\boldsymbol{d}}$	low-dimensional approximation of displacement field
$\hat{\boldsymbol{d}}$	generalized coordinates of displacement field
$\Delta\hat{\boldsymbol{d}}$	generalized coordinates increment for displacement field
p	dimension of low-dimensional subspace
$\boldsymbol{S}$	snapshot matrix
$\boldsymbol{\Phi}$	matrix with left singular vectors
$\boldsymbol{\Xi}$	diagonal matrix with singular values
$\boldsymbol{\Psi}$	matrix with right singular vectors
$\boldsymbol{\phi}_i$	left singular vector
$\boldsymbol{\xi}_i$	singular value
$\boldsymbol{\psi}_i$	right singular vector
$\boldsymbol{C}$	correlation matrix
$\hat{\boldsymbol{r}}$	dimensionally reduced residual
$\tilde{\boldsymbol{r}}$	hyper reduced residual
$\tilde{\boldsymbol{J}}_r$	hyper reduced residual Jacobian
$w^{(e)}$	ECSW weighting of element e

$\tilde{\mathcal{E}}$	index set of ECSW mesh elements
$\boldsymbol{w}$	ECSW element weighting vector
$\boldsymbol{A}$	ECSW system matrix
$\boldsymbol{b}$	ECSW system right hand side
ε_h	ECSW tolerance
$\bar{\boldsymbol{A}}^j$	ECSW subsystem matrix for subdomain j
$\bar{\boldsymbol{b}}^j$	ECSW subsystem right hand side for subdomain j
$\mathcal{E}^j$	element index set of subdomain j
N_s	number of ECSW subdomains

Other symbols

$\boldsymbol{I}$	identity matrix
$\delta\boldsymbol{u}$	weighting function
δW	virtual work
$\mathcal{P}$	parameter space
$n_{\mathcal{P}}$	dimension of parameter space
n_μ	number of design points to distribute
Σ_t	training grid
Σ_c	chosen points (e.g. by a specific design)
$\Sigma_{c,n_\mu}^{\mathrm{Mm}}$	maximin design with n_μ distributed points
$\Sigma_{c,n_\mu}^{\mathrm{mM}}$	minimax design with n_μ distributed points
$\boldsymbol{\mu}$	parameter vector
θ_k	subspace angle
Σ_{sd}	tuple with training grid subdomains
θ_m	maximum subspace angle
α_{incl}	subspace inclination angle
$\mathcal{E}_{\mathrm{cycle}}$	cycle error criterion
T_{cycle}	duration of one cardiac cycle
ξ_{th}	singular value threshold ratio
EF	ejection fraction
SV	stroke volume
EDV	end-diastolic volume
SW	stroke work
CO	cardiac output
ω	heart rate

1. Introduction

1.1. Motivation

Computational modeling for support of technical system design or general understanding of physical processes has become a valuable instrument for scientists and engineers. Increasing availability of high-performance computation clusters has been a key factor in development of sophisticated algorithms with real world applications. Besides technical systems, biological systems emerged as challenging, but rewarding field of application for computational modeling with great value for both physicians and patients. Examples are the application in understanding general disease progression [130], risk assessment [81, 106] or interventional planing [52, 82, 104]. Frequently, spatially discretized models with high resolution are a prerequisite for reliable results. Additionally, multiple evaluations of the resulting large models have to be performed due to the need for model calibration or statistical uncertainty in model parameters. Consequently, a large demand on computing resources emerges.

This demand introduces a significant bottleneck towards clinical application and substantiates the need for less computationally expensive models. As a result, model reduction with application to biomedical models motivates the work in this thesis. The focus lies on computational models of the cardiovascular system, in particular on cardiac and abdominal aortic aneurysm mechanics.

This thesis takes the perspective of computational and engineering science. Nevertheless, a certain amount of medical background is required for understanding the models at hand. The remainder of this section is used to provide background on some aspects of the cardiovascular system. In view of the applied models, emphasis is put on the abdominal aortic aneurysm and the mechanics of the beating heart.

1.2. Cardiovascular system

The human cardiovascular system is the combination of a complex network of blood vessels as well as the heart. At resting conditions, approximately five liters of blood are pumped by the heart every minute. Blood provides nutrients and oxygen to tissue and removes waste products and carbon dioxide from tissue, which makes a proper circulation of blood vitally important for health.

Blood vessels are distinguished into three types: arteries, veins and capillaries. Arterial blood flow is directed away from the heart, while venous blood flow is directed towards the heart. Consequently, arterial blood pressure is significantly higher than venous pressure and arterial wall structure must be mechanically stable to withstand the dynamic pressure load. Capillaries allow an exchange of chemicals between tissue and transported blood through their thin walls and can be found in arterial as well as venous parts of the blood vessel network.

The heart is located inside the pericardium, a sac built of the *fibrous pericardium* (outer layer) and the *serous pericardium* (inner layer), which itself consists of two layers forming a cavity. This so-called *pericardial cavity* contains lubricating fluid to avoid friction during heart contraction and expansion. The inner layer of the serous pericardium is called *epicardium* and is simultaneously the outer layer of the heart. The epicardium covers the *myocardium*, which is the muscle tissue actively contracting in the cardiac cycle. The innermost layer of the heart is called *endocardium*. Having blood contact, the endocardium avoids formation of blood clots and blood adhering to the walls of heart chambers [8].

In this thesis, the focus lies on two computational models in the context of the cardiovascular system. The following two sections provide brief medical background and establish a basis for an engineering understanding of the biomechanics models under consideration.

1.2.1. Abdominal aortic aneurysm

The aorta transports oxygenated blood from the left ventricle and is the biggest artery in the human body. Morphologically, the aorta consists of an ascending part starting at the heart, the aortic arch, the thoracic aorta as well as the abdominal aorta bifurcating into the common iliac arteries, see Figure 1.1.

The pathology under consideration in this thesis is the abdominal aortic aneurysm (AAA). An AAA corresponds to a permanent dilatation of the abdominal aorta as a consequence of preceding degeneration of aortic wall properties [119]. Degenerated wall properties on the one hand and increased blood pressure load due to increasing luminal surface on the other hand turn AAAs prone to rupture, which is a severe medical emergency with lethal outcome in at least 80% of incidences [36]. With age as a severe risk factor, the probability of developing an AAA increases during the course of human life. Further exemplary risk factors are male gender, comorbid cardiovascular diseases, hypertension, overweight as well as smoking history and familiar predisposition [67].

Most AAAs are asymptomatic, such that diagnosis frequently happens accidentally [77]. Treatment is carried out depending on the progress of the disease. Recommendation for elective repair is given by the Society for vascular surgery in case of a size $\geq 5.5\mathrm{cm}$ for fusiform AAAs and independently of AAAs size in case of saccular shape [19]. One type of surgical treatment is open repair, wherein a blood vessel prosthesis is introduced to replace the dilated section of the aorta via transabdominal access. A further, minimally invasive and in modern days more frequently applied type of surgical treatment is endovascular aneurysm repair, wherein a so-called stent-graft is deployed into the aorta [126]. Function of the stent-graft is to remove mechanical load from the diseased section of the aortic wall and prevent rupture.

Surgical intervention in AAA treatment is related to a variety of risks. The risk of death within 30 days of open repair intervention has been reported up to 8%, while endovascular aneurysm repair, regardless of its classification as minimally invasive interference, has a mortality rate up to 1.6% [19]. Postoperative risks are e.g. bowel obstruction, incisional hernia or graft infection [71] in case of open repair and e.g. endoleaks (blood leaking into the aneurysm), endograft migration (relocation of stent-graft after deployment) as well as endograft infection in case of endovascular aneurysm repair [32].

A central issue physicians face is opposing the risk of surgical intervention with the risk of AAA rupture, depending on the individual situation of every single patient. At the same time,

strict application of AAA size based criterion mentioned above might underestimate the complexity of the disease [42, 107]. In this context, state-of-the-art computational models have the potential to greatly support clinical decision making with a benefit for both physicians and patients. The computational model under consideration in this thesis consists of a 3D resolved aortic section fully including the dilated segment. Recently, model applications have been presented in the context of rupture risk assessment [14, 91] and in-silico modeling of endovascular aneurysm repair outcome [52, 53].

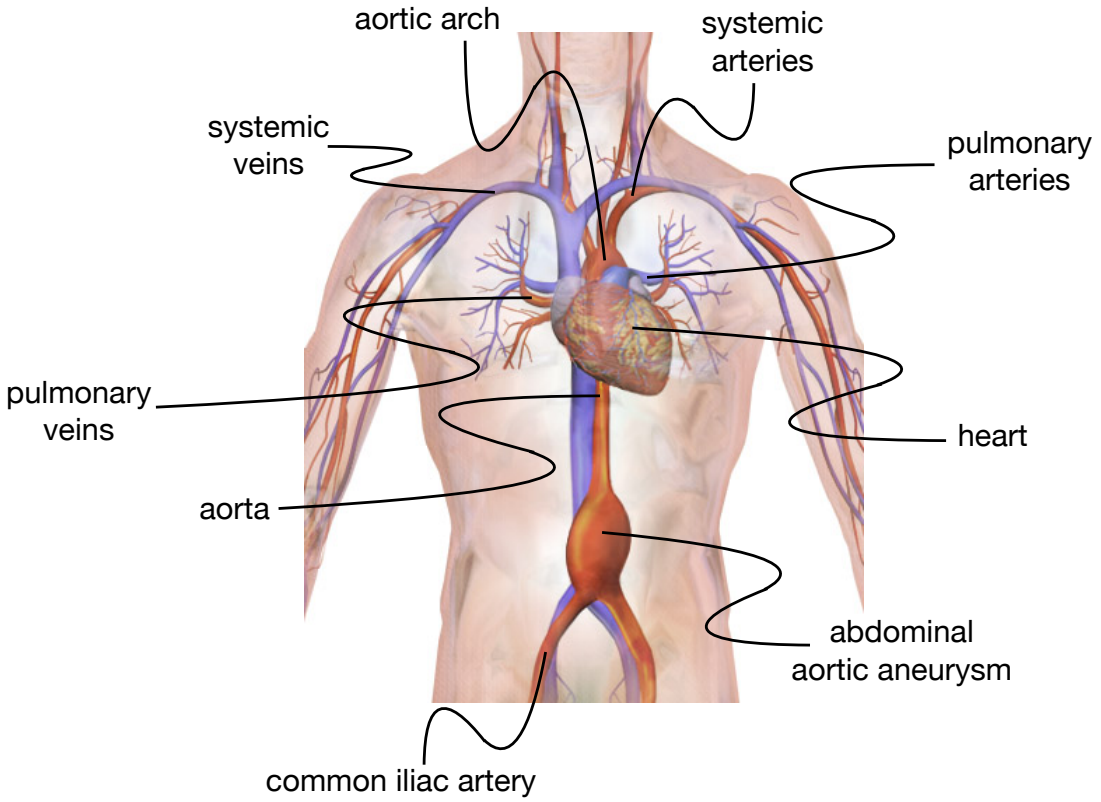

Figure 1.1.: Sketch of human cardiovascular system with infrarenal abdominal aortic aneurysm. Adapted with permission from [1] (published under CC BY license [27]). Added labeling, original image does not contain text.

1.2.2. Cardiac mechanics and heart failure

Figure 1.2 depicts a highly simplified sketch of the cardiovascular system including the heart and blood circulation. The heart contains four chambers, namely the left atrium, left ventricle, right atrium and right ventricle. Left and right heart chambers have been spatially separated in Figure 1.2 in order to illustrate the closed-loop nature of the circulation. Inside the heart, blood flows from atria to ventricles. Outside the heart, the left ventricle pumps blood through the systemic part of the circulation to the right atrium, while the right ventricle pumps blood through the pulmonary part of the circulation to the left atrium. Blood oxygenation takes place in the

lung as part of the pulmonary circulation. Blood deoxygenation is the consequence of oxygen consumption in e.g. the viscera, muscles, brain and skin as part of the systemic circulation [124].

The flow in Figure 1.2 is regulated by pressure gradients as well as four valves. All valves (in a healthy heart) close in case of a positive pressure gradient in direction of the main circulation and keep the flow unidirectional. The *mitral valve* is located between the left atrium and ventricle, the *tricuspid valve* between the right atrium and ventricle. These valves avoid ventricular backflow and are simultaneously referred to as *atrioventricular valves*. *Semilunar valves* simultaneously refer to the *aortic valve* between the left ventricle and aorta and the *pulmonary valve* between the right ventricle and pulmonary artery. Consequently, semilunar valves avoid arterial backflow.

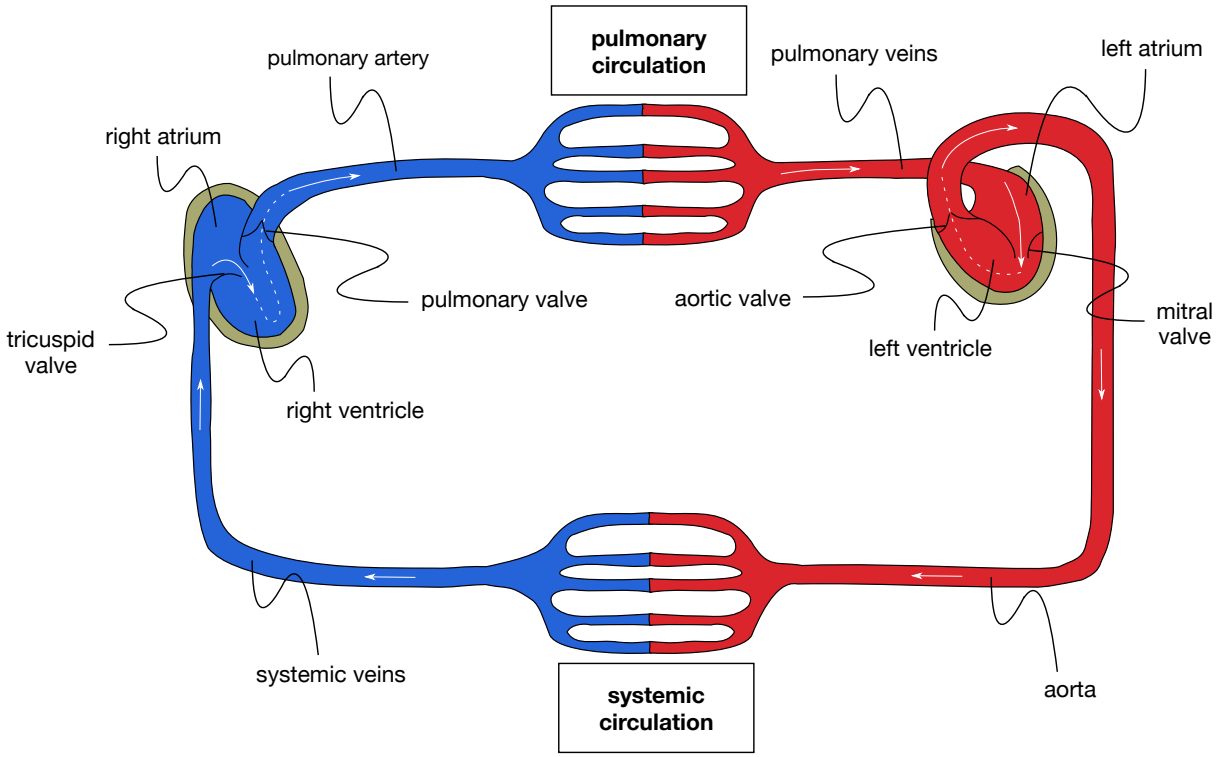

Figure 1.2.: Simplified scheme of the cardiovascular system. In order to highlight the closed loop nature of blood circulation, left heart chambers have been spatially separated from right heart chambers. The colors blue and red mark deoxygenated and oxygenated blood, respectively.

In more detail, a single heart beat can be subdivided in five phases [124]. Figure 1.3 contains a sketch of exemplary pressure and volume curves and serves for discussion of the five phases. *Atrial contraction* (phase 1, atrioventricular valves open, semimular valves closed) takes place in the timespan t_0 - t_1. Atrial contraction actively supports ventricular filling (ventricular volume increases), which in turn is completed at time t_1. Timespan t_1 - t_2 (phase 2, atrioventricular valves closed, semimular valves closed) is referred to as *isovolumetric ventricular contraction*. Given that all valves in this phase are closed, an increase of ventricular pressure at constant ventricular volume takes place. *Ventricular ejection* (phase 3, atrioventricular valves closed, semimular valves open) takes place in the timespan t_2 - t_3. Blood is pumped into the aorta and pulmonary artery. The consequence is a decrease of ventricular volume, left and right ventricular pressure

curves align with aortic and pulmonary artery pressure curves, respectively. *Isovolumetric relaxation* (phase 4, atrioventricular valves closed, semimular valves closed) takes place in the timespan t_3 - t_4. Ventricular pressure decreases at constant volume and the isovolumetric relaxation phase is completed with opening of atrioventricular valves at time t_4. Finally, left and right ventricles start to refill by receiving blood from the atria in the *ventricular filling* phase (phase 5, atrioventricular valves open, semimular valves closed). The cardiac cycle ends at time t_5 and the beginning atrial contraction initiates the next period.

Besides the presented five phases, the cardiac cycle is frequently partitioned in the *systole* and the *diastole*. The systole comprises ventricular contraction and ejection, that is the timespan t_1 - t_3 in Figure 1.3. The rest of the cardiac cycle including ventricular relaxation and ventricular filling corresponds to the diastole. Important quantities in this context are the end-diastolic ventricular volume (EDV) (i.e. ventricular volume at t_1) and the end-systolic ventricular volume (ESV) (i.e. ventricular volume at t_3).

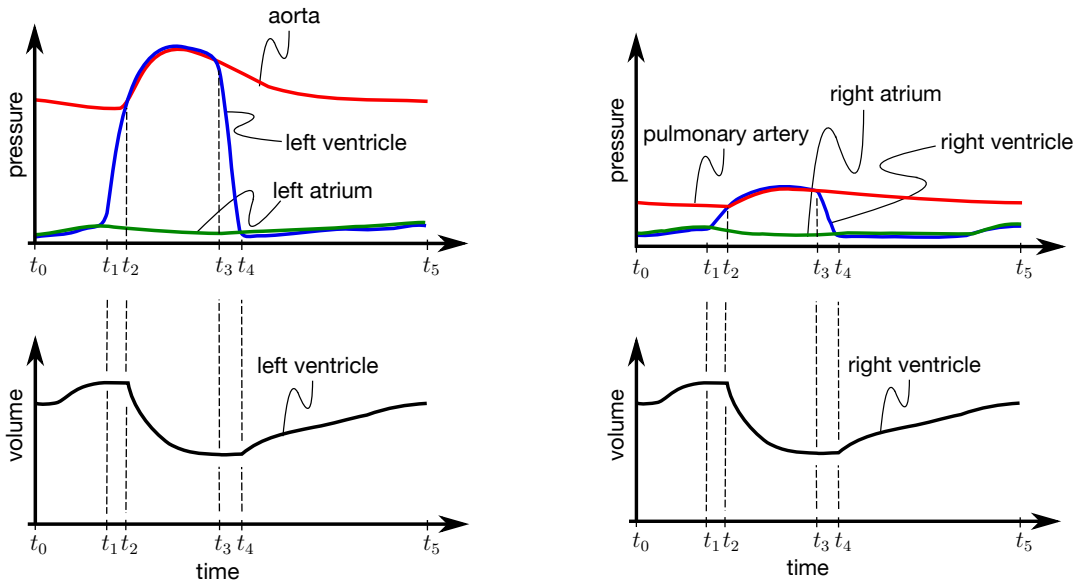

(a) Left atrium and ventricle

(b) Right atrium and ventricle

Figure 1.3.: Sketch of heart chamber pressures and ventricular volumes. Five phases of the cardiac cycle can be identified by t_0 - t_1: atrial contraction and active support of ventricular filling, t_1 - t_2: isovolumetric ventricular contraction, t_2 - t_3: ventricular ejection, t_3 - t_4: isovolumetric relaxation, t_4 - t_5: passive ventricular filling.

Individual changes in chamber pressures and volumes dependent on physical activity (e.g. resting vs. physically exercising person) are normal and important to meet body needs on the one hand. On the other hand, changes in pressure and volume characteristics over longer periods of time might indicate heart dysfunctioning. The term *heart failure* is used to reference a state at which the heart is unable to supply the body with sufficient blood circulation, which might lead to symptoms such as shortness of breath, reduced exercise capacity or fatigue. Distinction is made between *systolic* and *diastolic dysfunction*. In systolic dysfunction, the heart suffers from a reduced contractility. In diastolic dysfunction, ventricular filling is impaired [72].

Prevalence estimation of heart failure is difficult due to the heterogeneity of the disease. A recent review article [49] summarizes an adult population prevalence between 1% and 2% in developed countries in case of recognized heart failure. Prevalence of unrecognized heart failure (e.g. due to misclassification of symptoms) is estimated significantly higher. Besides prevalence, high mortality after a diagnosis outlines the severeness of the disease. A recent meta-analysis [65] of data from mainly Europe and North America states a 5-years survival rate of only 57%, decreasing to 35% for the 10-years survival rate. In summary, heart failure severely diminishes the quality of life by impairing heart performance. The computational model under consideration in this thesis is able to rate patient-specific heart performance from data gained by simulation of full cardiac cycles including a 3D resolved myocardium and a dimensionally reduced model for the blood circulation network. Recently, model application has been presented in the context of ventricular assist device development [59, 139].

1.3. Research objective

Referring back to Section 1.1, there is a high potential value of computational biomedical models in supporting clinical analysis and decision making, while at the same time, the demand on computational resource of large biomedical models quickly becomes a bottleneck in application. In view of this problematic nature, the objective of this thesis is the examination, adaption and extension of state of the art projection-based model order reduction (MOR) techniques to the cardiovascular system, in particular to abdominal aortic aneurysm and cardiac mechanics models.

The so-called *offline-stage* in projection-based MOR aims at the construction of the reduced-order model (ROM). The goal of the offline-stage is twofold: First, a low-dimensional subspace is constructed from processing multiple full-order model (FOM) solutions at selected parameter samples. Second, a small subset of finite elements of the FOM discretization is extracted and stored. Having completed the offline-stage once, a ROM results from a dimensional reduction by restriction of the solution to remain in the low-dimensional subspace and a nonlinear system assembly by evaluation of the extracted subset of mesh elements. The *online-stage* refers to the repeated evaluation of the ROM, which, once constructed, can be evaluated using significantly less computing resources than the FOM.

Contributions in this work are:

- **Model order reduction of prestressing**: In biomedical screening, imaged structures are frequently exposed to mechanical stress. From the viewpoint of structural continuum mechanics, this condition corresponds to a stressed reference configuration, significantly impacting the material response in case of further loading of the nonlinear model. *Prestressing* [46, 47], refers to the incorporation of the prevailing stress state into the fixed imaged configuration, e.g. aortic and cardiac stress due to vascular and ventricular blood pressure, respectively. The presented projection-based MOR framework consistently includes prestressing.

- **Full-order model sampling for reduced-order basis construction**: Referring to the experience of preceding contributions [14, 83, 106], the AAA is modeled by a stationary structural mechanics problem with the deformation under systolic pressure as the configuration of interest. To capture a low-dimensional subspace capable of accurately reproducing all parametrized deformation states, a sampling design based on a greedy maximin distance criterion [122] is proposed.

- **Consistent hyper reduction**: Nonlinear system components in biomedical modeling might be of different nature, requiring individual treatment in hyper reduction. Examples in structural mechanics are the internal force, which needs assembly over the entire mesh including evaluation of constitutive equations, and a nonlinear pressure load, which requires assembly over a surface mesh with exclusively information on the geometry of that surface. In this thesis, consistent hyper reduction means the application of the same hyper reduction algorithm (energy-conserving mesh sampling and weighting, see Section 3.2.2 for details) on different portions of the FOM mesh for different nonlinear system components.

- **Validation for AAA mechanics**: AAAs possess mechanically complex behavior due to phenomena such as nonlinear constitutive laws, prestressing, interaction of thrombus and aortic wall or deformation dependent load (e.g. blood load increases with inflating aneurysm due to increasing luminal surface even at constant pressure). Focusing on stress and strain states in the aneurysm wall, the influence of the quality of selected low-dimensional subspaces and the approximation accuracy of constructed ROMs is investigated.

- **Validation in the context of impaired cardiac functionality**: Heart failure mostly is a consequence of preceding cardiovascular diseases. The model at hand can reproduce pathological conditions by modification of model parameters. The influence of a disease on overall functionality of the heart can be evaluated from heart performance related mechanical quantities such as stroke work or cardiac output. Constructed ROMs resemble conditions in the functionally impaired heart and are evaluated with respect to their ability of predicting heart performance.

1.4. Outline

The content of this thesis is organized as follows:

- **Section 1** motivates the topic addressed in this thesis and gives medical background on the cardiovascular system from an engineering perspective. Focus is laid on the abdominal aortic aneurysm and on cardiac mechanics. Research objective and thesis outline are stated.
- **Section 2** briefly introduces fundamentals of continuum mechanics with focus on 3D solid mechanics as well as 0D (i.e. no resolution of fluid domain geometry) fluid mechanics. In a second step, spatial and temporal discretization methods are addressed and iterative solution techniques for nonlinear systems of equations are recalled.
- **Section 3** initially deals with the general idea of discrete projection on low-dimensional subspaces, which is then rigorously transferred to the application for dimensional reduction of discrete systems of equations. After addressing approaches for the construction of low-dimensional subspaces, the general idea of hyper reduction following narrowed focus on the energy-conserving mesh sampling and weighting method is presented. Both dimensional reduction and hyper reduction are exemplified by simple computational examples.
- **Section 4** deals with projection-based MOR of the AAA model. A discussion of the model is presented first. Special attention is paid to the prestressing stage and a reformulation of it in view of projection-based MOR. Next, the applied sampling algorithm for low-dimensional subspace construction is motivated and stated. Subsequent numerical experiments demonstrate application of the proposed sampling algorithm and hyper reduction to patient-specific AAA models.
- **Section 5** deals with projection-based MOR of the cardiac mechanics model. A discussion of the computational model is presented first, including particularities as the self-contracting myocardial tissue as well as the 0D vascular system. Next, the monolithic and two-way coupled ROM is stated. Subsequent numerical experiments discuss dimensional reducibility of the cardiac mechanics model, show ROM application to homeostatic state estimation and resembling impaired conditions of cardiac performance.

2. Fundamentals on continuum mechanics and finite elements

Biomechanics models introduced in this thesis are based on continuum mechanics. Finite element and finite difference methods are applied for discretization in space and time, respectively. This section focuses on the fundamentals of continuum mechanics, spatial and temporal discretization schemes as well as solution strategies for the resulting nonlinear systems of equations.

2.1. Modeling in continuous space and time

Continuum mechanics is a mathematical formalism that deals with the response of a continuum to environmental influences, whereas a continuum can be seen as a simplified model of matter. The formalism combines general physical principles (such as conservation laws) with a great degree of flexibility in modeling specific material behavior (constitutive laws), which explains the wide application of continuum mechanics in science and engineering. This section gives a brief introduction to continuum mechanics, specifically tailored to the needs of sections hereafter. For a general and more complete overview, the reader is referred to the textbook [60].

2.1.1. Kinematics

Figure 2.1 depicts the general problem setting in continuum mechanics. Starting at time $t = 0$, a body deforms continuously occupying different spatial domains. For the mathematical description of motion, a so-called *deformation map*

$$\boldsymbol{\varphi} : \begin{cases} (\Omega_0, [0, t_{\text{end}}]) \to \Omega \\ (\boldsymbol{x}_0, t) \mapsto \boldsymbol{\varphi}(\boldsymbol{x}_0, t) = \boldsymbol{x}(\boldsymbol{x}_0, t) \end{cases} \tag{2.1}$$

is used. This function maps the non-deforming *reference configuration* Ω_0 to the deforming *current configuration* Ω in the time interval of interest $t \in [0, t_{\text{end}}]$. Thereby, each material element can be referenced by its constant position vector $\boldsymbol{x}_0$ in the reference configuration, while the material element position vector in the current configuration is denoted by $\boldsymbol{x}$.

The following first-order tensor fields are introduced for the description of continuum motion. The *displacement field*

$$\boldsymbol{u}(\boldsymbol{x}_0, t) = \boldsymbol{x}(\boldsymbol{x}_0, t) - \boldsymbol{x}_0, \tag{2.2}$$

the *velocity field*

$$\boldsymbol{v} = \dot{\boldsymbol{u}} \tag{2.3}$$

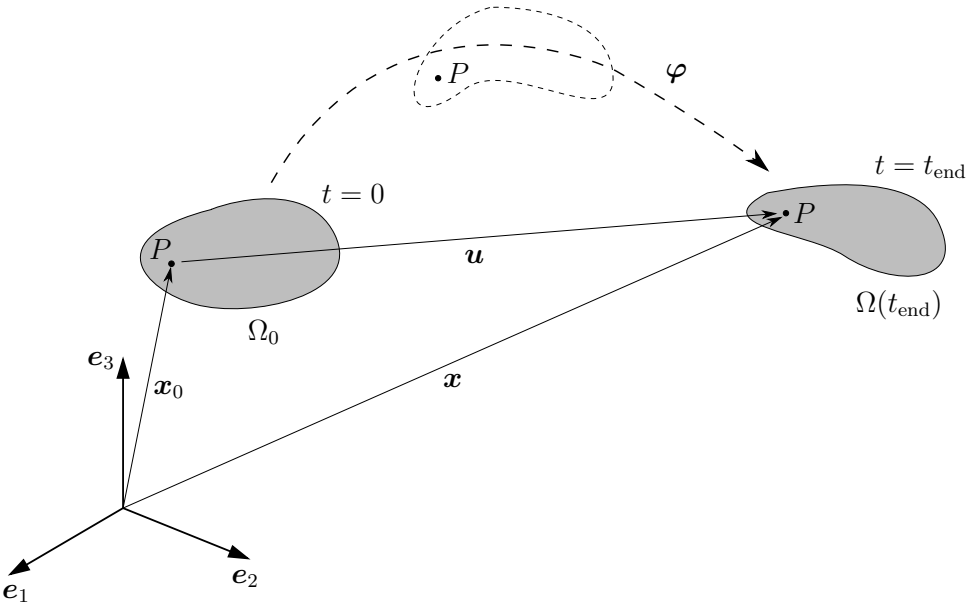

Figure 2.1.: General setting of solid body deformation in continuum mechanics. Deformation starts from the reference configuration $\Omega_0 = \Omega(0)$ at time $t = 0$ and ends at time $t = t_{\text{end}}$ and configuration $\Omega(t_{\text{end}})$.

and the *acceleration field*

$$\boldsymbol{a} = \dot{\boldsymbol{v}} = \ddot{\boldsymbol{u}}. \tag{2.4}$$

The dot $(\dot{\bullet})$ denotes the *material derivative*, which evaluates the temporal rate of change at a fixed material element

$$(\dot{\bullet}) = \frac{d}{dt}(\bullet)\bigg|_{\boldsymbol{x}_0=\text{const}}. \tag{2.5}$$

For description of point-wise continuum deformation, the following quantities are of interest. The *deformation gradient*

$$\boldsymbol{F} = \frac{\partial \boldsymbol{\varphi}(\boldsymbol{x}_0, t)}{\partial \boldsymbol{x}_0} \tag{2.6}$$

is a second-order tensor field which maps material fibers of infinitesimal length from their undeformed configuration $d\boldsymbol{x}_0$ to their deformed configuration $d\boldsymbol{x}$

$$d\boldsymbol{x} = \boldsymbol{F} d\boldsymbol{x}_0. \tag{2.7}$$

Also the deformation of an infinitesimal surface element ($d\boldsymbol{a}_0$ in reference configuration, $d\boldsymbol{a}$ in current configuration)

$$d\boldsymbol{a} = J\boldsymbol{F}^{-T} d\boldsymbol{a}_0 \tag{2.8}$$

as well as infinitesimal volume elements (dv_0 in reference configuration, dv in current configuration)

$$dv = J dv_0 \tag{2.9}$$

with

$$J = \det(\boldsymbol{F}). \tag{2.10}$$

The *right Cauchy-Green tensor* results from

$$\boldsymbol{C} = \boldsymbol{F}^T \boldsymbol{F}. \tag{2.11}$$

It returns the stretch λ of a material fiber $d\boldsymbol{x}_0 = \|d\boldsymbol{x}_0\|_2 \, \boldsymbol{n}_0$ oriented in direction $\boldsymbol{n}_0$ with $\|\boldsymbol{n}_0\|_2 = 1$ by

$$\lambda = \frac{\|d\boldsymbol{x}\|_2}{\|d\boldsymbol{x}_0\|_2} = \sqrt{\boldsymbol{n}_0^T \boldsymbol{C} \boldsymbol{n}_0}. \tag{2.12}$$

Based on the stretch λ, the *Green-Lagrange* strain is given by

$$\varepsilon^{GL} = \frac{1}{2}[\lambda^2 - 1]. \tag{2.13}$$

Using the *Green-Lagrange strain tensor*

$$\boldsymbol{E} = \frac{1}{2}[\boldsymbol{C} - \boldsymbol{I}], \tag{2.14}$$

the Green-Lagrange strain in reference configuration direction $\boldsymbol{n}_0$ can be computed by

$$\varepsilon^{GL} = \boldsymbol{n}_0^T \boldsymbol{E} \boldsymbol{n}_0. \tag{2.15}$$

Given a material fiber in current configuration $d\boldsymbol{x} = \|d\boldsymbol{x}\|_2 \, \boldsymbol{n}$ with orientation $\boldsymbol{n}$, the *Euler-Almansi* strain results from

$$\varepsilon^{EA} = \frac{1}{2}[1 - \lambda^{-2}]. \tag{2.16}$$

Using the *Euler-Almansi strain tensor*

$$\boldsymbol{e} = \frac{1}{2}[\boldsymbol{I} - \boldsymbol{F}^{-T} \boldsymbol{F}^{-1}] \tag{2.17}$$

yields

$$\varepsilon^{EA} = \boldsymbol{n}^T \boldsymbol{e} \boldsymbol{n}. \tag{2.18}$$

2.1.2. Traction and stress

A traction corresponds to a force per surface area and can be introduced as a local quantity using the force $d\boldsymbol{f}$ acting on an infinitesimal surface element of the continuum. Figure 2.2 illustrates the tractions which follow here; the *first Piola-Kirchhoff traction* $\boldsymbol{t}_0$ is defined if the surface element $d\boldsymbol{a}_0 = da_0 \boldsymbol{n}_0$ with $\|\boldsymbol{n}_0\|_2 = 1$ corresponds to the reference configuration

$$\boldsymbol{t}_0 = \frac{d\boldsymbol{f}}{da_0}, \tag{2.19}$$

while conversely a surface element $d\boldsymbol{a} = da\boldsymbol{n}$ on the current configuration in the denominator returns the *Cauchy traction*

$$\boldsymbol{t} = \frac{d\boldsymbol{f}}{da}. \tag{2.20}$$

Given the orientations $\boldsymbol{n}_0$ and $\boldsymbol{n}$ of the reference and current configuration surface elements, respectively, the *first Piola-Kirchhoff stress tensor* $\boldsymbol{P}$ yields the first Piola-Kirchhoff traction by

$$\boldsymbol{t}_0 = \boldsymbol{P}\boldsymbol{n}_0, \tag{2.21}$$

while the *Cauchy stress tensor* $\boldsymbol{\sigma}$ yields the Cauchy traction by

$$\boldsymbol{t} = \boldsymbol{\sigma}\boldsymbol{n}. \tag{2.22}$$

The *second Piola-Kirchhoff stress tensor* $\boldsymbol{S}$ results from

$$\boldsymbol{S} = \boldsymbol{F}^{-1}\boldsymbol{P}. \tag{2.23}$$

$\boldsymbol{S}$ can be interpreted as the work conjugate component to the Green-Lagrange strain tensor

$$J\boldsymbol{\sigma} : \nabla_{\boldsymbol{x}}\boldsymbol{v} = \boldsymbol{P} : \dot{\boldsymbol{F}} = \boldsymbol{S} : \dot{\boldsymbol{E}}. \tag{2.24}$$

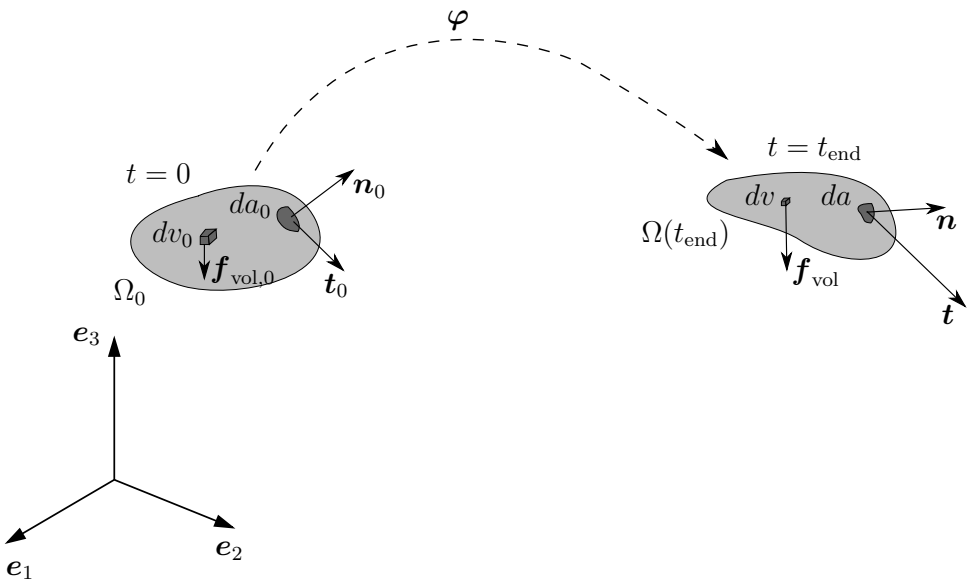

Figure 2.2.: Visualization of traction and volumetric force as well as corresponding surface and volume elements in reference and current configuration. The traction $\boldsymbol{t}_0$ and volumetric force $\boldsymbol{f}_{\text{vol},0}$ are parallel to the traction $\boldsymbol{t}$ and volumetric force $\boldsymbol{f}_{\text{vol}}$, respectively.

2.1.3. Constitutive modeling of a solid continuum

Constitutive modeling describes the stress response of a material, typically based on a strain measure and possibly additional internal variables. A well chosen constitutive law must on the one hand reflect the phenomenological behavior of the specific material such as elasticity, plasticity or viscosity and on the other hand be physically meaningful in that it satisfies thermodynamic

principles. In this thesis, homogeneous hyperelasticity is used. This class of constitutive laws can be modeled by a so-called strain energy density

$$\Psi = \Psi(I_1, I_2, I_3), \tag{2.25}$$

which can be expressed as a function of the three *principal invariants* of the right Cauchy-Green tensor

$$I_1 = \mathrm{tr}(\boldsymbol{C}), \tag{2.26}$$

$$I_2 = \frac{1}{2}[\mathrm{tr}(\boldsymbol{C})^2 - \mathrm{tr}(\boldsymbol{C}^2)], \tag{2.27}$$

$$I_3 = \det(\boldsymbol{C}). \tag{2.28}$$

The strain energy density maps a second-order tensor to a scalar and has units of energy per volume $[\mathrm{J/m^3}]$. Given the relations for the principle invariants (2.26) - (2.28), Ψ can equivalently be expressed as a function of $\boldsymbol{C}$, or as a function of $\boldsymbol{E}$ or $\boldsymbol{F}$, recalling relations (2.6), (2.11) and (2.14). In the remainder of this thesis, an implicit conversion of the functional dependency of the strain energy density function is assumed for notational convenience. For instance, the relation

$$\Psi(I_1, I_2, I_3) = \Psi(\boldsymbol{C}) = \Psi(\boldsymbol{E}) = \Psi(\boldsymbol{F}) \tag{2.29}$$

is assumed to hold by implicit conversion of functional dependencies. Following the *Coleman-Noll* procedure [25], an entropy inequality returns a relation between the strain energy density and the first Piola-Kirchhoff stress tensor

$$\boldsymbol{P} = \frac{\partial \Psi(\boldsymbol{F})}{\partial \boldsymbol{F}}. \tag{2.30}$$

Using the definition of the Green-Lagrange strain tensor (2.14) together with equation (2.23), constitutive relation (2.30) can be written in terms of the second Piola-Kirchhoff stress tensor

$$\boldsymbol{S} = \frac{\partial \Psi(\boldsymbol{E})}{\partial \boldsymbol{E}}. \tag{2.31}$$

2.1.4. Balance equations

In this thesis, purely mechanical solids (i.e. neglecting effects such as internal heat transfer, interaction with magnetic fields, etc.) and an incompressible, dimensionally reduced fluid network are under consideration. As a result, a mass balance as well as a momentum balance sufficiently describe the physics for evaluation of numerical simulations. Mass balance in the reference configuration reads

$$\dot{\rho}_0 = 0, \tag{2.32}$$

while the mass balance in current configuration is given by

$$\dot{\rho} + \rho \nabla_{\boldsymbol{x}} \cdot \boldsymbol{v} = 0. \tag{2.33}$$

The reference configuration density ρ_0 is the ratio of a material element mass dm to its undeformed volume dv_0

$$\rho_0 = \frac{dm}{dv_0}, \tag{2.34}$$

while the current configuration density ρ is the ratio of material element mass over its deformed volume

$$\rho = \frac{dm}{dv}. \tag{2.35}$$

The linear momentum balance in the reference configuration reads

$$\rho_0 \dot{\boldsymbol{v}} = \nabla_{\boldsymbol{x}_0} \cdot \boldsymbol{P} + \boldsymbol{f}_{\text{vol},0}, \tag{2.36}$$

while the linear momentum balance in current configuration is given by

$$\rho \dot{\boldsymbol{v}} = \nabla_{\boldsymbol{x}} \cdot \boldsymbol{\sigma} + \boldsymbol{f}_{\text{vol}}. \tag{2.37}$$

Analogous to the densities ρ_0 and ρ, the volumetric forces $\boldsymbol{f}_{\text{vol},0}$ and $\boldsymbol{f}_{\text{vol}}$ (see Figure 2.2) correspond to the material element force $d\boldsymbol{f}$ over its undeformed volume

$$\boldsymbol{f}_{\text{vol},0} = \frac{d\boldsymbol{f}}{dv_0} \tag{2.38}$$

and the material element force over its deformed volume

$$\boldsymbol{f}_{\text{vol}} = \frac{d\boldsymbol{f}}{dv}. \tag{2.39}$$

The angular momentum balance is satisfied by the symmetry of the Cauchy stress tensor, which also entails the symmetry of the second Piola-Kirchhoff stress tensor

$$\boldsymbol{\sigma} = \boldsymbol{\sigma}^T, \quad \boldsymbol{S} = \boldsymbol{S}^T. \tag{2.40}$$

In general, the first Piola-Kirchhoff stress tensor is not symmetric.

2.1.5. Dimensionally reduced modeling of fluid mechanics

In this thesis, a dimensionally reduced flow network is used for modeling blood flow in the vascular system. This network can be viewed as a circuit consisting of individual elements manipulating the flow, which in turn is modeled based on low-order 1D solutions of the full Navier-Stokes equations for incompressible flow [90]

$$\nabla_{\boldsymbol{x}} \cdot \boldsymbol{v} = 0, \tag{2.41}$$

$$\rho \dot{\boldsymbol{v}} = -\nabla_{\boldsymbol{x}} p + 2\nu_{\text{dyn}} \nabla_{\boldsymbol{x}} \cdot \boldsymbol{\tau} + \boldsymbol{f}_{\text{vol}}, \tag{2.42}$$

wherein ν_{dyn} is the (constant) dynamic viscosity (of dimension $\left[\frac{\text{kg}}{\text{m s}}\right]$) and $\boldsymbol{\tau}$ is the symmetric part of the velocity gradient

$$\boldsymbol{\tau} = \frac{1}{2}[\nabla_{\boldsymbol{x}} \boldsymbol{v} + [\nabla_{\boldsymbol{x}} \boldsymbol{v}]^T]. \tag{2.43}$$

The presented Navier-Stokes equations correspond to the mass balance (2.33) (with $\dot{\rho} = 0$ due to incompressibility) and the momentum balance (2.37) using the constitutive equation

$$\boldsymbol{\sigma} = -p\boldsymbol{I} + 2\nu_{\text{dyn}} \boldsymbol{\tau} \tag{2.44}$$

for Newtonian fluids [90]. Although blood in general is known to have non-Newtonian fluid properties [96], the modeling of hemodynamics using Newtonian flow equations is supposed as a valid approximation in this thesis [57].

For vascular system flows, so-called *windkessel* models have been developed and improved over time [103, 125, 138]. These models are very much analogous to electric circuits and consist of a combination of flow network elements such as resistances, capacitances and inertances. In the following, the network components applied in this thesis for modeling the vascular system in Section 5 are briefly introduced. A detailed derivation is shown in [57]. Following the terminology in [57], the network and its components are characterized as *0D*.

2.1.5.1. 0D flow network components

Pressure p and flow rate q (of dimension $\left[\frac{\mathrm{m}^3}{s}\right]$) are the two quantities of interest in 0D flow networks. There is a clear relation to electric circuits, wherein voltage and electric current can be seen as analogous to pressure and flow rate. In this section, several 0D flow elements, which combined can model complex flow networks, are introduced.

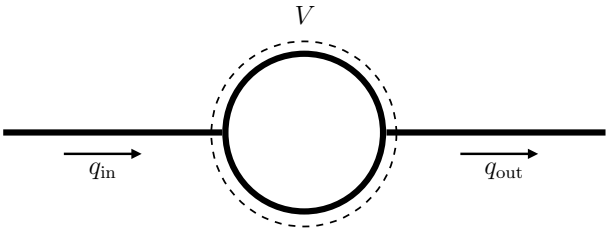

Figure 2.3.: Compartment element in 0D fluid flow.

Compartment: An elastic compartment (see Figure 2.3) corresponds to a volume that can accumulate and release fluid. As such, a decrease in the flow rate is described by the rate of volume change of the compartment

$$\frac{\mathrm{d}V}{\mathrm{d}t} = q_{\mathrm{in}} - q_{\mathrm{out}}. \tag{2.45}$$

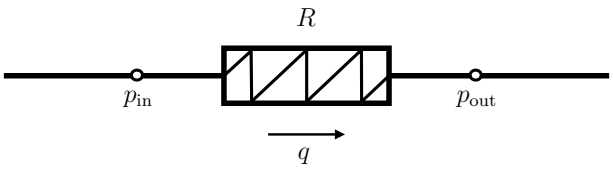

Figure 2.4.: Resistance element in 0D fluid flow.

Resistance: A resistance (see Figure 2.4) produces a pressure decrease which is proportional to the flow rate

$$Rq = p_{\mathrm{in}} - p_{\mathrm{out}}. \tag{2.46}$$

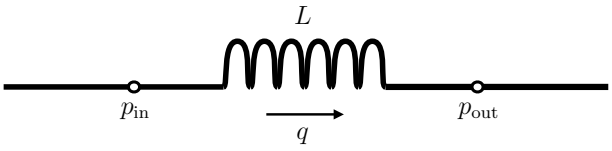

Figure 2.5.: Inertance element in 0D fluid flow.

Inertance: An inertance (see Figure 2.5) produces a pressure decrease which is proportional to the change of flow rate

$$L\frac{\mathrm{d}q}{\mathrm{d}t} = p_{\text{in}} - p_{\text{out}}. \tag{2.47}$$

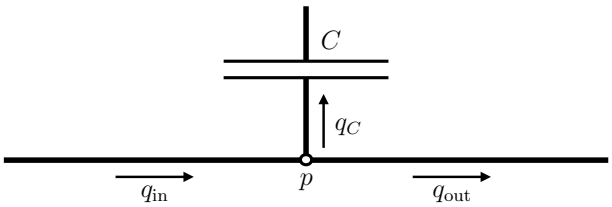

Figure 2.6.: Capacitance element in 0D fluid flow.

Capacitance: A capacitance (see Figure 2.6) is able to accumulate and release fluid as a reaction to a change in pressure

$$C\frac{\mathrm{d}p}{\mathrm{d}t} = q_{\text{in}} - q_{\text{out}}, \tag{2.48}$$

$$q_C = C\frac{\mathrm{d}p}{\mathrm{d}t}. \tag{2.49}$$

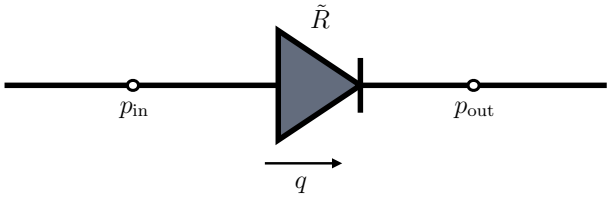

Figure 2.7.: Valve element in 0D fluid flow.

Valve: A valve (see Figure 2.7) yields a pressure decrease when a flow rate is present. In contrast to the resistance, the proportionality constant $\tilde{R}$ changes with the pressure gradient across the valve

$$\tilde{R}q = p_{\text{in}} - p_{\text{out}}, \tag{2.50}$$

$$\tilde{R} = \begin{cases} R^{\max} & \text{for } p_{\text{in}} < p_{\text{out}} \\ R^{\min} & \text{for } p_{\text{in}} \geq p_{\text{out}} \end{cases}. \tag{2.51}$$

0D network demonstrator: An exemplary derivation of equations describing a 0D flow system is presented in the following. The system is depicted in Figure 2.8, it combines two resistances, one capacitance and one inertance. In more detail, a set of equations that will describe the flow rate q_{out} and pressure p_{out} at the outlet given the quantities q_{in} and p_{in} at the inflow is wanted. From the mass balance (2.48), the wanted flow rate q_{out} is reduced by the flow rate into the capacitance q_C, which in turn following equation (2.49) depends on the rate of change of capacitance pressure. This quantity can be expressed as combination of the rate of change of inflow pressure as well the pressure decrease over the resistance, which reads

$$\frac{\mathrm{d}p_C}{\mathrm{d}t} = \frac{\mathrm{d}p_{\text{in}}}{\mathrm{d}t} - R_1 \frac{\mathrm{d}q_{\text{in}}}{\mathrm{d}t}. \tag{2.52}$$

As a result, the equation for the flow rate at the outflow is

$$q_{\text{out}} = q_{\text{in}} - C \left[\frac{\mathrm{d}p_{\text{in}}}{\mathrm{d}t} - R_1 \frac{\mathrm{d}q_{\text{in}}}{\mathrm{d}t} \right]. \tag{2.53}$$

The outflow pressure can be calculated from the inflow pressure and the accumulated pressure decrease over the involved 0D flow elements. The pressure decrease due to resistance is given in equation (2.46), while the pressure decrease due to inertance results from equation (2.47). Combining everything, the outflow pressure reads

$$p_{\text{out}} = p_{\text{in}} - R_1 q_{\text{in}} - R_2 q_{\text{out}} - L \frac{\mathrm{d}q_{\text{out}}}{\mathrm{d}t}. \tag{2.54}$$

As a result, given the flow rate and pressure at the inlet as a function of time, the flow rate and pressure at the outlet can be computed from equations (2.53) and (2.54).

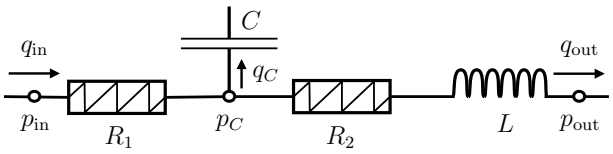

Figure 2.8.: Exemplary 0D flow system.

2.2. Model discretization and solution

The *finite element method* is well established for the spatial discretization of mathematical models. Starting from the weak form of the governing equations, the computational domain is approximated by a set of geometrically simple (e.g. tetrahedral, hexahedral, pyramid) shapes, the so-called finite elements. Defining *shape functions* per finite element results in a spatially discrete model as a result of approximating the solution by a weighted sum of all shape functions. These steps are depicted briefly in Section 2.2.1 and 2.2.2; for a more detailed presentation of the finite element method in the context of solid mechanics the reader is referred to the textbook [143].

In case of dynamic simulations, temporal discretization is additionally required to receive a numerically tractable computational model. The generalized-α (gen-α) method is applied for the

second-order ordinary differential equation (ODE) of spatially discretized structural mechanics, while a one-step-θ (OST) scheme is used for first-order ODEs. The time stepping methods are discussed in Section 2.2.3. Finally, iterative techniques for solving the resulting nonlinear systems of equations are presented in Section 2.2.4.

2.2.1. Weak form momentum equation

The weak form of the balance of linear momentum in the reference configuration (2.36) is derived by first contracting the momentum equation with an arbitrary *weighting function* $\delta\boldsymbol{u}$. This results in the scalar equation

$$[\rho_0\ddot{\boldsymbol{u}} - \nabla_{\boldsymbol{x}_0}\cdot\boldsymbol{P} - \boldsymbol{f}_{\text{vol},0}]\cdot\delta\boldsymbol{u} = 0 \quad \forall\delta\boldsymbol{u}. \tag{2.55}$$

Integration over the reference computational domain Ω_0 yields

$$\int_{\Omega_0}[\rho_0\ddot{\boldsymbol{u}}]\cdot\delta\boldsymbol{u}dv_0 - \int_{\Omega_0}[\nabla_{\boldsymbol{x}_0}\cdot\boldsymbol{P}]\cdot\delta\boldsymbol{u}dv_0 - \int_{\Omega_0}\boldsymbol{f}_{\text{vol},0}\cdot\delta\boldsymbol{u}dv_0 = 0 \quad \forall\delta\boldsymbol{u}. \tag{2.56}$$

Application of the divergence operator to the first Piola-Kirchhoff stress tensor is undesirable and can be avoided using

$$\int_{\Omega_0}[\nabla_{\boldsymbol{x}_0}\cdot\boldsymbol{P}]\cdot\delta\boldsymbol{u}dv_0 = \int_{\Omega_0}\left(\nabla_{\boldsymbol{x}_0}\cdot[\boldsymbol{P}^T\delta\boldsymbol{u}] - \boldsymbol{P}:\nabla_{\boldsymbol{x}_0}\delta\boldsymbol{u}\right)dv_0 \tag{2.57}$$

together with the *Neumann* boundary conditions in terms of a first Piola-Kirchhoff traction load $\boldsymbol{t}_0$

$$\int_{\Omega_0}\nabla_{\boldsymbol{x}_0}\cdot[\boldsymbol{P}^T\delta\boldsymbol{u}]dv_0 = \int_{\partial\Omega_0}[\boldsymbol{P}\boldsymbol{n}_0]\cdot\delta\boldsymbol{u}da_0 = \int_{\partial\Omega_0}\boldsymbol{t}_0\cdot\delta\boldsymbol{u}da_0, \tag{2.58}$$

wherein $\partial\Omega_0$ denotes the boundary of the computational domain. Finally, the weak form reads

$$\int_{\Omega_0}[\rho_0\ddot{\boldsymbol{u}}]\cdot\delta\boldsymbol{u}dv_0 + \int_{\Omega_0}\boldsymbol{P}:\nabla_{\boldsymbol{x}_0}\delta\boldsymbol{u}dv_0 - \int_{\Omega_0}\boldsymbol{f}_{\text{vol},0}\cdot\delta\boldsymbol{u}dv_0 - \int_{\partial\Omega_0}\boldsymbol{t}_0\cdot\delta\boldsymbol{u}da_0 = 0 \quad \forall\delta\boldsymbol{u}. \tag{2.59}$$

For structural dynamics problems, the weak form of momentum equations implies the principle of virtual work (PVW), if the weighing function $\delta\boldsymbol{u}$ is interpreted as a *virtual displacement field*. The PVW states that the imbalance of internal $\delta W_{\text{int}}(\boldsymbol{u},\delta\boldsymbol{u})$ and external $\delta W_{\text{ext}}(\boldsymbol{u},\delta\boldsymbol{u})$ virtual work corresponds to the variation of momentum

$$\int_{\Omega_0}[\rho_0\ddot{\boldsymbol{u}}]\cdot\delta\boldsymbol{u}dv_0 + \delta W_{\text{int}}(\boldsymbol{u},\delta\boldsymbol{u}) - \delta W_{\text{ext}}(\boldsymbol{u},\delta\boldsymbol{u}) = 0, \tag{2.60}$$

wherein

$$\delta W_{\text{int}}(\boldsymbol{u},\delta\boldsymbol{u}) = \int_{\Omega_0}\boldsymbol{P}:\nabla_{\boldsymbol{x}_0}\delta\boldsymbol{u}dv_0 \tag{2.61}$$

was used and

$$\delta W_{\text{ext}}(\boldsymbol{u},\delta\boldsymbol{u}) = \int_{\Omega_0}\boldsymbol{f}_{\text{vol},0}\cdot\delta\boldsymbol{u}dv_0 + \int_{\partial\Omega_0}\boldsymbol{t}_0\cdot\delta\boldsymbol{u}da_0. \tag{2.62}$$

For the definition of appropriate function spaces for the displacement field $\boldsymbol{u}$ and weighting function field $\delta\boldsymbol{u}$ in the weak form the reader is referred to [62].

2.2.2. Discretization in space

A brief review of the finite element method with a focus on structural mechanics problems is provided in this Section. In a first step, an approximation of the computational domain is subdivided into a set of N_e finite elements

$$\Omega_0 \approx \tilde{\Omega}_0 = \bigcup_{e=0}^{N_e-1} \Omega_0^{(e)}. \tag{2.63}$$

Finite elements can differ in several properties; their main characteristics however are their shape and order of interpolation, which in turn determines the number of element nodes n_n (see Figure 2.9). Each node holds a set of degrees of freedom (DOFs), in our case the set of DOFs corresponds to the nodal displacement in each of the three spatial directions. As a result, the number of element DOFs n_e results from $n_e = 3n_n$.

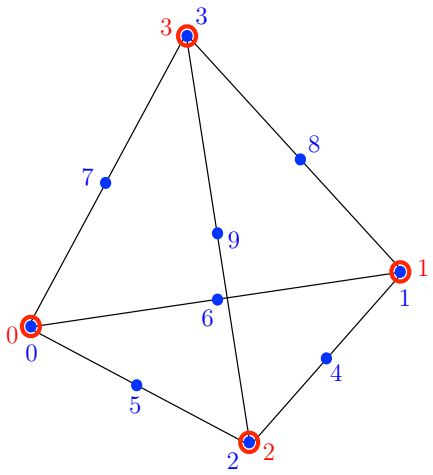

Figure 2.9.: Tetrahedral finite element with distribution and enumeration of nodes. Red circles indicate nodes of a linearly interpolating element. Blue dots indicate nodes of a quadratically interpolating element.

From a mathematical viewpoint, element nodes have associated *shape functions* $N_i(\boldsymbol{x}_0), i \in \{0, \ldots, n_n - 1\}$, which are unity at exactly one node and null at the remaining nodes. As a result, element-wise displacement and virtual displacement field can be interpolated by

$$\boldsymbol{u}^{(e)} = \boldsymbol{\Phi}^{(e)} \boldsymbol{d}^{(e)}, \tag{2.64}$$

$$\delta\boldsymbol{u}^{(e)} = \boldsymbol{\Phi}^{(e)} \delta\boldsymbol{d}^{(e)}, \tag{2.65}$$

using the element displacement DOF vector $\boldsymbol{d}^{(e)}$ and virtual displacement DOF vector $\delta\boldsymbol{d}^{(e)}$

$$\boldsymbol{d}^{(e)} = \begin{bmatrix} d_{0,0}^{(e)} \\ d_{0,1}^{(e)} \\ d_{0,2}^{(e)} \\ \vdots \\ d_{n_n-1,0}^{(e)} \\ d_{n_n-1,1}^{(e)} \\ d_{n_n-1,2}^{(e)} \end{bmatrix} \in \mathbb{R}^{n_e}, \quad \delta\boldsymbol{d}^{(e)} = \begin{bmatrix} \delta d_{0,0}^{(e)} \\ \delta d_{0,1}^{(e)} \\ \delta d_{0,2}^{(e)} \\ \vdots \\ \delta d_{n_n-1,0}^{(e)} \\ \delta d_{n_n-1,1}^{(e)} \\ \delta d_{n_n-1,2}^{(e)} \end{bmatrix} \in \mathbb{R}^{n_e} \tag{2.66}$$

with $d_{i,j}^{(e)}, \delta d_{i,j}^{(e)}$ denoting the displacement and virtual displacement of node i in spatial direction j, respectively. The element matrix $\boldsymbol{\Phi}^{(e)}$ contains the shape functions and is given by

$$\boldsymbol{\Phi}^{(e)} = \begin{bmatrix} N_0(\boldsymbol{x}_0) & 0 & 0 & \dots & N_{n_n-1}(\boldsymbol{x}_0) & 0 & 0 \\ 0 & N_0(\boldsymbol{x}_0) & 0 & \dots & 0 & N_{n_n-1}(\boldsymbol{x}_0) & 0 \\ 0 & 0 & N_0(\boldsymbol{x}_0) & \dots & 0 & 0 & N_{n_n-1}(\boldsymbol{x}_0) \end{bmatrix} \in \mathbb{R}^{3\times n_e}. \tag{2.67}$$

Thereby, $\boldsymbol{\Phi}^{(e)}$ is designed such that the discrete fields (2.64) and (2.65) fulfill the requirements on differentiability of the mentioned weak form function spaces.

Introducing the interpolation (2.64) and (2.65) into the principle of virtual work (2.59) yields a sum over finite elements

$$\begin{aligned} \sum_{e=0}^{N_e-1} \Bigg[\int_{\Omega_0^{(e)}} [\rho_0^{(e)} \ddot{\boldsymbol{u}}^{(e)}] \cdot \delta\boldsymbol{u}^{(e)} dv_0 + \int_{\Omega_0^{(e)}} \boldsymbol{P}^{(e)} : \nabla_{\boldsymbol{x}_0} \delta\boldsymbol{u}^{(e)} dv_0 - \int_{\Omega_0^{(e)}} \boldsymbol{f}_{\text{vol},0}^{(e)} \cdot \delta\boldsymbol{u}^{(e)} dv_0 \\ - \int_{\partial\Omega_0^{(e)}} \boldsymbol{t}_0^{(e)} \cdot \delta\boldsymbol{u}^{(e)} da_0 \Bigg] = 0 \quad \forall \delta\boldsymbol{u}^{(e)},\ e \in \{0, \dots, N_e - 1\}, \end{aligned} \tag{2.68}$$

wherein the integral $\int_{\partial\Omega_0^{(e)}} \boldsymbol{t}_0^{(e)} \cdot \delta\boldsymbol{u}^{(e)} da_0$ is simply evaluated to 0, if the element (e) is not intersecting with the computational domain boundary or if no traction $\boldsymbol{t}_0$ (i.e. zero traction) is defined on the corresponding element face. Equation (2.68) can be rewritten as

$$\sum_{e=0}^{N_e-1} [\boldsymbol{M}^{(e)} \ddot{\boldsymbol{d}}^{(e)} + \boldsymbol{f}_{\text{int}}^{(e)} - \boldsymbol{f}_{\text{ext}}^{(e)}] \cdot \delta\boldsymbol{d}^{(e)} = 0 \quad \forall \delta\boldsymbol{d}^{(e)},\ e \in \{0, \dots, N_e - 1\}. \tag{2.69}$$

The element mass matrix $\boldsymbol{M}^{(e)}$ fulfills

$$\int_{\Omega_0^{(e)}} [\rho_0^{(e)} \ddot{\boldsymbol{u}}^{(e)}] \cdot \delta\boldsymbol{u}^{(e)} dv_0 = [\boldsymbol{M}^{(e)} \ddot{\boldsymbol{d}}^{(e)}] \cdot \delta\boldsymbol{d}^{(e)}, \tag{2.70}$$

the element internal force vector $\boldsymbol{f}_{\text{int}}^{(e)}$ fulfills

$$\int_{\Omega_0^{(e)}} \boldsymbol{P}^{(e)} : \nabla_{\boldsymbol{x}_0} \delta\boldsymbol{u}^{(e)} dv_0 = \boldsymbol{f}_{\text{int}}^{(e)} \cdot \delta\boldsymbol{d}^{(e)} \tag{2.71}$$

and the element external force vector fulfills

$$\int_{\Omega_0^{(e)}} \boldsymbol{f}_{\text{vol},0}^{(e)} \cdot \delta \boldsymbol{u}^{(e)} dv_0 + \int_{\partial\Omega_0^{(e)}} \boldsymbol{t}_0^{(e)} \cdot \delta \boldsymbol{u}^{(e)} da_0 = \boldsymbol{f}_{\text{ext}}^{(e)} \cdot \delta \boldsymbol{d}^{(e)}, \tag{2.72}$$

wherein again the boundary integral vanishes in case of domain-internal elements or in the absence of boundary traction.

Introducing the global mass matrix $\boldsymbol{M} \in \mathbb{R}^{N\times N}$, global displacement and virtual displacement DOF vectors $\boldsymbol{d}, \delta\boldsymbol{d} \in \mathbb{R}^N$ and global internal and external force vector $\boldsymbol{f}_{\text{int}}, \boldsymbol{f}_{\text{ext}} \in \mathbb{R}^N$ (constructed by assembling the corresponding element quantities), equation (2.69) can be rewritten by including the summation implicitly into vector multiplication operations

$$[\boldsymbol{M}\ddot{\boldsymbol{d}} + \boldsymbol{f}_{\text{int}} - \boldsymbol{f}_{\text{ext}}] \cdot \delta\boldsymbol{d} = 0 \quad \forall \delta\boldsymbol{d} \tag{2.73}$$

which means that the expression inside the brackets must vanish

$$\boldsymbol{M}\ddot{\boldsymbol{d}} + \boldsymbol{f}_{\text{int}}(\boldsymbol{d}, t) - \boldsymbol{f}_{\text{ext}}(\boldsymbol{d}, t) = \boldsymbol{0}. \tag{2.74}$$

Equation (2.74) corresponds to a spatially discretized model of an undamped solid continuum. Explicitly added were the internal and external force arguments $(\boldsymbol{d}, t)$ in order to highlight the (potential) nonlinearity of the model. Damping is frequently added to the numerical model by applying the so-called *Rayleigh damping*. The idea here is to construct a global damping matrix from a weighted superposition of the mass matrix and referential internal force stiffness

$$\boldsymbol{D} = c_M \boldsymbol{M} + c_f \left.\frac{\partial \boldsymbol{f}_{\text{int}}(\boldsymbol{d}, t)}{\partial \boldsymbol{d}}\right|_{\boldsymbol{d}=\boldsymbol{0}} \tag{2.75}$$

with c_M and c_f as scalar factors. Including damping, the final spatially discretized computational model for solid dynamics reads

$$\boldsymbol{M}\ddot{\boldsymbol{d}} + \boldsymbol{D}\dot{\boldsymbol{d}} + \boldsymbol{f}_{\text{int}}(\boldsymbol{d}, t) - \boldsymbol{f}_{\text{ext}}(\boldsymbol{d}, t) = \boldsymbol{0}. \tag{2.76}$$

Equation (2.76) reduces to a steady-state expression, if inertial and damping effects are neglected. The steady state equations read

$$\boldsymbol{f}_{\text{int}}(\boldsymbol{d}) - \boldsymbol{f}_{\text{ext}}(\boldsymbol{d}) = \boldsymbol{0}. \tag{2.77}$$

2.2.3. Discretization in (pseudo)time

In this thesis, several time integration schemes for solving first- and second-order ODEs are applied. Also, the steady state problem (2.77) is solved by applying pseudo time steps, which is detailed in this section.

First-order ODE: For time integration of first-order ODEs of the form

$$\dot{\boldsymbol{q}} = \boldsymbol{f}(\boldsymbol{q}) \tag{2.78}$$

the one-step-θ (OST) scheme [128]

$$\frac{\boldsymbol{q}^n - \boldsymbol{q}^{n-1}}{\Delta t} = \theta \boldsymbol{f}(\boldsymbol{q}^n) + [1-\theta]\boldsymbol{f}(\boldsymbol{q}^{n-1}), \tag{2.79}$$

is used, wherein the superscript n denotes the time step and $\theta \in [0, 1]$ is a scalar parameter yielding explicit time stepping for $\theta = 0$.

Second-order ODE: Equation (2.76) corresponds to a second-order system of ODEs, which requires a temporal discretization scheme for the numerical solution. The generalized-α (gen-α) method [22] is used for the second-order ODE at hand. Thereby, the time-continuous system is solved iteratively for every time step n. The residual reads

$$\boldsymbol{r}^n(\boldsymbol{d}^n) = \boldsymbol{0} \tag{2.80}$$

with

$$\boldsymbol{r}^n(\boldsymbol{d}^n) = \boldsymbol{M}\boldsymbol{a}^{n-\alpha_m} + \boldsymbol{D}\boldsymbol{v}^{n-\alpha_f} + \boldsymbol{f}_{\text{int}}^{n-\alpha_f}(\boldsymbol{d}^n) - \boldsymbol{f}_{\text{ext}}^{n-\alpha_f}(\boldsymbol{d}^n). \tag{2.81}$$

Velocity, acceleration and internal as well as external forces result from a weighted combination of current and previous time step values

$$\boldsymbol{v}^{n-\alpha_f} = [1-\alpha_f]\boldsymbol{v}^n + \alpha_f \boldsymbol{v}^{n-1}, \tag{2.82}$$
$$\boldsymbol{a}^{n-\alpha_m} = [1-\alpha_m]\boldsymbol{a}^n + \alpha_m \boldsymbol{a}^{n-1}, \tag{2.83}$$
$$\boldsymbol{f}_{\text{int}}^{n-\alpha_f} = [1-\alpha_f]\boldsymbol{f}_{\text{int}}(\boldsymbol{d}^n, t^n) + \alpha_f \boldsymbol{f}_{\text{int}}(\boldsymbol{d}^{n-1}, t^{n-1}), \tag{2.84}$$
$$\boldsymbol{f}_{\text{ext}}^{n-\alpha_f} = [1-\alpha_f]\boldsymbol{f}_{\text{ext}}(\boldsymbol{d}^n, t^n) + \alpha_f \boldsymbol{f}_{\text{ext}}(\boldsymbol{d}^{n-1}, t^{n-1}), \tag{2.85}$$

wherein the constants $\alpha_m \in [0, 1]$ and $\alpha_f \in [0, 1]$ were introduced. In contrast to the displacement field, the velocity and acceleration field are not primary variables. The reconstruction of velocity and acceleration reads

$$\boldsymbol{v}^n = \frac{\gamma}{\beta\Delta t}[\boldsymbol{d}^n - \boldsymbol{d}^{n-1}] - \frac{\gamma-\beta}{\beta}\boldsymbol{v}^{n-1} - \frac{\gamma-2\beta}{2\beta}\Delta t\boldsymbol{a}^{n-1}, \tag{2.86}$$
$$\boldsymbol{a}^n = \frac{1}{\beta\Delta t^2}[\boldsymbol{d}^n - \boldsymbol{d}^{n-1}] - \frac{1}{\beta\Delta t}\boldsymbol{v}^{n-1} - \frac{1-2\beta}{2\beta}\boldsymbol{a}^{n-1} \tag{2.87}$$

using the constants $\gamma \in [0, 1]$ and $\beta \in [0, \frac{1}{2}]$. Numerical dissipation of the time integration algorithm can be adjusted by the parameter $\rho_\infty \in [0, 1]$ and choosing the remaining parameters as

$$\alpha_m = \frac{2\rho_\infty - 1}{\rho_\infty + 1}, \tag{2.88}$$
$$\alpha_f = \frac{\rho_\infty}{\rho_\infty + 1}, \tag{2.89}$$
$$\beta = \frac{1}{4}(1 - \alpha_m + \alpha_f)^2, \tag{2.90}$$
$$\gamma = \frac{1}{2} - \alpha_m + \alpha_f. \tag{2.91}$$

Steady-state system: The steady-state nonlinear system (2.77) typically arises from a problem setup, wherein the external load $\boldsymbol{f}_{\text{ext}}$ is prescribed (e.g. directly or by a surface traction requiring

surface integration and linearization), while a displacement field is calculated such that internal and external forces are in equilibrium. For large loads with pronounced continuum deformation, the numerical model may not converge, if the entire load is applied immediately. Therefore, *pseudo time steps* (which can be interpreted as load steps) are introduced for the steady-state problem. The residual notation reads

$$\boldsymbol{r}^n(\boldsymbol{d}^n) = \boldsymbol{f}^n_{\mathrm{int}}(\boldsymbol{d}^n) - \boldsymbol{f}^n_{\mathrm{ext}}(\boldsymbol{d}^n), \tag{2.92}$$

wherein the superscript ^{n} specifies the load step.

2.2.4. Nonlinear solution techniques

The spatially and temporally discretized systems presented above can be iteratively solved for the discretized displacement field $\boldsymbol{d}^n$ via Newton-Raphson iterations

$$\begin{aligned} \boldsymbol{J}^n_r(\boldsymbol{d}^n_i)\Delta\boldsymbol{d}^n_{i+1} &= -\boldsymbol{r}^n(\boldsymbol{d}^n_i) \\ \boldsymbol{d}^n_{i+1} &= \boldsymbol{d}^n_i + \Delta\boldsymbol{d}^n_{i+1}, \end{aligned} \tag{2.93}$$

wherein the residual Jacobian

$$\boldsymbol{J}^n_r(\boldsymbol{d}^n_i) \coloneqq \frac{\partial \boldsymbol{r}^n(\boldsymbol{d}^n_i)}{\partial \boldsymbol{d}} \tag{2.94}$$

was used. The iteration scheme (2.93) is terminated in case of a residual tolerance and a displacement increment tolerance criterion

$$\|\boldsymbol{r}^n(\boldsymbol{d}^n_i)\|_2 \leq \varepsilon_r, \quad \|\Delta\boldsymbol{d}^n_i\|_2 \leq \varepsilon_d. \tag{2.95}$$

For an improvement of convergence properties, the Newton-Raphson iteration scheme can be enhanced with the so-called pseudo-transient continuation (PTC) technique [43]. The basic idea is to increase diagonal values of the Jacobian, which results in a regularization of the linearized system of equations (2.93). Including PTC, the modified system (as compared to (2.93)) reads

$$[\boldsymbol{J}^n_r(\boldsymbol{d}^n_i) + k^{\mathrm{ptc}}_i \boldsymbol{I}]\Delta\boldsymbol{d}^n_{i+1} = -\boldsymbol{r}^n(\boldsymbol{d}^n_i) \tag{2.96}$$

$$\boldsymbol{d}^n_{i+1} = \boldsymbol{d}^n_i + \Delta\boldsymbol{d}^n_{i+1}, \tag{2.97}$$

with the scalar

$$k^{\mathrm{ptc}}_{i+1} = k^{\mathrm{ptc}}_i \frac{\left\|\boldsymbol{r}^n(\boldsymbol{d}^n_{i+1})\right\|_2}{\|\boldsymbol{r}^n(\boldsymbol{d}^n_i)\|_2}. \tag{2.98}$$

Please note, that the perturbation $k^{\mathrm{ptc}}_i \boldsymbol{I}$ diminishes with decreasing residual, such that standard Newton-Raphson iterations are recovered in proximity to a converged state at each time step. The initial value k^{ptc}_0 is a method parameter set by the user.

3. Projection-based model order reduction and hyper reduction

Depending on the number of degrees of freedom (DOFs), resolution in time and the number of desired model evaluations, the demand of computational resources for application of models introduced in Chapter 2 may surpass its availability. To mitigate the demand, projection-based model order reduction (MOR) has evolved to a powerful tool with a large community and many successful applications in science and engineering. This section presents the main steps in a typical MOR process in detail. Biomedical applications are presented in Section 4 and 5.

For substantial computational speedup of the reduced model, a two-step process is applied. In the first step, the full-order model (FOM) is reduced in the number of its DOFs. This results in a reduced-order model (ROM) (the term *order* can be understood as a synonym to *dimension*), or in more detail to a dimensionally reduced order model (DROM). For nonlinear problems, pure dimensional reduction does not decouple the resulting ROM from assembly of the FOM residual and possibly the FOM Jacobian, depending on the solution technique of the nonlinear system of equations. Therefore, a so called hyper reduction is required in a second step, which will result in a dimensionally reduced as well as hyper reduced order model (DHROM). In the following, ROM refers to both DROM and DHROM, a specification to DROM or DHROM is done whenever necessary.

3.1. Dimensional reduction

This section focuses on dimensional reduction of a nonlinear system of equations. More details can be found in the textbook [110].

3.1.1. Projection on low-dimensional subspaces

Discrete projection operators build a theoretical foundation for dimensional reduction and are discussed in this section. The following additive decomposition of the vector space $\mathbb{R}^N$ is assumed to hold

$$\mathbb{R}^N = \operatorname{span}(\boldsymbol{V}) \oplus \operatorname{span}(\boldsymbol{W})^{\perp}. \tag{3.1}$$

$\boldsymbol{V}, \boldsymbol{W} \in \mathbb{R}^{N \times p}$ with $N > p$ are full-rank matrices and the superscript $^{\perp}$ denotes the orthogonal complement. For $\mathcal{V} \subset \mathbb{R}^N$, the orthogonal complement is defined by the subspace

$$\mathcal{V}^{\perp} \coloneqq \{\boldsymbol{d} \in \mathbb{R}^N : \boldsymbol{d}^T \boldsymbol{y} = 0 \quad \forall \boldsymbol{y} \in \mathcal{V}\}. \tag{3.2}$$

A discrete projection operator $\mathcal{P}_{\boldsymbol{V}}^{\boldsymbol{W}} \in \mathbb{R}^{N \times N}$ (in the following simply referred to as *projector*) on the space $\operatorname{span}(\boldsymbol{V})$ in direction orthogonal to the space $\operatorname{span}(\boldsymbol{W})$ results from

$$\mathcal{P}_{\boldsymbol{V}}^{\boldsymbol{W}} = \boldsymbol{V}[\boldsymbol{W}^T \boldsymbol{V}]^{-1} \boldsymbol{W}^T, \tag{3.3}$$

presuming invertibility of the product $\boldsymbol{W}^T\boldsymbol{V}$. Figure 3.1 provides a geometrical interpretation of the projection using 2D subspaces in a 3D space.

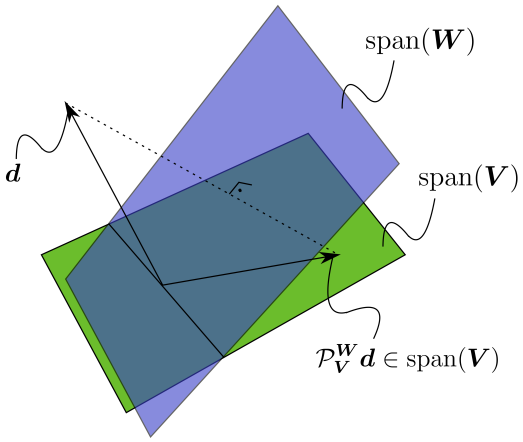

Figure 3.1.: Projection on $\mathrm{span}(\boldsymbol{V})$ in direction orthogonal to $\mathrm{span}(\boldsymbol{W})$.

Any square matrix $\boldsymbol{P} \in \mathbb{R}^{N\times N}$ with the property $\boldsymbol{P}\boldsymbol{P} = \boldsymbol{P}$ represents a projector. In particular, this holds for (3.3)

$$\mathcal{P}_{\boldsymbol{V}}^{\boldsymbol{W}}\mathcal{P}_{\boldsymbol{V}}^{\boldsymbol{W}} = \mathcal{P}_{\boldsymbol{V}}^{\boldsymbol{W}}, \tag{3.4}$$

which trivially gives

$$\mathcal{P}_{\boldsymbol{V}}^{\boldsymbol{W}}(\mathcal{P}_{\boldsymbol{V}}^{\boldsymbol{W}}\boldsymbol{d}) = \mathcal{P}_{\boldsymbol{V}}^{\boldsymbol{W}}\boldsymbol{d} \tag{3.5}$$

for any $\boldsymbol{d} \in \mathbb{R}^N$, stating that a projected vector will not change by re-application of the projection.

The special case of $\mathrm{span}(\boldsymbol{V}) = \mathrm{span}(\boldsymbol{W})$ corresponds to an orthogonal projection characterized by the property

$$\left\|\boldsymbol{d} - \mathcal{P}_{\boldsymbol{V}}^{\boldsymbol{W}}\boldsymbol{d}\right\|_2 = \min_{\boldsymbol{y}\in\mathrm{span}(\boldsymbol{V})} \|\boldsymbol{d} - \boldsymbol{y}\|_2 , \tag{3.6}$$

while the case $\mathrm{span}(\boldsymbol{V}) \neq \mathrm{span}(\boldsymbol{W})$ is referred to as oblique projection. Without loss of generality, the columns of $\boldsymbol{V}$ and $\boldsymbol{W}$ can be chosen as orthonormal bases for $\mathrm{span}(\boldsymbol{V})$ and $\mathrm{span}(\boldsymbol{W})$. As a result, the orthogonal projector can be represented as

$$\mathcal{P}_{\boldsymbol{V}}^{\boldsymbol{V}} = \boldsymbol{V}\boldsymbol{V}^T. \tag{3.7}$$

Figure 3.2 illustrates an orthogonal projection of a vector $\boldsymbol{d}$ in a high-dimensional ($N = 3948$) space on a low-dimensional ($p = 2$) subspace. The components of $\boldsymbol{d}$ are interpreted as nodal displacements of a reference shape in 3D space, such that elements of the space $\mathbb{R}^N$ can be interpreted and visualized as deformed shapes.

3.1.2. Projection-based dimensional reduction

Projection-based dimensional reduction aims at a decrease of the number of DOFs and achieves its goal applying a projection to the vector of residual equations $\boldsymbol{r}^n(\boldsymbol{d}^n) \in \mathbb{R}^N$ as well as to its argument

$$\mathcal{P}_{\boldsymbol{Y}}^{\boldsymbol{Z}}\,\boldsymbol{r}^n(\mathcal{P}_{\boldsymbol{V}}^{\boldsymbol{W}}\boldsymbol{d}^n) = \boldsymbol{0}. \tag{3.8}$$

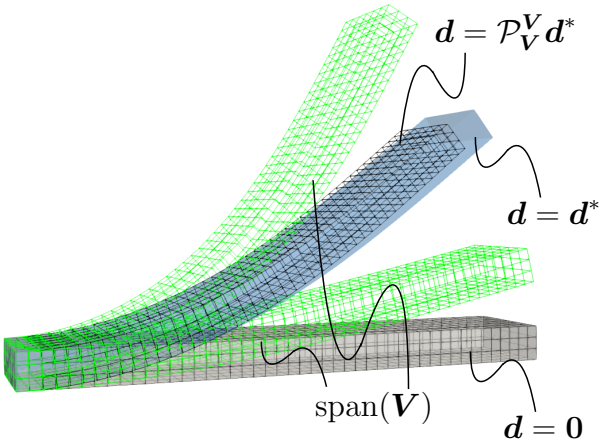

Figure 3.2.: Visualization of an orthogonal projection on a low-dimensional subspace. The reference shape $\boldsymbol{d} = \boldsymbol{0}$ (drawn for better illustration, not part of the projection) is depicted in light gray. The low-dimensional subspace is given by the span of two shapes (green wires). The orthogonally projected mode (black wires) is an optimal (in the sense of equation (3.6)) approximation to the light blue shape $\boldsymbol{d} = \boldsymbol{d}^*$ in the given low-dimensional subspace.

For generality, equation (3.8) contains two different oblique projections, which resolve to

$$\boldsymbol{Y}[\boldsymbol{Z}^T\boldsymbol{Y}]^{-1}\boldsymbol{Z}^T\boldsymbol{r}^n(\boldsymbol{V}[\boldsymbol{W}^T\boldsymbol{V}]^{-1}\boldsymbol{W}^T\boldsymbol{d}^n) = \boldsymbol{0}. \tag{3.9}$$

Recalling invertibility of $[\boldsymbol{Z}^T\boldsymbol{Y}]$ and the full-rank of $\boldsymbol{Y}$, equation (3.9) states that the residual vector must be in the kernel of $\boldsymbol{Z}^T$. At the same time, recalling invertibility of $[\boldsymbol{W}^T\boldsymbol{V}]$ and the full-rank of $\boldsymbol{W}^T$ gives $\mathrm{span}([\boldsymbol{W}^T\boldsymbol{V}]^{-1}\boldsymbol{W}^T) = \mathbb{R}^p$, such that the product $[\boldsymbol{W}^T\boldsymbol{V}]^{-1}\boldsymbol{W}^T\boldsymbol{d}$ with $\boldsymbol{d} \in \mathbb{R}^N$ can be replaced by the *generalized coordinates* $\hat{\boldsymbol{d}}$ with $\hat{\boldsymbol{d}} \in \mathbb{R}^p$. Equation (3.9) simplifies to

$$\boldsymbol{Z}^T\boldsymbol{r}^n(\boldsymbol{V}\hat{\boldsymbol{d}}^n) = \boldsymbol{0}, \tag{3.10}$$

which is referred to as the projected system of equations, even though projectors as introduced in Section 3.1.1 do not show up explicitly. Equation (3.10) can be solved for the generalized coordinates $\hat{\boldsymbol{d}}^n$. In case of well chosen $\boldsymbol{Z}$ and $\boldsymbol{V}$, a good approximation to the solution $\boldsymbol{d}^n$ is given by

$$\boldsymbol{d}^n \approx \tilde{\boldsymbol{d}}^n := \boldsymbol{V}\hat{\boldsymbol{d}}^n. \tag{3.11}$$

The matrices $\boldsymbol{V}$ and $\boldsymbol{Z}$ (or more precisely their column spans) are referred to as trial and test space, respectively. The case of different trial and test space $\boldsymbol{V} \neq \boldsymbol{Z}$ is called *Petrov-Galerkin projection*. A specific example of a Petrov-Galerkin projection is the *least-squares Petrov-Galerkin projection* [18]

$$\boldsymbol{V}^T\left[\boldsymbol{J}_r^n(\boldsymbol{V}\hat{\boldsymbol{d}}^n)\right]^T\boldsymbol{r}^n(\boldsymbol{V}\hat{\boldsymbol{d}}^n) = \boldsymbol{0} \tag{3.12}$$

with the non-constant test space $\boldsymbol{Z} = \boldsymbol{J}_r^n(\boldsymbol{V}\hat{\boldsymbol{d}}^n)\boldsymbol{V}$ and trial space $\boldsymbol{V}$. The least-squares Petrov-Galerkin projection (3.12) can be derived from the optimality condition of optimization problem

$$\hat{\boldsymbol{d}}^n = \arg\min_{\hat{\boldsymbol{y}}\in\mathbb{R}^p} \left\|\boldsymbol{r}^n(\boldsymbol{V}\hat{\boldsymbol{y}})\right\|_2, \tag{3.13}$$

which explains the term “least-squares”.

The special case of $\boldsymbol{V} = \boldsymbol{Z}$ gives

$$\boldsymbol{V}^T \boldsymbol{r}^n(\boldsymbol{V}\hat{\boldsymbol{d}}^n) = \boldsymbol{0} \tag{3.14}$$

and is called *Galerkin projection* [18]. This thesis makes use of the Galerkin projection exclusively. Nonlinear system of equations (3.14) can be solved by the Newton-Raphson iteration scheme (see equation (2.93) for the FOM) applying consistent linearization

$$\begin{aligned} \boldsymbol{V}^T \boldsymbol{J}_r^n(\boldsymbol{V}\hat{\boldsymbol{d}}_i^n)\boldsymbol{V}\Delta\hat{\boldsymbol{d}}_{i+1}^n &= -\boldsymbol{V}^T \boldsymbol{r}^n(\boldsymbol{V}\hat{\boldsymbol{d}}_i^n) \\ \hat{\boldsymbol{d}}_{i+1}^n &= \hat{\boldsymbol{d}}_i^n + \Delta\hat{\boldsymbol{d}}_i^n. \end{aligned} \tag{3.15}$$

Iterating is stopped at a prescribed residual $\left\| \boldsymbol{V}^T \boldsymbol{r}^n(\boldsymbol{V}\hat{\boldsymbol{d}}_i^n) \right\|_2 < \varepsilon_r$ and increment $\left\| \Delta\hat{\boldsymbol{d}}_i^n \right\|_2 < \varepsilon_d$ tolerance.

3.1.3. Construction of low-dimensional subspaces

Recalling equation (3.11), $\mathrm{span}(\boldsymbol{V})$ defines the low-dimensional subspace for approximation of the high-dimensional solution for both Petrov-Galerkin and Galerkin projection. This motivates the term reduced-order basis (ROB), which is frequently used for $\boldsymbol{V}$ besides trial space. For the Galerkin projection applied in this thesis, the ROB is the only component needed to construct a DROM from a given FOM. Construction of well-designed ROBs is motivated and detailed in this section. Simulation-free and data-driven approaches are reviewed as opposed concepts first. In the next step, focus is laid on the proper-orthogonal decomposition (POD) and greedy algorithms as most prominent representatives of data-driven approaches.

Equation (3.11) motivates an intuitive design criteria for a ROB: The column span of the ROB must be a good approximation to the space spanned by the solution $\boldsymbol{d}^n, n \in \{0, \dots, N_T - 1\}$, with N_T denoting the number of discrete time steps. This can be expressed by a low relative projection error

$$\left\| \boldsymbol{d}^n - \boldsymbol{V}\boldsymbol{V}^T \boldsymbol{d}^n \right\|_2 \ll \left\| \boldsymbol{d}^n \right\|_2, \; n \in \{0, \dots, N_T - 1\}. \tag{3.16}$$

Several approaches to reach this goal can be found in literature. The class of simulation-free approaches (see [118] for extensive overview) performs direct analysis of the system’s components (e.g. mass and stiffness matrix for structural dynamics) in case of linear systems in order to find a suitable trial space. Prominent method representatives are the balanced truncation [115] and Krylov subspace reduction [5]. For nonlinear systems, simulation-free approaches attempt to extend the linear system ROB by modes capturing the nonlinearity such as (static) modal derivatives [137].

Data-driven approaches in contrast pursue another strategy. They appear in the context of parametrized systems and a many query context. The basic idea is to compute the solutions of selected points in the parameter domain and derive a ROB from these solutions. The assumption thereby is that a low-dimensional subspace spanned by some selected solution vectors will catch the system dynamics for the entire parameter domain in the sense of equation (3.16).

Depending on the context of application, data-driven approaches may require data-compression for the ROM to become truly low-dimensional. Temporally resolved structures excited by a force pulse are an example for a great benefit of data-compression. Only few modes may be sufficient to represent the entire dynamics [76].

Proper orthogonal decomposition

A state of the art technique for data-compression widely applied in projection-based MOR is the POD [113, 123]. POD is based on the concept of the singular value decomposition (SVD) [127], which is reviewed in the following paragraph.

Assuming $\boldsymbol{S} \in \mathbb{R}^{N \times m}$ with $N \geq m$ to be a matrix of rank $r \leq m$, a thin SVD corresponds to a decomposition of $\boldsymbol{S}$ in terms of

$$\boldsymbol{S} = \boldsymbol{\Phi} \boldsymbol{\Xi} \boldsymbol{\Psi}^T, \tag{3.17}$$

with $\boldsymbol{\Phi} = [\boldsymbol{\phi}_0, \ldots, \boldsymbol{\phi}_{m-1}] \in \mathbb{R}^{N \times m}$, $\boldsymbol{\Psi} = [\psi_0, \ldots, \psi_{m-1}] \in \mathbb{R}^{m \times m}$ being orthonormal matrices with *left* and *right singular vectors* as columns, respectively, while $\boldsymbol{\Xi} = \operatorname{diag}(\boldsymbol{\xi}) \in \mathbb{R}^{m \times m}$ is a diagonal matrix holding *singular values* $\xi_i, i \in \{0, \ldots, m-1\}$ in descending order $\xi_i \geq \xi_j \geq 0$ for $i \leq j$ and $\xi_i = 0$ for $i > r$. Left and right singular vectors and singular values fulfill the relation

$$\boldsymbol{S} \boldsymbol{\phi}_i = \xi_i \boldsymbol{\psi}_i, \quad \boldsymbol{S}^T \boldsymbol{\psi}_i = \xi_i \boldsymbol{\phi}_i \qquad \text{for } i, j \in \{0 \ldots m-1\}. \tag{3.18}$$

Equation (3.17) can be equivalently rewritten using a sum of rank-1 matrices

$$\boldsymbol{S} = \sum_{i=0}^{m-1} \xi_i \boldsymbol{\phi}_i \otimes \boldsymbol{\psi}_i \tag{3.19}$$

with the following interpretation: Given descending ordering of the singular values, a truncation of the sum at $p < m$ frequently gives a good low-rank approximation of $\boldsymbol{S}$. In fact, the resulting p-rank approximation is optimal [127] in the sense of

$$\left\| \boldsymbol{S} - \sum_{i=0}^{p-1} \xi_i \boldsymbol{\phi}_i \otimes \boldsymbol{\psi}_i \right\|_F = \min_{\boldsymbol{B} \in \mathbb{R}^{N \times m},\, \operatorname{rank}(\boldsymbol{B}) \leq p} \|\boldsymbol{S} - \boldsymbol{B}\|_F \,, \tag{3.20}$$

with $\|(\bullet)\|_F$ denoting the Frobenius norm.

POD makes use of the SVD optimality property to achieve data compression. Thereby the ROB $\boldsymbol{V}$ is built by the first p left singular vectors while $\boldsymbol{S} \in \mathbb{R}^{N \times m}$ corresponds to the so-called *snapshot matrix* (same symbol as for the second Piola-Kirchhoff stress tensor (2.23), confusion is precluded by the context) with columns containing solution modes gathered during FOM sampling in the parameter domain. As a result, the orthogonal projection error of the snapshot matrix $\boldsymbol{S}$ is minimized in the Frobenius norm

$$\left\| \boldsymbol{S} - \boldsymbol{V} \boldsymbol{V}^T \boldsymbol{S} \right\|_F = \min_{\boldsymbol{W} \in \mathbb{R}^{N \times p}} \left\| \boldsymbol{S} - \boldsymbol{W} \boldsymbol{W}^T \boldsymbol{S} \right\|_F \,, \tag{3.21}$$

which is a consequence of optimal SVD low-rank approximation (3.20) and optimal orthogonal projection approximation property (3.6).

In large problems, typically $N \gg m$ holds, meaning that the number of model DOFs is much larger then the number or accumulated snapshots. For this special case, an efficient algorithm for computation of left singular vectors and singular values applying an eigendecomposition to a $m \times m$ sized matrix [110] is reviewed. In a first step the so-called *correlation-matrix* $\boldsymbol{C} \in \mathbb{R}^{m \times m}$ (same symbol as for the right Cauchy-Green tensor (2.11), confusion is precluded by the context) is computed by

$$\boldsymbol{C} = \boldsymbol{S}^T \boldsymbol{S} \tag{3.22}$$

and the singular value problem

$$\boldsymbol{C}\boldsymbol{\psi}_i = \xi_i^2 \boldsymbol{\psi}_i \qquad \text{for } i \in \{0, \dots, m-1\} \tag{3.23}$$

is solved. As indicated by equation (3.23), the eigenvalues of $\boldsymbol{C}$ correspond to the squared singular values and the eigenvectors coincide with the right singular vectors. The wanted left singular vectors then (see equation (3.18)) can be computed from

$$\boldsymbol{\phi}_i = \frac{1}{\xi_i}\boldsymbol{S}\boldsymbol{\psi}_i \qquad \text{for } i \in \{0, \dots, m-1\}. \tag{3.24}$$

Greedy algorithms

For parametrized models, *greedy algorithms* [79, 109, 117] are a prominent technique for the construction of ROBs. In every iteration loop, greedy algorithms attempt to solve an optimization problem, which explains the designation "greedy". The optimization problem is performed over an error estimator $\mathcal{Y}(\boldsymbol{V}, \boldsymbol{\mu})$, which returns an upper bound for the ROM error

$$\mathcal{Y}(\boldsymbol{V}, \boldsymbol{\mu}) \geq \left\| \boldsymbol{S}^{\mathrm{FOM}}(\boldsymbol{\mu}) - \boldsymbol{S}^{\mathrm{ROM}}(\boldsymbol{V}, \boldsymbol{\mu}) \right\|_F . \tag{3.25}$$

$\boldsymbol{S}^{\mathrm{FOM}}(\boldsymbol{\mu})$ denotes the FOM snapshot matrix at parametric configuration $\boldsymbol{\mu}$ and $\boldsymbol{S}^{\mathrm{ROM}}(\boldsymbol{V}, \boldsymbol{\mu})$ denotes the ROM snapshot matrix applying a ROB $\boldsymbol{V}$ at $\boldsymbol{\mu}$.

A basic greedy algorithm is depicted in Algorithm 1, while improvements and modifications can be found in literature [63]. As can be seen from Algorithm 1, the idea is to extend the trial space by FOM modes, which are represented worst as indicated by the error estimator using the ROB accumulated up to this point (line 5:). The ROB itself is extended by orthogonalization of FOM snapshots in every greedy iteration (line 4:).

Algorithm 1 GreedyAlgorithm$(\Sigma_t, \varepsilon_g, \boldsymbol{\mu}_i)$ (ROB construction by greedy algorithm)

Input: training grid $\Sigma_t \subset \mathcal{P}$, initial parametric configuration $\boldsymbol{\mu}_i \in \Sigma_t$, maximal error ε_g
Output: chosen grid points Σ_c, snapshot matrix $\boldsymbol{S}$, reduced-order basis $\boldsymbol{V}$

1: $\Sigma_c = \{\boldsymbol{\mu}_i\}$, $\boldsymbol{S} = []$, $\boldsymbol{V} = []$, $e_{\max} = \varepsilon_g + 1$, $\boldsymbol{\mu}_{\max} = \boldsymbol{\mu}_i$
2: **while** $e_{\max} > \varepsilon_g$ **do**
3: $\quad \boldsymbol{S} \leftarrow [\boldsymbol{S}, \boldsymbol{S}^{\mathrm{FOM}}(\boldsymbol{\mu}_{\max})]$
4: $\quad \boldsymbol{V} \leftarrow \mathrm{Orthogonalize}([\boldsymbol{V}, \boldsymbol{S}^{\mathrm{FOM}}(\boldsymbol{\mu}_{\max})])$
5: $\quad \boldsymbol{\mu}_{\max} = \arg\max_{\boldsymbol{\mu} \in \Sigma_t} \mathcal{Y}(\boldsymbol{V}, \boldsymbol{\mu})$
6: $\quad \Sigma_c \leftarrow \Sigma_c \cup \boldsymbol{\mu}_{\max}$, $e_{\max} = \mathcal{Y}(\boldsymbol{V}, \boldsymbol{\mu}_{\max})$
7: **end while**
8: return Σ_c, $\boldsymbol{S}$, $\boldsymbol{V}$

Computational feasibility of greedy algorithms relies on the error estimators (3.25), given that the true error is inaccessible for every training grid point due to computational complexity of the FOM. A well designed error estimator is sharp (close bounding of true error), asymptotically correct (i.e. approach zero, when trial space is refined) and computationally inexpensive [110].

3.1.4. Computational example for dimensional reduction

An application of POD and data compression is presented in the following numerical example. Figure 3.3 depicts the computational model. A beam with one clamped and one free end is deformed by an oscillating pressure load $p(t) = 50\ \text{Pa} * \sin(\omega t)$ with $\omega = 1$ Hz at the free end. Beam dimensions are given by $l = 150$ cm, $h = 10$ cm and $w = 30$ cm. A St. Venant-Kirchhoff material model with strain energy density

$$\Psi = \frac{E\nu}{2(1+\nu)(1-2\nu)}[\text{tr}(\boldsymbol{E})]^2 + \frac{E}{2(1+\nu)}\boldsymbol{E} : \boldsymbol{E} \tag{3.26}$$

is applied. Material parameters are the Young's modulus $E = 100$ kPa, Poisson's ratio $\nu = 0.3$ and reference configuration density $\rho_0 = 100\ \frac{\text{kg}}{\text{m}^3}$, damping is not considered. The computational model is spatially discretized using 828 linear, hexahedral finite elements with F-bar technology [34] resulting in 3948 DOFs. Temporal discretization is done by the generalized-α method (see Section 2.2.3) with parameters $\alpha_m = 0.5$, $\alpha_f = 0.5$, $\alpha_\beta = 0.25$ and $\alpha_\gamma = 0.5$. $N_T = 300$ time steps at equal time step size $\Delta t = 0.025$ are performed.

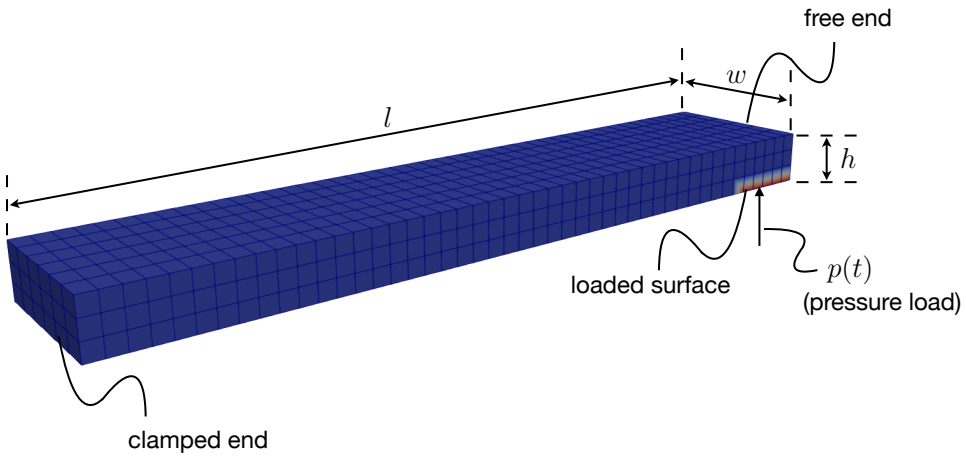

Figure 3.3.: Computational domain for oscillating beam simulation. The surface loaded by a pressure boundary condition at the free end is indicated by red coloring.

Figure 3.4 depicts selected deformation modes at several time steps of the oscillating beam. All modes are gathered in a snapshot matrix $\boldsymbol{S}^{\text{FOM}} \in \mathbb{R}^{3948\times 300}$ and a ROB $\boldsymbol{V} \in \mathbb{R}^{3948\times p}$ is computed by a SVD. Next, multiple Galerkin projection (3.14) ROMs are solved with different dimensions p, i.e. the ROB is truncated after the first p modes. Given the FOM and ROM snapshot matrices

$$\begin{aligned} \boldsymbol{S}^{\text{FOM}} &= [\boldsymbol{d}^0 \ldots, \boldsymbol{d}^{N_T-1}], \\ \boldsymbol{S}^{\text{ROM}} &= [\tilde{\boldsymbol{d}}^0, \ldots, \tilde{\boldsymbol{d}}^{N_T-1}], \end{aligned} \tag{3.27}$$

respectively, the relative error

$$RE(\boldsymbol{S}^{\text{FOM}}, \boldsymbol{S}^{\text{ROM}}) := \frac{\left\|\boldsymbol{S}^{\text{FOM}} - \boldsymbol{S}^{\text{ROM}}\right\|_F}{\left\|\boldsymbol{S}^{\text{FOM}}\right\|_F} \tag{3.28}$$

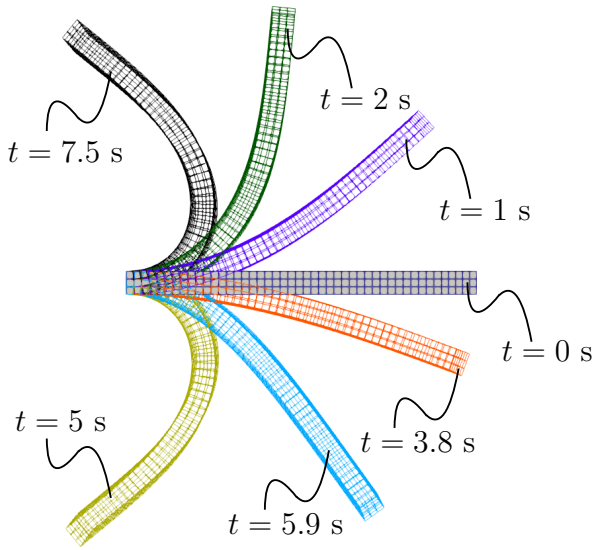

Figure 3.4.: Oscillating beam at different time instances. The depicted modes result from a finite element simulation with linear hexahedral elements and the gen-α method for spatial and temporal discretization, respectively.

is defined for comparison of FOM and ROM solution. Figure 3.5 depicts all ROB singular values and several relative errors (3.28). The strong initial decay of singular values indicates that significantly less modes are sufficient to span the FOM solution subspace with good accuracy. This also reflects in the relative error, which drops by 6 orders of magnitude if 50 modes are considered instead of 1. Further extension of the ROB yields a less effective improvement of the relative error.

3.2. Hyper reduction

The introduced Galerkin projection (3.14) yields a low-dimensional system approximation, only low-dimensional systems of equations have to be solved as can be seen from linearization (3.15). For linear system residuals, dimensional reduction frequently is sufficient to gain substantial computational speedup since FOM system components are linearly dependent on the solution and ROM system components can be precomputed in the offline stage. This is different for nonlinear systems, which require full re-assembly of some or all system components in every Newton-Raphson iteration. In particular for structural dynamics problems under consideration in this thesis, nonlinear system components are the internal force vector and potentially the external force vector as well as the corresponding Jacobians.

This section introduces *hyper reduction* as a concept aiming at a fast approximation of system nonlinearities. Section 3.2.1 qualitatively motivates the basic idea behind hyper reduction and gives a literature overview. Section 3.2.2, presents the details of the so-called energy-conserving mesh sampling and weighting (ECSW) hyper reduction method, which especially is tailored for finite element structural dynamics problems.

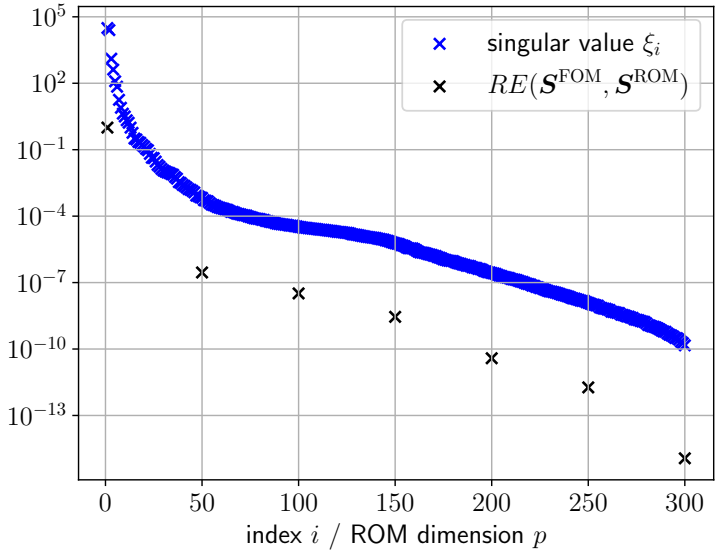

Figure 3.5.: Singular values and relative errors of snapshot matrix containing 300 displacement modes of simulated oscillating beam. Selected displacement modes are depicted in Figure 3.4.

3.2.1. General principle and overview of hyper reduction methods

Assembly of nonlinear systems of equations in the context of finite elements requires numerical integration over every finite element. Hyper reduction poses the question, whether a computationally cheap approximation of residual and Jacobian

$$\tilde{\boldsymbol{r}}^n(\boldsymbol{V}\hat{\boldsymbol{d}}^n) \approx \boldsymbol{r}^n(\boldsymbol{V}\hat{\boldsymbol{d}}^n), \tag{3.29}$$

$$\tilde{\boldsymbol{J}}_r^n(\boldsymbol{V}\hat{\boldsymbol{d}}^n) \approx \boldsymbol{J}_r^n(\boldsymbol{V}\hat{\boldsymbol{d}}^n) \tag{3.30}$$

or alternatively (in the context of Galerkin projection) an approximation of the projected residual and Jacobian

$$\boldsymbol{V}^T\tilde{\boldsymbol{r}}^n(\boldsymbol{V}\hat{\boldsymbol{d}}^n) \approx \boldsymbol{V}^T\boldsymbol{r}^n(\boldsymbol{V}\hat{\boldsymbol{d}}^n), \tag{3.31}$$

$$\boldsymbol{V}^T\tilde{\boldsymbol{J}}_r^n(\boldsymbol{V}\hat{\boldsymbol{d}}^n)\boldsymbol{V} \approx \boldsymbol{V}^T\boldsymbol{J}_r^n(\boldsymbol{V}\hat{\boldsymbol{d}}^n)\boldsymbol{V} \tag{3.32}$$

can be found. Note that fulfillment of approximations (3.31), (3.32) does not mean that approximations (3.29), (3.30) hold.

Several approaches for hyper reduction have been presented to date. Based on the theory of the *empirical interpolation method* [6], the discrete empirical interpolation method (DEIM) was introduced in [21]. Recalling the time-continuous dynamical system (2.76), DEIM can be used to assemble the nonlinear internal and/or external force evaluating only a small subset of mesh elements. The idea thereby is to apply an oblique projection

$$\boldsymbol{f}_\gamma(\boldsymbol{V}\hat{\boldsymbol{d}}, t) \approx \tilde{\boldsymbol{f}}_\gamma(\boldsymbol{V}\hat{\boldsymbol{d}}, t) = \boldsymbol{Y}_\gamma[\boldsymbol{Z}_\gamma^T\boldsymbol{Y}_\gamma]^{-1}\boldsymbol{Z}_\gamma^T\boldsymbol{f}_\gamma(\boldsymbol{V}\hat{\boldsymbol{d}}, t) \quad \gamma \in \{\mathrm{int}, \mathrm{ext}\}, \tag{3.33}$$

wherein $\boldsymbol{Y}_\gamma \in \mathbb{R}^{N\times n_\gamma}$ with $n_\gamma \ll N$ is a basis for $\boldsymbol{f}_\gamma(\boldsymbol{V}\hat{\boldsymbol{d}}, t)$ and $\boldsymbol{Z}_\gamma \in \mathbb{R}^{N\times n_\gamma}$ is a boolean matrix with exactly a single 1 per column. The computational saving results from simultaneous assembly of $\boldsymbol{Z}_\gamma^T\boldsymbol{f}_\gamma(\boldsymbol{V}\hat{\boldsymbol{d}}, t)$, recalling that the boolean shape of $\boldsymbol{Z}_\gamma$ will extract a subset of

vector function rows, remaining vector entries do not have to be evaluated. The basis $\boldsymbol{Y}_\gamma$ can be computed from a POD on snapshots of internal/external force vectors, while the selection of interpolation points resulting in $\boldsymbol{Z}_\gamma$ is computed by a greedy sampling algorithm [21]. For increase of efficiency in the finite element context, the so-called *unassembled* DEIM was proposed in [131]. A variant extending the DEIM to matrix interpolation is presented in [99].

The Gauss-Newton with approximated tensors (GNAT) method applies to fully (i.e. spatially and temporally) discretized systems [16, 17]. Hyper reduction is introduced inside the residual minimization formulation (3.13), which can be solved applying Gauss-Newton iterations

$$\begin{aligned} \Delta\hat{\boldsymbol{d}}^n_{i+1} &= \arg\min_{\hat{\boldsymbol{y}}\in\mathbb{R}^p} \left\| \boldsymbol{J}^n_r(\boldsymbol{V}\hat{\boldsymbol{d}}^n_i)\boldsymbol{V}\hat{\boldsymbol{y}} + \boldsymbol{r}^n(\boldsymbol{V}\hat{\boldsymbol{d}}^n_i) \right\|_2, \\ \hat{\boldsymbol{d}}^n_{i+1} &= \hat{\boldsymbol{d}}^n_i + \Delta\hat{\boldsymbol{d}}^n_{i+1}. \end{aligned} \tag{3.34}$$

Given a residual POD basis $\boldsymbol{Y}_r \in \mathbb{R}^{N\times p_r}$ and a Jacobian POD basis $\boldsymbol{Y}_J \in \mathbb{R}^{N\times p_J}$ (see [16] for details on construction of these bases) a gappy POD approach [39] is used to approximate components of system (3.34) by

$$\left\| \boldsymbol{J}^n_r(\boldsymbol{V}\hat{\boldsymbol{d}}^n_i)\boldsymbol{V}\boldsymbol{y} + \boldsymbol{r}^n(\boldsymbol{V}\hat{\boldsymbol{d}}^n_i) \right\|_2 \approx \left\| \boldsymbol{A}_J\boldsymbol{Z}^T\boldsymbol{J}^n_r(\boldsymbol{V}\hat{\boldsymbol{d}}^n_i)\boldsymbol{V}\boldsymbol{y} + \boldsymbol{A}_r\boldsymbol{Z}^T\boldsymbol{r}^n(\boldsymbol{V}\hat{\boldsymbol{d}}^n_i) \right\|_2 \tag{3.35}$$

with precomputable matrices $\boldsymbol{A}_J = \boldsymbol{Y}_J[\boldsymbol{Z}^T\boldsymbol{Y}_J]^+$ and $\boldsymbol{A}_r = \boldsymbol{Y}_r[\boldsymbol{Z}^T\boldsymbol{Y}_r]^+$ and $^+$ denoting the Moore-Penrose pseudo-inverse given by $\boldsymbol{A}^+ = [\boldsymbol{A}^T\boldsymbol{A}]^{-1}\boldsymbol{A}^T$ for a full rank matrix $\boldsymbol{A}$. Similar to DEIM, computational savings arise from the evaluation of $\boldsymbol{Z}^T\boldsymbol{J}^n_r(\boldsymbol{V}\hat{\boldsymbol{d}}^n_i)$ and $\boldsymbol{Z}^T\boldsymbol{r}^n(\boldsymbol{V}\hat{\boldsymbol{d}}^n_i)$ with the boolean matrix $\boldsymbol{Z} \in \mathbb{R}^{N\times p_Z}$ extracting individual matrix and vector rows. A greedy sampling algorithm for the construction of $\boldsymbol{Z}$ is presented in [16].

The ECSW [40, 41] hyper reduction method aims at an approximation of projected force vectors in structural dynamics problems by reduced cubature (= multidimensional quadrature). For a set of displacement modes, a subset of mesh elements is selected such that a weighted integration of the element subset yields a good approximation of the virtual work performed by the force. This approach is modified by the so-called empirical cubature method (ECM) [54] to Gauss point-wise cubature instead of element-wise cubature. The ECSW is structure preserving, i.e. a positive definite force Jacobian will remain positive definite. This numerical favourability together with its elegant combination with standard functionality of existing finite element code make ECSW the method of choice for hyper reduction in this thesis. A detailed presentation is given in Section 3.2.2.

In [73], a so-called *semihyper* reduction of nonlinear external forces is presented. The external forces are assumed to result from a nonlinear system of equations, such as the Reynolds equation describing the gap pressure in hydrodynamic lubrication. Starting from the standard ROB, a trial space for the nonlinear external force referred to as *stress modes* is derived. The authors refer to the method as "semihyper reduction", given that it aims at a reduced evaluation of the system's nonlinearity, although full decoupling of the FOM DOFs is not given. In [74], the application of stress modes is extended to a hyper reduction method in the conventional sense using the ECM.

3.2.2. Energy-conserving mesh sampling and weighting

In contrast to gappy data-reconstruction methods such as DEIM or GNAT, ECSW [40, 41] does not attempt to approximate the FOM residual (3.29) and Jacobian (3.30). Instead, the ROM residual (3.31) and Jacobian (3.32) are approximated directly. As motivated above, hyper reduction

is applied to the nonlinear part of the residual. For the structural dynamics system (2.76), this corresponds to the internal and external force $\boldsymbol{f}_\gamma$ with $\gamma \in \{\text{int}, \text{ext}\}$, resulting in the approximation

$$\boldsymbol{V}^T \tilde{\boldsymbol{f}}_\gamma(\boldsymbol{V}\hat{\boldsymbol{d}}, t) \approx \boldsymbol{V}^T \boldsymbol{f}_\gamma(\boldsymbol{V}\hat{\boldsymbol{d}}, t). \tag{3.36}$$

Equation (3.36) can be derived from a virtual work approximation, which is discussed in the following steps, closely to the presentation in [122]. Virtual work for a spatially discretized force and corresponding displacement field can be written as

$$\delta W_\gamma(\boldsymbol{d}, \delta\boldsymbol{d}, t) = \delta\boldsymbol{d}^T \boldsymbol{f}_\gamma(\boldsymbol{d}, t) \tag{3.37}$$

or after applying restriction to the ROB subspace $\boldsymbol{d}, \delta\boldsymbol{d} \in \text{span}(\boldsymbol{V})$

$$\delta \hat{W}_\gamma(\hat{\boldsymbol{d}}, \delta\hat{\boldsymbol{d}}, t) = \delta\hat{\boldsymbol{d}}^T \boldsymbol{V}^T \boldsymbol{f}_\gamma(\boldsymbol{V}\hat{\boldsymbol{d}}, t). \tag{3.38}$$

Using element-wise internal force vectors $\boldsymbol{f}_\gamma^{(e)}$, virtual work (3.38) can be equivalently written as a sum over the element index set $\mathcal{E}$

$$\delta \hat{W}_\gamma(\hat{\boldsymbol{d}}, \delta\hat{\boldsymbol{d}}, t) = \sum_{e\in\mathcal{E}} \delta\hat{\boldsymbol{d}}^T \boldsymbol{V}^T \boldsymbol{L}^{(e)} \boldsymbol{f}_\gamma^{(e)}(\boldsymbol{L}^{(e)T} \boldsymbol{V}\hat{\boldsymbol{d}}, t), \tag{3.39}$$

wherein $\boldsymbol{L}^{(e)}$ is the element-wise assembly operator towards the global system.

Starting point for building the ECSW hyper reduced system is an approximation of virtual work (3.38) by a virtual work $\tilde{W}_\gamma(\hat{\boldsymbol{d}}, \delta\hat{\boldsymbol{d}})$ resulting from a weighted sum over a small subset of mesh elements $\tilde{\mathcal{E}}$, that is

$$\delta \tilde{W}_\gamma(\hat{\boldsymbol{d}}, \delta\hat{\boldsymbol{d}}, t) \approx \delta \hat{W}_\gamma(\hat{\boldsymbol{d}}, \delta\hat{\boldsymbol{d}}, t) \tag{3.40}$$

with

$$\delta \tilde{W}_\gamma(\hat{\boldsymbol{d}}, \delta\hat{\boldsymbol{d}}, t) = \sum_{e\in\tilde{\mathcal{E}}} w^{(e)} \delta\hat{\boldsymbol{d}}^T \boldsymbol{V}^T \boldsymbol{L}^{(e)} \boldsymbol{f}_\gamma^{(e)}(\boldsymbol{L}^{(e)T} \boldsymbol{V}\hat{\boldsymbol{d}}, t) \tag{3.41}$$

using positive element weights $w^{(e)} \in \mathbb{R}^+$. Approximation (3.40) can be transformed into an optimization problem by restriction to a predefined set of modes $\hat{\boldsymbol{d}} \in \hat{\mathcal{S}} = \{\hat{\boldsymbol{d}}_0, \dots \hat{\boldsymbol{d}}_{m-1}\}$. Recalling that the displacement field variation is arbitrary $\delta\hat{\boldsymbol{d}} \in \mathbb{R}^p$, approximation (3.40) holds for the set of modes $\hat{\mathcal{S}}$, if

$$\sum_{e\in\tilde{\mathcal{E}}} w^{(e)} \boldsymbol{V}^T \boldsymbol{L}^{(e)} \boldsymbol{f}_\gamma^{(e)}(\boldsymbol{L}^{(e)T} \boldsymbol{V}\hat{\boldsymbol{d}}, t) \approx \sum_{e\in\mathcal{E}} \boldsymbol{V}^T \boldsymbol{L}^{(e)} \boldsymbol{f}_\gamma^{(e)}(\boldsymbol{L}^{(e)T} \boldsymbol{V}\hat{\boldsymbol{d}}, t) \quad \forall\hat{\boldsymbol{d}} \in \hat{\mathcal{S}} \tag{3.42}$$

holds true. In order to keep the cardinality of the reduced element set $|\tilde{\mathcal{E}}|$ low, equation (3.42) can be cast in a so-called sparse non-negative least-squares (SNNLS) optimization problem

$$\begin{aligned} &\underset{\boldsymbol{w}\in\mathbb{R}^{|\mathcal{E}|}}{\text{minimize}} && \|\boldsymbol{w}\|_0 \\ &\text{subject to} && \|\boldsymbol{A}\boldsymbol{w} - \boldsymbol{b}\|_2 \leq \varepsilon_h \|\boldsymbol{b}\|_2 \\ &&& \min(\boldsymbol{w}) \geq 0 \end{aligned} \tag{3.43}$$

with system matrix

$$\boldsymbol{A} = \begin{bmatrix} \boldsymbol{a}_{(0,0)} & \dots & \boldsymbol{a}_{(0,|\mathcal{E}|-1)} \\ \vdots & \ddots & \vdots \\ \boldsymbol{a}_{(m-1,0)} & \dots & \boldsymbol{a}_{(m-1,|\mathcal{E}|-1)} \end{bmatrix} \in \mathbb{R}^{p*m\times|\mathcal{E}|} \tag{3.44}$$

defined by its vector-valued entries

$$\boldsymbol{a}_{(i,j)} = \boldsymbol{V}^T \boldsymbol{L}^{(j)} \boldsymbol{f}_\gamma^{(j)}(\boldsymbol{L}^{(j)T} \boldsymbol{V}\ \hat{\boldsymbol{d}}_i, t_i) \tag{3.45}$$

and right-hand-side vector

$$\boldsymbol{b} = \begin{bmatrix} \boldsymbol{b}_0 \\ \vdots \\ \boldsymbol{b}_{m-1} \end{bmatrix} \in \mathbb{R}^{p*m} \tag{3.46}$$

defined by its vector-valued entries

$$\boldsymbol{b}_i = \sum_{e \in \mathcal{E}} \boldsymbol{a}_{(i,e)}. \tag{3.47}$$

The vector $\boldsymbol{w} \in \mathbb{R}^{|\mathcal{E}|}$ holds element weights $w^{(e)}$ and the zero-norm $\|(\bullet)\|_0$ returns the number of non-zero elements. As a result, optimization problem (3.43) attempts to minimize the number of non-zero element weights, which can be interpreted as minimization of the cardinality of the reduced element set $|\tilde{\mathcal{E}}|$, recalling that zero-weighted elements are not contained in the sum in equation (3.42). The constraints in optimization problem (3.43) ensure fulfillment of approximation (3.42) up to the relative tolerance ε_h and exclusively positive weights in the reduced element set $\tilde{\mathcal{E}}$. The positivity of weights is important for structure preservation and by this for numerical stability, see [41] for an in-depth discussion.

Algorithm 2 [40] returns a computationally affordable approximation to the solution of optimization problem (3.43). The algorithm is a variant of the non-negative least-squares solver stated in [80]. A notation similar to the presentation of the algorithm as depicted in [118] is used. At the core of Algorithm 2, a linear least-squares problem is solved (line 7:). Writing an index set to the right of a vector (e.g. $\boldsymbol{z}_{\tilde{\mathcal{E}}}$ in line 7:) denotes the extraction of vector rows contained in the index set, whereas an index set at the right of a matrix (e.g. $\boldsymbol{A}_{\tilde{\mathcal{E}}}$ in line 7:) denotes an extraction of matrix columns contained in the index set. The least-squares problem is embedded in two loops. The outer loop terminates at sufficient accuracy (line 2:), while the inner loop (line 5:) terminates (line 10:) at fulfillment of the positivity constraint (line 8:). On violation of the positivity constraint, Algorithm 2 forces the solution back to a valid state (line 14:).

For computational speedup, mesh sampling by ECSW can be executed on N_s computational subdomains (see [41] for derivation), wherein a computational subdomain defines a subset of mesh elements $\mathcal{E}^j \subset \mathcal{E},\ j \in \{0, \dots, N_s - 1\}$ with

$$\cup_{j=0}^{N_s-1} \mathcal{E}^j = \mathcal{E}, \quad \mathcal{E}^i \cap_{i \neq j} \mathcal{E}^j = \emptyset. \tag{3.48}$$

The columns of system matrix $\boldsymbol{A}$ are divided into sub-matrices

$$\bar{\boldsymbol{A}}^j = \boldsymbol{A}_{\mathcal{E}^j} \in \mathbb{R}^{p*n \times |\mathcal{E}^j|} \tag{3.49}$$

such that $\bar{\boldsymbol{A}}^j$ holds columns of $\boldsymbol{A}$ with column index in $\mathcal{E}^j$. Likewise, a subdomain specific right-hand-side vector $\bar{\boldsymbol{b}}^j$ is built by summation of selected columns of $\boldsymbol{A}$

$$\bar{\boldsymbol{b}}^j = \begin{bmatrix} \bar{\boldsymbol{b}}_0^j \\ \vdots \\ \bar{\boldsymbol{b}}_{m-1}^j \end{bmatrix} \in \mathbb{R}^{p*m} \tag{3.50}$$

Algorithm 2 SNNLSsolver($\boldsymbol{A}, \boldsymbol{b}, \varepsilon_h$) (solution of sparse non-negative least-squares problem)

Input: system matrix $\boldsymbol{A} \in \mathbb{R}^{p*m \times |\mathcal{E}|}$, right-hand-side vector $\boldsymbol{b} \in \mathbb{R}^{p*m}$, tolerance ε_h
Output: solution vector $\boldsymbol{w}$, index set $\tilde{\mathcal{E}}$

$\tilde{\mathcal{E}} = \{\}$, $\boldsymbol{w} = \boldsymbol{0} \in \mathbb{R}^{|\mathcal{E}|}$, $\boldsymbol{r} = \boldsymbol{b}$
while $\|\boldsymbol{r}\|_2 > \varepsilon_h \|\boldsymbol{b}\|_2$ **do**
  $i = \arg\max_{j \in \{0 \dots |\mathcal{E}|-1\}} [\boldsymbol{A}^T \boldsymbol{r}]_{\{j\}}$
  $\tilde{\mathcal{E}} \leftarrow \tilde{\mathcal{E}} \cup \{i\}$
  while True **do**
    $\boldsymbol{z} = \boldsymbol{0} \in \mathbb{R}^{|\mathcal{E}|}$
    $\boldsymbol{z}_{\tilde{\mathcal{E}}} = \arg\min_{\boldsymbol{y} \in \mathbb{R}^{|\tilde{\mathcal{E}}|}} \|\boldsymbol{A}_{\tilde{\mathcal{E}}} \boldsymbol{y} - \boldsymbol{b}\|_2$
    if $\min(\boldsymbol{z}_{\tilde{\mathcal{E}}}) > 0$ **then**
      $\boldsymbol{w} = \boldsymbol{z}$
      break
    end if
    $\mathcal{Z} = \{i \in \tilde{\mathcal{E}} | \boldsymbol{z}_{\{i\}} < 0\}$
    $\alpha = \min_{i \in \mathcal{Z}} \left\{ \frac{\boldsymbol{w}_{\{i\}}}{\boldsymbol{w}_{\{i\}} - \boldsymbol{z}_{\{i\}}} \right\}$
    $\boldsymbol{w} \leftarrow \boldsymbol{w} + \alpha[\boldsymbol{z} - \boldsymbol{w}]$
    $\tilde{\mathcal{E}} = \{i | \boldsymbol{w}_{\{i\}} \neq 0\}$
  end while
  $\boldsymbol{r} = \boldsymbol{b} - \boldsymbol{A}_{\tilde{\mathcal{E}}} \boldsymbol{w}_{\tilde{\mathcal{E}}}$
end while
return $\tilde{\mathcal{E}}$, $\boldsymbol{w}$

with vector-values entries

$$\bar{\boldsymbol{b}}_i^j = \sum_{e \in \mathcal{E}^j} \boldsymbol{a}_{(i,e)}. \tag{3.51}$$

Algorithm 2 can now be executed in parallel on individual subdomains by replacing $\boldsymbol{A}$ and $\boldsymbol{b}$ with $\bar{\boldsymbol{A}}^j$ and $\bar{\boldsymbol{b}}^j$, respectively. Subdomain specific tolerances can be computed by [41]

$$\varepsilon_h^j = \frac{\|\boldsymbol{b}\|_2}{N_s \left\|\bar{\boldsymbol{b}}^j\right\|_2} \varepsilon_h. \tag{3.52}$$

This ensures the fulfillment of the global tolerance ε_h, as can be seen from

$$\begin{aligned} \frac{\|\boldsymbol{A}\boldsymbol{w} - \boldsymbol{b}\|_2}{\|\boldsymbol{b}\|_2} &\leq \frac{\sum_{j=0}^{N_s-1} \left\|\bar{\boldsymbol{A}}^j \bar{\boldsymbol{w}}^j - \bar{\boldsymbol{b}}^j\right\|_2}{\|\boldsymbol{b}\|_2} \leq \frac{\sum_{j=0}^{N_s-1} \varepsilon_h^j \left\|\bar{\boldsymbol{b}}^j\right\|_2}{\|\boldsymbol{b}\|_2} \\ &= \frac{\sum_{j=0}^{N_s-1} \varepsilon_h \|\boldsymbol{b}\|_2}{N_s \|\boldsymbol{b}\|_2} = \frac{N_s \varepsilon_h \|\boldsymbol{b}\|_2}{N_s \|\boldsymbol{b}\|_2} = \varepsilon_h, \end{aligned} \tag{3.53}$$

wherein $\bar{\boldsymbol{w}}^j = \boldsymbol{w}_{\mathcal{E}^j} \in \mathbb{R}^{|\mathcal{E}^j|}$ was used to denote an extraction of vector rows corresponding to subdomain $\mathcal{E}^j$.

Having found a reduced element set $\tilde{\mathcal{E}}$ and the corresponding weights $w^{(e)}$ with $e \in \tilde{\mathcal{E}}$, the hyper reduced forces are assembled by

$$\tilde{\boldsymbol{f}}_\gamma(\boldsymbol{V}\hat{\boldsymbol{d}}, t) = \sum_{e \in \tilde{\mathcal{E}}} w^{(e)} \boldsymbol{L}^{(e)} \boldsymbol{f}_\gamma^{(e)}(\boldsymbol{L}^{(e)T} \boldsymbol{V}\hat{\boldsymbol{d}}, t) \tag{3.54}$$

with consistent Jacobians

$$\tilde{\boldsymbol{J}}_{f,\gamma}(\boldsymbol{V}\hat{\boldsymbol{d}}, t) = \sum_{e \in \tilde{\mathcal{E}}} w^{(e)} \boldsymbol{L}^{(e)} \boldsymbol{J}_{f,\gamma}^{(e)}(\boldsymbol{L}^{(e)T} \boldsymbol{V}\hat{\boldsymbol{d}}, t) \boldsymbol{L}^{(e)T}. \tag{3.55}$$

The hyper reduced residual $\tilde{\boldsymbol{r}}^n(\boldsymbol{V}\hat{\boldsymbol{d}}^n)$ results from first replacing $\boldsymbol{f}_\gamma$ by $\tilde{\boldsymbol{f}}_\gamma$ in (2.76) for dynamic and in (2.77) for steady state problems. Secondly, the Galerkin projection (3.14) is applied (after time discretization for dynamic problems). A consistent Jacobian of the hyper reduced residual $\tilde{\boldsymbol{J}}_r^n(\boldsymbol{V}\hat{\boldsymbol{d}}^n)$ is built from the contributions in equation (3.55). The resulting DHROM system solved by Newton-Raphson iterations reads (see FOM system (2.93) and DROM system (3.15))

$$\begin{aligned} \boldsymbol{V}^T \tilde{\boldsymbol{J}}_r^n(\boldsymbol{V}\hat{\boldsymbol{d}}_i^n) \boldsymbol{V} \Delta\hat{\boldsymbol{d}}_{i+1}^n &= -\boldsymbol{V}^T \tilde{\boldsymbol{r}}^n(\boldsymbol{V}\hat{\boldsymbol{d}}_i^n) \\ \hat{\boldsymbol{d}}_{i+1}^n &= \hat{\boldsymbol{d}}_i^n + \Delta\hat{\boldsymbol{d}}_i^n. \end{aligned} \tag{3.56}$$

3.2.3. Computational example for hyper reduction

The same setup for the presented computational example as given in Section 3.1.4 is used. Referring to Figure 3.5, 50 POD modes yield a sufficiently accurate ROM. Consequently, 50 POD modes for the ROB and every 10th displacement mode of the oscillating beam simulation $\boldsymbol{S} = [\boldsymbol{d}^0, \boldsymbol{d}^9, \boldsymbol{d}^{19}, \ldots, \boldsymbol{d}^{299}] \in \mathbb{R}^{3948 \times 31}$ are selected to build the set $\hat{\mathcal{S}}$ (cf. Section 3.2.2) by the columns of matrix $\boldsymbol{V}^T\boldsymbol{S}$. Algorithm 2 aiming at hyper reduction of internal force assembly is executed with four different tolerances ε_h. As a result, four different reduced meshes emerge, Figure 3.6 depicts an exemplary reduced mesh at the tolerance $\varepsilon_h = 10^{-4}$. Table 3.1 depicts the number of selected elements as well as the relative error (3.28), which is computed after evaluating the four DHROMs. As expected, stricter tolerances result in more selected mesh elements, while at the same time the relative error decreases.

Table 3.1.: Number of selected mesh elements and accuracy in terms of the relative error for different ECSW tolerances ε_h, cf. Algorithm 2.

ε_h	10^{-1}	10^{-2}	10^{-3}	10^{-4}
$\lvert\tilde{\mathcal{E}}\rvert$	96	137	174	224
$RE(\boldsymbol{S}^{\mathrm{FOM}}, \boldsymbol{S}^{\mathrm{ROM}})$	$7.04 \cdot 10^{-2}$	$4.31 \cdot 10^{-4}$	$2.02 \cdot 10^{-5}$	$4.98 \cdot 10^{-7}$

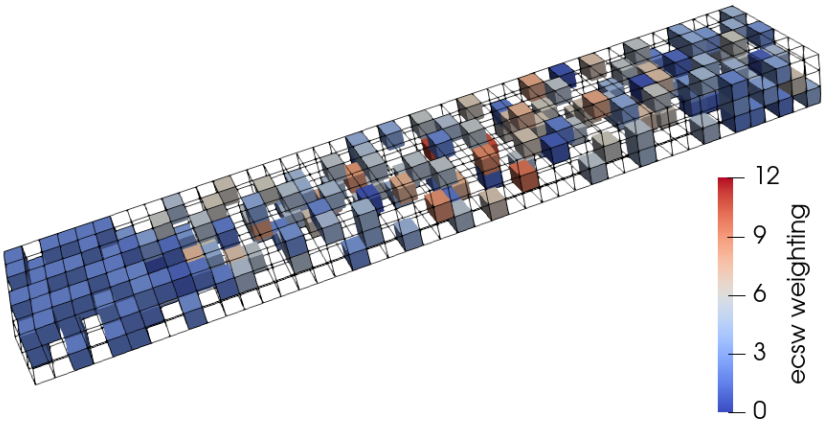

Figure 3.6.: Element selection and weights resulting from Algorithm 2. Only colored elements are evaluated in the assembly of the internal force vector. ECSW tolerance of the depicted reduced mesh is $\varepsilon_h = 10^{-4}$, which leads to a selection of 224 elements.

4. Model reduction of the aneurysmatic abdominal aorta

The abdominal aortic aneurysm (AAA) has been introduced as a central aspect for the motivation of this thesis in Section 1.1. If left untreated, dramatic outcomes in case of rupture are the consequence. Aiming at a support of clinical decision making and treatment, the potential of state-of-the-art computational analysis has been investigated recently [10, 14, 52, 81, 104, 106].

Computational modeling of AAA mechanics is subject to uncertainties as a consequence of large intra- and inter-patient variability of material and geometric properties [112, 114] in combination with the limited approachability of data. As a result, statistical methods aiming at the quantification of model uncertainties have become a common factor in many works. This development in turn introduces a computational bottleneck on the application of large and nonlinear models, given that the number of model evaluations from statistical requirements quickly becomes unreachable. In this section, a projection-based model reduction framework for computational speedup of solid mechanics AAA analysis is developed. The content is a revised version of the publication [122].

Addressing the computational bottleneck, several approaches have been presented to date in the realm of AAA analysis. In [106, 111, 120], computationally cheap intermediate mappings (inverse power-law function, polynomial chaos expansion, stochastic collocation) are built in order to model quantities of interest (QOIs) without the need of evaluating the original full-order model (FOM). A multi-fidelity approach is presented under Refs. [9, 10]. Therein, the used low-fidelity model can be inaccurate in terms of the QOIs, the only prerequisite is a similar stochastic structure compared to the FOM. A surrogate model replacing the FOM is not created.

Surrogates by the mentioned intermediate mappings are based on data from model evaluations, the FOM residual is not directly incorporated within the surrogate. This is different in projection-based model order reduction (MOR), wherein the relation between the FOM residual (and by this the FOM physics) and the reduced-order model (ROM) residual is a projection operation. Application of projection-based MOR to AAA hemodynamics is presented in the Refs. [20, 98].

This section introduces the computational AAA model used in this thesis at first. Next, emphasis is laid on a methodology for the construction of a reduced-order basis (ROB) as well as gathering displacement modes for energy-conserving mesh sampling and weighting (ECSW). Finally, computational experiments on ROM accuracy, application in a statistical context and speedup are performed on three patient-specific AAAs.

4.1. Computational modeling of abdominal aortic aneurysms

Starting from the aorta inside the human body as the object of interest, several steps need to be performed to receive a computational model. The following discussion comprises key points of the entire modeling process from imaging and segmentation over continuum mechanics equations towards the final discrete model, which can be evaluated for the quantity of interest.

4.1.1. In silico model

A description of the AAA computational model is provided in this section, the model was originally developed in [92]. Governing equations are stated. Special emphasis is devoted to the so-called *prestressing stage*, given that it poses a specific challenge to the snapshot collection and subsequent dimensional reduction process for projection-based MOR. Finally, model parameters common to all AAA models investigated in this thesis are given.

Computational domain: The challenge of numerical computations performed on AAAs starts with the identification of the computational domain. Several investigations using generic (i.e. not generated from imaging data) AAA shapes for computational analysis can be found in literature [4, 20]. Generic AAA models are independent from patient-specific data, which simply might not be available or raising ethical issues when gathered on the one hand. On the other hand, influence of AAA shape parametrizations can be investigated. Patient-specific aneurysm models in contrast typically are subject to uncertainties. Therefore, they are frequently investigated in combination with approaches for the quantification of these uncertainties [10, 14, 106].

Geometry data on patient-specific AAA models is obtained from medical screening such as computed tomography (CT) or magnetic resonance imaging (MRI). Both technologies return images of structures inside the body, while different physical principles are used. CT uses a rotating X-rays source, while MRI applies a magnetic field and radio waves for image capturing. A frequently named disadvantage of CT as compared to MRI scans are the exposure to harmful radiation. MRI disadvantages in turn are unpleasant noise and long duration of screening.

Assuming available image data of a patient-specific AAA, *segmentation* is performed to receive a 3D model geometry, which finally can be used as the computational domain for the finite element model [92]. Segmentation in medical context is the process of identifying anatomical structures in a set of given images. In more detail, imaged AAAs can be segmented by extracting the intraluminal thrombus (ILT) volume. The AAA wall can only be reconstructed in a second step (e.g. by extrusion of abluminal ILT surface), given that image resolution is insufficient [35]. For consistent results of segmentation across operators, the segmentation protocol as presented in [92] is followed in this thesis.

The mentioned ILT is prevailing in most AAAs and corresponds to a fibrin structure adhering to the vessel wall [135]. ILT mechanics has been extensively examined in literature [45, 81, 136], a non-negligible influence on AAA mechanics is found. As a consequence, AAA models in this thesis contain both ILT and AAA wall.

Figure 4.1 depicts an exemplary patient-specific computational domain Ω_0 on the left. The domain consists of the aneurysm sac, a small segment of the healthy aorta on the top and the

aortic bifurcation at the bottom. A cut through the AAA on the right reveals a separation into vessel wall and the ILT. Several surfaces are introduced for convenient reference. Γ_c denotes the proximal and distal cut surfaces, Γ_o is the outer AAA wall surface and Γ_l is the luminal ILT surface.

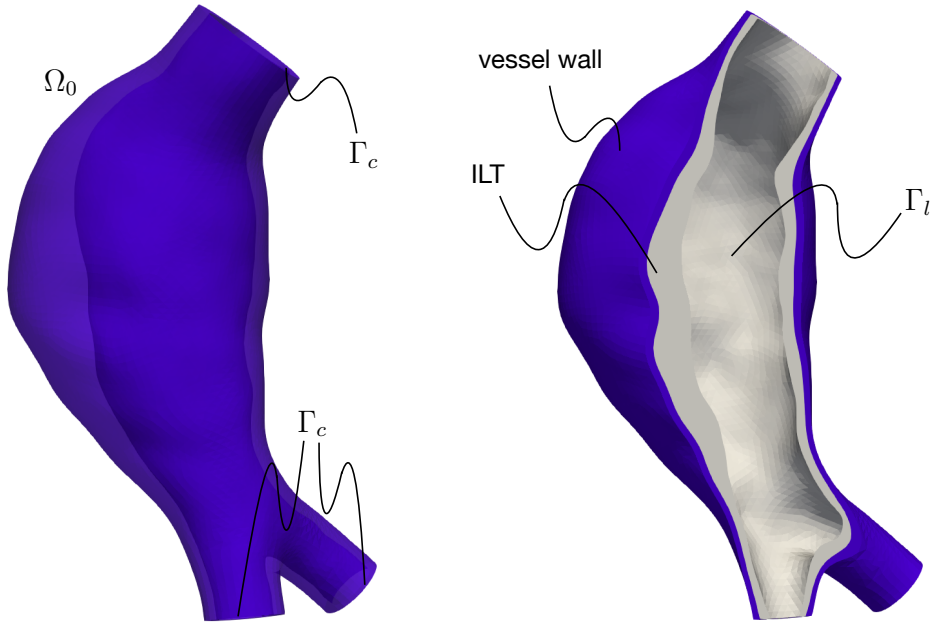

Figure 4.1.: Patient-specific AAA computational domain. The full domain is depicted on the left, while a cut through the AAA exposing the vessel wall (in blue) and the ILT (in light grey) is depicted on the right. Adapted with permission from [122] (published under CC BY license [28]). Adapted labeling to match the nomenclature in this thesis.

Constitutive modeling: Both ILT and arterial wall material behavior are modeled using an isochoric-volumetric split for the strain-energy density function

$$\Psi^{\mathrm{ILT}}(\bar{I}_1, \bar{I}_2, J) = \Psi^{\mathrm{ILT}}_{\mathrm{iso}}(\bar{I}_1, \bar{I}_2) + \Psi^{\mathrm{ILT}}_{\mathrm{vol}}(J), \tag{4.1}$$

$$\Psi\mathrm{wall}(\bar{I}_1, J) = \Psi^{\mathrm{wall}}_{\mathrm{iso}}(\bar{I}_1) + \Psi^{\mathrm{wall}}_{\mathrm{vol}}(J) \tag{4.2}$$

with the principal invariants

$$\bar{I}_1 = \mathrm{tr}(\bar{\boldsymbol{C}}), \tag{4.3}$$

$$\bar{I}_2 = \frac{1}{2}[\mathrm{tr}(\bar{\boldsymbol{C}})^2 - \mathrm{tr}(\bar{\boldsymbol{C}}^2)] \tag{4.4}$$

of the *modified right Cauchy-Green tensor*

$$\bar{\boldsymbol{C}} = \boldsymbol{F}^T_{\mathrm{iso}} \boldsymbol{F}_{\mathrm{iso}} \tag{4.5}$$

given

$$\boldsymbol{F}_{\mathrm{iso}} = J^{-\frac{1}{3}} \boldsymbol{F}. \tag{4.6}$$

The isochoric part of the strain-energy density exclusively models volume preserving continuum deformation, recalling equation (2.9) together with $\det(\boldsymbol{F}_{\text{iso}}) = 1$. The volumetric part in turn models constitutive response exclusively from the change of material element volume. The isochoric ILT strain-energy density reads

$$\Psi_{\text{iso}}^{\text{ILT}}(\bar{I}_1, \bar{I}_2) = c[\bar{I}_1^2 - 2\bar{I}_2 - 3]. \tag{4.7}$$

The material parameter c refers to material stiffness, which is spatially varying across the ILT [45]. To account for this spatial variation, c is interpolated linearly from a value at the luminal ILT surface c_{lum} to a medial value c_{med} and from c_{med} to a value at the abluminal surface c_{abl}.

The isochoric vessel wall contribution is given by

$$\Psi_{\text{iso}}^{\text{wall}}(\bar{I}_1) = \alpha[\bar{I}_1 - 3] + \beta[\bar{I}_1 - 3]^2 \tag{4.8}$$

and depends on the two material parameters α and β. For only slight continuum deformation, the contribution $[\bar{I}_1 - 3]$ dominates over $[\bar{I}_1 - 3]^2$, while the opposite occurs for large deformation. As a result, α can be interpreted as low-strain range stiffness, while β refers to a high-strain range stiffness. These parameters are referred to as α-stiffness and β-stiffness in the following.

Both volumetric strain-energy density contributions are modeled by the ansatz

$$\Psi_{\text{vol}}^{\text{x}}(J) = \frac{\kappa^{\text{x}}}{4}[J^2 - 2\ln(J) - 1] \tag{4.9}$$

with $\text{x} \in \{\text{ILT}, \text{wall}\}$. The volumetric bulk modulus κ^{x} is chosen sufficiently large, such that the strain-energy density mimics almost incompressible material behavior.

Governing equations: A finite element solution for the following set of equations is to be found

$$\nabla_{\boldsymbol{x}_0} \cdot \boldsymbol{P} = \boldsymbol{0} \qquad \text{in } \Omega_0, \tag{4.10}$$

$$\boldsymbol{P} \cdot \boldsymbol{n}_0 = \boldsymbol{t}_{p,0} \qquad \text{on } \Gamma_l, \tag{4.11}$$

$$\boldsymbol{u} = \boldsymbol{0} \qquad \text{on } \Gamma_c. \tag{4.12}$$

Referring to the balance of linear momentum (2.36), equation (4.10) corresponds to a steady-state momentum balance without volumetric forces. Exerted blood pressure p on the luminal ILT surface is modeled by the boundary condition (4.11), wherein the first Piola-Kirchhoff traction $\boldsymbol{t}_0$ results from the pressure load

$$\boldsymbol{t}_{p,0} = -pJ\boldsymbol{F}^{-T} \cdot \boldsymbol{n}_0. \tag{4.13}$$

Prestressing: Patient-specific AAA geometries are reconstructed from medical screening. The screening takes place in vivo, which means that the imaged geometry is under blood pressure. From a continuum mechanics perspective, this corresponds to a non stress-free reference configuration that needs special treatment in the simulation process and impacts results of AAA finite element analysis [47, 89].

To appropriately account for the non stress-free reference configuration, a stress state has to be evaluated for the spatially imaged configuration. This process is called *prestressing*. In literature, several approaches for aortic prestressing have been presented, such as the *inverse design*

method [46, 89]. The idea therein is to find a stress-free reference configuration, which will transform to the (imaged) known configuration after application of the load under consideration. In inverse design, the finite element problem is reformulated such that a deformation from stressed to stress-free configuration is retrieved. An alternative method for prestressing is the *backward incremental method* [33]. It makes use of multiple forward simulations and iteratively updates the stress-free configuration until convergence.

The modified updated Lagrangian formulation (MULF) [46, 47] is motivated by the need for a computationally efficient and reliable AAA prestressing method. Using MULF, the load under consideration is (incrementally) applied on the fixed imaged configuration, while a deformation gradient is accumulated from all preceding load steps

$$\boldsymbol{F}_p = \boldsymbol{F}^{n-1}\boldsymbol{F}^{n-2}\dots\boldsymbol{F}^{0}. \tag{4.14}$$

Recalling relation (2.30), the accumulated deformation gradient results in a stress state imprinted into the imaged configuration. By this, an approximation of the stress state in a fixed configuration is computed without direct reconstruction of the stress-free configuration. When a *deformation stage* (i.e. a simulation, wherein the geometry is deformed by the applied load) follows the prestressing stage, the accumulated deformation gradient $\boldsymbol{F}_p$ is used to "lift" the deformation stage displacement gradient $\boldsymbol{F}_d$ to the total deformation gradient $\boldsymbol{F}$

$$\boldsymbol{F} = \boldsymbol{F}_d\boldsymbol{F}_p. \tag{4.15}$$

Due to its computational efficiency and robustness, MULF is the method of choice for prestressing in this thesis. Given that the prestressing stage aims at computing a deformation gradient instead of a displacement field as primary variable, MULF prestressing in its original formulation is not suited for snapshot collection in the offline-stage of projection-based MOR. Here, a reformulation of the MULF prestressing stage motivated by the application in projection-based MOR is discussed following the presentation of the original article in [122].

Given a spatial configuration $\Omega \ni \boldsymbol{x}$, a reference configuration $\Omega_0 \ni \boldsymbol{x}_0$ and a virtual configuration $\tilde{\Omega}_0 \ni \tilde{\boldsymbol{x}}_0$, the relation

$$\boldsymbol{x} = \tilde{\boldsymbol{x}}_0 + \tilde{\boldsymbol{u}} = \boldsymbol{x}_0 + \boldsymbol{u} \tag{4.16}$$

holds, assuming that $\boldsymbol{u}$ and $\tilde{\boldsymbol{u}}$ denote the displacement fields from $\boldsymbol{x}_0$ and $\tilde{\boldsymbol{x}}_0$ to $\boldsymbol{x}$, respectively. Introducing the deformation gradient $\boldsymbol{F} = \frac{\partial \boldsymbol{x}}{\partial \boldsymbol{x}_0}$ and a virtual deformation gradient $\tilde{\boldsymbol{F}} = \frac{\partial \tilde{\boldsymbol{x}}_0}{\partial \boldsymbol{x}_0}$, the following kinematic relation can be stated

$$\boldsymbol{F} = \boldsymbol{I} + \frac{\partial \boldsymbol{u}}{\partial \boldsymbol{x}_0} = \frac{\partial[\boldsymbol{x}_0 + \boldsymbol{u}]}{\partial \boldsymbol{x}_0} = \frac{\partial[\tilde{\boldsymbol{x}}_0 + \tilde{\boldsymbol{u}}]}{\partial \boldsymbol{x}_0} = \frac{\partial[\tilde{\boldsymbol{x}}_0 + \tilde{\boldsymbol{u}}]}{\partial \tilde{\boldsymbol{x}}_0}\frac{\partial \tilde{\boldsymbol{x}}_0}{\partial \boldsymbol{x}_0} = \left[\boldsymbol{I} + \frac{\partial \tilde{\boldsymbol{u}}}{\partial \tilde{\boldsymbol{x}}_0}\right] \cdot \tilde{\boldsymbol{F}}. \tag{4.17}$$

Using equation (4.17), the identical first Piola-Kirchhoff stress field can be expressed in terms of a deformation gradient, a displacement field or virtual displacement field and deformation gradient

$$\boldsymbol{P} = \boldsymbol{P}_F(\boldsymbol{F}), \tag{4.18}$$
$$\boldsymbol{P} = \boldsymbol{P}_u(\boldsymbol{u}), \tag{4.19}$$
$$\boldsymbol{P} = \boldsymbol{P}_{u,F}(\tilde{\boldsymbol{u}}, \tilde{\boldsymbol{F}}), \tag{4.20}$$

wherein

$$\boldsymbol{P}_F : \boldsymbol{F} \mapsto \frac{\partial \Psi}{\partial \boldsymbol{F}}(\boldsymbol{F}), \tag{4.21}$$

$$\boldsymbol{P}_u : \boldsymbol{u} \mapsto \frac{\partial \Psi}{\partial \boldsymbol{F}} \left(\boldsymbol{I} + \frac{\partial \boldsymbol{u}}{\partial \boldsymbol{x}_0} \right), \tag{4.22}$$

$$\boldsymbol{P}_{u,F} : (\tilde{\boldsymbol{u}}, \tilde{\boldsymbol{F}}) \mapsto \frac{\partial \Psi}{\partial \boldsymbol{F}} \left(\left[\boldsymbol{I} + \frac{\partial \tilde{\boldsymbol{u}}}{\partial \tilde{\boldsymbol{x}}_0} \right] \cdot \tilde{\boldsymbol{F}} \right). \tag{4.23}$$

was defined. Recalling MULF prestressing, the virtual deformation gradient $\tilde{\boldsymbol{F}}$ can be interpreted as the prestress deformation gradient $\boldsymbol{F}_p$, while the bracket $[\boldsymbol{I} + \frac{\partial \tilde{\boldsymbol{u}}}{\partial \tilde{\boldsymbol{x}}_0}]$ corresponds to the deformation gradient from deformation stage. Using kinematic relation (4.17), the identical first Piola-Kirchhoff stress field can be expressed by

$$\boldsymbol{P} = \boldsymbol{P}_{u,F}(\boldsymbol{u}_d, \boldsymbol{F}_p) = \boldsymbol{P}_u(\boldsymbol{u}_d + \boldsymbol{u}_p), \tag{4.24}$$

wherein $\boldsymbol{u}_p$ is a *prestress displacement field* which is consistent with the prestress deformation gradient, that is

$$\boldsymbol{F}_p = \boldsymbol{I} + \frac{\partial \boldsymbol{u}_p}{\partial \boldsymbol{x}_0} \tag{4.25}$$

and $\boldsymbol{u}_d$ is the deformation stage displacement field. Consequently, instead of multiplicatively extending the deformation gradient (see equation (4.15)), the displacement field is extended additively by the prestress displacement field $\boldsymbol{u}_p$ (see equation (4.24)). In analogy to the displacement field, the prestress displacement field modes can be gathered in the offline-stage for ROB construction, see Section 3.1.3.

Summed up, the set of equations (4.10) - (4.12) is solved during prestressing for $\boldsymbol{u}_p$ with a first Piola-Kirchhoff traction load $\boldsymbol{t}_0$ evaluated on Ω_0, given that the spatial configuration is assumed fixed. Thereby, the pressure in equation (4.11) is increased up to diastolic blood pressure $p = p_{\text{dia}}$. In the subsequent deformation stage, the set of equations (4.10) - (4.12) is solved for the deformation stage displacement field $\boldsymbol{u}_d$, using the known prestress displacement field $\boldsymbol{u}_p$ for evaluation of the first Piola-Kirchhoff stress field (equation (4.24)). The boundary condition traction $\boldsymbol{t}_0$ is evaluated on the deforming configuration $\Omega \ni \boldsymbol{x}_0 + \boldsymbol{u}$, while the load is increased from diastolic pressure $p = p_{\text{dia}}$ to systolic pressure $p = p_{\text{sys}}$.

Model parameters, discretization and nonlinear solution: Data on model parameters and the discretization common to all performed AAA simulations in this thesis is provided here. α- and β-stiffness of the AAA wall together with the wall thickness t_w are given in terms of probability distributions (see Section 4.3) with the purpose of modeling patient-specific uncertainty. The ILT stiffness interpolation points are $c_{\text{lum}} = 2.62\,\text{kPa}$, $c_{\text{med}} = 1.98\,\text{kPa}$ and $c_{\text{abl}} = 1.73\,\text{kPa}$ [45]. The diastolic blood pressure value is assumed as $p_{\text{dia}} = 87\ \text{mmHg}\ (11.6\ \text{kPa})$, while the systolic value is $p_{\text{sys}} = 121\ \text{mmHg}\ (16.1\ \text{kPa})$.

A discretization with linear hexahedral finite elements with F-bar technology [34] is used for the AAA wall. The ILT is discretized with linear tetrahedral finite elements, while a layer of pyramidal finite elements with F-bar technology is used for the transition between the hexahedral and tetrahedral meshes. An exemplary mesh is depicted in Figure 4.2. The pressure load is applied in 25 steps, wherein 15 load steps are used for the prestressing stage and 10 load steps

for the deformation stage. Following the steps for spatial discretization as presented in Section 2, the finite element model residual reads

$$\boldsymbol{r}: \begin{cases} \mathbb{R}^N \to \mathbb{R}^N \\ \\ \text{for prestressing stage :} \\ \boldsymbol{d}_p \mapsto \boldsymbol{f}_{\text{int}}(\boldsymbol{d}_p) - \boldsymbol{f}_{\text{ext}}(\boldsymbol{0}, p_{\text{dia}}) \\ \\ \text{for deformation stage (with given } \boldsymbol{d}_p\text{) :} \\ \boldsymbol{d}_d \mapsto \boldsymbol{f}_{\text{int}}(\boldsymbol{d}_d + \boldsymbol{d}_p) - \boldsymbol{f}_{\text{ext}}(\boldsymbol{d}_d, p_{\text{sys}}) \end{cases}, \tag{4.26}$$

wherein $\boldsymbol{f}_{\text{ext}}(\boldsymbol{d}, p)$ was introduced as external force assembled from a pressure load p on a configuration following from displacement field $\boldsymbol{d}$. The nonlinear system of equations reads

$$\boldsymbol{r}^n(\boldsymbol{d}^n) = \boldsymbol{0}, \tag{4.27}$$

with n denoting the load step index (see Section 2.2.3).

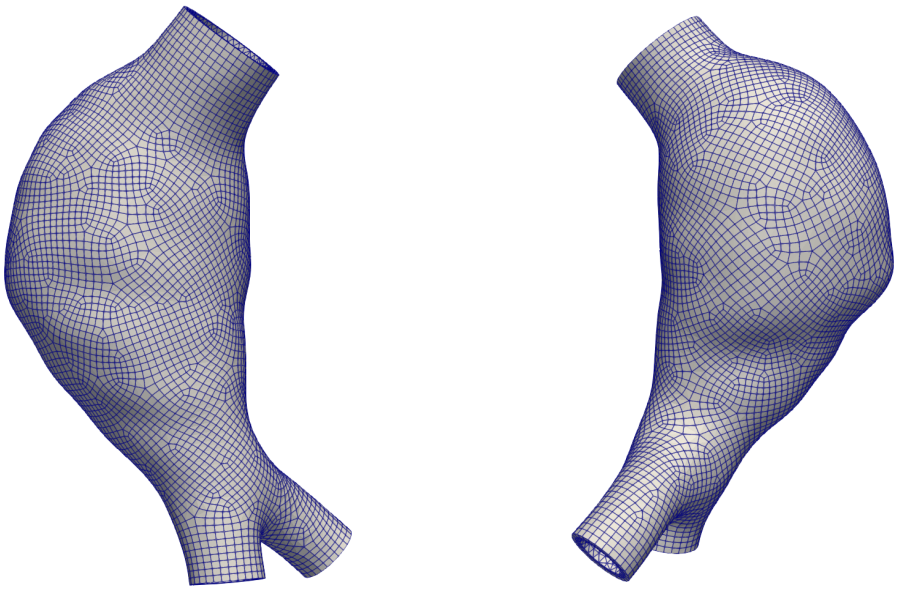

Figure 4.2.: Finite element mesh of the patient-specific AAA computational model.

The nonlinear models are iteratively solved applying Newton-Raphson iterations. Arising linear systems of equations in case of the FOM are solved using a parallel GMRES solver including an algebraic multigrid preconditioner from the software package Trilinos [55], while ROM linear systems of equations are solved using a direct solver [31].

4.1.2. Exemplary computation

An exemplary model evaluation at the parametrization of α-stiffness $\alpha = 169.38\,\text{kPa}$, β-stiffness $\beta = 541.45\,\text{kPa}$ and AAA wall thickness $t_w = 1.09\,\text{mm}$ is presented. The model is discretized by 140,019 finite elements with 109,587 degrees of freedom. Figure 4.3 depicts the prestress

displacement field $\boldsymbol{d}_p$ (i.e. the finite element approximation of $\boldsymbol{u}_p$), the deformation stage displacement field $\boldsymbol{d}_d$ (i.e. the finite element approximation of $\boldsymbol{u}_d$) and the resulting von Mises stress field at three different load levels.

Recalling that the prestressing stage is performed up to diastolic blood pressure load, the prestress displacement field evolves until $p = p_{\mathrm{dia}}$. In the deformation stage performed for a loading from diastolic to systolic blood pressure, the prestress displacement field remains unchanged. The opposite observation occurs for the deformation stage displacement field, which remains unchanged during prestressing and evolves during deformation stage. Finally, the von Mises stress increases in both stages, wherein imprinting into the undeformed configuration takes place in prestressing stage (given that $\boldsymbol{d}_d = \boldsymbol{0}$), while the systolic pressure load von Mises stress is given in a deformed configuration (given that $\boldsymbol{d}_d \neq \boldsymbol{0}$).

4.2. Reduced-order basis construction

Referring to Section 3, projection-based dimensional reduction builds upon a low-dimensional trial and test space for the nonlinear residual. Consequently, modes contained in the ROB must be chosen carefully in order to represent the solution subspace. If data-driven approaches including model evaluations in a parameter domain are used, the selection of ROB modes is directly related to the selection of points in the parameter domain.

The AAA model under consideration is stationary and only returns two modes of interest, namely the prestress displacement and the deformation stage displacement. In Section 4.2.3, a sampling strategy based on a so-called greedy maximin distance design and subspace angles as a termination criterion is presented. Maximin distance sampling and subspace angles are introduced as individual concepts in Section 4.2.1 and 4.2.2 first.

4.2.1. Space-filling designs and maximin distance sampling

Maximin distance sampling corresponds to a *space-filling design*, wherein space-filling designs are a topic in the research field "design of (computer) experiments (DOE)", please refer to [121] for a general DOE overview and space-filling designs in general. As the name suggests, space-filling designs attempt to distribute points evenly throughout the parameter domain, assuming that important features of the model output can be observed in the entire domain. Thereby, the exact meaning of "distribute evenly" depends on the applied sampling algorithm. At the same time, space-filling designs avoid model evaluations in close proximity to already evaluated points, in practice, the same point will never be evaluated twice. This feature is especially valuable for computer experiments having full control of model inputs and noise, such that replicated evaluation of a point will not reveal new information.

An intuitive example of a space filling design is the *factorial design* [26]. Given $n_{\mathcal{P}}$ as the dimension of the parameter space $\mathcal{P} \in \mathbb{R}^{n_{\mathcal{P}}}$ and $n_{\mathcal{P}i}, i \in \{0, \ldots, n_{\mathcal{P}}-1\}$, as the number of values taken by parameter i, a *full factorial design* claims $\prod_{i=0}^{n_{\mathcal{P}}-1} n_{\mathcal{P}i}$ model evaluations. As a result, whenever the number of model evaluations is limited, factorial designs might not be appropriate. Alternatively, statistical sampling methods can be used to produce space-filling designs. *Simple random sampling* is a popular choice, although a small number of samples frequently results in an unsatisfactory point distribution in terms of space-filling. An alternative is *stratified random*

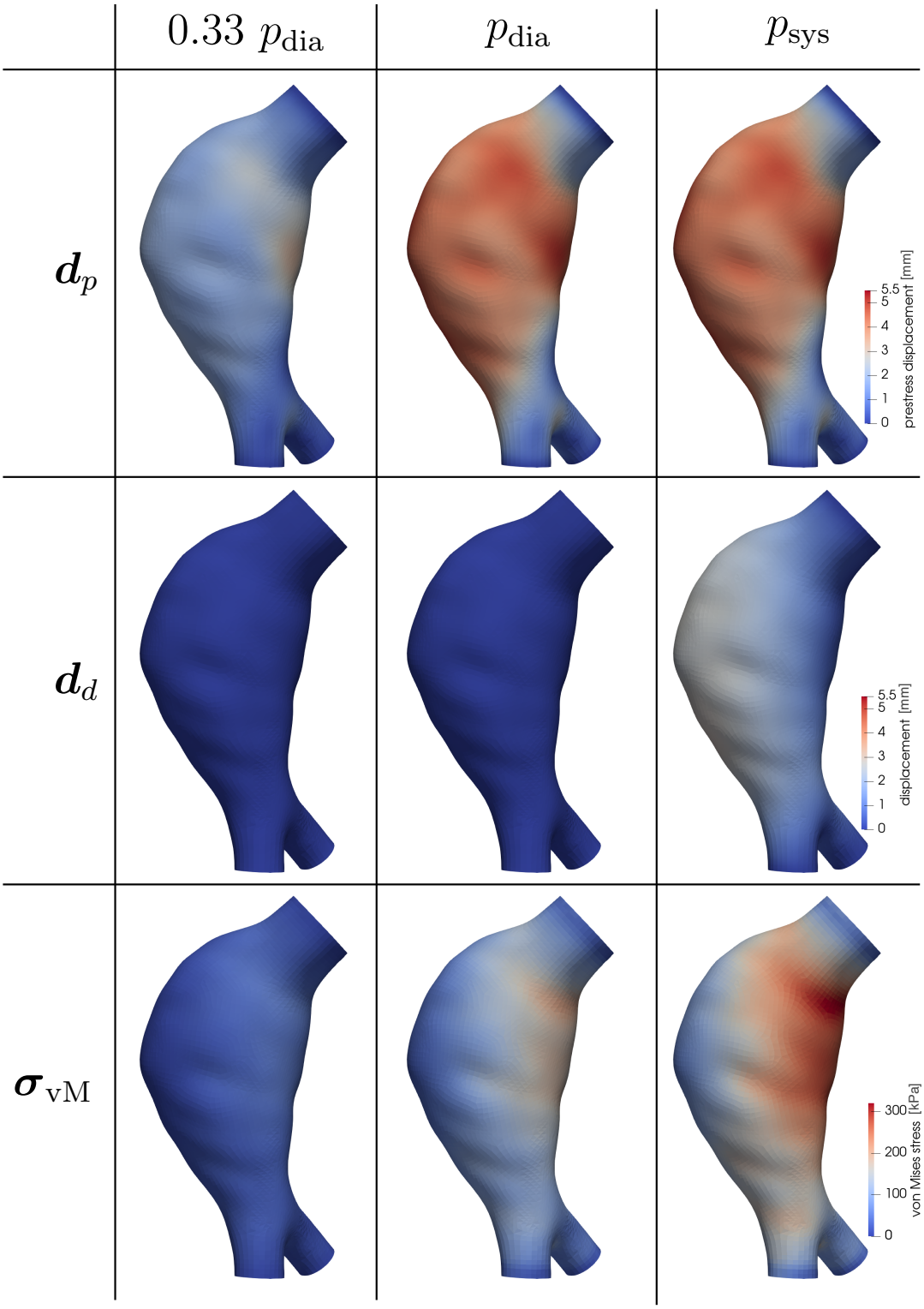

Figure 4.3.: Visualization of the prestressing stage displacement field (first row), deformation stage displacement field (second row) and von Mises stress field (third row) at different pressure loads.

sampling, wherein the parameter domain is first divided into subdomains, random sampling in each subdomain is performed next. Stratified random sampling typically results in better space-filling properties than simple random sampling [121].

Latin hypercube is another popular class of sampling designs. Assuming a $\mathcal{P} = [0,1]^{n_\mathcal{P}}$ parameter domain, $\mathcal{P}$ is divided into $n_a^{n_\mathcal{P}}$ equal subdomains (or cells), with $n_a \in \mathbb{N}_+$ indicating the number divisions for every parameter interval. A Latin hypercube design places n_a points in different cells. Thereby, the cells are selected in a way such that their midpoints result in equidistant distributions, if projected on any of the parameter domain axes. In 2D, a Latin hypercube design results in a point distribution with exactly one point in each row of cells and each column of cells. A Latin hypercube design as described will not necessarily have good space-filling properties, an intuitive example (with bad space-filling properties) is the selection of diagonal cells in 2D. Consequently, extensions have been presented in order to improve the original formulation [141].

The maximin distance design (MmD) under consideration in this thesis corresponds to the class of distance based sampling designs. MmD as well as the minimax distance design (mMD) have been introduced in [64], a recent review can be found in [108]. If given a training grid $\Sigma_t \subset [0,1]^{n_\mathcal{P}}$ and a set of n_μ chosen points $\boldsymbol{p}_i \in \Sigma_{n_\mu}^{\mathrm{Mm}} \subset \Sigma_t, i \in \{0,\dots,n_\mu - 1\}$, then $\Sigma_{n_\mu}^{\mathrm{Mm}}$ is a MmD with respect to the euclidean norm if

$$\min_{\boldsymbol{p}_i,\boldsymbol{p}_j \in \Sigma_{n_\mu}^{\mathrm{Mm}}} \|\boldsymbol{p}_i - \boldsymbol{p}_j\|_2 = \max_{\Sigma_{n_\mu} \subset \Sigma_t} \left[\min_{\boldsymbol{p}_i,\boldsymbol{p}_j \in \Sigma_{n_\mu}} \|\boldsymbol{p}_i - \boldsymbol{p}_j\|_2 \right] \qquad \forall i,j \in \{0,\dots,n_\mu - 1\} \text{ with } i \neq j \tag{4.28}$$

holds, wherein Σ_{n_μ} denotes an arbitrary subset of Σ_t with n_μ elements. In words, a MmD distributes points such that the minimal distance between any two selected points is maximized. The mMD $\Sigma_{n_\mu}^{\mathrm{mM}} \subset \Sigma_t$ in contrast distributes points such that

$$\max_{\boldsymbol{p} \in \Sigma_t} \left[\min_{\boldsymbol{p}_i \in \Sigma_{n_\mu}^{\mathrm{mM}}} \|\boldsymbol{p} - \boldsymbol{p}_i\|_2 \right] = \min_{\Sigma_{n_\mu} \subset \Sigma_t} \left[\max_{\boldsymbol{p} \in \Sigma_t} \left[\min_{\boldsymbol{p}_i \in \Sigma_{n_\mu}} \|\boldsymbol{p} - \boldsymbol{p}_i\|_2 \right] \right] \qquad \forall i \in \{0,\dots,n_\mu - 1\} \tag{4.29}$$

holds. Consequently, the mMD organizes points such that any training grid point $\boldsymbol{p} \in \Sigma_t$ is as closely as possible to another point from the design $\Sigma_{n_\mu}^{\mathrm{mM}}$. For clear distinction between maximin and minimax, please note that a MmD (4.28) results from a maximization over all possible designs $\max_{\Sigma_{n_\mu} \subset \Sigma_t}$, while a mMD (4.29) results from a minimization over possible designs $\min_{\Sigma_{n_\mu} \subset \Sigma_t}$. General surrogate modeling by MmDs has been discussed broadly [29, 44, 132, 142]. Specific applications related to radial-basis-function surrogates can be found in e.g. [88] using the maximin distance criterion to sample cut lines and planes and in [15] to place points in Voronoi cells.

Both MmD as well as mMD are computationally demanding optimization problems, which require initial knowledge about the number of points to distribute. In [95], a greedy version of a MmD solving a local optimization problem in every iteration has been presented. Algorithm 3 depicts the selection of a single greedy maximin distance design (GMmD) point from an input grid $\Sigma_i \subset \Sigma_t \subset \mathcal{P}$, given a set of previously chosen points $\Sigma_c \subset \Sigma_t \subset \mathcal{P}$. Thereby, the maximin criterion is evaluated on a reference hypercube, which is possible after transformation

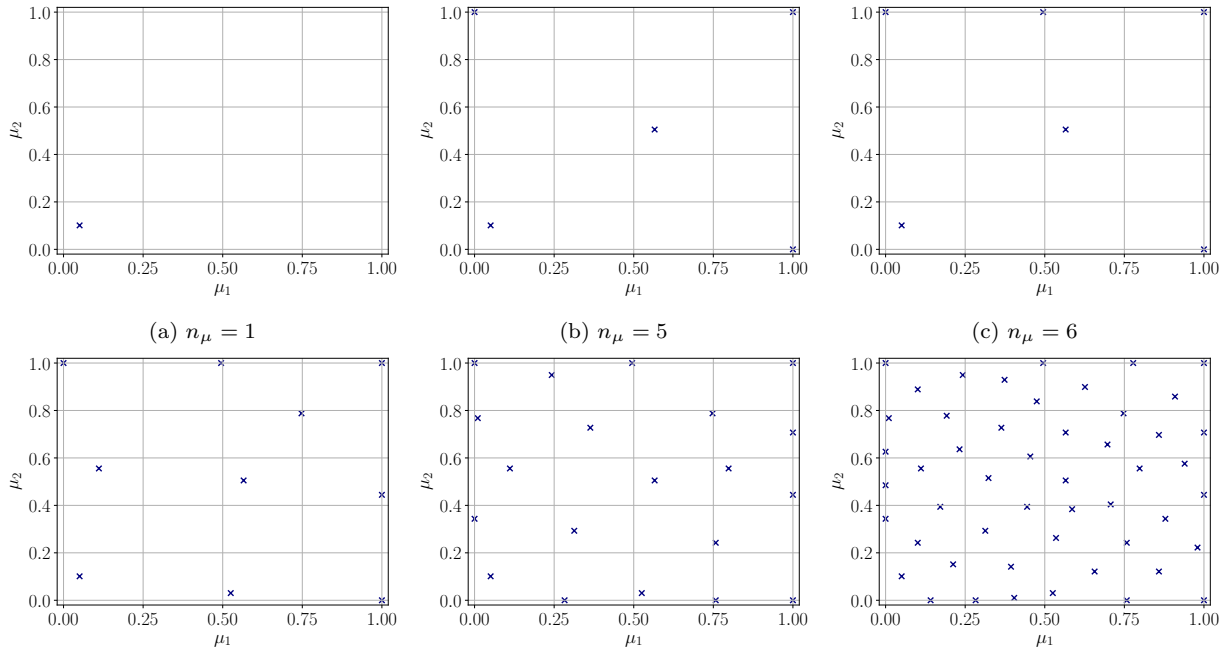

(a) $n_\mu = 1$ (b) $n_\mu = 5$ (c) $n_\mu = 6$

(d) $n_\mu = 10$ (e) $n_\mu = 20$ (f) $n_\mu = 50$

Figure 4.4.: Exemplary GMmD design with first point chosen at random. Reproduced with permission from [122] (published under CC BY license [28]).

by the map χ from physical domain to reference hypercube. Algorithm 4 depicts the steps for the construction of a full GMmD, given a single initial point. Figure 4.4 visualizes several GMmD designs at different n_μ. The space-filling property together with an increased exploration of the domain boundary can be observed.

Algorithm 3 MaxiMinPoint(Σ_i, Σ_c) (select a GMmD point)

Input: input grid $\Sigma_i \subset \Sigma_t$, previously chosen points $\Sigma_c \subset \Sigma_t$
Output: selected grid point $\boldsymbol{\mu}$

1: $\tilde{\Sigma}_i = \chi(\Sigma_i)$, $\tilde{\Sigma}_c = \chi(\Sigma_c)$ ▷ transform grids to reference hypercube
2: $\tilde{\boldsymbol{\mu}} = \arg\max_{\tilde{\boldsymbol{q}} \in \tilde{\Sigma}_i} \left(\min_{\tilde{\boldsymbol{p}} \in \tilde{\Sigma}_c} \|\tilde{\boldsymbol{q}} - \tilde{\boldsymbol{p}}\|_2 \right)$ ▷ get next point in reference hypercube
3: $\boldsymbol{\mu} = \chi^{-1}(\tilde{\boldsymbol{\mu}})$ ▷ transform point to physical domain
4: return $\boldsymbol{\mu}$ ▷ return point in physical domain

4.2.2. Subspace angles

In this thesis, *subspace angles* (or *principle angles*) are used to quantify the difference between subspaces. Subspace angles are known from matrix computations [48]. For subspaces given by the column spans of two matrices $\boldsymbol{Y} \in \mathbb{R}^{N \times n}$ and $\boldsymbol{Z} \in \mathbb{R}^{N \times m}$ with $n \leq m$, subspace angles can be defined recursively by

$$\theta_k = \min_{\boldsymbol{y} \in \boldsymbol{Y}_k^\perp, \boldsymbol{z} \in \boldsymbol{Z}_k^\perp} \arccos(\boldsymbol{y}^T \boldsymbol{z}) \quad \text{with } k \in \{0, \ldots, n-1\}. \tag{4.30}$$

Algorithm 4 MaxiMinDesign$(\Sigma_t, \boldsymbol{\mu}, n_\mu)$ (construct GMmD design)

Input: training grid $\Sigma_t \subset \mathcal{P}$, starting point $\boldsymbol{\mu} \in \Sigma_t$, number of points to select n_μ
Output: chosen points Σ_c

1: $\Sigma_c = \{\boldsymbol{\mu}\}$
2: **for** $i \in (0, \ldots, n_\mu - 1)$ **do**
3: $\quad \boldsymbol{\mu} = \mathrm{MaxiMinPoint}(\Sigma_\mathrm{t}, \Sigma_\mathrm{c})$
4: $\quad \Sigma_c \leftarrow \Sigma_c \cup \boldsymbol{\mu}$
5: **end for**
6: return Σ_c

The mentioned recursion becomes apparent when defining the complements

$$\begin{aligned} \boldsymbol{Y}_k^\perp &= \{\boldsymbol{y} : \boldsymbol{y} \in \mathrm{span}(\boldsymbol{Y}), \|\boldsymbol{y}\| = 1\} \\ \boldsymbol{Z}_k^\perp &= \{\boldsymbol{z} : \boldsymbol{z} \in \mathrm{span}(\boldsymbol{Z}), \|\boldsymbol{z}\| = 1\} \\ &\qquad \text{for } k = 0 \end{aligned} \tag{4.31}$$

and

$$\begin{aligned} \boldsymbol{Y}_k^\perp &= \{\boldsymbol{y} : \boldsymbol{y} \in \mathrm{span}(\boldsymbol{Y}), \|\boldsymbol{y}\| = 1, \boldsymbol{y}^T \boldsymbol{y}_j = 0\} \\ \boldsymbol{Z}_k^\perp &= \{\boldsymbol{z} : \boldsymbol{z} \in \mathrm{span}(\boldsymbol{Z}), \|\boldsymbol{z}\| = 1, \boldsymbol{z}^T \boldsymbol{z}_j = 0\} \\ &\quad \text{for } j \in \{0, \ldots, k-2\},\ k \in \{1, \ldots, n-1\}, \end{aligned} \tag{4.32}$$

which for $k \neq 0$ are defined in terms of the *principle vectors* $\boldsymbol{y}_j, \boldsymbol{z}_j$ with $j \in \{0, \ldots, k-2\}$. Definition of the complements is completed by providing the principle vectors as the minimization arguments of equation (4.30)

$$\boldsymbol{y}_k, \boldsymbol{z}_k = \arg \min_{\boldsymbol{y} \in \boldsymbol{Y}_k^\perp, \boldsymbol{z} \in \boldsymbol{Z}_k^\perp} \arccos(\boldsymbol{y}^T \boldsymbol{z}) \quad \text{with } k \in \{0, \ldots, n-1\}. \tag{4.33}$$

Please note, that the $\arccos : [-1; 1] \mapsto [0°; 180°]$ operation in (4.30) is valid given that $|\boldsymbol{y}^T \boldsymbol{z}| \leq 1$, as can be seen from the definition of $\boldsymbol{Y}_k^\perp$ and $\boldsymbol{Z}_k^\perp$. Equation (4.30) also reveals why the maximum subspace angle can be interpreted as a measure for difference of subspaces. A maximum subspace angle of $\theta_{n-1} = 90°$ indicates that there is at least one direction in $\mathrm{span}(\boldsymbol{Y})$ orthogonal to $\mathrm{span}(\boldsymbol{Z})$. As a result, there are vectors in $\mathrm{span}(\boldsymbol{Y})$ not representable by $\mathrm{span}(\boldsymbol{Z})$. A maximum subspace angle of $\theta_{n-1} = 0°$ indicates that $\mathrm{span}(\boldsymbol{Y}) \subset \mathrm{span}(\boldsymbol{Z})$ and consequently that any vector in $\mathrm{span}(\boldsymbol{Y})$ is representable in $\mathrm{span}(\boldsymbol{Z})$. In the following, the maximum subspace angle is referred to as the subspace angle distance (SAD). Figure 4.5 provides a geometrical interpretation of subspace angles in 3D.

Projection-based MOR has seen multiple applications of subspace angles. An interpolation of ROB subspace angles for flow problems is presented in [85–87]. Application of subspace angle interpolation to a Diffusion-Convection-Reaction problem is presented in [2]. The use of subspace angles as a stopping criterion has been demonstrated in [7, 66, 133] with focus on linear time-invariant state-space systems [7, 133] and trajectory piecewise linear approximation [66].

Numerical computation of subspace angles does not require the recursive solution of optimization formulation (4.30). Instead, a singular value decomposition can be applied, as depicted

in Algorithm 5 [48]. The arccos operation in line 3 is valid, given that $\boldsymbol{Q}_Y, \boldsymbol{Q}_Z$ are orthonormal matrices, such that $|\xi_i| \leq 1$ holds for the entries of the singular values vector $\boldsymbol{\xi}$.

Algorithm 5 SSA($\boldsymbol{Y}, \boldsymbol{Z}$) (computation of subspace angles)

Input: $\boldsymbol{Y} \in \mathbb{R}^{N \times n}$, $\boldsymbol{Z} \in \mathbb{R}^{N \times m}$ with $n \leq m$

Output: subspace angles $\boldsymbol{\theta}$

1: $\boldsymbol{Y} = \boldsymbol{Q}_Y \boldsymbol{R}_Y$, $\boldsymbol{Z} = \boldsymbol{Q}_Z \boldsymbol{R}_Z$ ▷ perform thin QR factorization [48]

2: $\boldsymbol{Q}_Y^T \boldsymbol{Q}_Z = \boldsymbol{U} \mathrm{diag}(\boldsymbol{\xi}) \boldsymbol{Q}^T$ ▷ perform thin singular value decomposition [48]

3: $\boldsymbol{\theta} = \arccos(\boldsymbol{\xi})$ ▷ transform to angle

4: return $\boldsymbol{\theta}$

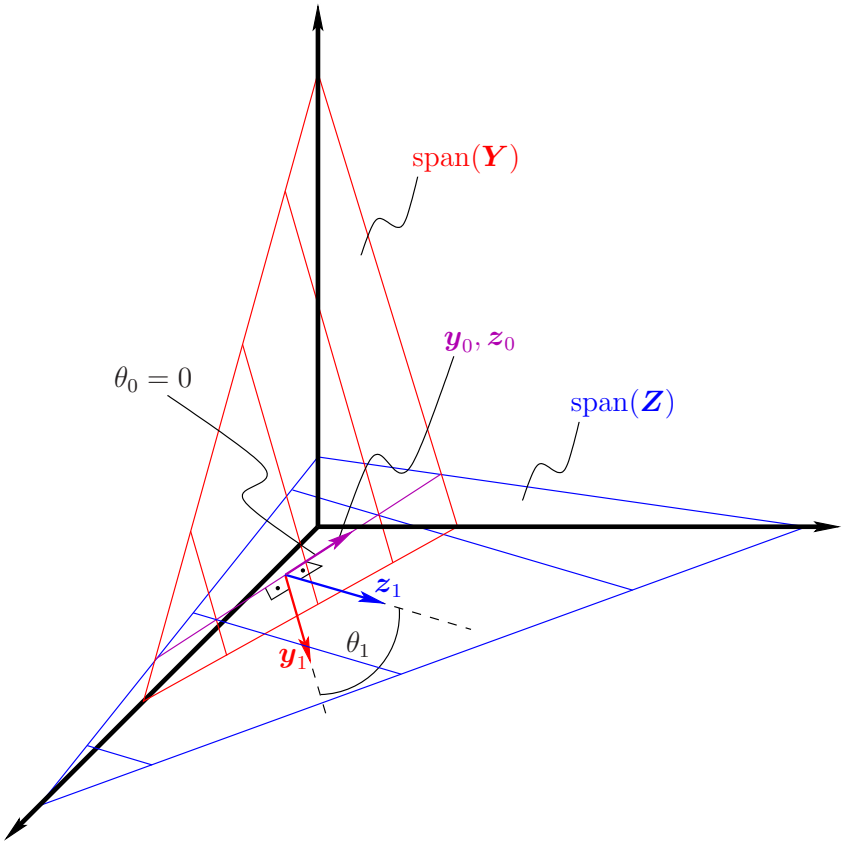

Figure 4.5.: Geometrical interpretation of subspace angles in 3D space between 2D subspaces. The 2D subspaces are visualized by the red and blue plane and correspond to the column span of $\boldsymbol{Y} \in \mathbb{R}^{3\times2}$ and $\boldsymbol{Z} \in \mathbb{R}^{3\times2}$, respectively. The principle vectors $\boldsymbol{y}_0, \boldsymbol{y}_1 \in \mathrm{span}(\boldsymbol{Y})$ and $\boldsymbol{z}_0, \boldsymbol{z}_1 \in \mathrm{span}(\boldsymbol{Z})$ enclose the corresponding subspace angles θ_0 and θ_1. Reproduced with permission from [122] (published under CC BY license [28]).

The application of the SAD is exemplified for quantifying the difference of subspaces using the package numpy (version 1.16.2) [51] from the Python programming language. For this,

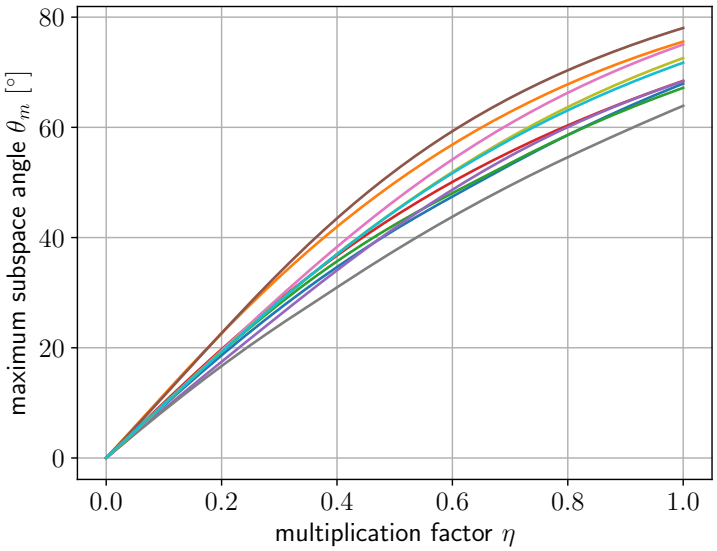

Figure 4.6.: Maximum subspace angle between matrices $\boldsymbol{Y}_0 \in \mathbb{R}^{100\times 20}$ and $\boldsymbol{Y}_1 \in \mathbb{R}^{100\times 20}$ over perturbation factor η from equation (4.34) for ten different realizations. Large perturbations are indicated by large maximum subspace angles.

the matrices $\boldsymbol{Y}_0, \boldsymbol{Z} \in \mathbb{R}^{100\times 20}$ are created. Both matrices contain uniformly distributed random entries in the interval $[0, 1]$. A third random matrix $\boldsymbol{Y}_1$ is generated by

$$\boldsymbol{Y}_1 = \boldsymbol{Y}_0 + \eta \boldsymbol{Z} \tag{4.34}$$

introducing a scalar η. By this, η gives control of the difference between $\boldsymbol{Y}_0$ and $\boldsymbol{Y}_1$ as well as the subspaces spanned by the columns of $\boldsymbol{Y}_0$ and $\boldsymbol{Y}_1$ by scaling a normed perturbation $\boldsymbol{Z}$. Figure 4.6 depicts the maximum subspace angle over the multiplication factor η for ten different realizations of $\boldsymbol{Y}_0$ and $\boldsymbol{Z}$ ($\boldsymbol{Y}_1$ follows from (4.34)). For every single realization, large perturbations are indicated by a large maximum subspace angle.

4.2.3. Construction of low-dimensional solution subspaces by greedy maximin distance sampling

The two concepts of GMmD sampling and subspace angles are combined to an efficient sampling algorithm aiming at the construction of a ROB as well as a snapshot matrix with modes used for subsequent hyper reduction by ECSW, see Section 3.2.2. Thereby, GMmD sampling is used to scatter new points, while subspace angles are evaluated aiming at a termination criterion. In more detail, the parameter domain is subdivided into n_{sd} subdomains $\Sigma_{sd,i},\ i \in \{0, \dots, n_{sd} - 1\}$ with $\Sigma_{sd,i} \cap_{i\neq j} \Sigma_{sd,j} = \emptyset$ for $i, j \in \{0, \dots, n_{sd} - 1\}$ and $\cup_{i=0}^{n_{sd}-1} \Sigma_{sd,i} = \Sigma_t$, which are subsequently excluded from sampling based on a subspace angle criterion. By introducing subdomains, the sampling algorithm becomes adaptive. Feedback from the parametric domain in terms of subspace angles is processed and used for exclusion of subdomains, such that individual subdomains might receive more detailed sampling than others.

Algorithm 6 depicts the individual steps. First, the FOM is evaluated at a starting parametric configuration $\boldsymbol{\mu}$. The local snapshot matrix $\boldsymbol{s}(\boldsymbol{\mu})$ is orthogonalized (line 1:) and used for the

Algorithm 6 SDMaxiMinSampling($\Sigma_{sd}, \boldsymbol{\mu}, \theta_{\text{th}}$) (GMmD sampling on subdomains)

Input: subdomain set $\Sigma_{sd} = \{\Sigma_{sd,0} \ldots, \Sigma_{sd,n_{sd}-1}\}$, starting point $\boldsymbol{\mu} \in \Sigma_{sd,0}$, threshold angle θ_{th}
Output: chosen grid points $\Sigma_c = \{\boldsymbol{\mu}_0, \ldots, \boldsymbol{\mu}_{n_\mu-1}\}$, ROB $\boldsymbol{V}$, snapshot matrix $\boldsymbol{S}$

$\boldsymbol{s}(\boldsymbol{\mu}) = \boldsymbol{Q}\boldsymbol{R}$ ▷ thin QR factorization [48] of initial snapshot matrix
$\boldsymbol{V} = \boldsymbol{Q}$
$\boldsymbol{S} = \boldsymbol{s}(\boldsymbol{\mu})$
$\Sigma_c = \{\boldsymbol{\mu}\}$
$\Sigma = (\Sigma_{sd,1}, \ldots, \Sigma_{sd,n_{sd}-1}, \Sigma_{sd,0})$ ▷ define subdomain tuple for iteration
while True **do**
    for $\Sigma_{sd,i} \in \Sigma$ **do** ▷ iterate over subdomains
        $\boldsymbol{\mu} = \text{MaxiMinPoint}(\Sigma_{sd,i}, \Sigma_c)$
        $\Sigma_c \leftarrow \Sigma_c \cup \boldsymbol{\mu}$
        $\boldsymbol{\theta} = \text{SSA}(\boldsymbol{V}, \boldsymbol{s}(\boldsymbol{\mu}))$
        $\theta_m = \max(\boldsymbol{\theta})$
        if $\theta_m < \theta_{\text{th}}$ **then** ▷ in case of small maximum subspace angle
            $\Sigma \leftarrow \Sigma \backslash \Sigma_{sd,i}$ ▷ exclude subdomain from sampling
        end if
        $\boldsymbol{V} \leftarrow \text{Orthogonalize}([\boldsymbol{V}, \boldsymbol{s}(\boldsymbol{\mu})])$ ▷ extend ROB
        $\boldsymbol{S} \leftarrow [\boldsymbol{S}, \boldsymbol{s}(\boldsymbol{\mu})]$ ▷ extend snapshot matrix
    end for
    if $\Sigma = \emptyset$ **then** ▷ if no subdomain left
        break ▷ stop algorithm
    end if
end while
return $\Sigma_c, \boldsymbol{V}, \boldsymbol{S}$

initialization of the ROB (line 2:) and the snapshot matrix (line 3:). Looping through each active subdomain (line 7:), a new point is set by a GMmD step (line 8). A local snapshot matrix $\boldsymbol{s}(\boldsymbol{\mu})$ is evaluated (line 10:) and used to extend the ROB (line 15:) and the global snapshot matrix (line 16:). Please note, that the ROB extension strategy ensures that $\mathrm{span}(\boldsymbol{V}_i) \subset \mathrm{span}(\boldsymbol{V}_j)$ for $j \geq i$, assuming $\boldsymbol{V}_i$ and $\boldsymbol{V}_j$ to represent ROBs after GMmD iteration i and j, respectively. Additionally, the maximum subspace angle θ_m (line 10:, 11:) is computed. A small θ_m indicates, that the snapshot matrix is well representable within the accumulated ROB, see Section 4.2.2. If θ_m is below a predefined threshold subspace angle θ_{th} (line 12:) the current subdomain is excluded from sampling (line 13:). Sampling stops and the algorithm terminates, if all subdomains have been excluded (line 18:, 19:).

The terminology used in [29] allows the following classification of the presented sampling algorithm:

- global: A single ROB is built for the entire computational domain.
- sequential / adaptive: In contrast to *one-shot* designs (i.e. designs with point distributions which can be determined before the first simulation), points are distributed iteratively including analysis of data from previous simulations.
- fine-grained: Only one point is selected per iteration.
- explorative: Initial iterations over all subdomains ensure coverage of the entire domain.
- exploitive: With increasing number of excluded subdomains, the algorithm gains the property of exploitation by concentrated sampling of domain regions of interest.
- collapsing: In a *non-collapsing* design, any two selected points will not take the same value in any parameter domain axis. This property is not ensured by GMmD sampling.

4.3. Results and discussion

In this section, three patient-specific computational AAA models are investigated. GMmD is applied for construction of dimensionally reduced order models (DROMs) and ECSW for hyper reduction, which yields dimensionally reduced as well as hyper reduced order models (DHROMs). Both ROMs are evaluated in terms of accuracy and speedup. Direct Monte Carlo sampling applied to the DHROMs is shown to be accurate in the estimation of AAA wall maximum von Mises stress and maximum von Mises strain probability distributions.

4.3.1. Subspace inclination

In this introductory numerical experiment, the influence of the solution subspace inclination on model accuracy is investigated, wherein model accuracy is assessed in terms of the final (i.e. after fully performing prestressing stage and deformation stage) von Mises stress field and the von Mises strain field in the AAA wall as quantity of interest. The evaluation of the presented exemplary computation (see Section 4.1.2) is used as the baseline solution and a ROB $\boldsymbol{V}$ is built from a subspace spanned by prestressing stage and deformation stage displacement field.

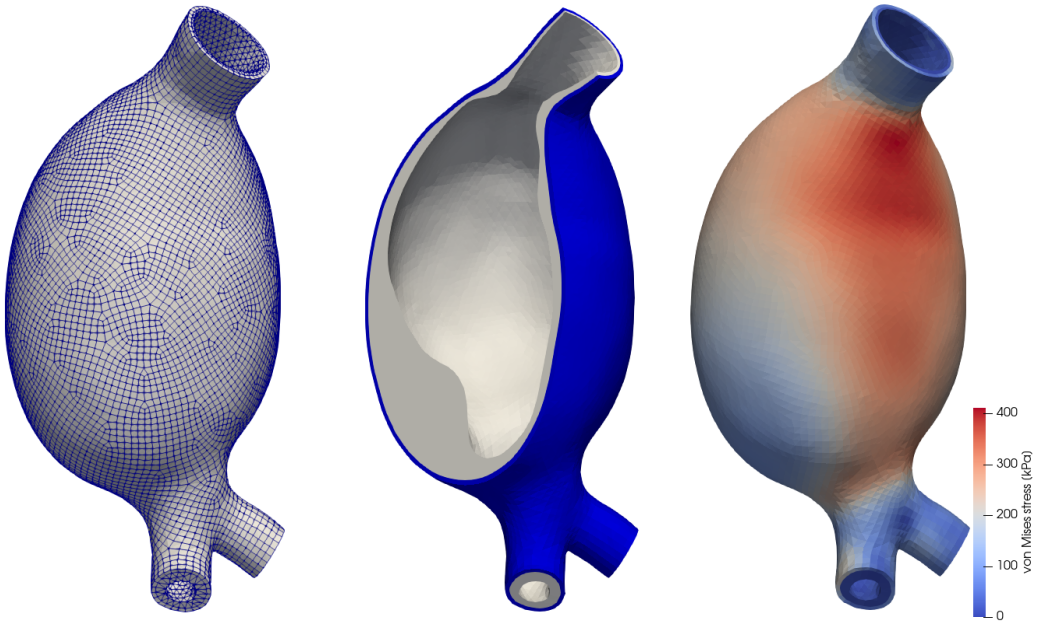

(a) (b) (c)

Figure 4.7.: Patient 2 mesh (a), cut exposing ILT (b), exemplary von Mises stress distribution (c). Reproduced with permission from [122] (published under CC BY license [28]).

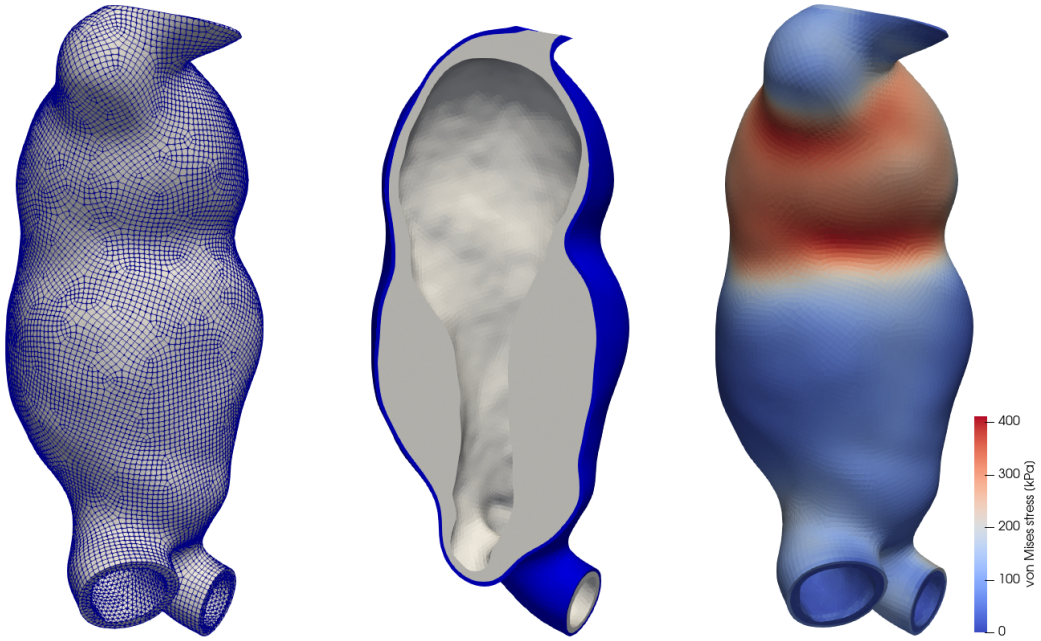

(a) (b) (c)

Figure 4.8.: Patient 3 mesh (a), cut exposing ILT (b), exemplary von Mises stress distribution (c). Reproduced with permission from [122] (published under CC BY license [28]).

The generated FOM solution subspace $\mathrm{span}(\boldsymbol{V})$ can be interpreted as perfectly tailored for the exemplary computation. This can be seen from the resulting DROM, which returns relative

errors of $RE(\tilde{\boldsymbol{\sigma}}_{\mathrm{vM}}, \boldsymbol{\sigma}_{\mathrm{vM}}) = 1.5 \cdot 10^{-11}$ and $RE(\tilde{\boldsymbol{e}}_{\mathrm{vM}}, \boldsymbol{e}_{\mathrm{vM}}) = 8.2 \cdot 10^{-12}$. The relative (l2-norm) error is defined by

$$RE(\tilde{\boldsymbol{x}}, \boldsymbol{x}) = \frac{\|\tilde{\boldsymbol{x}} - \boldsymbol{x}\|_2}{\|\boldsymbol{x}\|_2}, \qquad RE(\tilde{x}, x) = \frac{|\tilde{x} - x|}{|x|} \tag{4.35}$$

with $\boldsymbol{x}, x$ representing FOM solution quantities and $\tilde{\boldsymbol{x}}, \tilde{x}$ representing ROM solution approximations and usage of l2-norm $\|\bullet\|_2$ in case of vector valued quantities and the absolute value $|\bullet|$ for scalar valued quantities.

In this section, the perfectly tailored subspace is perturbed by inclination with a given angle α_{incl}. Consequently, the level of perturbation is controlled by the value of α_{incl}. The other component in subspace inclination are the directions of inclination, which are constructed as vectors of unit length being orthogonal with respect to each other and to the perfectly tailored subspace, see Figure 4.9 for an illustration.

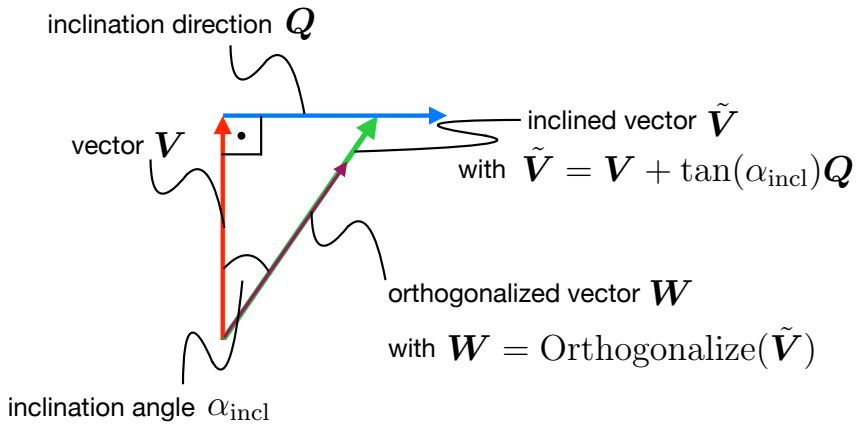

Figure 4.9.: Inclination of a subspace represented by $\mathrm{span}(\boldsymbol{V})$. The direction of inclination is $\boldsymbol{Q}$ and the angle of inclination is α_{incl}. The inclined subspace is $\mathrm{span}(\boldsymbol{W})$. Following relations hold: $\|\boldsymbol{V}\|_2 = \|\boldsymbol{Q}\|_2 = \|\boldsymbol{W}\|_2 = 1$, $\boldsymbol{V}^T\boldsymbol{Q} = 0$, $\boldsymbol{V}^T\boldsymbol{W} = \cos(\alpha_{\mathrm{incl}})$.

Summed up, a set of inclined subspaces $\mathrm{span}(\boldsymbol{W}_{ij})$ has been created by inclination of the perfectly tailored ROB vectors with an angle $\alpha_{\mathrm{incl},i}$ (index i) in directions given by matrix $\boldsymbol{Q}_j$ (same shape as $\boldsymbol{V}$, index j)

$$\tilde{\boldsymbol{V}}_{ij} = \boldsymbol{V} + \tan(\alpha_{\mathrm{incl},i})\boldsymbol{Q}_j \tag{4.36}$$

and subsequent orthogonalization

$$\boldsymbol{W}_{ij} = \mathrm{Orthogonalize}(\tilde{\boldsymbol{V}}_{ij}). \tag{4.37}$$

10 exemplary inclination angles $\alpha_{\mathrm{incl}} \in \{0.01° \cdot 3^0, 0.01° \cdot 3^1, \ldots, 0.01° \cdot 3^8, 90°\}$ and 100 inclination directions $\boldsymbol{Q}_j,\ j \in \{0, \ldots, 99\}$ are chosen. The $\boldsymbol{Q}_j$ are created using random number generated matrices (uniform distributions in the range [0,1]) with subsequent orthogonalization, which ensures that the resulting inclination directions are orthogonal to the tailored ROB, i.e. $\boldsymbol{V}^T\boldsymbol{Q}_j = \boldsymbol{0}$, orthonormal to themselves, i.e. $\boldsymbol{Q}_j^T\boldsymbol{Q}_j = \boldsymbol{I}$ and orthogonal to each other in order to have independence in the sense of $\boldsymbol{Q}_j^T\boldsymbol{Q}_i = \boldsymbol{0}$ for $i \neq j$. Additionally, inclination directions

are modified to preserve zero value Dirichlet boundary conditions by setting the corresponding values in the $\boldsymbol{Q}_j$ to zero.

Figure 4.10 depicts the resulting relative l2-errors for the quantities of interest over subspace inclination angles. In more detail, a DROM simulation is evaluated for every point and the relative l2-error with respect to the FOM solution is calculated. Applied ROBs result from inclination of the FOM solution subspace in direction of $\boldsymbol{Q}_j, j \in \{0, \ldots, 99\}$ (each color corresponds to one distinct inclination direction) by several angles (horizontal axes in Figure 4.10). Following observations can be made. Small inclination angles result in small relative l2-errors and the direction of inclination does not have a significant influence. The latter also applies to large inclination angles. For moderate inclinations, the relative l2-error scatters over a pronounced range. Obviously, inclining subspaces with a given angle in certain directions introduces significantly more or less distortion in the quantities of interest than other inclination directions. Also, this tendency is preserved over different inclination angles, which can be seen from the similar stacking of colors for different angles. For instance, one of the randomly generated inclination directions is significantly less distorting the solution than the remaining directions (one point in light blue tends to smaller errors than all others points). This holds for the entire range of moderate inclination angles.

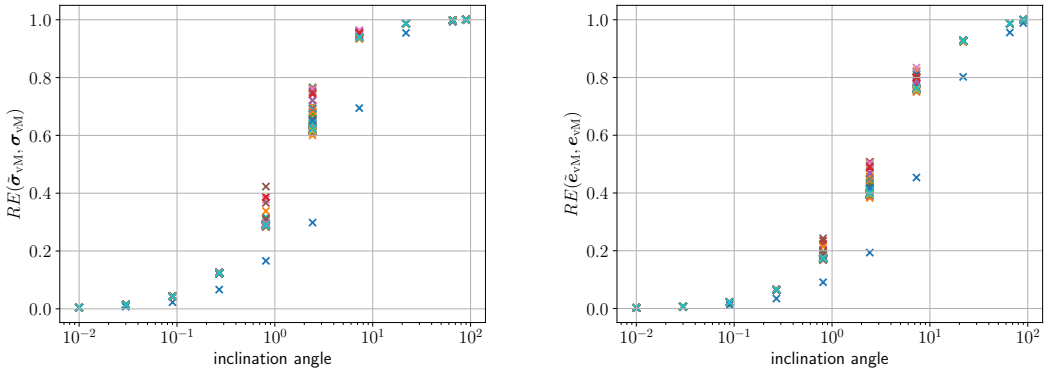

Figure 4.10.: AAA wall von Mises stress field (left plot) and von Mises strain field (right plot) relative errors over an inclination of the FOM solution subspace using patient 1 as computational example. Different colors indicate different directions of inclination, in total 100 DROM model evaluations have been performed per inclination angle. While low inclination and high inclination angles yield similar relative l2-errors across different directions of inclination, pronounced differences in the l2-error arise for the mid range, depending on the direction of inclination.

4.3.2. Patient-specific parametrization and computational models

The first patient-specific computational model has been presented in Section 4.1, see Figures 4.1, 4.2 and 4.3 for the computational domain, mesh and exemplary von Mises stress distributions. Figures 4.7 and 4.8 depict the computational models for patient 2 and patient 3, respectively. Table 4.1 provides quantitative data on spatial discretization per patient, please refer to Section 4.1.1 for further common information on AAA modeling.

Table 4.1.: Number of degrees of freedom N and number of elements N_e for patient-specific computational models

	patient 1	patient 2	patient 3
N [-]	109,587	189,504	479,487
N_e [-]	140,019	149,499	776,106

The models are parametrized in their α-stiffness and β-stiffness material property as well as their wall thickness t_w

$$\boldsymbol{\mu} = \begin{bmatrix} \alpha \\ \beta \\ t_w \end{bmatrix} \in \mathcal{P} = [\alpha_l; \alpha_u] \times [\beta_l; \beta_u] \times [t_l; t_u] \subset \mathbb{R}^3, \tag{4.38}$$

wherein the subscripts $_l$ and $_u$ were used to denote lower and upper bounds, respectively. The selected parametrization is motivated by typical model uncertainties given that neither exact data on material parameters, nor wall thickness (due to restricted resolution [35]) can be identified non-invasively by medical screening.

Parameter domain bounds are estimated from the 0.025-percentile and 0.975-percentile values

$$(\gamma_l, \gamma_u) = (Q_{\log}(0.025; \mu_\gamma, \sigma_\gamma), Q_{\log}(0.975; \mu_\gamma, \sigma_\gamma)) \quad \text{for } \gamma \in \{\alpha, \beta, t_w\} \tag{4.39}$$

of patient-specific Log-normal probability distributions for each parameter, wherein

$$Q_{\log}(p; \mu_\gamma, \sigma_\gamma) = \exp(\mu_\gamma + \sqrt{2}\sigma_\gamma \mathrm{erf}^{-1}(2p - 1)) \tag{4.40}$$

return the p-percentile value of a Log-normal probability distribution with expectation μ_γ, standard deviation σ_γ and erf denoting the *error function*. The bounds given in (4.39) consequently represent the mid 95 % of realizations of parametric configurations $\boldsymbol{\mu}$. The patient-specific Log-normal probability distributions result from the methodology presented in [11]. Table 4.2 depicts the derived lower and upper bounds per patient.

Table 4.2.: Patient-specific bounds for the parameter domain

	patient 1	patient 2	patient 3
$[\alpha_l; \alpha_u]$ [kPa]	$[28.23; 345.22]$	$[18.15; 344.07]$	$[26.46; 503.16]$
$[\beta_l; \beta_u]$ [kPa]	$[541.46; 6164.14]$	$[543.15; 9686.14]$	$[450.97; 7986.08]$
$[t_{w,l}; t_{w,u}]$ [mm]	$[1.09; 2.66]$	$[0.94; 2.46]$	$[1.03; 2.73]$

4.3.3. Full-order model greedy maximin distance sampling

Analysis of the GMmD sampling is started by distributing 200 points to each patient-specific parameter domain as defined in Table 4.2. Only one subdomain (corresponding to the entire

parameter domain) is used, such that the resulting point distributions can be classified as a one-shot design and result from Algorithm 6 with inputs $\Sigma_{sd} = \{\Sigma_t\}$, $\theta_{\text{th}} = 0$ together with a break of the algorithm at $|\Sigma_c| = 200$. The training grid is a full factorial with 100 equidistant points per parameter domain axis, while the initial point for each patient is chosen as $\boldsymbol{\mu} = [\alpha_l, \beta_l, t_{w,l}]^T$.

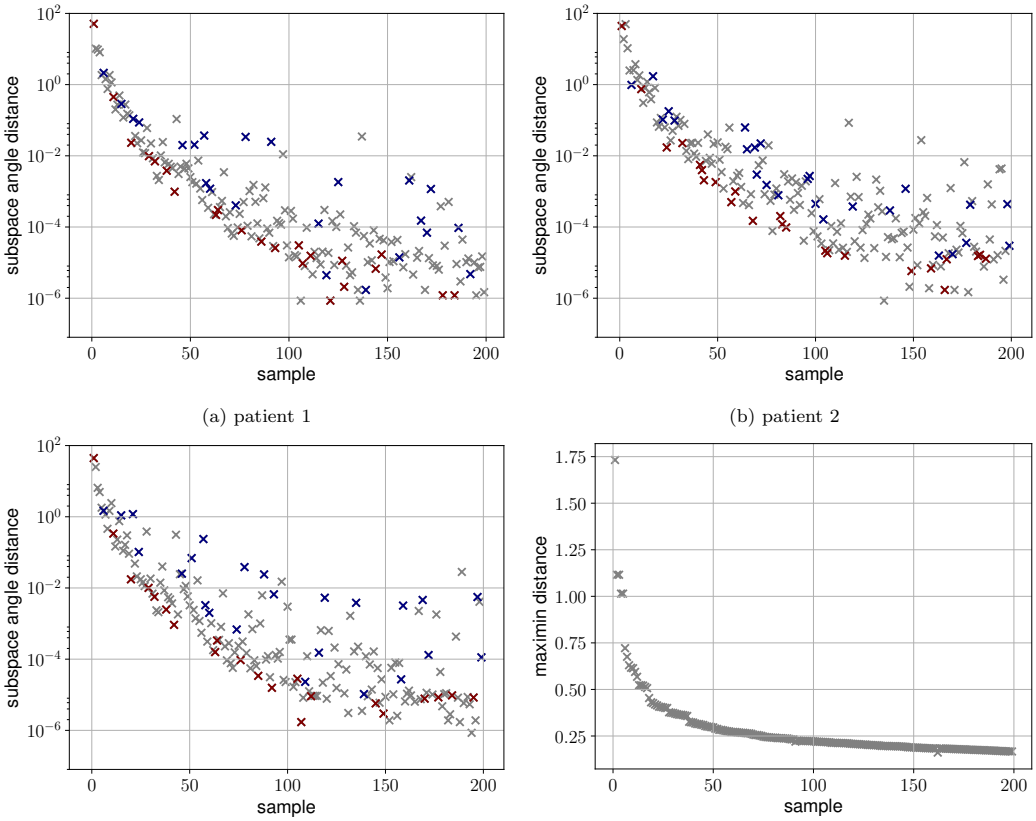

(a) patient 1 (b) patient 2

(c) patient 3 (d) patient 1,2,3

Figure 4.11.: Decay of SADs for 200 points (one subdomain) distributed by GMmD is depicted in subfigures (a)-(c) for each patient-specific computational model. The maximin distance coincides for each patient (given that the design under consideration does not contain adaptivity) and is depicted in subfigure (d). Blue markers in subfigures (a)-(c) indicate parametric configurations in the $(---)$-octant, red markers indicate parametric configurations in the $(+++)$-octant. Reproduced with permission from [122] (published under CC BY license [28]).

For each point, the AAA computational model is evaluated, individual failed simulations are shifted to neighboring points on the parameter domain grid. Additionally, the SAD (see Algorithm 5) is calculated between solution snapshots and the accumulated ROB. Figure 4.11 depicts the SADs in a scatter plot together with the euclidean maximin distance of points in the reference hypercube. Recalling that the point distributions correspond to a one-shot design, maximin distances in the reference hypercube coincide for all patients.

The distribution of SADs is influenced by two contributions. First, the euclidean distance to a neighboring point plays a significant role. For all patients, SADs show a pronounced decay initially and begin to scatter with increasing number of samples. An initial decay can also be

observed for the maximin distance, while scattering of SADs coincides with a stagnation of the maximin distance. As will be demonstrated in the following, only the region of a pronounced decay of subspace angles is of interest. Second, subspace angles depend on the sensitivity of the parameter domain. For demonstration, blue markers were introduced to highlight parametric configurations in the $(---)$-octant of the parameter domain and red markers for parametric configurations in the $(+++)$-octant, wherein the $(---)$-octant is given by $\alpha < \alpha_{\text{mid}}, \beta < \beta_{\text{mid}}$ and $t_w < t_{w,\text{mid}}$ and the $(+++)$-octant by $\alpha > \alpha_{\text{mid}}, \beta > \beta_{\text{mid}}$ and $t_w > t_{w,\text{mid}}$ with

$$\begin{bmatrix} \alpha_{\text{mid}} \\ \beta_{\text{mid}} \\ t_{w,\text{mid}} \end{bmatrix} = \frac{1}{2} \left[\begin{bmatrix} \alpha_l \\ \beta_l \\ t_{w,l} \end{bmatrix} + \begin{bmatrix} \alpha_u \\ \beta_u \\ t_{w,u} \end{bmatrix} \right] \tag{4.41}$$

as domain midpoints. Clearly, $(---)$-octant parametric configurations are predominantly associated with lower SADs as opposed to $(+++)$-octant parametric configurations.

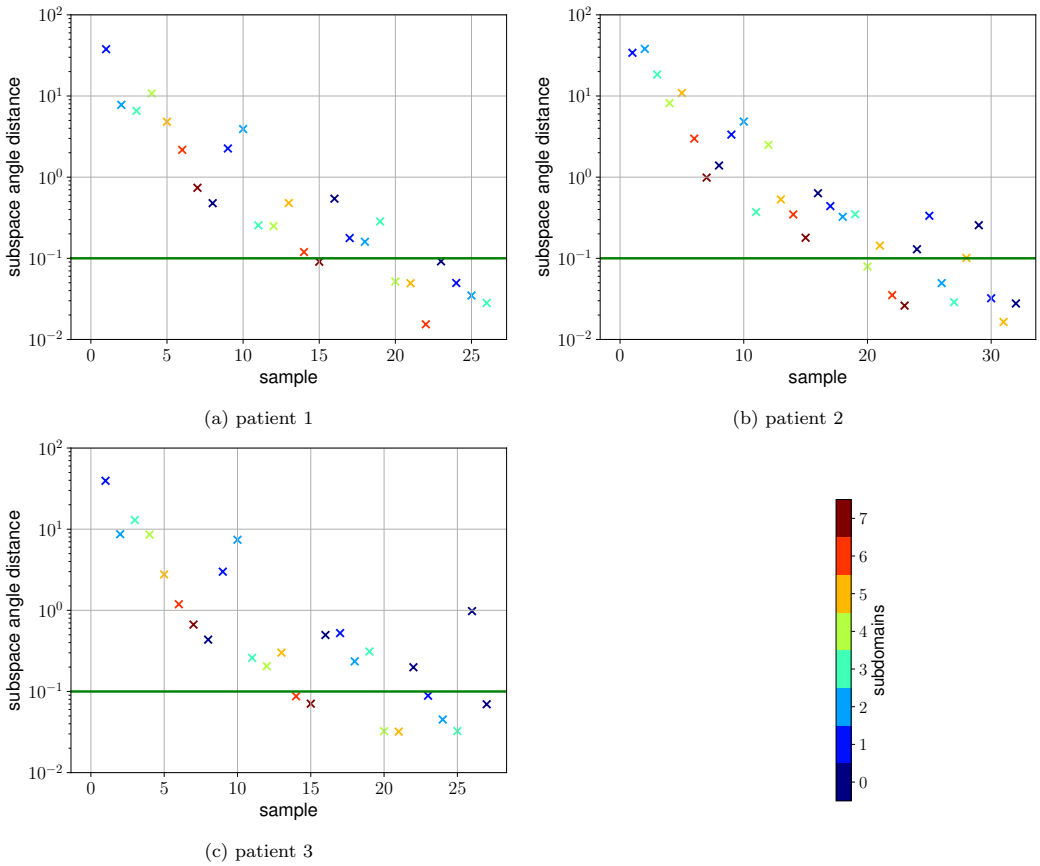

(a) patient 1

(b) patient 2

(c) patient 3

Figure 4.12.: Decay of SADs for points distributed by GMmD on 8 subdomains. The green horizontal line marks the threshold for the stopping criterion $\theta_{\text{th}} = 0.1$. Point colors indicate their domain correspondence. Reproduced with permission from [122] (published under CC BY license [28]).

In our next design, the one-shot design is turned into an adaptive design by including eight subdomains, which are equally shaped and correspond to the (ijk)-octants with $i, j, k \in \{-, +\}$

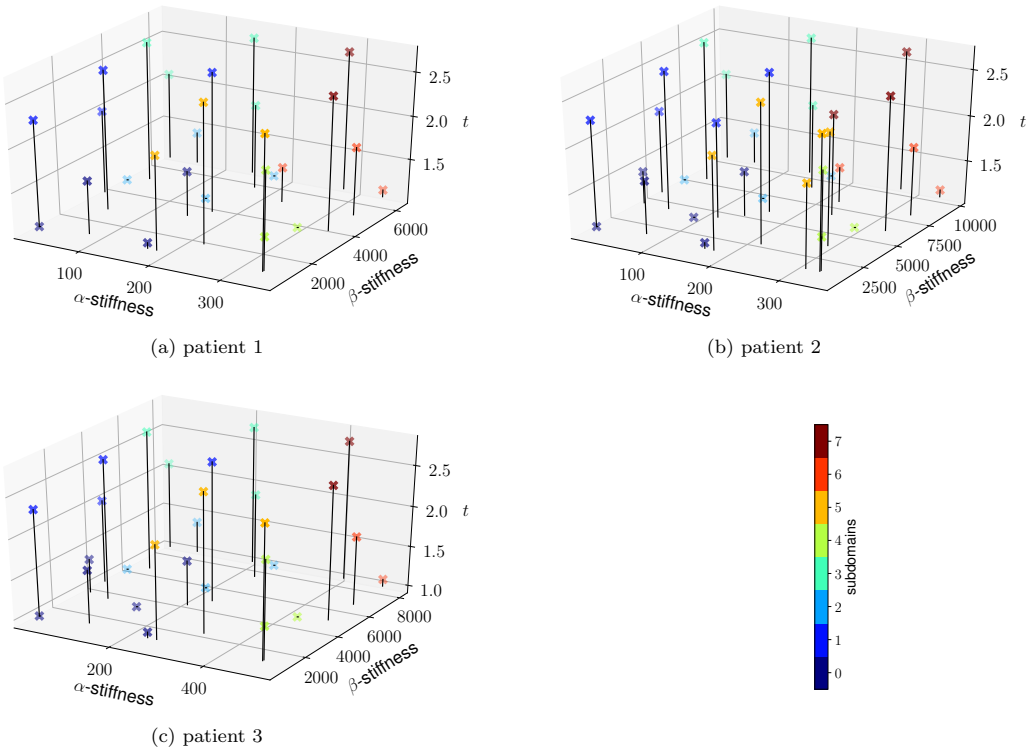

(a) patient 1

(b) patient 2

(c) patient 3

Figure 4.13.: Parametric configurations in the physical parameter domain gained from GMmD sampling on 8 subdomains. Corresponding subspace angles are depicted in Figure 4.12. Reproduced with permission from [122] (published under CC BY license [28]).

of the parameter domain. Algorithm 6 is consequently restarted with $\Sigma_{sd} = \{\Sigma_0, \ldots, \Sigma_7\}$, the initial configuration remains $\boldsymbol{\mu} = [\alpha_l, \beta_l, t_{w,l}]^T$ and the termination criterion is chosen as $\theta_m = 0.1$. Figure 4.12 depicts the decay of SADs for each patient together with a green horizontal line indicating the termination criterion. Sampling continues until the SAD is found below θ_m in each subdomain. The parametric configurations themselves are depicted in Figure 4.13.

Table 4.3.: Number of points distributed in each subdomain by GMmD sampling. A visualization of the parametric configurations in the physical domain is depicted in Figure 4.13.

subdomain	0	1	2	3	4	5	6	7
patient 1	4	4	4	4	3	3	3	2
patient 2	6	5	4	4	3	5	3	3
patient 3	6	4	4	4	3	3	2	2

Table 4.3 depicts the number of points distributed to each subdomain. For instance, subdomain 0 receives more points than subdomain 7 across all patients, the difference is especially prominent for patient 3. Referring to Figure 4.13, subdomain 0 corresponds to the $(---)$-octant, while subdomain 7 is the $(+++)$-octant, such that low-stiffness and thin walled AAAs receive

Table 4.4.: Number of degrees of freedom p for patient-specific ROMs, number of assembled elements for internal force n_e^{int} and number of assembled elements for the luminal pressure force n_e^{lp}.

	patient 1	patient 2	patient 3
p [-]	54	66	56
n_e^{int} [-]	945	1579	1482
n_e^{lp} [-]	411	692	590

more samples than high-stiffness and thick walled. This is plausible from a physical perspective, given that the low-stiffness and thin walled structures undergo larger deformation.

4.3.4. Reduced-order model accuracy and speedup

For all three patients under consideration a ROB is built from application of Algorithm 6 as discussed in Section 4.3.3 ($n_{\mathrm{sd}} = 8, \theta_{\mathrm{th}} = 0.1$). For DHROM construction, hyper reduction by ECSW is performed, see Section 3.2.2. Both nonlinear internal force as well as luminal pressure force vectors are hyper reduced, the full model mesh as well as the luminal surface mesh are sampled independently. The parallelization strategy based on domain decomposition as presented in Section 3.2.2 is used and sampling is performed on 4 processors with global tolerance $\varepsilon_h = 10^{-3}$ for internal force sampling and $\varepsilon_h = 10^{-4}$ for luminal pressure force sampling. Figure A.2 depicts selected mesh elements for both the internal force as well as the luminal pressure force assembly. Especially accurate sampling for internal force assembly is performed in proximity to the vessel fixation and in regions of high wall curvature. Table 4.4 summarizes the number of DOFs and evaluated mesh elements for the patient-specific DROMs and DHROMs.

DROM as well as DHROM accuracy is examined on a test grid including 1000 points from a full factorial design with 10 equidistantly placed points in each domain axis. Consequently, the test grid is built independently from the ROB construction points selected by the GMmD. The quantities of interest are the von Mises stress field $\boldsymbol{\sigma}_{\mathrm{vM}}$ and the von Mises strain field $\boldsymbol{e}_{\mathrm{vM}}$ in the AAA wall at the fully loaded state (i.e. completed prestressing and deformation stage).

Figures A.3 and A.4 show relative errors (4.35) for the three patients under consideration. Individual samples have relative errors above 1%, while the majority ($> 98\%$ for DROM, $> 97\%$ for DHROM) of samples is below 1%. Mean relative errors $\overline{RE}_{\sigma_{\mathrm{vM}}}, \overline{RE}_{e_{\mathrm{vM}}}$ are reported in Table 4.5, wherein

$$\overline{RE}_{\sigma_{\mathrm{vM}}} = \frac{1}{n_{\mathrm{sim}}} \sum_{i=0}^{n_{\mathrm{sim}}-1} RE_i(\tilde{\boldsymbol{\sigma}}_{\mathrm{vM}}, \boldsymbol{\sigma}_{\mathrm{vM}}), \quad \overline{RE}_{e_{\mathrm{vM}}} = \frac{1}{n_{\mathrm{sim}}} \sum_{i=0}^{n_{\mathrm{sim}}-1} RE_i(\tilde{\boldsymbol{e}}_{\mathrm{vM}}, \boldsymbol{e}_{\mathrm{vM}}) \tag{4.42}$$

is used n_{sim} as the number of drawn samples and RE_i as the relative error of sample i. The conclusion is, that caution is required whenever DROM or DHROM are used for evaluations of single point estimates, while both ROMs are accurate in a statistical sense.

Next, the threshold SAD θ_{th} and the ECSW tolerance $\varepsilon_{\mathrm{th}}$ are modified in order to demonstrate the influence of these algorithmic parameters. In more detail, Algorithm 6 is performed

several times for patient 1 with $\theta_{\text{th}} \in \{0.1, 0.5, 2, 5, 10, 20\}$ and the DROM mean l2-error (4.42) is evaluated over the test grid using the resulting ROBs. Furthermore, ECSW mesh sampling for internal force assembly is performed several times for patient 1 choosing convergence tolerances of $\varepsilon_h \in \{10^{-4}, 1.5 \cdot 10^{-4}, 10^{-3}, 1.5 \cdot 10^{-3}, 10^{-2}, 1.5 \cdot 10^{-2}, 10^{-1}\}$, while assemble of the luminal pressure force is left without hyper reduction. Again, the DHROM l2-error is evaluated over the test grid. Figure 4.14 depicts the result. As can be seen from the left plot, lowering the threshold SAD termination criterion results in a monotonically decreasing mean relative l2-error, while the number of selected ROB modes increases and reflects the extension of the low-dimensional solution subspace. A similar behavior is depicted with respect to the ECSW convergence tolerance ε_h in the right plot. The mean relative l2-error decreases with decreasing ε_h, while the number of selected mesh elements increases and represents the more accurate mesh sampling.

Table 4.5.: Mean values of relative errors for von Mises stress and von Mises strain field in AAA wall. FOM evaluations serve as reference. The test grid is built from a full factorial design with 1000 points in the parameter domain.

	value	patient 1	patient 2	patient 3
DROM	$\overline{RE}_{\sigma_{\text{vM}}}$	$2.2 \cdot 10^{-4}$	$9.9 \cdot 10^{-4}$	$1.1 \cdot 10^{-3}$
	$\overline{RE}_{e_{\text{vM}}}$	$1.5 \cdot 10^{-4}$	$6.1 \cdot 10^{-4}$	$6.2 \cdot 10^{-4}$
DHROM	$\overline{RE}_{\sigma_{\text{vM}}}$	$4.4 \cdot 10^{-4}$	$1.7 \cdot 10^{-3}$	$1.6 \cdot 10^{-3}$
	$\overline{RE}_{e_{\text{vM}}}$	$3.2 \cdot 10^{-4}$	$1.1 \cdot 10^{-3}$	$8.7 \cdot 10^{-4}$

Computational speedup of the ROMs is evaluated next. In order to weaken dependency on specific parameterizations, the speedup is computed as the mean value from seven simulations, wherein the parameterization is chosen as the midpoint of the parameter domain (see Table 4.2) together with the midpoints of the six parameter domain hypercube faces. All simulations are performed on 4 cores (Intel Xeon W-2133 (3.60GHz)). As can be seen from Table 4.6, DROMs yield only small computational savings, given that the system assembly is not accelerated. A larger speedup is gained by DHROMs.

Table 4.6.: Speedup of DROM and DHROM with FOM timing as reference. The speedup is calculated as the mean value of seven simulations per patient.

	model	speedup [-]
patient 1	DROM	1.6
	DHROM	32.2
patient 2	DROM	1.5
	DHROM	22.7
patient 3	DROM	1.8
	DHROM	60.2

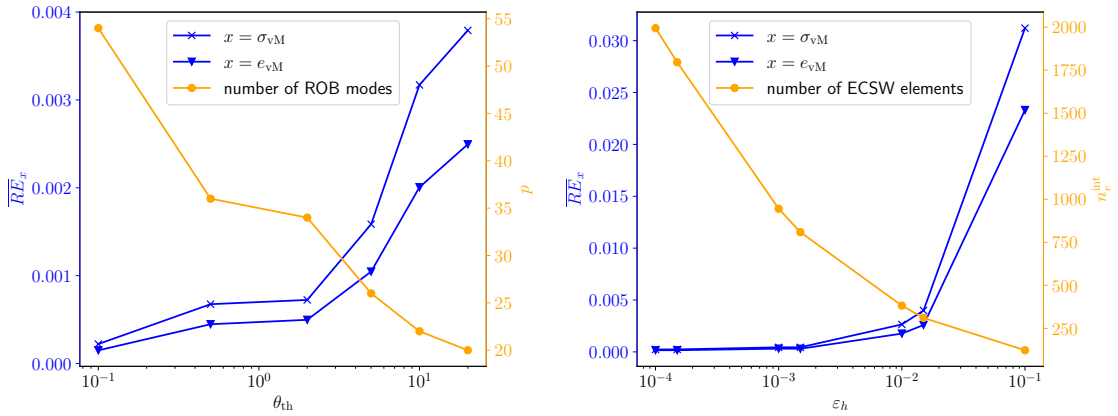

(a) mean error vs. threshold SAD

(b) mean error vs. ECSW tolerance

Figure 4.14.: Influence of algorithmic parameters using patient 1 as computational example. The left plot depicts mean relative l2-errors (evaluated on a full factorial design with 1000 points in the parameter domain) together with the corresponding number of selected ROB modes over the threshold SAD θ_{th}. The right plot depicts mean relative l2-errors with the corresponding number of selected mesh elements for internal force assembly over the ECSW tolerance ε_h. Adapted with permission from [122] (published under CC BY license [28]). Adapted axes labeling to match the nomenclature in this thesis.

4.3.5. Application to Monte Carlo sampling

The DHROM described in Section 4.3.4 is now used for the estimation of stress and strain probability distributions. In more detail, the quantity of interest is the 99.9-th percentile value of the element-wise von Mises stress and von Mises strain field in the AAA wall, for simplicity denoted as maximum von Mises stress and maximum von Mises strain in the following. For this purpose, 10,000 randomly generated points are drawn per patient from the corresponding parameter domains and FOM as well as DHROM are evaluated at these points.

Table 4.7 depicts mean values and standard deviations for maximum von Mises stress and maximum von Mises strain per patient for both FOM and DHROM. Relative errors of all values are below 1%. Figure A.5 depicts probability distributions from Gaussian kernel-density-estimations (scipy.stats.gaussian_kde from SciPy [134] (version 1.3.0) package of the Python programming language). Differences between reference solution and approximated probability distributions are negligible.

Table 4.7.: Mean values $\mu_{\text{stress}}^{\text{vMmax}}, \mu_{\text{strain}}^{\text{vMmax}}$ and standard deviations $\sigma_{\text{stress}}^{\text{vMmax}}, \sigma_{\text{strain}}^{\text{vMmax}}$ for reference (FOM) and approximate (DHROM) probability distributions of maximum von Mises stress and maximum von Mises strain. The statistical data is computed from 10,000 identical samples per individual patients.

	value	patient 1	patient 2	patient 3
FOM	$\mu_{\text{stress}}^{\text{vMmax}}$ [kPa]	205.57	276.84	302.49
	$\sigma_{\text{stress}}^{\text{vMmax}}$ [kPa]	44.950	65.926	71.761
	$\mu_{\text{strain}}^{\text{vMmax}}$ [−]	0.17320	0.19404	0.19070
	$\sigma_{\text{strain}}^{\text{vMmax}}$ [−]	0.038272	0.052792	0.049465
DHROM	$\mu_{\text{stress}}^{\text{vMmax}}$ [kPa]	205.83	277.24	302.19
	$\sigma_{\text{stress}}^{\text{vMmax}}$ [kPa]	45.073	65.844	71.795
	$\mu_{\text{strain}}^{\text{vMmax}}$ [−]	0.17358	0.19423	0.19063
	$\sigma_{\text{strain}}^{\text{vMmax}}$ [−]	0.038452	0.052746	0.049578

5. Model reduction of the beating heart

As stated in Section 1.1, reduction of a computational cardiac mechanics model is one central aspect for the motivation of this thesis. The cardiac mechanics model under consideration is a 3D spatially resolved model including anisotropic as well as actively contracting material models.

Following the presentation in the review article in [101], studies on active muscle mechanics can be traced back to an early article [56] in the year 1938. Computational models of the full organ emerged later, an early ventricular model with focus on pressure-volume relations and transmural distribution of sarcomere length can be found in [3] from the year 1979. In the following, geometrically or computationally enhanced models for ventricular mechanics have been published [50, 69, 97, 129]. A further step towards model accuracy has been made with the application of geometrically patient-specific computational models [30, 100, 140] and the application of sophisticated boundary conditions such as closed-loop circulation models [58, 70] or fluid-structure interaction [102, 116]. Also, the phenomenon of cardiac tissue growth and remodeling has gained increasing attention in computational cardiac mechanics [38, 68, 75].

The cardiac mechanics model under consideration in this thesis is a full organ model developed in [57] with a geometry gained from medical screening. The solid mechanics part is coupled to a system of ordinary differential equations modeling the closed-loop blood circulation and returning dynamic pressure load boundary conditions for the cardiac chambers. Accurate computational results require high resolution in both space and time, entailing large demand on computational resources and motivating application of model reduction methods.

Although efficient and accurate reduced-order models (ROMs) in cardiac structural mechanics are crucial for many applications such as uncertainty quantification or optimization, relatively few publications on projection-based model reduction in this context exist. Application of proper-orthogonal decomposition (POD) and the (matrix) discrete empirical interpolation method (M)DEIM together with model reduction of idealized and patient-specific single ventricle models is addressed in Refs. [13, 23, 93]. Extended focus on model reduction of cardiac electromechanics can be found in [12], wherein again POD subspace reduction as well as hyper reduction by (M)DEIM or the Broyden method (Jacobian approximation by rank one matrix updates) are used. Blood circulation mechanics is excluded from modeling. A Galerkin projection on POD subspaces in the context of optimization can be found in [57, 105]. Only the 3D structural mechanics component of the 3D-0D cardiac models is dimensionally reduced, hyper reduction is not included. Finally, a recent publication motivates the use of deep neural networks for hyper reduction [24]. The idea therein is to learn the approximation of projected residuals and Jacobians as a function of the parameter vector, the time step as well as the Newton-Raphson iteration index.

In this thesis, model reduction of a prestressed, patient-specific, biventricular solid dynamics model is presented. Thereby, blood circulation is taken into account by a two-way coupling

of the solid dynamics model to a closed-loop 0D fluid mechanics model. Hyper reduction by the energy-conserving mesh sampling and weighting (ECSW) method is applied to all involved forces requiring reassembly, i.e. the internal force, the ventricular pressure force and the embedding tissue force. Both, prestressing stage as well as dynamic cycling stage are subject to dimensional reduction and hyper reduction.

5.1. Computational modeling of cardiac mechanics

5.1.1. In silico model

In the following, the applied heart computational model is described. In more detail, the computational domain and constitutive as well as governing equations for the structural part together with the system of ordinary differential equations (ODEs) for the vascular system are presented. Coupling between the 3D structure and the 0D flow network is explained and finally model parameters are stated.

Computational domain: The challenge in the identification of the computational domain in biomedical simulations has already been addressed in Section 4.1.1, the process from imaging to simulation in case of the heart model under consideration can be found in [57]. In brief, the heart geometry is extracted from a computed tomography scan of a porcine heart. The lumina of cardiac chambers as well as the outermost layer of the heart muscle are segmented and a boolean operation is performed to subtract the chamber lumina. Segmentation is performed at 80 % of the diastolic phase time interval.

The atria are not part of the computational domain, only ventricular dynamics is simulated. To extract the domain of interest, the geometry is truncated by the *atrioventricular plane*. This plane cuts the posterior mitral valve leaflet and is orthogonal to the axis from the lowest left ventricular point to the center of the aortic valve. Two artificial lids are introduced in order to create closed ventricular volumes, which have been cut open by the atrioventricular plane. Additionally, bulk material is extended $10\ \mathrm{mm}$ at the heart base.

Figure 5.1 depicts the full computational domain on the left and a cut exposing ventricular lumina on the right. Several surfaces are introduced for convenient reference in following sections. Γ_b (heart base) refers to the top of the extended bulk material. Γ_e refers to the epicardial surface and Γ_{lid} is the abluminal surface of the covering lids. Left and right ventricle surfaces are denoted by $\Gamma_{\mathrm{v}}^{\ell}$ and Γ_{v}^{r}, wherein the luminal surfaces of the covering lids are not part of $\Gamma_{\mathrm{v}}^{\ell}$ and Γ_{v}^{r}.

Constitutive modeling: Myocardial tissue has orthotropic material behavior [61], wherefore two families of fibers are generated and enter the constitutive equation. One fiber direction corresponds to the muscle fiber direction $\boldsymbol{f}_0$, the second direction is the *sheet direction* $\boldsymbol{s}_0$ [57], which is orthogonal to the fiber direction and approximately in-plane with the wall. The muscle fiber inclination starts with -60° measured from the circumferential ventricle directions on the epicardium and varies continuously in transmural direction to an inclination of 60° at the endocardium. Figure 5.2 illustrates fiber and sheet direction.

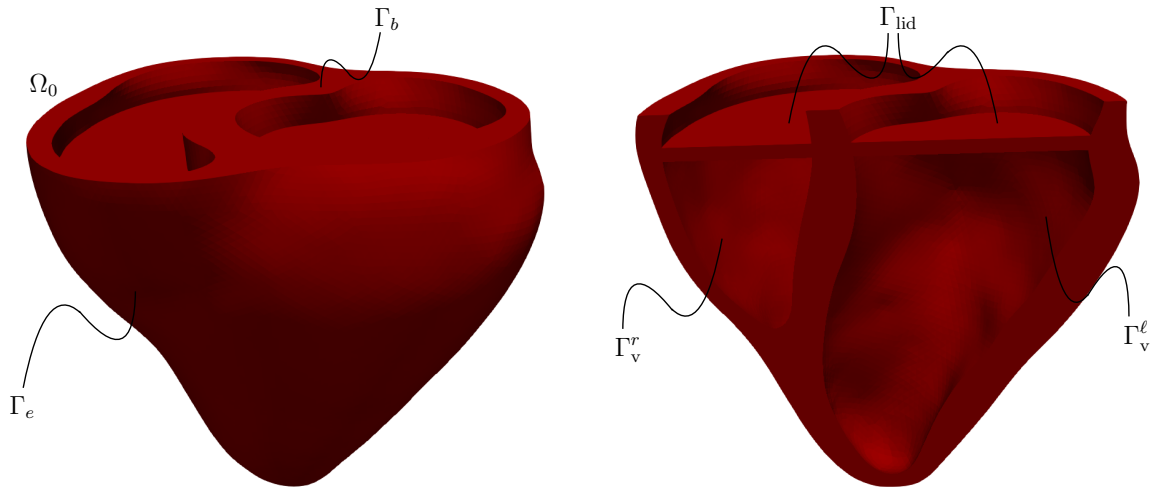

Figure 5.1.: Porcine heart computational domain. The full domain is depicted on the left, while a cut exposing the ventricular lumina is depicted on the right. Ventricles are closed by artificial lids. Atria are not part of the solid mechanics computational domain.

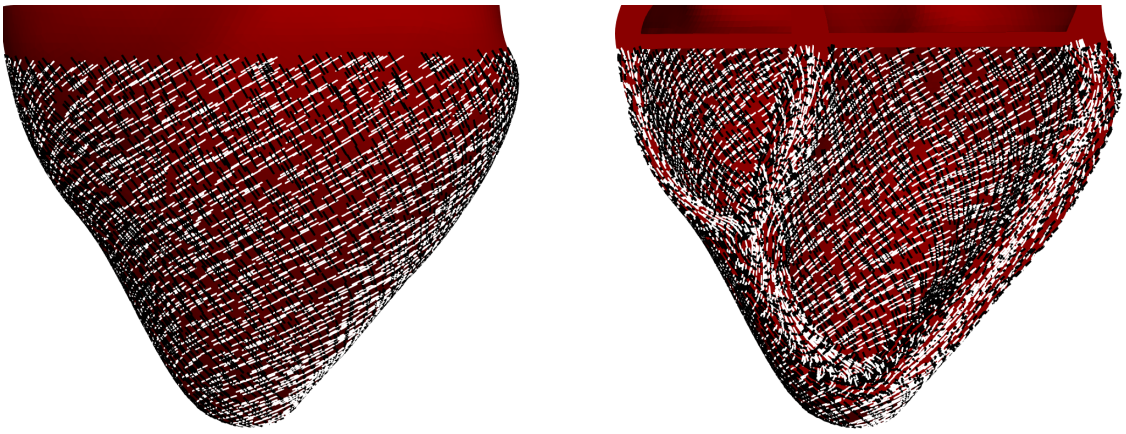

Figure 5.2.: Visualization of fiber and sheet direction on epicardial surface (left) and on endocardial surface (right). Black dashes correspond to fiber direction $\boldsymbol{f}_0$, white dashes correspond to sheet direction $\boldsymbol{s}_0$.

The constitutive model for the myocardial tissue (i.e. the entire computational domain except for the lids, see Figure 5.1) consists of the sum of passive material and active stress contribution

$$\boldsymbol{S} = \frac{\partial \Psi}{\partial \boldsymbol{E}} + \tau_a(t)\boldsymbol{f}_0 \otimes \boldsymbol{f}_0. \tag{5.1}$$

The strain energy density for the passive material behavior contains eight material constants $(a_0, b_0, \kappa, a_f, b_f, a_s, b_s, a_{fs}, b_{fs})$ and reads [61]

$$\begin{aligned}\Psi =& \frac{a_0}{2b_0}\left[e^{b_0[\bar{I}_1-3]}-1\right] + \frac{\kappa}{2}[J-1]^2 + \frac{a_f}{2b_f}\left[e^{b_f[\boldsymbol{f}_0^T\boldsymbol{C}\boldsymbol{f}_0-1]^2}-1\right] \\ &+ \frac{a_s}{2b_s}\left[e^{b_s[\boldsymbol{s}_0^T\boldsymbol{C}\boldsymbol{s}_0-1]^2}-1\right] + \frac{a_{fs}}{2b_{fs}}\left[e^{b_{fs}[\boldsymbol{f}_0^T\boldsymbol{C}\boldsymbol{s}_0]^2}-1\right].\end{aligned} \tag{5.2}$$

The first two summands model the isotropic part of material response under an isochoric-volumetric split with $\bar{I}_1$ as the first principal invariant of the modified Cauchy-Green tensor (4.3). The remaining three summands model the anisotropic, passive material response.

The second summand in equation (5.1) models the force-generating behavior of the heart, that is its property to contract. Thereby, a temporally varying *active stress* of magnitude $\tau_a(t)$ is generated in fiber direction $\boldsymbol{f}_0$, whereby $\tau_a(t)$ is the solution of the ODE [57]

$$\dot{\tau}_a(t) = -|u(t)|\tau_a(t) + \sigma_0 \max(0, u(t)). \tag{5.3}$$

The scalar σ_0 adjusts the maximum of the active stress and is referred to as *contractility*. The function $u(t)$ is defined in terms of the upstroke rate $\alpha_{\max}$, relaxation rate $\alpha_{\min}$ and an activation function $\hat{f}(t)$

$$u(t) = \hat{f}(t) \cdot \alpha_{\max} + [1 - \hat{f}(t)] \cdot \alpha_{\min} \tag{5.4}$$

with

$$\begin{aligned} \hat{f}(t) =& [K[t - c_1] + 1] \cdot \mathcal{H}(K[t - c_1] + 1) - K[t - c_1]\mathcal{H}(K[t - c_1]) \\ & - K[t - c_2] \cdot \mathcal{H}(K[t - c_2]) + [K[t - c_2] - 1] \cdot \mathcal{H}(K[t - c_2] - 1) \end{aligned} \tag{5.5}$$

using the Heaviside function

$$\mathcal{H} : \begin{cases} \mathbb{R} \to \{0, 1\} \\ x \mapsto \begin{cases} 0 & \text{for } x < 0 \\ 1 & \text{for } x \geq 0 \end{cases} \end{cases} . \tag{5.6}$$

K, c_1 and c_2 are constants, wherein c_1 and c_2 are defined in terms of the time of active stress initialization t_{contr} and relaxation t_{relax}

$$c_1 = t_{\text{contr}} + \frac{\alpha_{\max}}{K[\alpha_{\max} - \alpha_{\min}]}, \tag{5.7}$$

$$c_2 = t_{\text{relax}} - \frac{\alpha_{\max}}{K[\alpha_{\max} - \alpha_{\min}]}. \tag{5.8}$$

Figure 5.3 depicts an exemplary active stress curve over one cardiac cycle. The $10\ \text{mm}$ bulk material extension of the heart mentioned above is not subject to generation of active stress.

The covering lids are modeled using a Neo-Hookean material under a volumetric-isochoric split

$$\Psi = \frac{\mu_{\text{lid}}}{2}[\bar{I}_1 - 3] + \frac{\kappa_{\text{lid}}}{2}[J - 1]^2, \tag{5.9}$$

wherein the material parameters μ_{lid} and κ_{lid} were introduced.

Structural dynamics governing equations: Analogous to the abdominal aortic aneurysm (AAA), the imaged heart configuration is under blood pressure and therefore not stress-free. As a result, the heart simulation consists of a prestressing and a deformation stage. In the prestressing stage, the heart is loaded at a fixed spatial configuration to the diastolic ventricle pressures. In the deformation stage, a temporally discretized cardiac cycle is simulated with heart contraction triggered by active stress ODE (5.3).

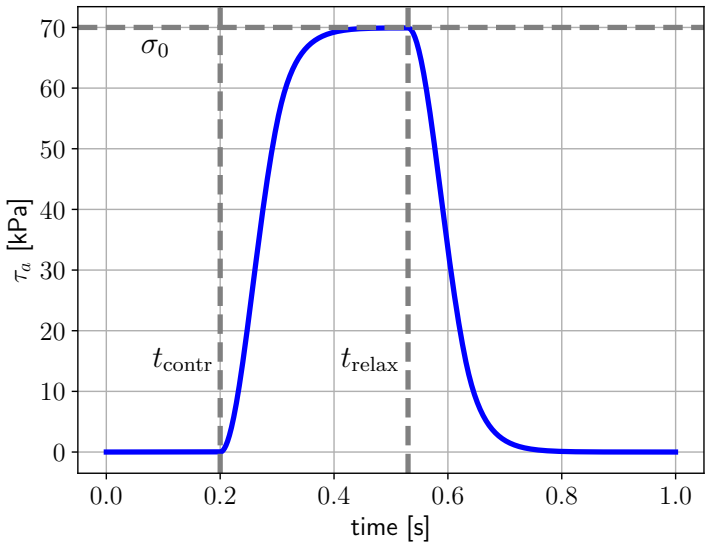

Figure 5.3.: Exemplary active stress evolution over one cardiac cycle with period $T_{\text{cycle}} = 1$ s. The curve is generated from an implicit Euler temporal discretization of equation (5.3).

The following governing equations are solved in the prestressing stage

$$\nabla_{\boldsymbol{x}_0} \cdot \boldsymbol{P} = \boldsymbol{0} \qquad \text{in } \Omega_0, \tag{5.10}$$

$$\boldsymbol{P} \cdot \boldsymbol{n}_0 = \boldsymbol{t}^i_{p,0} \qquad \text{on } \Gamma^i_{\text{v}},\ i \in \{\ell, r\}, \tag{5.11}$$

$$\boldsymbol{P} \cdot \boldsymbol{n}_0 = \boldsymbol{t}^b_{k,0} + \boldsymbol{t}^{b\perp}_{k,0} \qquad \text{on } \Gamma_b, \tag{5.12}$$

$$\boldsymbol{P} \cdot \boldsymbol{n}_0 = \boldsymbol{t}^{i\perp}_{k,0} \qquad \text{on } \Gamma_i,\ i \in \{e, \text{lid}\}. \tag{5.13}$$

Boundary condition (5.11) corresponds to a diastolic blood pressure load exerted on endocardial surfaces (see Figure 5.1) with first Piola-Kirchhoff traction introduced in equation (4.13). Boundary conditions (5.12) and (5.13) model embedding tissue at the heart base as well as covering lids and epicardial surface by introducing a traction that is locally proportional to displacement. The traction is either a response to the full displacement

$$\boldsymbol{t}^b_{k,0} = -k_b \boldsymbol{u} \tag{5.14}$$

or a response to the displacement in direction of the reference surface normal

$$\boldsymbol{t}^{i\perp}_{k,0} = -k_{i\perp}(\boldsymbol{u} \cdot \boldsymbol{n}_0)\boldsymbol{n}_0, \quad i \in \{b, e, \text{lid}\}. \tag{5.15}$$

The proportionality constants $k_{i\perp}, i \in \{b, e, \text{lid}\}$ and k_b can be interpreted as spring stiffness per reference surface area and are of physical unit $\left[\frac{\text{kPa}}{\text{mm}}\right]$. In the prestressing stage, embedding tissue boundary conditions are evaluated based on the prestress displacement field.

The deformation stage governing equations read

$$\nabla_{\boldsymbol{x}_0} \cdot \boldsymbol{P} = \rho_0 \dot{\boldsymbol{v}} \qquad \text{in } \Omega_0, \tag{5.16}$$

$$\boldsymbol{P} \cdot \boldsymbol{n}_0 = \boldsymbol{t}^i_{p,0} \qquad \text{on } \Gamma^i_{\text{v}},\ i \in \{\ell, r\}, \tag{5.17}$$

$$\boldsymbol{P} \cdot \boldsymbol{n}_0 = \boldsymbol{t}^b_{kc,0} + \boldsymbol{t}^{b\perp}_{kc,0} \qquad \text{on } \Gamma_b, \tag{5.18}$$

$$\boldsymbol{P} \cdot \boldsymbol{n}_0 = \boldsymbol{t}^{i\perp}_{kc,0} \qquad \text{on } \Gamma_i,\ i \in \{e, \text{lid}\}. \tag{5.19}$$

When compared to the steady state equations (5.10) - (5.13), an additional inertia term can be found in the momentum equation (5.16). The ventricle pressure load boundary condition (5.17) is evaluated on the deformed geometry. The embedding tissue boundary conditions (5.17) - (5.19) is extended with a velocity proportional contribution in velocity direction

$$\boldsymbol{t}^{b}_{kc,0} = -k_b \boldsymbol{u} - c_b \dot{\boldsymbol{u}} \tag{5.20}$$

and in reference configuration normal direction

$$\boldsymbol{t}^{i\perp}_{kc,0} = -k_{i\perp}(\boldsymbol{u}\cdot\boldsymbol{n}_0)\boldsymbol{n}_0 - c_{i\perp}(\dot{\boldsymbol{u}}\cdot\boldsymbol{n}_0)\boldsymbol{n}_0, \quad i \in \{b, e, \mathrm{lid}\}. \tag{5.21}$$

The constants $c_{i\perp},\ i \in \{b, e, \mathrm{lid}\}$ and c_b can be interpreted as dashpot stiffness per unit reference surface and are of physical unit $\left[\frac{\mathrm{kPa\ s}}{\mathrm{mm}}\right]$. In the deformation stage, embedding tissue boundary conditions are evaluated on the sum of prestress and deformation stage displacement field, that is the prestressing of embedding tissue is maintained. The velocity proportional contribution of embedding tissue remains independent from prestressing, given that the prestressing stage displacement field remains constant in the deformation stage.

Flow network governing equations: Simplified modeling of the vascular network has been discussed in several contributions in literature [103, 125, 138], the approach followed in this thesis is presented in [57]. The flow network is built from elements introduced in Section 2.1.5 and is depicted in Figure 5.4. The 16 equations (5.22) - (5.37) describe the system dynamics in terms of 8 pressure states

p^{ℓ}_{at} : left atrial pressure,
p^{r}_{at} : right atrial pressure,
p^{ℓ}_{v} : left ventricular pressure,
p^{r}_{v} : right ventricular pressure,
$p^{\mathrm{sys}}_{\mathrm{ar}}$: systemic arterial pressure,
$p^{\mathrm{pul}}_{\mathrm{ar}}$: pulmonary arterial pressure,
$p^{\mathrm{sys}}_{\mathrm{ven}}$: systemic venous pressure,
$p^{\mathrm{pul}}_{\mathrm{ven}}$: pulmonary venous pressure

and 8 flow rates

$q^{\ell}_{\mathrm{v,in}}$: inflow rate left ventricle,
$q^{r}_{\mathrm{v,in}}$: inflow rate right ventricle,
$q^{\ell}_{\mathrm{v,out}}$: outflow rate left ventricle,
$q^{r}_{\mathrm{v,out}}$: outflow rate right ventricle,
$q^{\mathrm{sys}}_{\mathrm{ar}}$: systemic arterial flow rate,
$q^{\mathrm{pul}}_{\mathrm{ar}}$: pulmonary arterial flow rate,
$q^{\mathrm{sys}}_{\mathrm{ven}}$: systemic venous flow rate,
$q^{\mathrm{pul}}_{\mathrm{ven}}$: pulmonary venous flow rate.

$$\frac{\mathrm{d}V_{\mathrm{at}}^{\ell}}{\mathrm{d}t} - q_{\mathrm{ven}}^{\mathrm{pul}} + q_{\mathrm{v,in}}^{\ell} = 0, \tag{5.22}$$

$$\frac{1}{\tilde{R}_{\mathrm{v,in}}^{\ell}}[p_{\mathrm{at}}^{\ell} - p_{\mathrm{v}}^{\ell}] - q_{\mathrm{v,in}}^{\ell} = 0, \tag{5.23}$$

$$\frac{\mathrm{d}V_{\mathrm{v}}^{\ell}}{\mathrm{d}t} - q_{\mathrm{v,in}}^{\ell} + q_{\mathrm{v,out}}^{\ell} = 0, \tag{5.24}$$

$$\frac{1}{\tilde{R}_{\mathrm{v,out}}^{\ell}}[p_{\mathrm{v}}^{\ell} - p_{\mathrm{ar}}^{\mathrm{sys}}] - q_{\mathrm{v,out}}^{\ell} = 0, \tag{5.25}$$

$$C_{\mathrm{ar}}^{\mathrm{sys}}\left[\frac{\mathrm{d}p_{\mathrm{ar}}^{\mathrm{sys}}}{\mathrm{d}t} - Z_{\mathrm{ar}}^{\mathrm{sys}}\frac{\mathrm{d}q_{\mathrm{v,out}}^{\ell}}{\mathrm{d}t}\right] - q_{\mathrm{v,out}}^{\ell} + q_{\mathrm{ar}}^{\mathrm{sys}} = 0, \tag{5.26}$$

$$\frac{L_{\mathrm{ar}}^{\mathrm{sys}}}{R_{\mathrm{ar}}^{\mathrm{sys}}}\frac{\mathrm{d}q_{\mathrm{ar}}^{\mathrm{sys}}}{\mathrm{d}t} + \frac{1}{R_{\mathrm{ar}}^{\mathrm{sys}}}[p_{\mathrm{ven}}^{\mathrm{sys}} - p_{\mathrm{ar}}^{\mathrm{sys}} + Z_{\mathrm{ar}}^{\mathrm{sys}}q_{\mathrm{v,out}}^{\ell}] + q_{\mathrm{ar}}^{\mathrm{sys}} = 0, \tag{5.27}$$

$$C_{\mathrm{ven}}^{\mathrm{sys}}\frac{\mathrm{d}p_{\mathrm{ven}}^{\mathrm{sys}}}{\mathrm{d}t} - q_{\mathrm{ar}}^{\mathrm{sys}} + q_{\mathrm{ven}}^{\mathrm{sys}} = 0, \tag{5.28}$$

$$\frac{L_{\mathrm{ven}}^{\mathrm{sys}}}{R_{\mathrm{ven}}^{\mathrm{sys}}}\frac{\mathrm{d}q_{\mathrm{ven}}^{\mathrm{sys}}}{\mathrm{d}t} + \frac{1}{R_{\mathrm{ven}}^{\mathrm{sys}}}[p_{\mathrm{ar}}^{r} - p_{\mathrm{ven}}^{\mathrm{sys}}] + q_{\mathrm{ven}}^{\mathrm{sys}} = 0, \tag{5.29}$$

$$\frac{\mathrm{d}V_{\mathrm{at}}^{r}}{\mathrm{d}t} - q_{\mathrm{ven}}^{\mathrm{sys}} + q_{\mathrm{v,in}}^{r} = 0, \tag{5.30}$$

$$\frac{1}{\tilde{R}_{\mathrm{v,in}}^{r}}[p_{\mathrm{at}}^{r} - p_{\mathrm{v}}^{r}] - q_{\mathrm{v,in}}^{r} = 0, \tag{5.31}$$

$$\frac{\mathrm{d}V_{\mathrm{v}}^{r}}{\mathrm{d}t} - q_{\mathrm{v,in}}^{r} + q_{\mathrm{v,out}}^{r} = 0, \tag{5.32}$$

$$\frac{1}{\tilde{R}_{\mathrm{v,out}}^{r}}[p_{\mathrm{v}}^{r} - p_{\mathrm{ar}}^{\mathrm{pul}}] - q_{\mathrm{v,out}}^{r} = 0, \tag{5.33}$$

$$C_{\mathrm{ar}}^{\mathrm{pul}}\left[\frac{\mathrm{d}p_{\mathrm{ar}}^{\mathrm{pul}}}{\mathrm{d}t} - Z_{\mathrm{ar}}^{\mathrm{pul}}\frac{\mathrm{d}q_{\mathrm{v,out}}^{r}}{\mathrm{d}t}\right] - q_{\mathrm{v,out}}^{r} + q_{\mathrm{ar}}^{\mathrm{pul}} = 0, \tag{5.34}$$

$$\frac{L_{\mathrm{ar}}^{\mathrm{pul}}}{R_{\mathrm{ar}}^{\mathrm{pul}}}\frac{\mathrm{d}q_{\mathrm{ar}}^{\mathrm{pul}}}{\mathrm{d}t} + \frac{1}{R_{\mathrm{ar}}^{\mathrm{pul}}}[p_{\mathrm{ven}}^{\mathrm{pul}} - p_{\mathrm{ar}}^{\mathrm{pul}} + Z_{\mathrm{ar}}^{\mathrm{pul}}q_{\mathrm{v,out}}^{r}] + q_{\mathrm{ar}}^{\mathrm{pul}} = 0, \tag{5.35}$$

$$C_{\mathrm{ven}}^{\mathrm{pul}}\frac{\mathrm{d}p_{\mathrm{ven}}^{\mathrm{pul}}}{\mathrm{d}t} - q_{\mathrm{ar}}^{\mathrm{pul}} + q_{\mathrm{ven}}^{\mathrm{pul}} = 0, \tag{5.36}$$

$$\frac{L_{\mathrm{ven}}^{\mathrm{pul}}}{R_{\mathrm{ven}}^{\mathrm{pul}}}\frac{\mathrm{d}q_{\mathrm{ven}}^{\mathrm{pul}}}{\mathrm{d}t} + \frac{1}{R_{\mathrm{ven}}^{\mathrm{pul}}}[p_{\mathrm{at}}^{\ell} - p_{\mathrm{ven}}^{\mathrm{pul}}] + q_{\mathrm{ven}}^{\mathrm{pul}} = 0. \tag{5.37}$$

Additional time dependent system variables are the left atrium cavity volume V_{at}^{ℓ}, left ventricle cavity volume V_{v}^{ℓ}, right atrium cavity volume V_{at}^{r} and right ventricle cavity volume V_{v}^{r}. In contrast to the pressures and flow rates, cavity volumes are not regarded as primary variables of the system. The ventricle volumes are calculated from the 3D structure model, while the atrial volumes are gained from *elastance* models. An atrial elastance $\left[\frac{\mathrm{kPa}}{\mathrm{mm}^3}\right]$ is the proportionality value between the volume change with respect to an initial value $V_{\mathrm{at,u}}^{i},\ i \in \{\ell, r\}$ and the atrial pressure

$$p_{\mathrm{at}}^{i} = E_{\mathrm{at}}^{i}(t) \cdot [V_{\mathrm{at}}^{i} - V_{\mathrm{at,u}}^{i}] \quad i \in \{\ell, r\}. \tag{5.38}$$

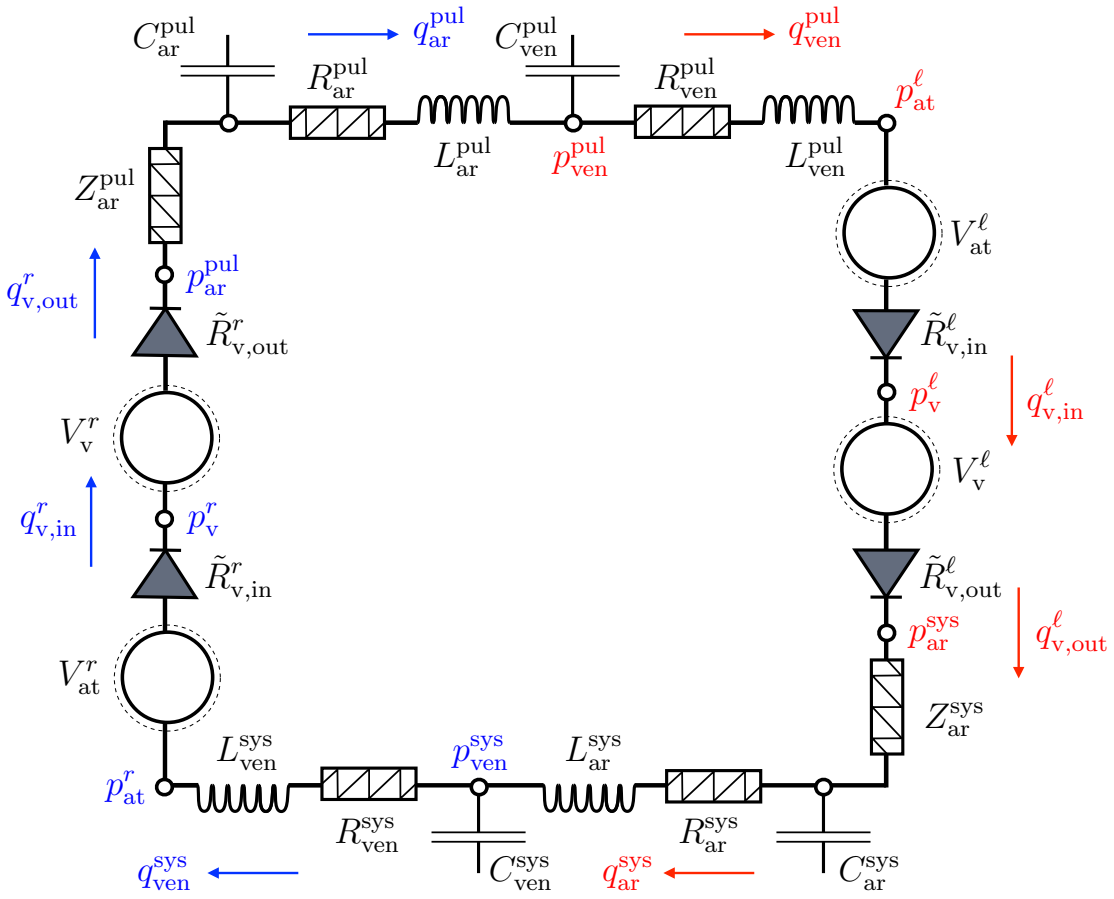

Figure 5.4.: Dimensionally reduced vascular system network including pulmonary and systemic circulation. The four heart chambers are modeled as compartments. Two-way coupling to the 3D structural mechanics model is achieved via the ventricular compartments (please refer to the main text for a detailed explanation). Atrial compartments are modeled by an elastance model (5.38). Quantities highlighted in red correspond to oxygenated blood flow, while quantities in blue correspond to deoxygenated blood flow.

Atrial contraction and relaxation can be modeled by time varying elastances

$$E_{\text{at}}^{i}(t) = [E_{\text{at,max}}^{i} - E_{\text{at,min}}^{i}] \cdot y_{\text{at}}^{i}(t) + E_{\text{at,min}}^{i} \quad i \in \{\ell, r\} \tag{5.39}$$

with the minimum and maximum elastance values $E_{\text{at,min}}^{i}, E_{\text{at,max}}^{i},\ i \in \{\ell, r\}$ and the activation function

$$y_{\text{at}}^{i} : \begin{cases} \mathbb{R} \to [0,1] \\ t \mapsto \begin{cases} \frac{1}{2}\left[1 - \cos\left(\frac{2\pi t}{\Delta t_{\text{at,act}}}\right)\right] & \text{for} \quad t \leq \Delta t_{\text{at,act}}, \qquad i \in \{\ell, r\} \\ 0 & \text{for} \quad t > \Delta t_{\text{at,act}} \end{cases} \end{cases} \tag{5.40}$$

using $\Delta t_{\text{at,act}}$ as the duration of atrial activation. Figure 5.5 depicts an exemplary evolution of atrial elastance.

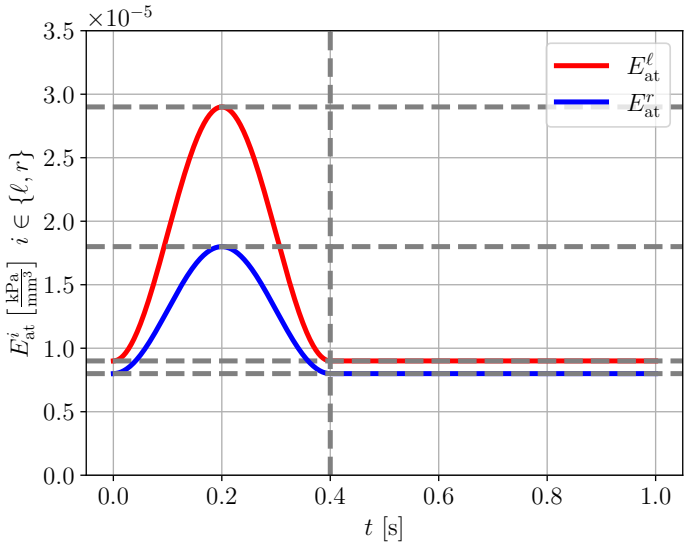

Figure 5.5.: Exemplary evolution of left and right atrial elastance over one cardiac cycle.

Several system constants have been introduced in the set of equations (5.22) - (5.37), see Figure 5.4. Valve resistances $\tilde{R}^\ell_{\text{v,in}}$, $\tilde{R}^\ell_{\text{v,out}}$, $\tilde{R}^r_{\text{v,in}}$ and $\tilde{R}^r_{\text{v,out}}$ model the influence of mitral, aortic, tricuspid and pulmonary valve, respectively. The capacitances C^j_i, resistances R^j_i and inertances L^j_i are given for systemic arterial, systemic venous, pulmonary arterial and pulmonary venous flows with $i \in \{\text{sys}, \text{pul}\}$ and $j \in \{\text{ar}, \text{ven}\}$ indicating the corresponding value. Finally, the resistances $Z^{\text{sys}}_{\text{ar}}$ and $Z^{\text{pul}}_{\text{ar}}$ can be found upstream of systemic and pulmonary arterial inertance-resistance-capacitance combinations.

In the order given, equations (5.22) - (5.37) can be interpreted as (5.22): left atrial mass balance, (5.23): mitral valve momentum balance, (5.24): left ventricular mass balance, (5.25): aortic valve momentum balance, (5.26): systemic arterial mass balance, (5.27): systemic arterial momentum balance, (5.28): systemic venous mass balance, (5.29): systemic venous momentum balance, (5.30): right atrial mass balance, (5.31): tricuspid valve momentum balance, (5.32): right ventricular mass balance, (5.33): pulmonary valve momentum balance, (5.34): pulmonary arterial mass balance, (5.35): pulmonary arterial momentum balance, (5.36): pulmonary venous mass balance and (5.37): pulmonary venous momentum balance.

Discretization, coupling and model parameters: The heart model under consideration is discretized with linear, tetrahedral finite elements with an edge length of approximately 1.5mm, Figure 5.6 depicts the discretization. In total, this results in 489,365 finite elements with 284,163 DOFs. As a model assumption, a cardiac cycle triggered by active stress generation lasts for $T_{\text{cycle}} = 1\text{s}$. The temporal discretization of the structural model deformation stage is performed by the generalized-α method (see Section 2.2.3) using 500 time steps of size 0.002 s and $\rho_\infty = 0.8$. Temporal discretization of the flow network equations is done by one-step-θ (see Section 2.2.3) time integration using $\theta = 0.5$. During prestressing of the full-order model (FOM), ventricular pressure load is applied in 10 steps using a pseudo-transient continuation (PTC) enhanced Newton-Raphson nonlinear solver (see Section 2.2.4) with initial value $k^{\text{ptc}}_0 = 3.33$. For ROM prestressing, 20 load steps with a pure Newton-Raphson nonlinear solver are applied.

Coupling between structural dynamics (5.16) - (5.19) and flow network equations (5.22) - (5.37) takes place at the luminal surfaces of the ventricles as given in equation (5.17). In words, the ventricle pressures state variables of the flow network are applied as boundary condition on the structural heart model. On the other hand, the structural heart model returns ventricle volumes, which enter the flow network by the left and right ventricular mass balances (5.24) and (5.32).

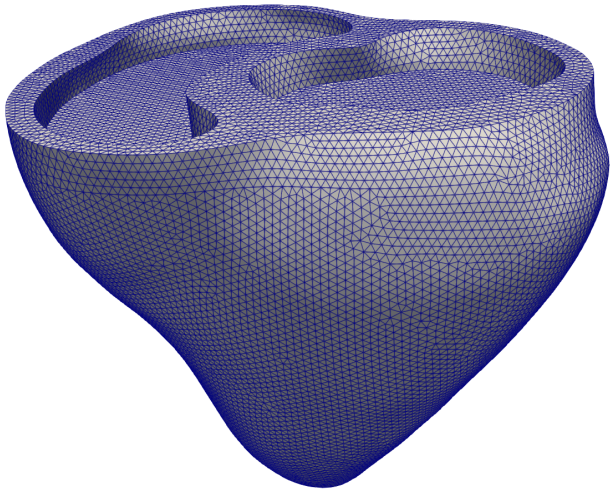

Figure 5.6.: Visualization of heart finite element discretization.

The fully discretized residual reads

$$\boldsymbol{r}_{\mathrm{sf}}^{n}(\boldsymbol{d}^{n},\boldsymbol{q}^{n}) = \begin{bmatrix} \boldsymbol{r}^{n}(\boldsymbol{d}^{n},\boldsymbol{q}^{n}) \\ \boldsymbol{g}^{n}(\boldsymbol{d}^{n},\boldsymbol{q}^{n}) \end{bmatrix} \in \mathbb{R}^{N+z}, \tag{5.41}$$

wherein $\boldsymbol{g}^{n}(\boldsymbol{d}^{n},\boldsymbol{q}^{n})$ denotes the temporally discretized residual of the $z = 16$ flow network equations and

$$\begin{aligned} \boldsymbol{q}^{n} = [&p_{\mathrm{at}}^{\ell}, p_{\mathrm{at}}^{r}, p_{\mathrm{v}}^{\ell}, p_{\mathrm{v}}^{r}, p_{\mathrm{ar}}^{\mathrm{sys}}, p_{\mathrm{ar}}^{\mathrm{pul}}, p_{\mathrm{ven}}^{\mathrm{sys}}, p_{\mathrm{ven}}^{\mathrm{pul}}, \\ &q_{\mathrm{v,in}}^{\ell}, q_{\mathrm{v,in}}^{r}, q_{\mathrm{v,out}}^{\ell}, q_{\mathrm{v,out}}^{r}, q_{\mathrm{ar}}^{\mathrm{sys}}, q_{\mathrm{ar}}^{\mathrm{pul}}, q_{\mathrm{ven}}^{\mathrm{sys}}, q_{\mathrm{ven}}^{\mathrm{pul}}]^{n} \end{aligned} \tag{5.42}$$

denotes the DOF vector of the flow network state. Dependency of the structural residual on flow network DOFs and vice versa follows from coupling of the two systems as explained above. The full system is solved monolithically by Newton-Raphson iterations using a block Jacobian

$$\begin{bmatrix} \boldsymbol{J}_{r,d}^{n}(\boldsymbol{d}_{i}^{n},\boldsymbol{q}_{i}^{n}) & \boldsymbol{J}_{r,q}^{n}(\boldsymbol{d}_{i}^{n},\boldsymbol{q}_{i}^{n}) \\ \boldsymbol{J}_{g,d}^{n}(\boldsymbol{d}_{i}^{n},\boldsymbol{q}_{i}^{n}) & \boldsymbol{J}_{g,q}^{n}(\boldsymbol{d}_{i}^{n},\boldsymbol{q}_{i}^{n}) \end{bmatrix} \begin{bmatrix} \Delta\boldsymbol{d}_{i+1}^{n} \\ \Delta\boldsymbol{q}_{i+1}^{n} \end{bmatrix} = - \begin{bmatrix} \boldsymbol{r}^{n}(\boldsymbol{d}_{i}^{n},\boldsymbol{q}_{i}^{n}) \\ \boldsymbol{g}^{n}(\boldsymbol{d}_{i}^{n},\boldsymbol{q}_{i}^{n}) \end{bmatrix} \tag{5.43}$$

$$\begin{bmatrix} \boldsymbol{d}_{i+1}^{n} \\ \boldsymbol{q}_{i+1}^{n} \end{bmatrix} = \begin{bmatrix} \boldsymbol{d}_{i}^{n} \\ \boldsymbol{q}_{i}^{n} \end{bmatrix} + \begin{bmatrix} \Delta\boldsymbol{d}_{i+1}^{n} \\ \Delta\boldsymbol{q}_{i+1}^{n} \end{bmatrix} \tag{5.44}$$

wherein

$$\boldsymbol{J}_{r,d}^{n}(\boldsymbol{d}^{n},\boldsymbol{q}^{n}) \coloneqq \frac{\partial \boldsymbol{r}^{n}(\boldsymbol{d}^{n},\boldsymbol{q}^{n})}{\partial \boldsymbol{d}} \in \mathbb{R}^{N\times N}, \quad \boldsymbol{J}_{r,q}^{n}(\boldsymbol{d}^{n},\boldsymbol{q}^{n}) \coloneqq \frac{\partial \boldsymbol{r}^{n}(\boldsymbol{d}^{n},\boldsymbol{q}^{n})}{\partial \boldsymbol{q}} \in \mathbb{R}^{N\times z}, \tag{5.45}$$

$$\boldsymbol{J}_{g,d}^{n}(\boldsymbol{d}^{n},\boldsymbol{q}^{n}) \coloneqq \frac{\partial \boldsymbol{g}^{n}(\boldsymbol{d}^{n},\boldsymbol{q}^{n})}{\partial \boldsymbol{d}} \in \mathbb{R}^{z\times N}, \quad \boldsymbol{J}_{g,q}^{n}(\boldsymbol{d}^{n},\boldsymbol{q}^{n}) \coloneqq \frac{\partial \boldsymbol{g}^{n}(\boldsymbol{d}^{n},\boldsymbol{q}^{n})}{\partial \boldsymbol{q}} \in \mathbb{R}^{z\times z}. \tag{5.46}$$

were introduced. For details on the evaluation of these Jacobians the reader is referred to [57].

The linear block systems are iteratively solved using a parallel GMRES solver implemented in the software package Trilinos [55] in combination with SIMPLE type preconditioning [37] for the full block system and algebraic multigrid preconditioning for the structural block.

Physical baseline parameters for the structural heart model and the flow network model are given in Table 5.1 and 5.3, respectively, for detailed information on parameter estimation see [57]. Flow network system resistances / inertances as well as capacitances are given in dependency of the systemic arterial resistance $R_{\text{ar}}^{\text{sys}}$ and the so-called systemic arterial windkessel time constant $\tau_{\text{ar}}^{\text{sys}} = 1.652\ \text{s}$ and pulmonary arterial windkessel time constant $\tau_{\text{ar}}^{\text{pul}} = 0.3\ \text{s}$.

Table 5.1.: Baseline parameters for structural heart. See equations referenced in the first column for interpretation of physical meaning.

equation	symbol	value
boundary conditions		
(5.14), (5.20)	k_b	$0.25\ \frac{\text{kPa}}{\text{mm}}$
(5.21), (5.15)	$k_{b\perp}$	$1.25\ \frac{\text{kPa}}{\text{mm}}$
(5.21), (5.15)	$k_{e\perp}$	$0.075\ \frac{\text{kPa}}{\text{mm}}$
(5.21), (5.15)	$k_{\text{lid}\perp}$	$0.05\ \frac{\text{kPa}}{\text{mm}}$
(5.20)	c_b	$0.0005\ \frac{\text{kPa}}{\text{mm}}$
(5.21)	$c_{b\perp}$	$0.0005\ \frac{\text{kPa}}{\text{mm}}$
(5.21)	$c_{e\perp}$	$0.0005\ \frac{\text{kPa}}{\text{mm}}$
(5.21)	$c_{\text{lid}\perp}$	$0.0005\ \frac{\text{kPa}}{\text{mm}}$
active contraction		
(5.3)	σ_0	70 kPa
(5.5), (5.7), (5.8)	K	5
(5.4), (5.7), (5.8)	α_{max}	$10\ \frac{1}{\text{s}}$
(5.4), (5.7), (5.8)	α_{min}	$-30\ \frac{1}{\text{s}}$
(5.7)	t_{contr}	0.2 s
(5.8)	t_{relax}	0.53 s

equation	symbol	value
passive myocardial material		
(5.2)	a_0	0.059 kPa
(5.2)	a_f	18.472 kPa
(5.2)	a_s	2.481 kPa
(5.2)	a_{fs}	0.216 kPa
(5.2)	b_0	8.023
(5.2)	b_f	16.026
(5.2)	b_s	11.120
(5.2)	b_{fs}	11.436
(5.2)	κ	10^3 kPa
(5.16)	ρ_0	$10^{-6}\ \frac{\text{kg}}{\text{mm}^3}$
covering lids		
(5.9)	μ_{lid}	50 kPa
(5.9)	κ_{lid}	10 kPa
(5.16)	ρ_0	$10^{-6}\ \frac{\text{kg}}{\text{mm}^3}$

5.1.2. Exemplary computation

An exemplary computation of a FOM heart beat is presented together with a discussion on output quantities of interest. The heart model as introduced in Section 5.1.1 is used for estimation of the homeostatic state, that is, periodically steady conditions of the beating heart. In more detail, the homeostatic state is assumed as given if the so-called cycle error criterion (CER) $\mathcal{E}_{\text{cycl}}$ is below

Table 5.3.: Baseline parameters for flow network. See equations referenced in the first column for interpretation of physical meaning.

equation	symbol	value
atrial models		
(5.40)	$\Delta t_{\mathrm{at,act}}$	$0.4\ \mathrm{s}$
(5.39)	$E^{\ell}_{\mathrm{at,min}}$	$9 \cdot 10^{-6}\ \frac{\mathrm{kPa}}{\mathrm{mm}^3}$
(5.39)	$E^{\ell}_{\mathrm{at,max}}$	$29 \cdot 10^{-6}\ \frac{\mathrm{kPa}}{\mathrm{mm}^3}$
(5.39)	$E^{r}_{\mathrm{at,min}}$	$8 \cdot 10^{-6}\ \frac{\mathrm{kPa}}{\mathrm{mm}^3}$
(5.39)	$E^{r}_{\mathrm{at,max}}$	$18 \cdot 10^{-6}\ \frac{\mathrm{kPa}}{\mathrm{mm}^3}$
valve resistances		
(2.51), (5.23)	$R^{\ell,\mathrm{min}}_{\mathrm{v,in}}$	$10^{-6}\ \frac{\mathrm{kPa\cdot s}}{\mathrm{mm}^3}$
(2.51), (5.23)	$R^{\ell,\mathrm{max}}_{\mathrm{v,in}}$	$10\ \frac{\mathrm{kPa\cdot s}}{\mathrm{mm}^3}$
(2.51), (5.25)	$R^{\ell,\mathrm{min}}_{\mathrm{v,out}}$	$10^{-6}\ \frac{\mathrm{kPa\cdot s}}{\mathrm{mm}^3}$
(2.51), (5.25)	$R^{\ell,\mathrm{max}}_{\mathrm{v,out}}$	$10\ \frac{\mathrm{kPa\cdot s}}{\mathrm{mm}^3}$
(2.51), (5.31)	$R^{r,\mathrm{min}}_{\mathrm{v,in}}$	$10^{-6}\ \frac{\mathrm{kPa\cdot s}}{\mathrm{mm}^3}$
(2.51), (5.31)	$R^{r,\mathrm{max}}_{\mathrm{v,in}}$	$10\ \frac{\mathrm{kPa\cdot s}}{\mathrm{mm}^3}$
(2.51), (5.33)	$R^{r,\mathrm{min}}_{\mathrm{v,out}}$	$10^{-6}\ \frac{\mathrm{kPa\cdot s}}{\mathrm{mm}^3}$
(2.51), (5.33)	$R^{r,\mathrm{max}}_{\mathrm{v,out}}$	$10\ \frac{\mathrm{kPa\cdot s}}{\mathrm{mm}^3}$
system inertances		
(5.27)	$L^{\mathrm{sys}}_{\mathrm{ar}}$	$0.667 \cdot 10^{-6}\,\frac{\mathrm{kPa\cdot s}^2}{\mathrm{mm}^3}$
(5.29)	$L^{\mathrm{sys}}_{\mathrm{ven}}$	$0\ \frac{\mathrm{kPa\cdot s}^2}{\mathrm{mm}^3}$
(5.35)	$L^{\mathrm{pul}}_{\mathrm{ar}}$	$0\ \frac{\mathrm{kPa\cdot s}^2}{\mathrm{mm}^3}$
(5.37)	$L^{\mathrm{pul}}_{\mathrm{ven}}$	$0\ \frac{\mathrm{kPa\cdot s}^2}{\mathrm{mm}^3}$

equation	symbol	value
system resistance / impedances		
(5.27)	$R^{\mathrm{sys}}_{\mathrm{ar}}$	$120 \cdot 10^{-6}\ \frac{\mathrm{kPa\cdot s}}{\mathrm{mm}^3}$
(5.29)	$R^{\mathrm{sys}}_{\mathrm{ven}}$	$\frac{1}{5} R^{\mathrm{sys}}_{\mathrm{ar}}$
(5.35)	$R^{\mathrm{pul}}_{\mathrm{ar}}$	$\frac{1}{8} R^{\mathrm{sys}}_{\mathrm{ar}}$
(5.37)	$R^{\mathrm{pul}}_{\mathrm{ven}}$	$\frac{1}{8} R^{\mathrm{sys}}_{\mathrm{ar}}$
(5.26), (5.27)	$Z^{\mathrm{sys}}_{\mathrm{ar}}$	$\frac{1}{20} R^{\mathrm{sys}}_{\mathrm{ar}}$
(5.34), (5.35)	$Z^{\mathrm{pul}}_{\mathrm{ar}}$	$0\ \frac{\mathrm{kPa\cdot s}}{\mathrm{mm}^3}$
system capacitances		
(5.26)	$C^{\mathrm{sys}}_{\mathrm{ar}}$	$\frac{\tau^{\mathrm{sys}}_{\mathrm{ar}}}{R^{\mathrm{sys}}_{\mathrm{ar}}}$
(5.28)	$C^{\mathrm{sys}}_{\mathrm{ven}}$	$30 C^{\mathrm{sys}}_{\mathrm{ar}}$
(5.34)	$C^{\mathrm{pul}}_{\mathrm{ar}}$	$\frac{8\tau^{\mathrm{pul}}_{\mathrm{ar}}}{R^{\mathrm{sys}}_{\mathrm{ar}}}$
(5.36)	$C^{\mathrm{pul}}_{\mathrm{ven}}$	$2.5 C^{\mathrm{pul}}_{\mathrm{ar}}$

a prescribed tolerance $\mathcal{E}_{\mathrm{cycl}} \leq \varepsilon_{\mathrm{cycle}}$ with

$$\begin{aligned}\mathcal{E}_{\mathrm{cycl}} = \max\Bigg(&\left|\frac{p^{\mathrm{sys}}_{\mathrm{ar}}(T_{\mathrm{cycl}}) - p^{\mathrm{sys}}_{\mathrm{ar}}(0)}{p^{\mathrm{sys}}_{\mathrm{ar}}(0)}\right|, \left|\frac{p^{\mathrm{pul}}_{\mathrm{ar}}(T_{\mathrm{cycl}}) - p^{\mathrm{pul}}_{\mathrm{ar}}(0)}{p^{\mathrm{pul}}_{\mathrm{ar}}(0)}\right|, \\ &\left|\frac{p^{\mathrm{sys}}_{\mathrm{ven}}(T_{\mathrm{cycl}}) - p^{\mathrm{sys}}_{\mathrm{ven}}(0)}{p^{\mathrm{sys}}_{\mathrm{ven}}(0)}\right|, \left|\frac{p^{\mathrm{pul}}_{\mathrm{ven}}(T_{\mathrm{cycl}}) - p^{\mathrm{pul}}_{\mathrm{ven}}(0)}{p^{\mathrm{pul}}_{\mathrm{ven}}(0)}\right|, \\ &\left|\frac{V^{\ell}_{\mathrm{v}}(T_{\mathrm{cycl}}) - V^{\ell}_{\mathrm{v}}(0)}{V^{\ell}_{\mathrm{v}}(0)}\right|, \left|\frac{V^{r}_{\mathrm{v}}(T_{\mathrm{cycl}}) - V^{r}_{\mathrm{v}}(0)}{V^{r}_{\mathrm{v}}(0)}\right|, \left|\frac{\mathrm{SV}^{\ell}_{\mathrm{v}} - \mathrm{SV}^{r}_{\mathrm{v}}}{\mathrm{SV}^{\ell}_{\mathrm{v}}}\right|\Bigg).\end{aligned} \tag{5.47}$$

The ventricular stroke volume

$$SV^{i}_{\mathrm{v}} = EDV^{i}_{\mathrm{v}} - ESV^{i}_{\mathrm{v}} \quad \text{with } i \in \{\ell, r\} \tag{5.48}$$

corresponds to the amount of ejected blood during one cardiac cycle and can be computed from the difference between the end-diastolic volume EDV_{v}^{i} and end-systolic volume ESV_{v}^{i}, with $i \in \{\ell, r\}$.

All quantities in equation (5.47) evaluated at time $t = T_{\mathrm{cycl}}$ result from the evaluation of one cardiac cycle starting from given values at time $t = 0$. Consequently, the problem of identifying the homeostatic state can be understood as finding a set of initial conditions $\boldsymbol{q}(t = 0)$ for the flow network variables (5.42), such that the flow network state at the end of the cardiac cycle $\boldsymbol{q}(t = T_{\mathrm{cycl}})$ fulfills the cycle error criterion (5.47).

A strategy to find such initial conditions is described in [57]. Therein, multiple cardiac cycles are evaluated successively updating the initial conditions by $\boldsymbol{q}(t = 0) \leftarrow \boldsymbol{q}(t = T_{\mathrm{cycl}})$, that is, the flow network state at the end of the cardiac cycle is used as initial condition for the following cardiac cycle, Figure 5.7 depicts the iterative process in a flow chart. A tolerance of $\varepsilon_{\mathrm{cycle}} = 0.05$ is used and convergence is received after 6 cardiac cycles. Table 5.5 reveals the initially chosen flow network state variables, which also are used as initial conditions for all presented simulations in the following, except explicitly stated otherwise.

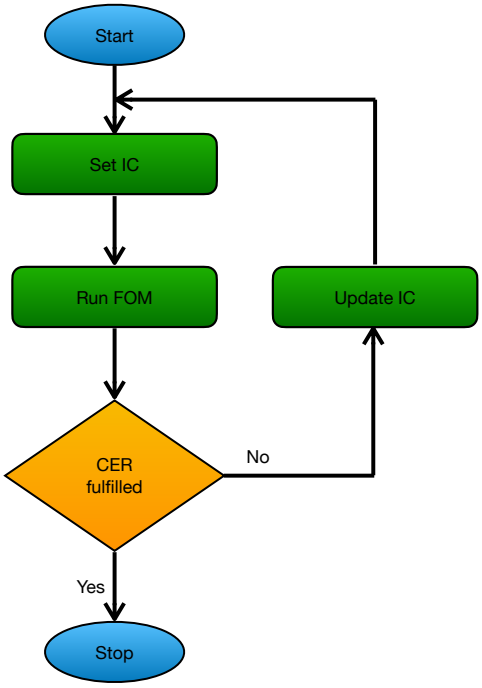

Figure 5.7.: Flow chart for homeostatic state computation of the beating heart. Abbreviations included are IC: initial condition, CER: cycle error criterion, FOM: full-order model.

The homeostatic state flow network variables are depicted in Figure 5.8 together with pressure-volume curves and volumes of left and right ventricle. Cardiac cycle phases described in Section 1.2.2 can be identified. Starting from $t = 0$ s, atrial contraction and final ventricular filling proceeds until closing of atrioventricular valves, which can be seen from the separation of the p_{v}^{ℓ}-curve and the p_{at}^{ℓ}-curve in Figure 5.8a at $t = 0.2$ s. Next, isovolumetric contraction takes place until opening of semilunar valves entailing ventricular ejection, which starts with joining of the $p_{\mathrm{ar}}^{\mathrm{sys}}$-curve with the p_{v}^{ℓ}-curve at $t = 0.27$ s. Ventricular ejection ends with closing of semilunar

Table 5.5.: Baseline initial flow network state variables.

pressure [kPa]	initial condition	flow rate $\left[\frac{\text{ml}}{\text{s}}\right]$	initial condition
p_{at}^{ℓ}	0.606	$q_{\text{v,in}}^{\ell}$	0
p_{v}^{ℓ}	0.6	$q_{\text{v,out}}^{\ell}$	0
$p_{\text{ar}}^{\text{sys}}$	12	$q_{\text{ar}}^{\text{sys}}$	0
$p_{\text{ven}}^{\text{sys}}$	2.266	$q_{\text{ven}}^{\text{sys}}$	0
p_{at}^{r}	0.606	$q_{\text{v,in}}^{r}$	0
p_{v}^{r}	0.6	$q_{\text{v,out}}^{r}$	0
$p_{\text{ar}}^{\text{pul}}$	2.400	$q_{\text{ar}}^{\text{pul}}$	0
$p_{\text{ven}}^{\text{pul}}$	1.6	$q_{\text{ven}}^{\text{pul}}$	0

valves at diverging p_{v}^{ℓ}-curve and $p_{\text{ar}}^{\text{sys}}$-curve at $t = 0.54$ s. Isovolumetric relaxation follows at closed valves until joining of p_{v}^{ℓ}-curve and p_{at}^{ℓ}-curve at $t = 0.65$ s. Ventricular refilling claims the remaining of the cardiac cycle until $t = 1$ s.

Figure 5.9 depicts 3D heart configurations at different instances in time, namely the initial configuration at $t = 0$ s, the configuration prior to left ventricular ejection at $t = 0.27$ s (see $q_{\text{v,out}}^{\ell}$ in Figure 5.8c), the configuration prior to left ventricular filling (see $q_{\text{v,in}}^{\ell}$ in Figure 5.8c) at $t = 0.65$ s and the final configuration at $t = 1$ s. As a consequence of homeostasis, the initial and final configurations are visually indistinguishable. The configurations prior to ventricular ejection and filling clearly show differences in ventricular volumes and shapes.

5.2. Reduced-order model

The dimensionally reduced order model (DROM) and dimensionally reduced as well as hyper reduced order model (DHROM) follow the principles of Section 3 applying a Galerkin projection as well ECSW hyper reduction. A specific feature of the given computational model is the subdivision of the residual in a structural and a flow network part (5.41). Model reduction is exclusively applied to the structural dynamics part, given that the flow network residual consists of very few equation with low computational cost in comparison to the structural dynamics residual. Arising linear problems are of small size and therefore solved using a direct solver [31].

Monolithic DROM equations: Pure dimensional reduction of the coupled model has been presented in [57, 105]. In order to exclude the flow network residual from dimensional reduction, the applied reduced-order basis (ROB) is of block-diagonal shape

$$\boldsymbol{V}_{\text{sf}} = \begin{bmatrix} \boldsymbol{V} & \boldsymbol{0} \\ \boldsymbol{0} & \boldsymbol{I} \end{bmatrix} \in \mathbb{R}^{(N+z)\times(N+z)} \tag{5.49}$$

yielding the Galerkin projection

$$\hat{\boldsymbol{r}}_{\text{sf}}^{n}(\hat{\boldsymbol{d}}^{n}, \boldsymbol{q}^{n}) = \boldsymbol{V}_{\text{sf}}^{T} \boldsymbol{r}_{\text{sf}}^{n}(\boldsymbol{V}\hat{\boldsymbol{d}}^{n}, \boldsymbol{q}^{n}) \tag{5.50}$$

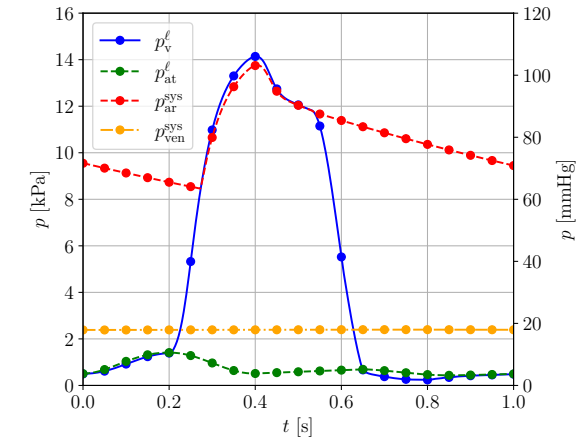

(a) Systemic and left heart chamber pressures

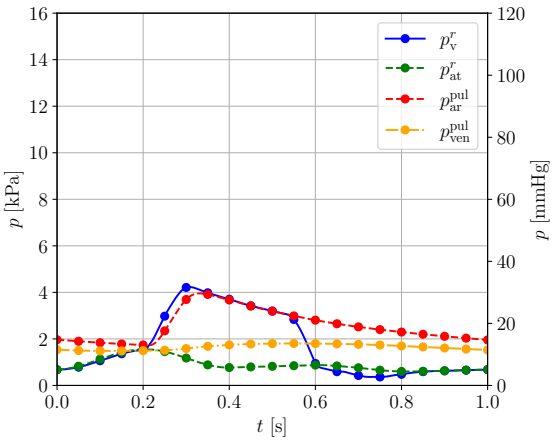

(b) Pulmonary and right heart chamber pressures

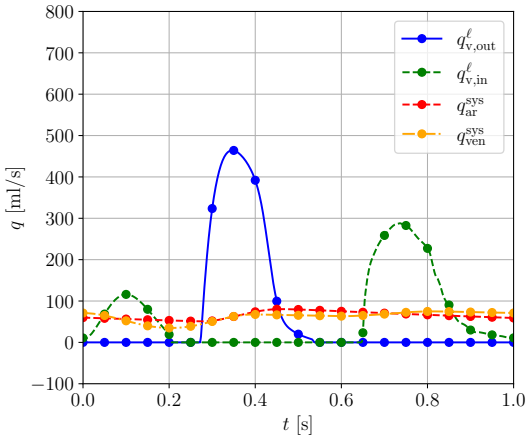

(c) Systemic and left ventricular fluxes

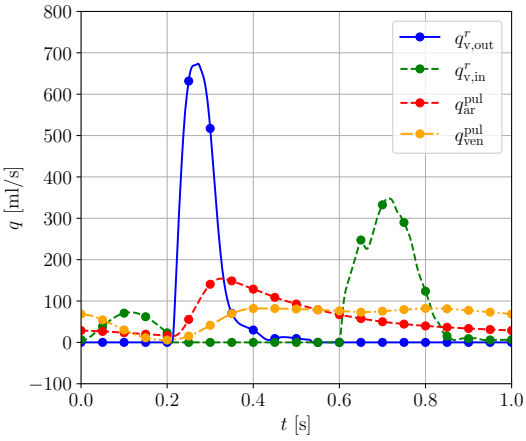

(d) Pulmonary and right ventricular fluxes

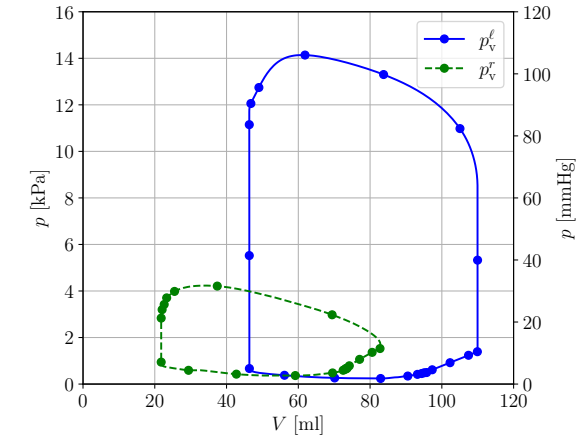

(e) Ventricular pressure-volumes

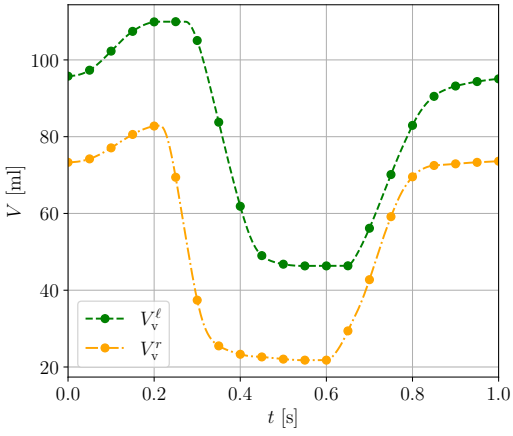

(f) Ventricular volume curves

Figure 5.8.: Flow network state variables and ventricular volumes temporally resolved over one cardiac cycle at homeostasis.

and consequently

$$\hat{\boldsymbol{r}}_{\mathrm{sf}}^{n}(\hat{\boldsymbol{d}}^{n}, \boldsymbol{q}^{n}) = \begin{bmatrix} \boldsymbol{V}^{T}\boldsymbol{r}^{n}(\boldsymbol{V}\hat{\boldsymbol{d}}^{n}, \boldsymbol{q}^{n}) \\ \boldsymbol{g}^{n}(\boldsymbol{d}^{n}, \boldsymbol{q}^{n}) \end{bmatrix} \in \mathbb{R}^{p+z}. \tag{5.51}$$

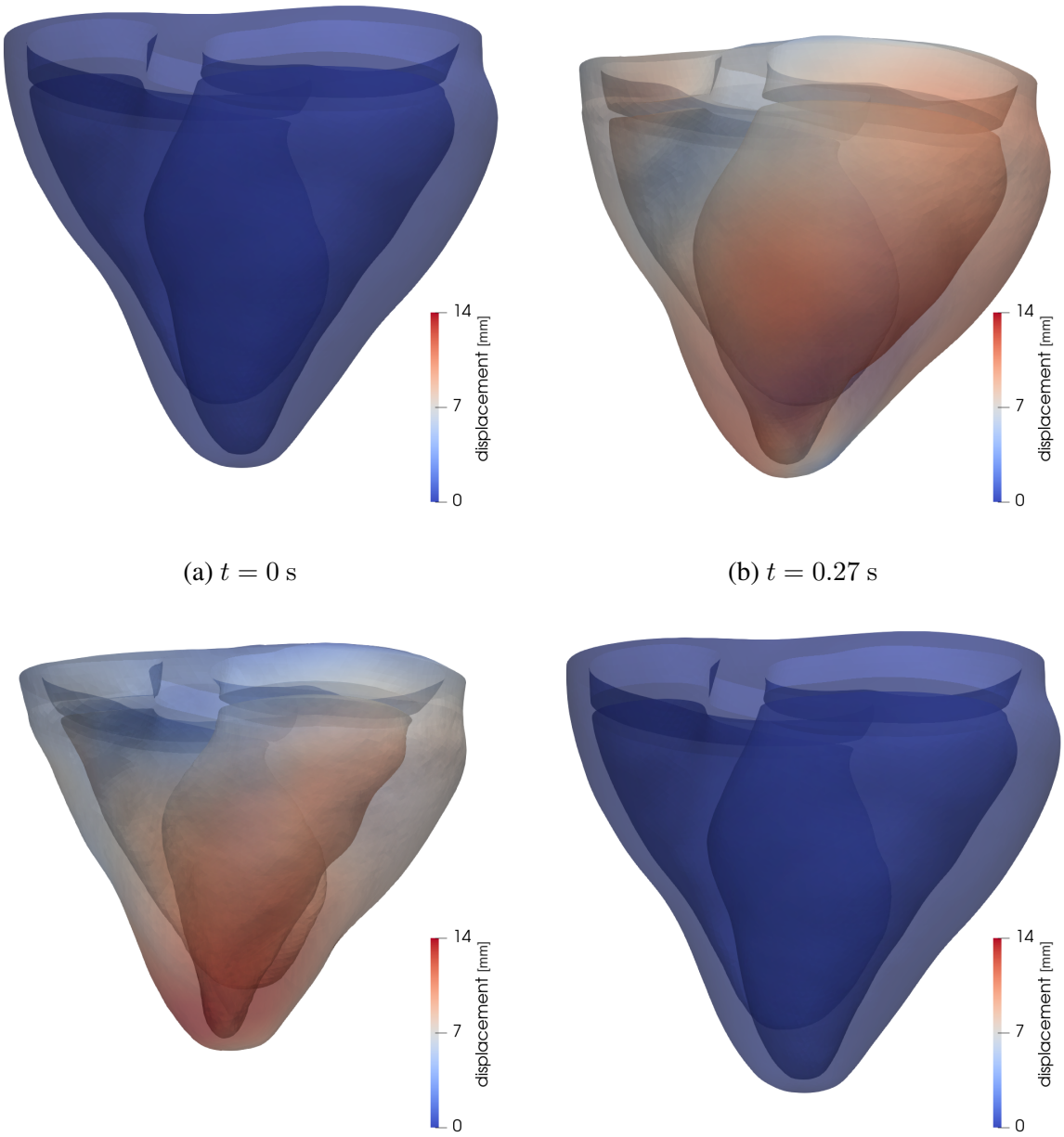

(a) $t = 0$ s

(b) $t = 0.27$ s

(c) $t = 0.65$ s

(d) $t = 1$ s

Figure 5.9.: Deformation stage displacement field of heart cycle at different time instances, in more detail (a): configuration at 80% of the diastolic phase, (b): configuration prior to left ventricular ejection, (c): configuration prior to left ventricular refilling, (d): configuration at 80% of the diastolic phase of the upcoming heart beat. The heart is at homeostasis.

The corresponding Newton-Raphson iterations result from linearization of residual (5.51) and read

$$\begin{bmatrix} \boldsymbol{V}^T \boldsymbol{J}^n_{r,d}(\boldsymbol{V}\hat{\boldsymbol{d}}^n_i, \boldsymbol{q}^n_i)\boldsymbol{V} & \boldsymbol{V}^T \boldsymbol{J}^n_{r,q}(\boldsymbol{V}\hat{\boldsymbol{d}}^n_i, \boldsymbol{q}^n_i) \\ \boldsymbol{J}^n_{g,d}(\boldsymbol{V}\hat{\boldsymbol{d}}^n_i, \boldsymbol{q}^n_i)\boldsymbol{V} & \boldsymbol{J}^n_{g,q}(\boldsymbol{V}\hat{\boldsymbol{d}}^n_i, \boldsymbol{q}^n_i) \end{bmatrix} \begin{bmatrix} \Delta\hat{\boldsymbol{d}}^n_{i+1} \\ \Delta\boldsymbol{q}^n_{i+1} \end{bmatrix} = - \begin{bmatrix} \boldsymbol{V}^T \boldsymbol{r}^n(\boldsymbol{V}\hat{\boldsymbol{d}}^n_i, \boldsymbol{q}^n_i) \\ \boldsymbol{g}^n(\boldsymbol{d}^n_i, \boldsymbol{q}^n_i) \end{bmatrix}$$
$$\begin{bmatrix} \hat{\boldsymbol{d}}^n_{i+1} \\ \boldsymbol{q}^n_{i+1} \end{bmatrix} = \begin{bmatrix} \hat{\boldsymbol{d}}^n_i \\ \boldsymbol{q}^n_i \end{bmatrix} + \begin{bmatrix} \Delta\hat{\boldsymbol{d}}^n_{i+1} \\ \Delta\boldsymbol{q}^n_{i+1} \end{bmatrix}, \tag{5.52}$$

wherein the Jacobian blocks have been defined in equation (5.45) and (5.46).

Monolithic DHROM equations: Hyper reduction is performed on top of the dimensional reduction of the structural dynamics part. The hyper reduced residual reads

$$\tilde{\boldsymbol{r}}^n_{\mathrm{sf}}(\hat{\boldsymbol{d}}^n, \boldsymbol{q}^n) = \begin{bmatrix} \boldsymbol{V}^T \tilde{\boldsymbol{r}}^n(\boldsymbol{V}\hat{\boldsymbol{d}}^n, \boldsymbol{q}^n) \\ \boldsymbol{g}^n(\boldsymbol{d}^n, \boldsymbol{q}^n) \end{bmatrix} \in \mathbb{R}^{p+z}, \tag{5.53}$$

wherein $\tilde{\boldsymbol{r}}^n(\boldsymbol{V}\hat{\boldsymbol{d}}^n, \boldsymbol{q}^n)$ denotes a residual gained from weighted assembly of a small subset of computational mesh elements identified from ECSW, see Section 3.2.2. Consistent linearization yields a Newton-Raphson iteration scheme

$$\begin{bmatrix} \boldsymbol{V}^T \tilde{\boldsymbol{J}}^n_{r,d}(\boldsymbol{V}\hat{\boldsymbol{d}}^n_i, \boldsymbol{q}^n_i)\boldsymbol{V} & \boldsymbol{V}^T \tilde{\boldsymbol{J}}^n_{r,q}(\boldsymbol{V}\hat{\boldsymbol{d}}^n_i, \boldsymbol{q}^n_i) \\ \boldsymbol{J}^n_{g,d}(\boldsymbol{V}\hat{\boldsymbol{d}}^n_i, \boldsymbol{q}^n_i)\boldsymbol{V} & \boldsymbol{J}^n_{g,q}(\boldsymbol{V}\hat{\boldsymbol{d}}^n_i, \boldsymbol{q}^n_i) \end{bmatrix} \begin{bmatrix} \Delta\hat{\boldsymbol{d}}^n_{i+1} \\ \Delta\boldsymbol{q}^n_{i+1} \end{bmatrix} = - \begin{bmatrix} \boldsymbol{V}^T \tilde{\boldsymbol{r}}^n(\boldsymbol{V}\hat{\boldsymbol{d}}^n_i, \boldsymbol{q}^n_i) \\ \boldsymbol{g}^n(\boldsymbol{d}^n_i, \boldsymbol{q}^n_i) \end{bmatrix}$$
$$\begin{bmatrix} \hat{\boldsymbol{d}}^n_{i+1} \\ \boldsymbol{q}^n_{i+1} \end{bmatrix} = \begin{bmatrix} \hat{\boldsymbol{d}}^n_i \\ \boldsymbol{q}^n_i \end{bmatrix} + \begin{bmatrix} \Delta\hat{\boldsymbol{d}}^n_{i+1} \\ \Delta\boldsymbol{q}^n_{i+1} \end{bmatrix} \tag{5.54}$$

with Jacobians $\tilde{\boldsymbol{J}}^n_{r,d}(\boldsymbol{V}\hat{\boldsymbol{d}}^n_i, \boldsymbol{q}^n_i)$ and $\tilde{\boldsymbol{J}}^n_{r,q}(\boldsymbol{V}\hat{\boldsymbol{d}}^n_i, \boldsymbol{q}^n_i)$ assembled from weighted contributions of previously selected ECSW elements, see equation (3.55).

In more detail, equations (5.10) to (5.13) and (5.16) to (5.19) reveal three force contributions which require re-assembly at every time step, namely the internal force vector, the ventricular pressure (external) force vector and the embedding tissue (external) force vector. Each of these residual contributions is independently sampled using ECSW. As a result, ECSW is performed independently on first: the full computational mesh, second: the lumimal ventricular surface mesh, and third: the epicardial, heart base and external lids surface mesh.

Selection of POD modes: ROBs for the heart model are constructed by POD of a snapshot matrix containing displacement modes from FOM solutions. Since a cardiac cycle includes a prestressing stage followed by a dynamic deformation stage, both prestessing and deformation stage modes are gathered in the snapshot matrix. Referring to Section 3.1.3, only POD modes with large singular values (relative to the spectrum of singular values) are of interest. As a result, the POD basis is truncated after p modes. Recalling the descending ordering of singular values ξ_i, p is selected such that [118]

$$\xi_{\mathrm{th}} \leq \frac{\xi_p}{\xi_1} \quad \text{and} \quad \xi_{\mathrm{th}} > \frac{\xi_{p+1}}{\xi_1} \tag{5.55}$$

using a threshold ratio $0 < \xi_{\mathrm{th}} < 1$. Consequently, the significance of POD modes is weighted relatively to the very first POD mode and adjusted by ξ_{th}.

5.3. Results and discussion

5.3.1. Dimensional reducibility

The dimensional reducibility of a simulation can be assessed by the singular values of a solution snapshot matrix, see Section 3.1.3. The exemplary computation from Section 5.1.2 is used and the homeostatic state solution, that is the last cardiac cycle with fulfilled cycle error criterion (5.47), is examined. One heart beat is assumed to last for $1\ \mathrm{s}$, which is temporally discretized by 500 time steps. Consequently, 500 displacement stage deformation modes can be gathered. The resulting snapshot matrix is decomposed by a singular value decomposition, see Section 3.1.3, and the ordered singular values are depicted in Figure 5.10.

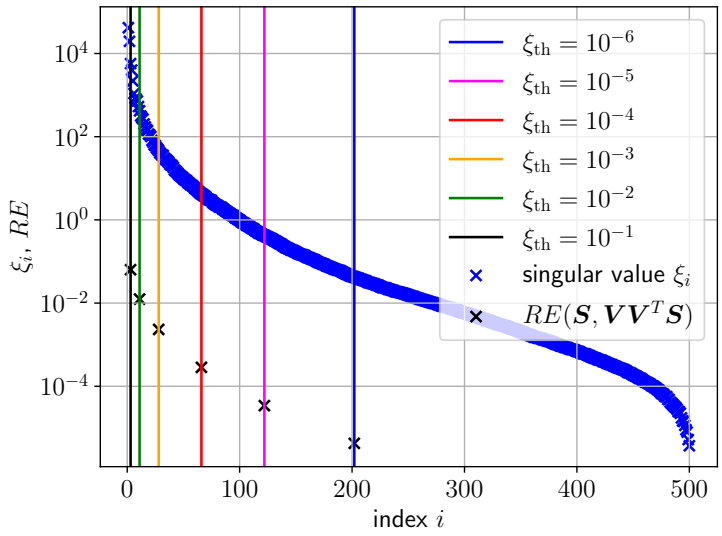

Figure 5.10.: Decay of singular values (blue markers) for deformation stage displacement modes for a homeostatic heart beat. The vertical lines indicate truncation of POD modes controlled by the threshold ration ξ_{th} (see equation (5.55)). Additionally, relative orthogonal projection errors (black markers) are depicted for several ROBs as indicated by the ξ_{th} mode truncation criterion.

A pronounced initial decay of singular values indicates good dimensional reducibility. Additionally, vertical lines visualize the POD modes selection criterion (5.55) for different values of the threshold ratio ξ_{th}. As a result, an initial decay of singular values of for instance three orders of magnitude ($\xi_{\mathrm{th}} = 10^{-3}$) is achieved by only 29 modes.

In order to demonstrate the relation between singular values and the quality of the extracted POD mode subspace, the relative orthogonal projection errors between snapshot matrix $\boldsymbol{S}$ and ROB $\boldsymbol{V}$, that is

$$RE(\boldsymbol{S}, \boldsymbol{V}\boldsymbol{V}^T\boldsymbol{S}) = \frac{\left\|\boldsymbol{S} - \boldsymbol{V}\boldsymbol{V}^T\boldsymbol{S}\right\|_F}{\|\boldsymbol{S}\|_F} \tag{5.56}$$

are also depicted in Figure 5.10. Thereby, several ROBs are constructed from POD modes using a mode truncation as indicated by the threshold ratio ξ_{th}. As expected, the relative orthogonal projection error decreases monotonically.

5.3.2. Application to homeostatic state estimation

The exemplary computation in Section 5.1.2 presented a strategy for homeostatic state estimation. The strategy included repeated computation of cardiac cycles together with adjustment of initial conditions until fulfillment of the cycle error criterion (5.47), see Figure 5.7. In this section, computational speedup of homeostatic state calculation by application of a DHROM is demonstrated. Figure 5.11 depicts the proposed approach. Starting from the first guess of initial conditions, one single cardiac cycle on the FOM is evaluated. Data from this cardiac cycle can be used in a second step to build a DHROM (or a DROM, if hyper reduction is not implemented) and to update the initial conditions. Finally, iterations until convergence similar to the original flow chart in Figure 5.11 are performed on the DHROM.

In more detail, a snapshot matrix including prestressing load step 5 and 10 and each fifth displacement mode from deformation stage is built, such that the snapshot matrix in total contains 102 modes. Using a threshold ratio of $\xi_{\mathrm{th}} = 10^{-4}$ (see Section 5.2) returns 61 POD modes, which yield the ROB. The obtained ROB is used together with the snapshot matrix for ECSW hyper reduction. Thereby, mesh sampling is performed independently for internal force vector, ventricular pressure load vector and embedding tissue load vector, see governing equations (5.10) - (5.13) for prestressing stage and (5.16) - (5.19) for deformation stage. The domain decomposition strategy described in Section 3.2.2 is used for parallelization and mesh sampling is performed on 4 processors. Figure 5.12 depicts the reduced mesh. The internal force vector is assembled as element subset of the full mesh, the ventricular load force vector as element subset of the ventricular surface mesh and the embedding tissue force vector as element subset of epicardial, heart base and abluminal surface of the covering lids. As a result, 1010 volume elements (0.21% of the full mesh), 232 surface elements (1.18% of the full mesh) and 200 surface elements (0.65% of the full mesh) are selected for internal force, ventricular pressure load and embedding tissue force vector, respectively.

Figure A.6 depicts temporally resolved pressures, flow rates, ventricular volumes and ventricular pressure-volume curves for both FOM and DHROM simulations. Qualitative, good coincidence of reference FOM and DHROM curves can be seen. Most pronounced deviations arise in proximity to peaks of the flow rate curves. Table 5.7 quantifies DHROM quality in terms of the relative l2-error.

DHROM enhanced results as depicted in Figure A.6 (flow chart in Figure 5.11) are retrieved with a speedup factor of 4.05 compared to pure FOM results (flow chart in Figure 5.7). All simulations as well as ECSW sampling were executed on 4 cores (Intel Xeon W-2133 (3.60GHz)). Homeostasis for both FOM cycling and DHROM enhanced cycling is reached after 6 heart beats (for DHROM enhanced cycling, the initial FOM cycle is included in the 6 cycles). Note that the given statement on speedup in the current example does not compare a single FOM vs. DHROM simulation, instead the entire Algorithm in Figure 5.11 is compared with the Algorithm in Figure 5.7. Thereby, the initial FOM simulation in Figure 5.11 takes 66.2 % of the full simulation time until homeostasis.

5.3.3. Application to heart performance estimation

Referring to Section 1, heart failure is a life-threatening condition which should be diagnosed as early as possible. Thereby, several heart performance related parameters can be used as indicators

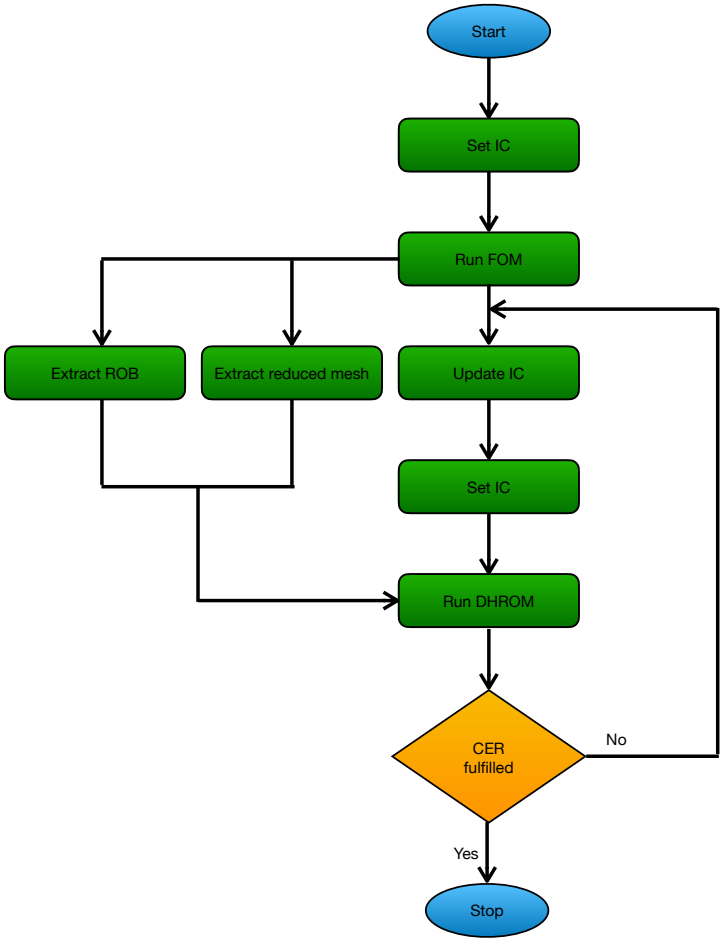

Figure 5.11.: Flow chart for homeostatic state computation of the beating heart including DHROM speedup. Abbreviations included are IC: initial condition, CER: cycle error criterion, FOM: full-order model, DHROM: dimensionally and hyper reduced-order model, ROB: reduced-order basis.

for heart failure. The ejection fraction

$$EF_{\mathrm{v}} = \frac{SV_{\mathrm{v}}}{EDV_{\mathrm{v}}} \tag{5.57}$$

relates ventricular stroke volume $SV_{\mathrm{v}} = EDV_{\mathrm{v}} - ESV_{\mathrm{v}}$ (with the end-diastolic volume EDV_{v} and the end-systolic volume ESV_{v}) to the end-diastolic volume EDV_{v}. Normal ranges for left ventricular ejection fraction have been reported as 0.52 - 0.72 (male) and 0.54 - 0.74 (female) [78].

A further heart performance estimator including ventricular pressure is the stroke work

$$SW_{\mathrm{v}} = \oint -p_{\mathrm{v}} dV_{\mathrm{v}}, \tag{5.58}$$

which is frequently approximated in literature by the relation $SW_{\mathrm{v}} = SV_{\mathrm{v}} \cdot \bar{p}$ with $\bar{p}$ as a pressure mean value (e.g. mean arterial pressure). This computational experiment demonstrates that the

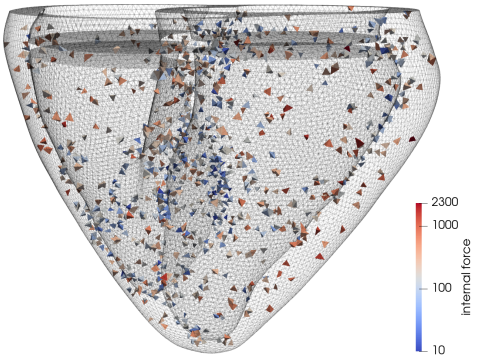

(a) Element weightings for assembly of internal force vector

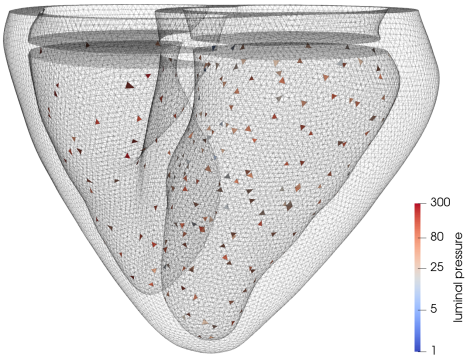

(b) Element weightings for assembly of ventricular pressure force

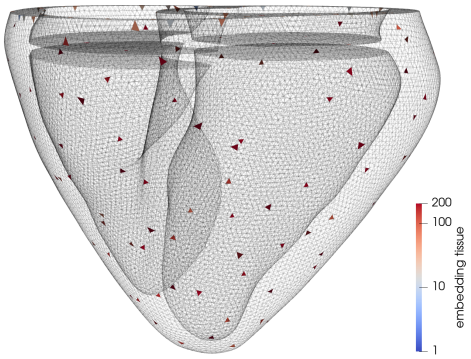

(c) Element weightings for assembly of embedding tissue force

Figure 5.12.: Reduced mesh for structural part of heart model. The reduced mesh consists of an element subset of the full computational mesh (internal force vector), an element subset of the luminal ventricular surface mesh (ventricular pressure force vector) and an element subset of the epicardial, heart base and covering lids surface (embedding tissue force vector). Only colored elements are evaluated during assembly of the individual residual contributions.

proposed DHROM is able to accurately estimate cardiac performance at various conditions of the beating heart. In more detail, the condition of mitral valve stenosis and aortic valve stenosis are examined at different states of afterload and contraction.

The mentioned conditions and states are generated by a model parameterization in terms of the contractility, opened mitral and opened aortic valve resistance as well as systemic arterial

Table 5.7.: Relative l2-errors of temporally resolved state variables and ventricular volumes for DHROM homeostatic state estimation.

quantity	relative l2-error	quantity	relative l2-error
p_{at}^{ℓ}	$9.86 \cdot 10^{-3}$	$q_{\mathrm{v,in}}^{\ell}$	$8.77 \cdot 10^{-2}$
p_{v}^{ℓ}	$1.08 \cdot 10^{-2}$	$q_{\mathrm{v,out}}^{\ell}$	$4.00 \cdot 10^{-2}$
$p_{\mathrm{ar}}^{\mathrm{sys}}$	$3.88 \cdot 10^{-3}$	$q_{\mathrm{ar}}^{\mathrm{sys}}$	$2.27 \cdot 10^{-3}$
$p_{\mathrm{ven}}^{\mathrm{sys}}$	$6.90 \cdot 10^{-4}$	$q_{\mathrm{ven}}^{\mathrm{sys}}$	$7.01 \cdot 10^{-3}$
p_{at}^{r}	$1.29 \cdot 10^{-2}$	$q_{\mathrm{v,in}}^{r}$	$6.80 \cdot 10^{-2}$
p_{v}^{r}	$1.22 \cdot 10^{-2}$	$q_{\mathrm{v,out}}^{r}$	$3.44 \cdot 10^{-2}$
$p_{\mathrm{ar}}^{\mathrm{pul}}$	$6.69 \cdot 10^{-3}$	$q_{\mathrm{ar}}^{\mathrm{pul}}$	$1.01 \cdot 10^{-2}$
$p_{\mathrm{ven}}^{\mathrm{pul}}$	$5.33 \cdot 10^{-3}$	$q_{\mathrm{ven}}^{\mathrm{pul}}$	$6.58 \cdot 10^{-3}$

quantity	relative l2-error
V_{v}^{ℓ}	$8.33 \cdot 10^{-3}$
V_{v}^{r}	$9.69 \cdot 10^{-3}$

resistance

$$\boldsymbol{\mu} = \begin{bmatrix} \sigma_0 \\ R_{\mathrm{v,in}}^{\ell,\min} \\ R_{\mathrm{v,out}}^{\ell,\min} \\ R_{\mathrm{sys}}^{\mathrm{ar}} \end{bmatrix} \tag{5.59}$$

with a parameter domain (cf. [57]) given by $\sigma_0 \in [30, 100]$, $R_{\mathrm{v,in}}^{\ell,\min} \in \{10^{-6}, 2.5 \cdot 10^{-6}\}$, $R_{\mathrm{v,out}}^{\ell,\min} \in \{10^{-6}, 5 \cdot 10^{-6}\}$ and $R_{\mathrm{sys}}^{\mathrm{ar}} \in [40 \cdot 10^{-6}, 220 \cdot 10^{-6}]$. Figure 5.13 exemplifies the simulated influence of the introduced parametrization on left ventricular pressure-volume relations with respect to a baseline state $\boldsymbol{\mu}_{\mathrm{base}} = [70\ \mathrm{kPa}, 10^{-6}, 10^{-6}, 120 \cdot 10^{-6}]$, each subfigure corresponds to a variation of one parameter. All subfigures show homeostatic states, which are retrieved by the Algorithm in Figure 5.7 for variation of σ_0 and $R_{\mathrm{sys}}^{\mathrm{ar}}$. Computation of homeostatic state in case of modified valve resistances $R_{\mathrm{v,in}}^{\ell,\min}$ and $R_{\mathrm{v,out}}^{\ell,\min}$ is computed by a transition from the baseline state. In more detail, the baseline homeostatic state is used as initial condition for the 0D circulation and ventricular prestressing pressure, while the transition to homeostasis with impaired valve resistance is computed without re-iterating the prestressing stage, see [57].

As depicted in Figure 5.13a, a change in contractility has significant influence on the stroke work as well as stroke volume, while the end-diastolic volume is approximately preserved. Figure 5.13b mimics conditions of mitral stenosis, wherein opening of the mitral valve is impaired. This complicates left ventricular filling and leads to an increased pressure gradient from left atrium to left ventricle. End-diastolic volume decreases and yields a lower stroke volume. Next, a condition of aortic valve stenosis is simulated by increased opened aortic valve resistance, which can be found in Figure 5.13c. In this case, opening of the aortic valve is impaired which leads to an increased pressure gradient from left ventricle to the aorta. As a result, the maximum ventricular pressure increases significantly. Finally, Figure 5.13d depicts the pressure-volume response for the variation of ventricular afterload, which is achieved by different values of the systemic arterial resistance. At high values of systemic arterial resistance, the aortic pressure is elevated, such that left ventricular pressure also has to increase in order to eject blood. Low sys-

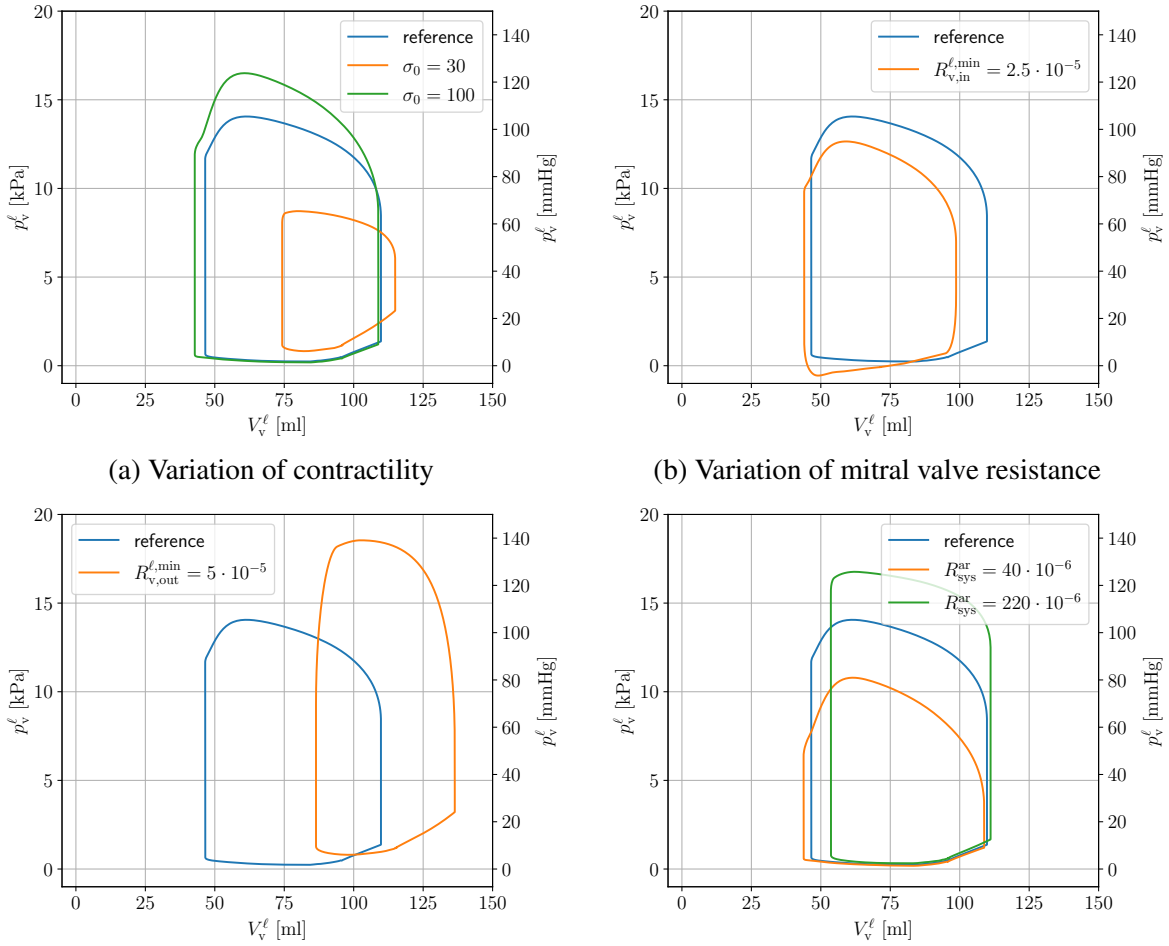

(a) Variation of contractility

(b) Variation of mitral valve resistance

(c) Variation of aortic valve resistance

(d) Variation of system arterial resistance

Figure 5.13.: Effects of parameter variations on left ventricular pressure-volume curves. The reference state is assumed with a contractility $\sigma_0 = 70\mathrm{kPa}$, resistance for opened mitral valve $R^{\ell,\min}_{\mathrm{v,in}} = 10^{-6}$, resistance for opened aortic valve $R^{\ell,\min}_{\mathrm{v,out}} = 10^{-6}$ and resistance of systemic arterial circulation $R^{\mathrm{sys}}_{\mathrm{ar}} = 120 \cdot 10^{-6}$. Each (non-reference) curve represents a deviation from the reference curve in one of the mentioned parameters.

temic arterial resistance yields lower left ventricular pressure during ejection. The stroke volume decreases at an approximately preserved end-diastolic volume.

A DHROM is constructed as follows. A training set of 36 FOM simulations is evaluated on all combinations of the parameters $\sigma_0 \in \{30, 65, 100\}$, $R^{\ell,\min}_{\mathrm{v,in}} \in \{10^{-6}, 2.5 \cdot 10^{-6}\}$, $R^{\ell,\min}_{\mathrm{v,out}} \in \{10^{-6}, 5 \cdot 10^{-6}\}$ and $R^{\mathrm{ar}}_{\mathrm{sys}} \in [40 \cdot 10^{-6}, 130 \cdot 10^{-6}, 220 \cdot 10^{-6}]$. As a result, parameter domain bounds as well as domain mid points of σ_0 and $R^{\mathrm{ar}}_{\mathrm{sys}}$ are sampled. Iterations to homeostatic conditions are stopped after 25 cycles or a cycle-error criterion (5.47) of $\mathcal{E}_{\mathrm{cycl}} = 0.05$.

Since heart performance at homeostasis is of interest, only simulation data of the last cycle is stored and processed. As described in Section 5.1.1, each model yields one prestress displacement field as well as 500 displacement fields from dynamic cycling. The ROB is sup-

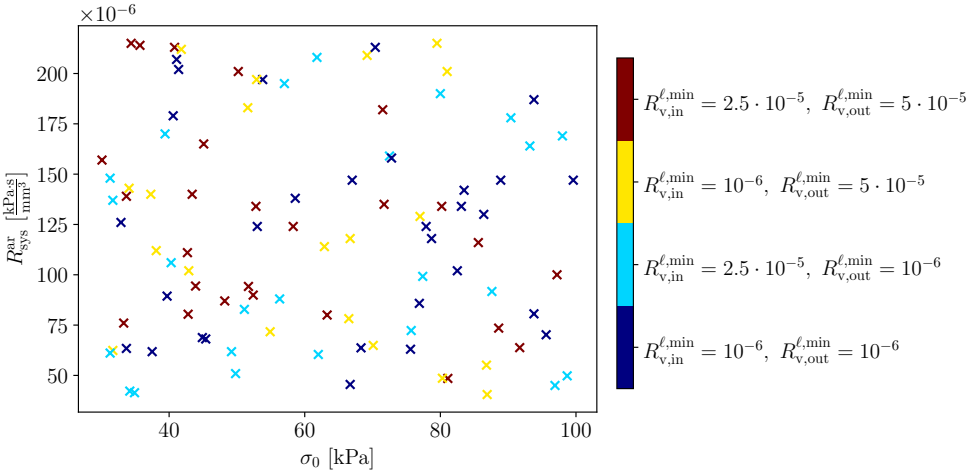

Figure 5.14.: Random grid with 100 points in the parameters $R_{\mathrm{sys}}^{\mathrm{ar}}$, σ_0, $R_{\mathrm{v,in}}^{\ell,\mathrm{min}}$ and $R_{\mathrm{v,out}}^{\ell,\mathrm{min}}$. The colors indicate all combinations of the discrete parameter values $R_{\mathrm{v,in}}^{\ell,\mathrm{min}}$ and $R_{\mathrm{v,out}}^{\ell,\mathrm{min}}$.

Table 5.9.: Relative l2-error for DHROM estimated heart performance quantities.

quantity	max. relative l2-error	mean relative l2-error
EF_{v}^{ℓ}	$1.18 \cdot 10^{-2}$	$0.22 \cdot 10^{-2}$
EF_{v}^{r}	$0.72 \cdot 10^{-2}$	$0.24 \cdot 10^{-2}$
SW_{v}^{ℓ}	$1.13 \cdot 10^{-2}$	$0.47 \cdot 10^{-2}$
SW_{v}^{r}	$2.46 \cdot 10^{-2}$	$0.72 \cdot 10^{-2}$

posed to span an accurate subspace for the system dynamics. Given that POD is applied for data-compression, a high sampling rate for displacement fields can be chosen (the initially chosen sampling rate for displacement modes does not directly determine the dimension of the ROM). A time interval of $0.01\mathrm{s}$ is chosen. This results in 100 deformation stage displacement modes per simulation. Together with one prestress displacement mode per simulation, in total $36 \cdot 101 = 3636$ displacement modes enter the snapshot matrix. Applying POD with a threshold ratio (5.55) of $\xi_{\mathrm{th}} = 10^{-3}$ results in a subspace of dimension 57 spanned by the columns of the ROB $\boldsymbol{V}$.

Additionally, ECSW requires a set of displacement modes for mesh sampling. In contrast to the snapshot matrix for ROB construction, ECSW displacement modes are used to reconstruct specific states of the nonlinear system and are not subject to a data-compression step, each mode directly enters into the optimization problem (3.43). A time interval of $0.05\mathrm{s}$ is chosen, which (together with the prestress displacement mode) results in $26 \cdot 36 = 936$ modes in total. ECSW sampling is performed in parallel on 16 cores with a global tolerance of $\varepsilon_h = 10^{-2}$ (see Algorithm 2) and results in a selection of 4075 elements (0.83% of the full mesh) for internal force assembly, 417 elements (2.11% of the full mesh) for ventricular pressure force assembly and 359 elements (1.16% of the full mesh) for embedding tissue force assembly. Both ROB as well as ECSW mesh yield the DHROM with nonlinear iterations as given in equation (5.54).

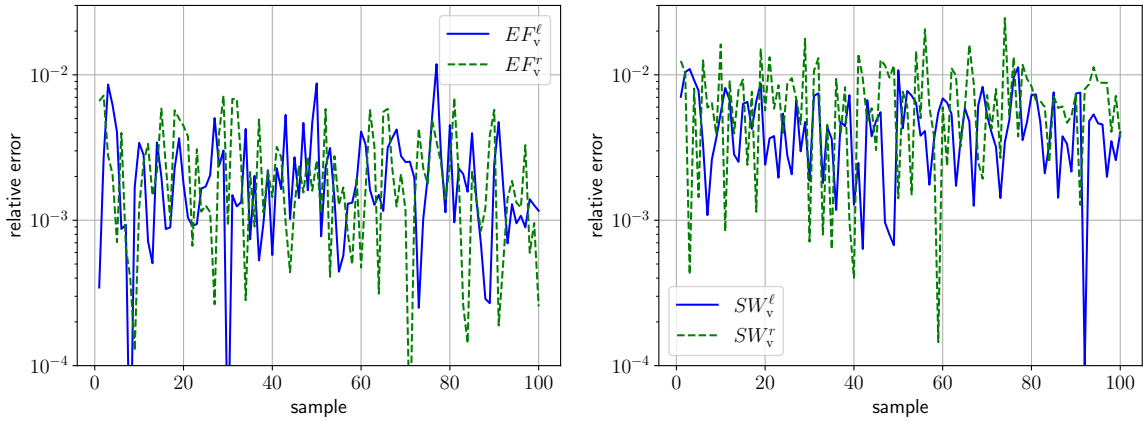

(a) Ejection fraction

(b) Stroke work

Figure 5.15.: Relative DHROM errors in heart performance assessed by ejection fraction and stroke work.

Accuracy of the DHROM is tested by 100 samples from a random grid (uniform probability distribution) in the parameter space. Figure 5.14 depicts the grid, recalling that valve diseases are either present or not (i.e. $R_{\mathrm{v,in}}^{\ell,\min}$ and $R_{\mathrm{v,out}}^{\ell,\min}$ each can take the "normal" or "diseased" value), while σ_0 and $R_{\mathrm{sys}}^{\mathrm{ar}}$ can take any value in the parameter domain. Relative errors in the ejection fraction as well as the stroke work are depicted in Figure 5.15. Most values are below 1%, Table 5.9 depicts maximum and mean relative l2-error for the quantities of interest.

For the assessment of computational speedup, the mean value of 7 simulations is taken at randomly selected points (uniform probability distribution) in the parameter domain. Thereby, one single cardiac cycle is taken into account. Table 5.10 depicts the selected points as well as the speedup. For comparison, also the speedup of DROMs is stated. The DROMs result from dimensional reduction without hyper reduction, the corresponding nonlinear iterations are given in equation (5.52). A mean speedup of 3.28 and 14.69 is measured for the DROM and DHROM, respectively.

Table 5.10.: Speedup for ROM and DHROM for one cardiac cycle at randomly selected samples.

sample				speedup	
σ_0 [kPa]	$R_{\mathrm{v,in}}^{\ell,\min}$	$R_{\mathrm{v,out}}^{\ell,\min}$	$R_{\mathrm{ar}}^{\mathrm{sys}}$	DROM	DHROM
93.95	$2.50 \cdot 10^{-5}$	$5.00 \cdot 10^{-5}$	$1.94 \cdot 10^{-4}$	3.18	14.36
91.88	$1.00 \cdot 10^{-6}$	$5.00 \cdot 10^{-5}$	$1.71 \cdot 10^{-4}$	3.20	14.26
87.01	$2.50 \cdot 10^{-5}$	$1.00 \cdot 10^{-6}$	$1.31 \cdot 10^{-4}$	3.39	15.10
61.10	$1.00 \cdot 10^{-6}$	$5.00 \cdot 10^{-5}$	$1.80 \cdot 10^{-4}$	3.27	14.63
98.89	$2.50 \cdot 10^{-5}$	$1.00 \cdot 10^{-6}$	$9.66 \cdot 10^{-5}$	3.41	15.20
59.16	$1.00 \cdot 10^{-6}$	$1.00 \cdot 10^{-6}$	$7.18 \cdot 10^{-5}$	3.28	14.77
53.40	$1.00 \cdot 10^{-6}$	$5.00 \cdot 10^{-5}$	$1.40 \cdot 10^{-4}$	3.24	14.49

5.3.4. Application to simulation of functional impairment by myocardial infarction

A *heart attack* is a medical emergency that mostly sets in as a consequence of sudden occlusion of a coronary artery. Coronary arteries supply the heart muscle with oxygenated blood, which is vitally important for functioning of myocardial tissue. If that supply is greatly restricted or even interrupted, tissue cells die in the affected region. This damage is called myocardial infarction. Exemplary risk factors for experiencing a heart attack are age, a lack of physical activity, hypertension, diabetes, obesity and smoking. The occlusion of a coronary artery itself is frequently initiated by atherosclerotic plaque [94].

Dead myocardial tissue following a heart attack becomes stiffer, impairs contraction as well as cardiac output and eventually leads to *growth and remodeling*, which is an adaption process of biological tissue in order to maintain blood circulation. Computational modeling of myocardial infarction faces high complexity due to phenomena such as border zone (i.e. the region between dead and healthy tissue) development, scar formation or the mentioned growth and remodeling and consequently is currently subject to research [84]. For simplicity, infarct tissue is modeled following the approach in [57] by assuming dead cells to loose the ability of active force generation. Consequently, infarct tissue resembles passive myocardial material.

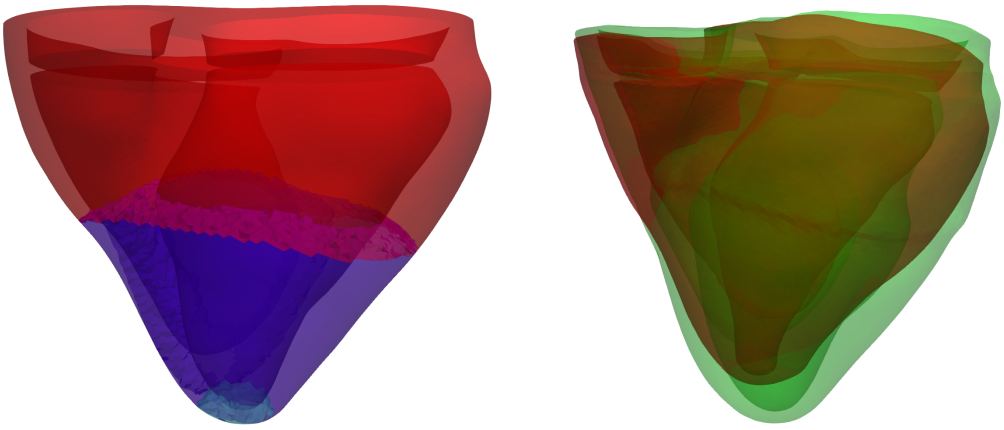

(a) Infarct tissue (b) Contracted state at $t = 0.54\text{s}$

Figure 5.16.: Subfigure (a): Visualization of infarct tissue. Cyan region (apex) and blue region correspond to 1cm and 6cm infarct radius, respectively. Healthy tissue is colored in red. Subfigure (b): Contracted state after ventricular ejection ($t = 0.54\text{s}$, see Section 5.1.2) during dynamic cycling for 1cm infarction (red) and 6cm infarction (light green).

The heart model under consideration is extended with myocardial infarction, Figure 5.16a depicts infarct tissue. In more detail, infarct cells are selected given a center point (located at the apex) and a radius r. If all nodes of a cell (i.e. a finite element) are located within a sphere with radius r, the cell is assumed as dead. The cyan and blue region correspond to infarct tissue in case of $r = 1\text{cm}$ and $r = 6\text{cm}$, respectively. Figure 5.16b depicts the contracted state after ventricular ejection for $r = 1\text{cm}$ (red) and $r = 6\text{cm}$ (light green). The contracted shapes differ significantly. The higher loss in contractility for $r = 6\text{cm}$ manifests in a “weaker” heart beat,

the apex lifts significantly less. Also in the region of the heart base a lower contraction can be identified.

In the focus of this computational experiment is the performance of a DHROM designed for approximating functional impairment by infarction assuming an infarction radius $r \in [1\text{cm}, 6\text{cm}]$. In more detail, the homeostatic state as computed in the example from Section 5.1.2 is used as starting point. Next, infarction is introduced by modifying material properties and the new homeostatic state is computed as a transition from the healthy homeostatic state (analogous to valve disease transition as described in Section 5.3.3). In the offline stage, five samples $r \in \{1\text{cm}, 2.25\text{cm}, 3.50\text{cm}, 4.75\text{cm}, 6\text{cm}\}$ are taken and (analogous to the computational experiment presented in Section 5.3.3) 100 deformation state displacement modes (sampling time interval of 0.01s) as well as one prestress displacement per simulation are organized in a snapshot matrix. Using POD with a threshold ratio of $\xi_{\text{th}} = 10^{-3}$, 49 modes are extracted as optimal low-dimensional subspace. For ECSW (analogous to the computational experiment presented in Section 5.3.3), 20 deformation stage displacement modes (sampling time interval of 0.05s) as well as one prestress displacement mode per simulation are extracted. Mesh sampling is performed on 4 cores with a global tolerance of $\varepsilon_h = 10^{-2}$. As a result, 1892 elements (0.39% of the full mesh) for internal force assembly, 236 elements (1.20% of the full mesh) for ventricular pressure force assembly and 218 elements (0.71% of the full mesh) for embedding tissue force assembly are extracted.

For assessment of DHROM accuracy, 25 equidistantly placed points are sampled in the parameter domain for both FOM and DHROM. The ventricular cardiac output

$$CO_{\text{v}}^i = SV_{\text{v}}^i \cdot \omega \quad \text{with } i \in \{\ell, r\} \tag{5.60}$$

is used as the quantity of interest, recalling that the reduced amount of contracting tissue reflects in this quantity. The symbol ω denotes the heart rate, i.e. the number of heart beats per second. In our case $\omega = 1\text{Hz}$, see Section 5.1.1.

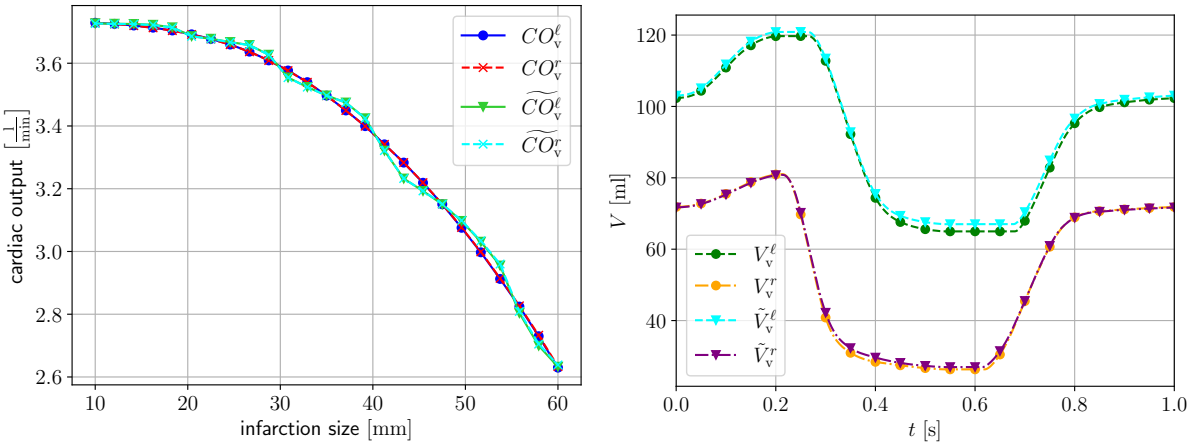

(a) Cardiac output

(b) Time resolved volumes at maximum error

Figure 5.17.: Sampled cardiac output and time resolved ventricular volumes for sample with maximum cardiac output error.

Table 5.11.: Speedup for DROM and DHROM for one cardiac cycle at randomly selected samples.

sample	speedup	
$r\,[\mathrm{cm}]$	DROM	DHROM
5.71	3.44	16.59
2.24	3.35	15.95
3.94	3.34	15.93
3.54	3.41	16.30
3.80	3.43	16.39
3.07	3.46	16.38
4.93	3.49	16.34

Figure 5.17 depicts the cardiac output over infarction size as well as relative DHROM errors (4.35). Starting discussion with FOM curves, the cardiac output decreases with increasing infarction size as expected. At the same time, left ventricular and right ventricular curves overlap, which can also be expected, given that left and right stroke volume match in case of homeostasis. The DHROM approximation resembles the FOM curve, a maximum relative error of 1.55% and 1.56% for the left and right ventricular cardiac output can be observed, respectively.

DROM and DHROM speedup is measured as the mean of 7 randomly selected samples (uniform probability distribution) for the infarct radius. Thereby, one cardiac cycle is evaluated, starting from the healthy homeostatic state as described above. Table 5.11 depicts the individual speedups and yields a mean speedup of 3.42 and 16.27 for the DROM and DHROM, respectively.

6. Summary and Outlook

The work presented in this thesis was motivated by medical applications of computational biomechanics models. Accurate results require fine spatial resolution, while at the same time a large number of model evaluations in a parameter space frequently results in a bottleneck regarding computing resources. To overcome this burden, methods for computationally inexpensive high-dimensional model approximations were in the focus of this thesis.

More specifically, the application, adaption and extension of projection-based model order reduction (MOR) techniques to large computational models of the cardiovascular system, in particular that of the abdominal aortic aneurysm and of cardiac mechanics, has been presented. The patient-specific abdominal aortic aneurysm (AAA) model consisted of an imaged aortic segment fully including the aneurysm as well as a non-dilated part at the proximal and the aortic bifurcation at the distal ending. The intraluminal thrombus (ILT) and the aortic wall were both modeled including individual constitutive behavior and blood load was applied as hydrostatic pressure on the luminal surface of the ILT, wherein the mechanical state of interest corresponded to a systolic blood pressure load. The cardiac mechanics model consisted of a 3D resolved biventricular structure and a 0D (i.e. no resolution of geometry) model for blood flow in the systemic and pulmonary vascular system represented by a set of ordinary differential equations. The biventricular structure was two-way coupled to the vascular system and the arising equations were monolithically solved using consistent linearization. Pumping of the heart was triggered by the active stress component of the applied material model, wherein a contracting force was generated in direction of fibers placed in the reference configuration.

With prestressing (i.e. introduction of a stress state into a structure without deforming it) as a relevant part for computational modeling in biomechanics, a consistent inclusion of a modified updated Lagrangian formulation prestressing stage into projection-based MOR was presented. Aiming at accurate reduced-order models (ROMs) in patient-specific parameter domains, a greedy maximin distance design (GMmD) and a termination criterion based on subspace angles for reduced-order basis construction was introduced. The effect of altering a perfectly tailored subspace by increasing inclination has been discussed and investigated by computational experiments in case of AAAs. The proposed GMmD has been applied to three patient-specific AAA computational models achieving similar results in terms of dimensionality reduction. The energy-conserving mesh sampling and weighting method has been applied for hyper reduction, which has been used on system components requiring re-assembly during Newton-Raphson iterations (i.e. internal force, luminal pressure force, embedding tissue force). The hyper reduced monolithic block system model for cardiac mechanics has been stated, wherein model reduction has been applied to the 3D structure exclusively. Dimensional reducibility has been demonstrated regarding singular values of heart beat deformation modes. The performance of several ROMs has been investigated for homeostatic state estimation and impaired cardiac functionality in terms of different states of contractility, afterload, valve diseases and myocardial infarction.

Future investigations on projection-based MOR and hyper reduction of cardiovascular system models could include more detailed patient-specific models. For the AAA, examples are the incorporation of calcification or the distinction between “healthy” and “diseased” aortic wall in terms of constitutive behavior. Likewise, the active stress generation of the presented cardiac mechanics model was strongly simplified using an ordinary differential equation. Here, coupling of the mechanical contraction to a spatially resolved propagation of the action potential would better represent physiology. Another important extension would be cross-patient model reduction, that has the ability to determine low-dimensional subspaces and hyper reduction components while working simultaneously on different geometries. One decisive challenge here is that finite element simulations rely on computational meshes, which would have to be related across patients.

A. Appendix

A.1. ECSW meshes of AAA models

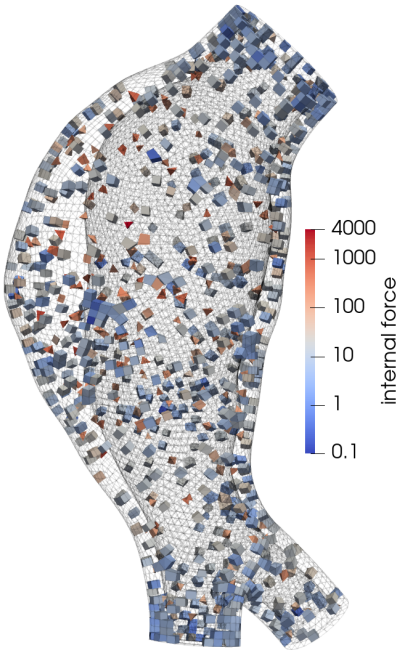

(a) Patient 1: element weightings for assembly of internal force vector

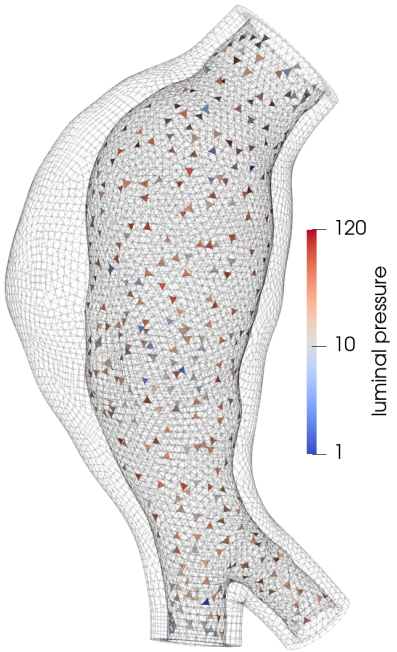

(b) Patient 1: element weightings for assembly of luminal pressure force

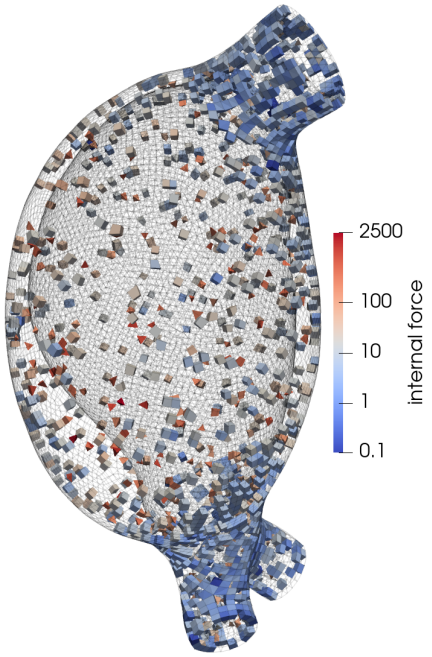

(a) Patient 2: element weightings for assembly of internal force vector

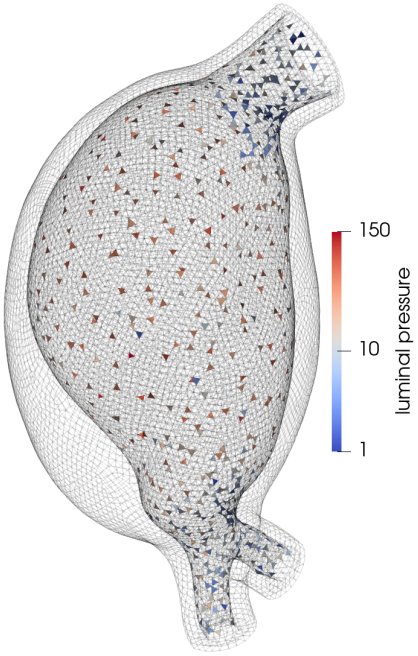

(b) Patient 2: element weightings for assembly of luminal pressure force

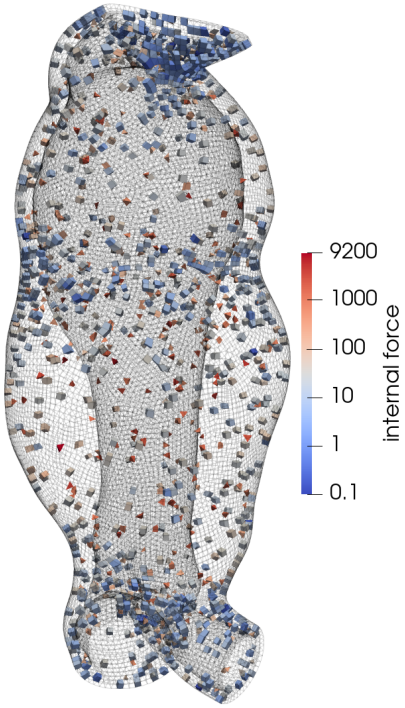

(c) Patient 3: element weightings for assembly of internal force vector

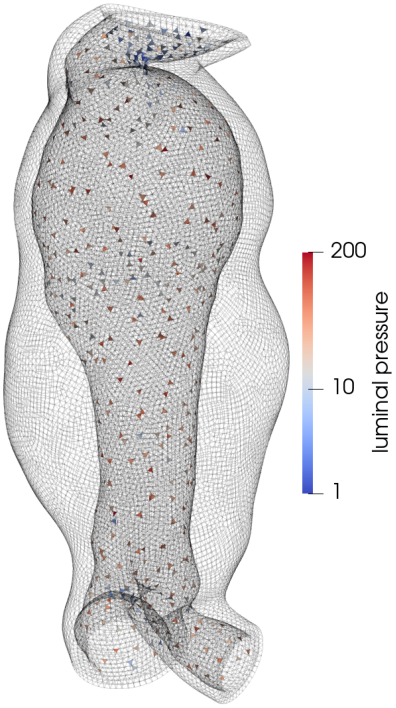

(d) Patient 3: element weightings for assembly of luminal pressure force

Figure A.2.: Reduced mesh for patient-specific AAA models. Only colored elements are evaluated during assembly of the nonlinear force contributions. Left column depicts the subset of mesh elements for assembly of internal force, right column for assembly of luminal pressure force.

A.2. Relative DROM errors of AAA models

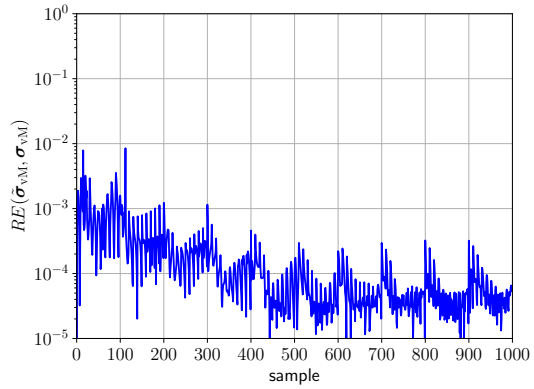

(a) Patient 1: von Mises stress field relative error

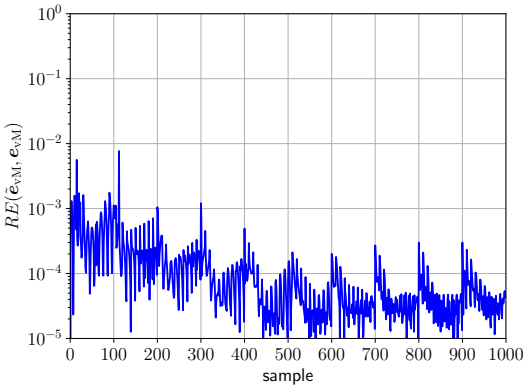

(b) Patient 1: von Mises strain field relative error

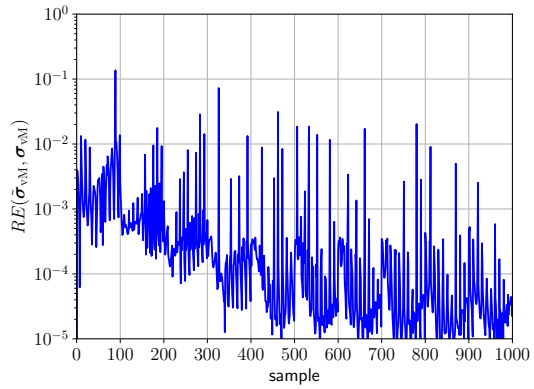

(c) Patient 2: von Mises stress field relative error

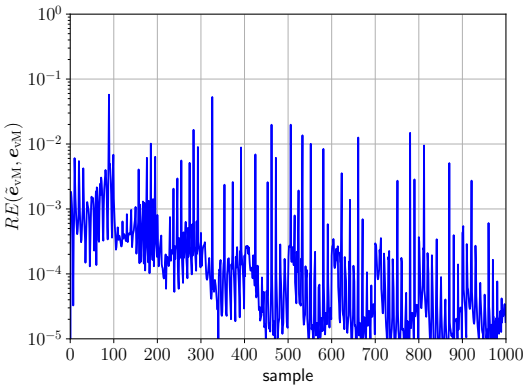

(d) Patient 2: von Mises strain field relative error

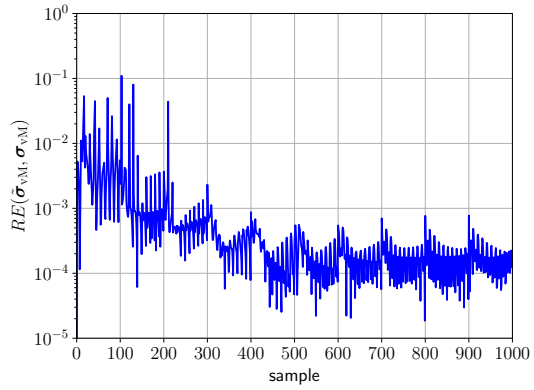

(e) Patient 3: von Mises stress field relative error

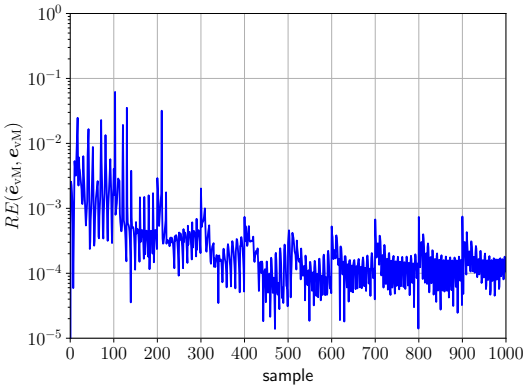

(f) Patient 3: von Mises strain field relative error

Figure A.3.: Relative DROM errors for von Mises stress and von Mises strain fields in the AAA wall. The test grid results from a full factorial design of 1000 points in the parameter domain. Most samples ($> 98\%$) have a relative error below 1%.

A.3. Relative DHROM errors of AAA models

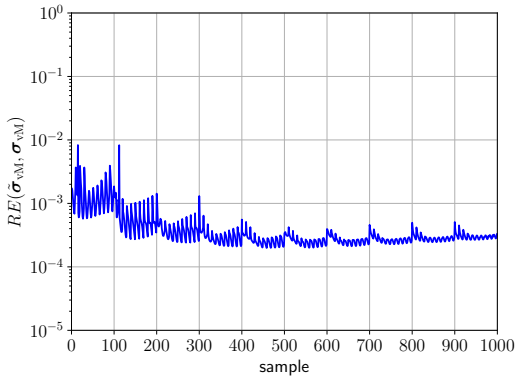

(a) Patient 1: von Mises stress field relative error

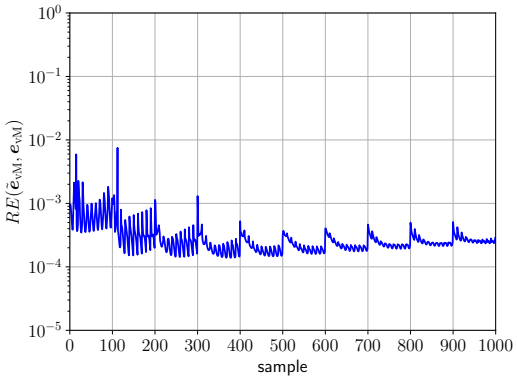

(b) Patient 1: von Mises strain field relative error

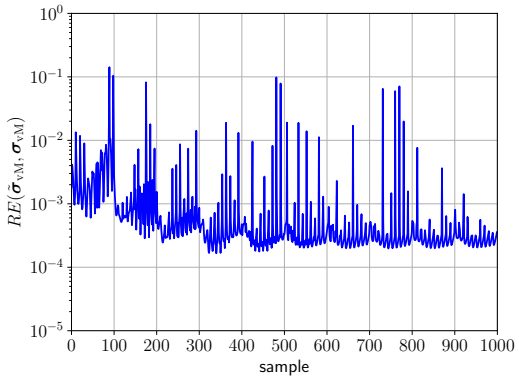

(c) Patient 2: von Mises stress field relative error

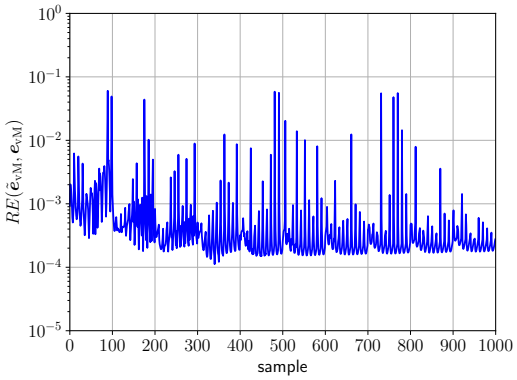

(d) Patient 2: von Mises strain field relative error

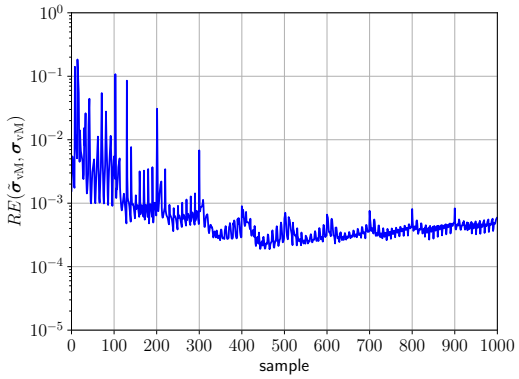

(e) Patient 3: von Mises stress field relative error

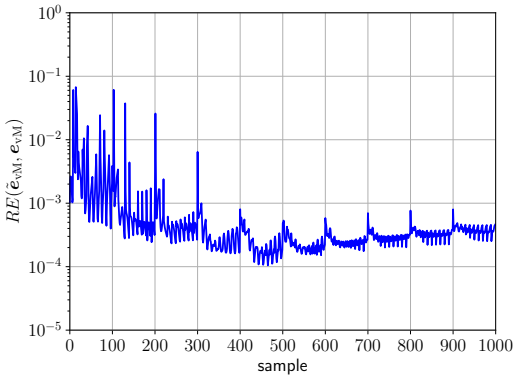

(f) Patient 3: von Mises strain field relative error

Figure A.4.: Relative DHROM errors for von Mises stress and von Mises strain fields in the AAA wall. The test grid results from a full factorial design of 1000 points in the parameter domain. Most samples ($> 97\%$) have a relative error below 1%.

A.4. Probability distribution approximation of AAA models

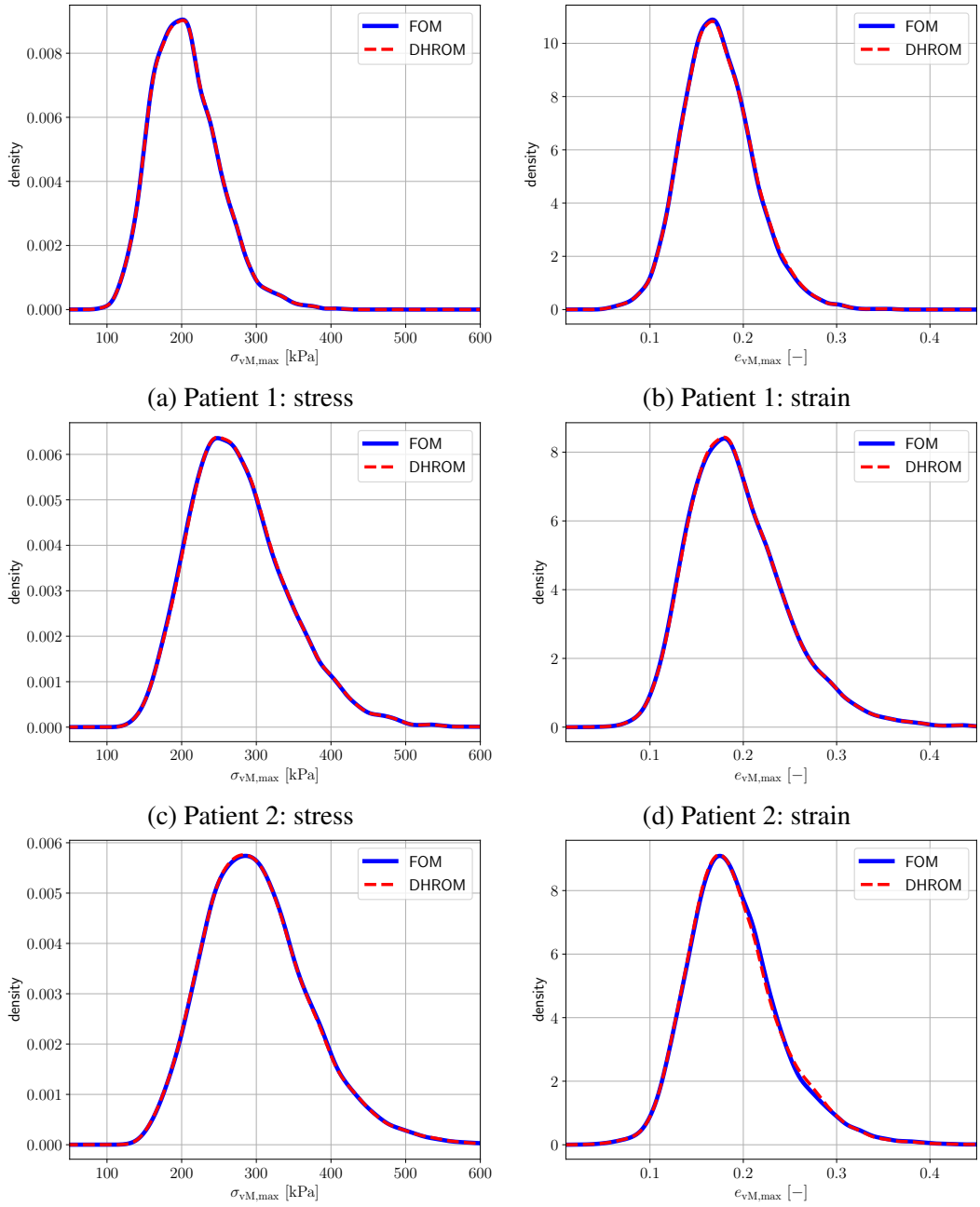

(a) Patient 1: stress

(b) Patient 1: strain

(c) Patient 2: stress

(d) Patient 2: strain

(e) Patient 3: stress

(f) Patient 3: strain

Figure A.5.: Maximum von Mises stress and maximum von Mises strain probability distributions from kernel-density-estimation (Gaussian kernel). 10^4 identical (per patient) samples have been evaluated for both FOM (reference solution) and DHROM (approximated solution). See Table 4.7 for quantitative data on the probability distributions.

A.5. DHROM approximation of cardiac homeostasis

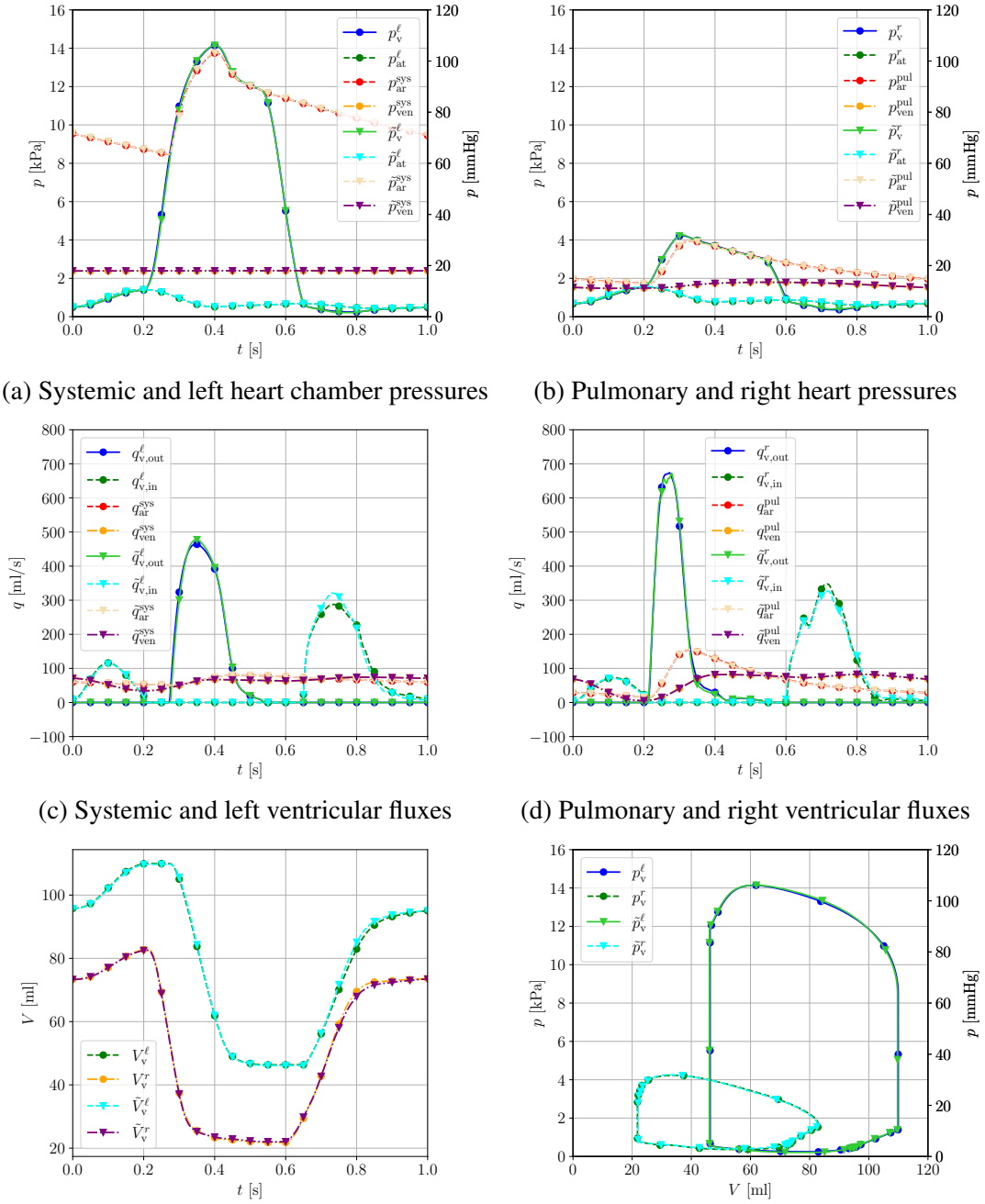

(a) Systemic and left heart chamber pressures

(b) Pulmonary and right heart pressures

(c) Systemic and left ventricular fluxes

(d) Pulmonary and right ventricular fluxes

(e) Ventricular volume curves

(f) Ventricular pressure-volumes

Figure A.6.: Temporally resolved state variables and ventricular volumes for FOM and DHROM homeostatic state. Most pronounced deviations arise in proximity to peaks of flow rates.

Bibliography

[1] Blausen.com staff (2014). "Medical gallery of Blausen Medical 2014". WikiJournal of Medicine 1 (2). DOI:10.15347/wjm/2014.010. ISSN 2002-4436.

[2] T. Akman, Local improvements to reduced-order approximations of optimal control problems governed by diffusion–convection–reaction equation, *Computers & Mathematics with Applications* **70**, 104–131, 2015.

[3] T. Arts, R. S. Reneman, and P. C. Veenstra, A model of the mechanics of the left ventricle, *Annals of biomedical engineering* **7**, 299–318, 1979.

[4] D. Azar, D. Ohadi, A. Rachev, J. F. Eberth, M. J. Uline, and T. Shazly, Mechanical and geometrical determinants of wall stress in abdominal aortic aneurysms: A computational study, *PLoS One* **13**, e0192032, 2018.

[5] Z. Bai, Krylov subspace techniques for reduced-order modeling of large-scale dynamical systems, *Applied numerical mathematics* **43**, 9–44, 2002.

[6] M. Barrault, Y. Maday, N. C. Nguyen, and A. T. Patera, An 'empirical interpolation'method: application to efficient reduced-basis discretization of partial differential equations, *Comptes Rendus Mathematique* **339**, 667–672, 2004.

[7] M. A. Bazaz, S. Nahve, M. Nabi, S. Janardhanan, and M. Rehman, Adaptive parameter space sampling in matrix interpolatory pmor, In *2015 International Conference on Recent Developments in Control, Automation and Power Engineering (RDCAPE)*, pages 83–89. IEEE, 2015.

[8] J. G. Betts, K. A. Young, J. A. Wise, E. Johnson, B. Poe, D. H. Kruse, O. Korol, J. E. Johnson, M. Womble, and P. DeSaix, *Anatomy and physiology*, 2013.

[9] J. Biehler and W. Wall, The impact of personalized probabilistic wall thickness models on peak wall stress in abdominal aortic aneurysms, *International journal for numerical methods in biomedical engineering* **34**, e2922, 2018.

[10] J. Biehler, M. W. Gee, and W. A. Wall, Towards efficient uncertainty quantification in complex and large-scale biomechanical problems based on a bayesian multi-fidelity scheme, *Biomechanics and modeling in mechanobiology* **14**, 489–513, 2015.

[11] J. Biehler, S. Kehl, M. W. Gee, F. Schmies, J. Pelisek, A. Maier, C. Reeps, H.-H. Eckstein, and W. A. Wall, Probabilistic noninvasive prediction of wall properties of abdominal aortic aneurysms using bayesian regression, *Biomechanics and modeling in mechanobiology* **16**, 45–61, 2017.

[12] D. BONOMI, *Reduced order models for the parametrized cardiac electromechanical problem*, PhD thesis, Italy, 2017.

[13] D. Bonomi, A. Manzoni, and A. Quarteroni, A matrix deim technique for model reduction of nonlinear parametrized problems in cardiac mechanics, *Computer Methods in Applied Mechanics and Engineering* **324**, 300–326, 2017.

[14] L. Bruder, J. Pelisek, H.-H. Eckstein, and M. W. Gee, Biomechanical rupture risk assessment of abdominal aortic aneurysms using clinical data: A patient-specific, probabilistic framework and comparative case-control study, *PloS one* **15**, e0242097, 2020.

[15] X. Cai, H. Qiu, L. Gao, L. Wei, and X. Shao, Adaptive radial-basis-function-based multifidelity metamodeling for expensive black-box problems, *AIAA Journal*, 2424–2436, 2017.

[16] K. Carlberg, C. Bou-Mosleh, and C. Farhat, Efficient non-linear model reduction via a least-squares petrov–galerkin projection and compressive tensor approximations, *International Journal for numerical methods in engineering* **86**, 155–181, 2011.

[17] K. Carlberg, C. Farhat, J. Cortial, and D. Amsallem, The gnat method for nonlinear model reduction: effective implementation and application to computational fluid dynamics and turbulent flows, *Journal of Computational Physics* **242**, 623–647, 2013.

[18] K. Carlberg, M. Barone, and H. Antil, Galerkin v. least-squares petrov–galerkin projection in nonlinear model reduction, *Journal of Computational Physics* **330**, 693–734, 2017.

[19] E. L. Chaikof, R. L. Dalman, M. K. Eskandari, B. M. Jackson, W. A. Lee, M. A. Mansour, T. M. Mastracci, M. Mell, M. H. Murad, L. L. Nguyen, et al., The society for vascular surgery practice guidelines on the care of patients with an abdominal aortic aneurysm, *Journal of vascular surgery* **67**, 2–77, 2018.

[20] G. H. Chang, C. M. Schirmer, and Y. Modarres-Sadeghi, A reduced-order model for wall shear stress in abdominal aortic aneurysms by proper orthogonal decomposition, *Journal of biomechanics* **54**, 33–43, 2017.

[21] S. Chaturantabut and D. C. Sorensen, Nonlinear model reduction via discrete empirical interpolation, *SIAM Journal on Scientific Computing* **32**, 2737–2764, 2010.

[22] J. Chung and G. Hulbert, A time integration algorithm for structural dynamics with improved numerical dissipation: the generalized-α method, *Journal of Applied Mechanics*, 1993.

[23] L. Cicci, S. Fresca, S. Pagani, A. Manzoni, and A. Quarteroni, Projection-based reduced order models for parameterized nonlinear time-dependent problems arising in cardiac mechanics, Technical report, tech. rep., 2021. submitted. MOX Report, 2021.

[24] L. Cicci, S. Fresca, A. Manzoni, and A. Quarteroni, Efficient approximation of cardiac mechanics through reduced order modeling with deep learning-based operator approximation, *arXiv preprint arXiv:2202.03904*, 2022.

[25] B. D. Coleman and W. Noll, The thermodynamics of elastic materials with heat conduction and viscosity, In *The foundations of mechanics and thermodynamics*, pages 145–156, Springer, 1974.

[26] D. R. Cox and N. Reid, *The theory of the design of experiments*, CRC Press, 2000.

[27] Creative Commons. Online resource on license CC BY 3.0, Access date: 2022-05-31. URL https://creativecommons.org/licenses/by/3.0/.

[28] Creative Commons. Online resource on license CC BY 4.0, Access date: 2022-05-31. URL https://creativecommons.org/licenses/by/4.0/.

[29] K. Crombecq, E. Laermans, and T. Dhaene, Efficient space-filling and non-collapsing sequential design strategies for simulation-based modeling, *European Journal of Operational Research* **214**, 683–696, 2011.

[30] A. Crozier, B. Blazevic, P. Lamata, G. Plank, M. Ginks, S. Duckett, M. Sohal, A. Shetty, C. A. Rinaldi, R. Razavi, et al., The relative role of patient physiology and device optimisation in cardiac resynchronisation therapy: a computational modelling study, *Journal of Molecular and Cellular Cardiology* **96**, 93–100, 2016.

[31] T. A. Davis, Algorithm 832: Umfpack v4. 3—an unsymmetric-pattern multifrontal method, *ACM Transactions on Mathematical Software (TOMS)* **30**, 196–199, 2004.

[32] D. Daye and T. G. Walker, Complications of endovascular aneurysm repair of the thoracic and abdominal aorta: evaluation and management, *Cardiovascular diagnosis and therapy* **8**, S138, 2018.

[33] S. De Putter, B. Wolters, M. Rutten, M. Breeuwer, F. Gerritsen, and F. Van de Vosse, Patient-specific initial wall stress in abdominal aortic aneurysms with a backward incremental method, *Journal of biomechanics* **40**, 1081–1090, 2007.

[34] E. de Souza Neto, D. Perić, M. Dutko, and D. Owen, Design of simple low order finite elements for large strain analysis of nearly incompressible solids, *International Journal of Solids and Structures* **33**, 3277–3296, 1996.

[35] B. J. Doyle, A. Callanan, and T. M. McGloughlin, A comparison of modelling techniques for computing wall stress in abdominal aortic aneurysms, *Biomedical engineering online* **6**, 1–12, 2007.

[36] H.-H. Eckstein, D. Böckler, I. Flessenkämper, T. Schmitz-Rixen, S. Debus, and W. Lang, Ultrasonographic screening for the detection of abdominal aortic aneurysms, *Deutsches Ärzteblatt International* **106**, 657, 2009.

[37] H. Elman, V. E. Howle, J. Shadid, R. Shuttleworth, and R. Tuminaro, A taxonomy and comparison of parallel block multi-level preconditioners for the incompressible navier–stokes equations, *Journal of Computational Physics* **227**, 1790–1808, 2008.

[38] A. C. Estrada, K. Yoshida, J. J. Saucerman, and J. W. Holmes, A multiscale model of cardiac concentric hypertrophy incorporating both mechanical and hormonal drivers of growth, *Biomechanics and Modeling in Mechanobiology* **20**, 293–307, 2021.

[39] R. Everson and L. Sirovich, Karhunen–loeve procedure for gappy data, *JOSA A* **12**, 1657–1664, 1995.

[40] C. Farhat, P. Avery, T. Chapman, and J. Cortial, Dimensional reduction of nonlinear finite element dynamic models with finite rotations and energy-based mesh sampling and weighting for computational efficiency, *International Journal for Numerical Methods in Engineering* **98**, 625–662, 2014.

[41] C. Farhat, T. Chapman, and P. Avery, Structure-preserving, stability, and accuracy properties of the energy-conserving sampling and weighting method for the hyper reduction of nonlinear finite element dynamic models, *International Journal for Numerical Methods in Engineering* **102**, 1077–1110, 2015.

[42] M. F. Fillinger, M. L. Raghavan, S. P. Marra, J. L. Cronenwett, and F. E. Kennedy, In vivo analysis of mechanical wall stress and abdominal aortic aneurysm rupture risk, *Journal of vascular surgery* **36**, 589–597, 2002.

[43] K. R. Fowler and C. T. Kelley, Pseudo-transient continuation for nonsmooth nonlinear equations, *SIAM journal on numerical analysis* **43**, 1385–1406, 2005.

[44] S. S. Garud, I. A. Karimi, and M. Kraft, Design of computer experiments: A review, *Computers & Chemical Engineering* **106**, 71–95, 2017.

[45] T. C. Gasser, G. Görgülü, M. Folkesson, and J. Swedenborg, Failure properties of intraluminal thrombus in abdominal aortic aneurysm under static and pulsating mechanical loads, *Journal of vascular surgery* **48**, 179–188, 2008.

[46] M. W. Gee, C. Förster, and W. Wall, A computational strategy for prestressing patient-specific biomechanical problems under finite deformation, *International Journal for Numerical Methods in Biomedical Engineering* **26**, 52–72, 2010.

[47] M. Gee, C. Reeps, H. Eckstein, and W. Wall, Prestressing in finite deformation abdominal aortic aneurysm simulation, *Journal of biomechanics* **42**, 1732–1739, 2009.

[48] G. H. Golub and C. F. Van Loan, *Matrix computations*, Johns Hopkins University Press, 3 Edition, 1996.

[49] A. Groenewegen, F. H. Rutten, A. Mosterd, and A. W. Hoes, Epidemiology of heart failure, *European journal of heart failure* **22**, 1342–1356, 2020.

[50] J. M. Guccione, A. D. McCulloch, and L. Waldman, Passive material properties of intact ventricular myocardium determined from a cylindrical model, *Journal of Biomedical Engineering*, 1991.

[51] C. R. Harris, K. J. Millman, S. J. van der Walt, R. Gommers, P. Virtanen, D. Cournapeau, E. Wieser, J. Taylor, S. Berg, N. J. Smith, R. Kern, M. Picus, S. Hoyer, M. H. van Kerkwijk, M. Brett, A. Haldane, J. F. del Río, M. Wiebe, P. Peterson, P. Gérard-Marchant, K. Sheppard, T. Reddy, W. Weckesser, H. Abbasi, C. Gohlke, and T. E. Oliphant, Array programming with NumPy, *Nature* **585**, 357–362, 2020.

[52] A. Hemmler, B. Lutz, G. Kalender, C. Reeps, and M. W. Gee, Patient-specific in silico endovascular repair of abdominal aortic aneurysms: application and validation, *Biomechanics and modeling in mechanobiology* **18**, 983–1004, 2019.

[53] A. Hemmler, A. Lin, N. Thierfelder, T. Franz, M. W. Gee, and D. Bezuidenhout, Customized stent-grafts for endovascular aneurysm repair with challenging necks: A numerical proof of concept, *International journal for numerical methods in biomedical engineering* **36**, e3316, 2020.

[54] J. A. Hernandez, M. A. Caicedo, and A. Ferrer, Dimensional hyper-reduction of nonlinear finite element models via empirical cubature, *Computer methods in applied mechanics and engineering* **313**, 687–722, 2017.

[55] M. A. Heroux and J. M. Willenbring, Trilinos users guide, Technical report, Sandia National Laboratories, 2003.

[56] A. V. Hill, The heat of shortening and the dynamic constants of muscle, *Proceedings of the Royal Society of London. Series B-Biological Sciences* **126**, 136–195, 1938.

[57] M. Hirschvogel, *Computational modeling of patient-specific cardiac mechanics with model reduction-based parameter estimation and applications to novel heart assist technologies*, PhD thesis, Technische Universität München, 2018.

[58] M. Hirschvogel, M. Bassilious, L. Jagschies, S. M. Wildhirt, and M. W. Gee, A monolithic 3d-0d coupled closed-loop model of the heart and the vascular system: experiment-based parameter estimation for patient-specific cardiac mechanics, *International journal for numerical methods in biomedical engineering* **33**, e2842, 2017.

[59] M. Hirschvogel, L. Jagschies, A. Maier, S. M. Wildhirt, and M. W. Gee, An in silico twin for epicardial augmentation of the failing heart, *International journal for numerical methods in biomedical engineering* **35**, e3233, 2019.

[60] G. A. Holzapfel, *Nonlinear solid mechanics - A continuum approach for engineering*, John Wiley & Sons, LTD, 2000.

[61] G. A. Holzapfel and R. W. Ogden, Constitutive modelling of passive myocardium: a structurally based framework for material characterization, *Philosophical Transactions of the Royal Society A: Mathematical, Physical and Engineering Sciences* **367**, 3445–3475, 2009.

[62] T. J. Hughes, *The finite element method: linear static and dynamic finite element analysis*, Courier Corporation, 2012.

[63] J. Jiang and Y. Chen, Adaptive greedy algorithms based on parameter-domain decomposition and reconstruction for the reduced basis method, *International Journal for Numerical Methods in Engineering* **121**, 5426–5445, 2020.

[64] M. E. Johnson, L. M. Moore, and D. Ylvisaker, Minimax and maximin distance designs, *Journal of statistical planning and inference* **26**, 131–148, 1990.

[65] N. R. Jones, A. K. Roalfe, I. Adoki, F. R. Hobbs, and C. J. Taylor, Survival of patients with chronic heart failure in the community: a systematic review and meta-analysis, *European journal of heart failure* **21**, 1306–1325, 2019.

[66] S. Kalra and M. Nabi, Tpwl simulation of large nonlinear circuits using subspace angle based adaptive sampling, *IEEE Transactions on Circuits and Systems II: Express Briefs* **67**, 575–579, 2019.

[67] K. C. Kent, R. M. Zwolak, N. N. Egorova, T. S. Riles, A. Manganaro, A. J. Moskowitz, A. C. Gelijns, and G. Greco, Analysis of risk factors for abdominal aortic aneurysm in a cohort of more than 3 million individuals, *Journal of vascular surgery* **52**, 539–548, 2010.

[68] R. C. Kerckhoffs, Computational modeling of cardiac growth in the post-natal rat with a strain-based growth law, *Journal of biomechanics* **45**, 865–871, 2012.

[69] R. C. Kerckhoffs, O. P. Faris, P. H. Bovendeerd, F. W. Prinzen, K. Smits, E. R. McVEIGH, and T. Arts, Timing of depolarization and contraction in the paced canine left ventricle: model and experiment, *Journal of Cardiovascular Electrophysiology* **14**, S188–S195, 2003.

[70] R. C. Kerckhoffs, M. L. Neal, Q. Gu, J. B. Bassingthwaighte, J. H. Omens, and A. D. McCulloch, Coupling of a 3d finite element model of cardiac ventricular mechanics to lumped systems models of the systemic and pulmonic circulation, *Annals of biomedical engineering* **35**, 1–18, 2007.

[71] W. Kieffer, S. Sonnenberg, R. Windhaber, N. Pal, and R. Pemberton, Complications and reintervention following elective open abdominal aortic aneurysm repair: a 10-year retrospective analysis, *The Annals of The Royal College of Surgeons of England* **94**, 177–180, 2012.

[72] R. Klabunde, *Cardiovascular physiology concepts*, Lippincott Williams & Wilkins, 2011.

[73] L. Koller, W. Witteveen, F. Pichler, and P. Fischer, Semihyper-reduction for finite element structures with nonlinear surface loads on the basis of stress modes, *Journal of Computational and Nonlinear Dynamics* **15**, 2020.

[74] L. Koller, W. Witteveen, F. Pichler, and P. Fischer, A general hyper-reduction strategy for finite element structures with nonlinear surface loads based on the calculus of variations and stress modes, *Computer Methods in Applied Mechanics and Engineering* **379**, 113744, 2021.

[75] W. Kroon, T. Delhaas, T. Arts, and P. Bovendeerd, Computational modeling of volumetric soft tissue growth: application to the cardiac left ventricle, *Biomechanics and modeling in mechanobiology* **8**, 301–309, 2009.

[76] P. Krysl, S. Lall, and J. E. Marsden, Dimensional model reduction in non-linear finite element dynamics of solids and structures, *International Journal for numerical methods in engineering* **51**, 479–504, 2001.

[77] A. Kühnl, A. Erk, M. Trenner, M. Salvermoser, V. Schmid, and H.-H. Eckstein, Incidence, treatment and mortality in patients with abdominal aortic aneurysms: An analysis of hospital discharge data from 2005–2014, *Deutsches Ärzteblatt International* **114**, 391, 2017.

[78] R. M. Lang, L. P. Badano, V. Mor-Avi, J. Afilalo, A. Armstrong, L. Ernande, F. A. Flachskampf, E. Foster, S. A. Goldstein, T. Kuznetsova, et al., Recommendations for cardiac chamber quantification by echocardiography in adults: an update from the american society of echocardiography and the european association of cardiovascular imaging, *European Heart Journal-Cardiovascular Imaging* **16**, 233–271, 2015.

[79] T. Lassila, A. Manzoni, A. Quarteroni, and G. Rozza, Generalized reduced basis methods and n-width estimates for the approximation of the solution manifold of parametric pdes, In *Analysis and numerics of partial differential equations*, pages 307–329, Springer, 2013.

[80] C. L. Lawson and R. J. Hanson, *Solving least squares problems*, SIAM, 1995.

[81] J. R. Leach, E. Kao, C. Zhu, D. Saloner, and M. D. Hope, On the relative impact of intraluminal thrombus heterogeneity on abdominal aortic aneurysm mechanics, *Journal of Biomechanical Engineering* **141**, 2019.

[82] L. C. Lee, L. Ge, Z. Zhang, M. Pease, S. D. Nikolic, R. Mishra, M. B. Ratcliffe, and J. M. Guccione, Patient-specific finite element modeling of the cardiokinetix parachute® device: effects on left ventricular wall stress and function, *Medical & biological engineering & computing* **52**, 557–566, 2014.

[83] J. H. Leung, A. R. Wright, N. Cheshire, J. Crane, S. A. Thom, A. D. Hughes, and Y. Xu, Fluid structure interaction of patient specific abdominal aortic aneurysms: a comparison with solid stress models, *Biomedical engineering online* **5**, 1–15, 2006.

[84] W. Li, Biomechanics of infarcted left ventricle: a review of modelling, *Biomedical Engineering Letters* **10**, 387–417, 2020.

[85] T. Lieu and C. Farhat, Adaptation of aeroelastic reduced-order models and application to an f-16 configuration, *AIAA journal* **45**, 1244–1257, 2007.

[86] T. Lieu and M. Lesoinne, Parameter adaptation of reduced order models for three-dimensional flutter analysis, In *42nd AIAA Aerospace Sciences Meeting and Exhibit*, 2004.

[87] T. Lieu, C. Farhat, and M. Lesoinne, Reduced-order fluid/structure modeling of a complete aircraft configuration, *Computer methods in applied mechanics and engineering* **195**, 5730–5742, 2006.

[88] H. Liu, J.-R. Hervas, Y.-S. Ong, J. Cai, and Y. Wang, An adaptive rbf-hdmr modeling approach under limited computational budget, *Structural and Multidisciplinary Optimization* **57**, 1233–1250, 2018.

[89] J. Lu, X. Zhou, and M. L. Raghavan, Inverse elastostatic stress analysis in pre-deformed biological structures: demonstration using abdominal aortic aneurysms, *Journal of biomechanics* **40**, 693–696, 2007.

[90] G. Łukaszewicz and P. Kalita, *Navier–Stokes Equations: An Introduction with Applications*, Springer, 2016.

[91] A. Maier, M. Gee, C. Reeps, J. Pongratz, H.-H. Eckstein, and W. Wall, A comparison of diameter, wall stress, and rupture potential index for abdominal aortic aneurysm rupture risk prediction, *Annals of biomedical engineering* **38**, 3124–3134, 2010.

[92] A. Maier, *Computational modeling of rupture risk in abdominal aortic aneurysms*, PhD thesis, Technische Universität München, 2012.

[93] A. Manzoni, D. Bonomi, and A. Quarteroni, Reduced order modeling for cardiac electrophysiology and mechanics: new methodologies, challenges and perspectives, In *Mathematical and Numerical Modeling of the Cardiovascular System and Applications*, pages 115–166, Springer, 2018.

[94] R. Miller, D. Marlevi, W. Zhang, M. Hirschvogel, M. Hadjicharalambous, A. Capilnasiu, M. Balmus, S. Hager, J. Jilberto, M. Bonini, et al., Modeling biomechanics in the healthy and diseased heart, In *Modeling Biomaterials*, pages 141–239, Springer, 2021.

[95] W. G. Müller, Coffee-house designs, In A. Atkinson, B. Bogacka, and A. A. Zhigljavsky (eds.), *Optimum design 2000*, pages 241–248, Springer, 2001.

[96] E. Nader, S. Skinner, M. Romana, R. Fort, N. Lemonne, N. Guillot, A. Gauthier, S. Antoine-Jonville, C. Renoux, M.-D. Hardy-Dessources, et al., Blood rheology: key parameters, impact on blood flow, role in sickle cell disease and effects of exercise, *Frontiers in physiology* **10**, 1329, 2019.

[97] M. P. Nash and P. J. Hunter, Computational mechanics of the heart, *Journal of elasticity and the physical science of solids* **61**, 113–141, 2000.

[98] F. Negri, *Efficient Reduction Techniques for the Simulation and Optimization of Parametrized Systems*, PhD thesis, Ecole Polytechnique Fédérale de Lausanne, 2015.

[99] F. Negri, A. Manzoni, and D. Amsallem, Efficient model reduction of parametrized systems by matrix discrete empirical interpolation, *Journal of Computational Physics* **303**, 431–454, 2015.

[100] S. A. Niederer, G. Plank, P. Chinchapatnam, M. Ginks, P. Lamata, K. S. Rhode, C. A. Rinaldi, R. Razavi, and N. P. Smith, Length-dependent tension in the failing heart and the efficacy of cardiac resynchronization therapy, *Cardiovascular research* **89**, 336–343, 2011.

[101] S. A. Niederer, K. S. Campbell, and S. G. Campbell, A short history of the development of mathematical models of cardiac mechanics, *Journal of molecular and cellular cardiology* **127**, 11–19, 2019.

[102] D. Nordsletten, M. McCormick, P. Kilner, P. Hunter, D. Kay, and N. Smith, Fluid–solid coupling for the investigation of diastolic and systolic human left ventricular function, *International Journal for Numerical Methods in Biomedical Engineering* **27**, 1017–1039, 2011.

[103] F. Otto, Die grundform des arteriellen pulses, *Zeitung fur Biologie* **37**, 483–586, 1899.

[104] D. Perrin, P. Badel, L. Orgeas, C. Geindreau, S. rolland du Roscoat, J.-N. Albertini, and S. Avril, Patient-specific simulation of endovascular repair surgery with tortuous aneurysms requiring flexible stent-grafts, *Journal of the mechanical behavior of biomedical materials* **63**, 86–99, 2016.

[105] M. R. Pfaller, M. Cruz Varona, J. Lang, C. Bertoglio, and W. A. Wall, Using parametric model order reduction for inverse analysis of large nonlinear cardiac simulations, *International journal for numerical methods in biomedical engineering* **36**, e3320, 2020.

[106] S. Polzer and T. C. Gasser, Biomechanical rupture risk assessment of abdominal aortic aneurysms based on a novel probabilistic rupture risk index, *Journal of The Royal Society Interface* **12**, 20150852, 2015.

[107] S. Polzer, J. Kracík, T. Novotnỳ, L. Kubíček, R. Staffa, and M. L. Raghavan, Methodology for estimation of annual risk of rupture for abdominal aortic aneurysm, *Computer Methods and Programs in Biomedicine* **200**, 105916, 2021.

[108] L. Pronzato, Minimax and maximin space-filling designs: some properties and methods for construction, *Journal de la Societe Francaise de Statistique* **158**, 7–36, 2017.

[109] C. Prud'Homme, D. V. Rovas, K. Veroy, L. Machiels, Y. Maday, A. T. Patera, and G. Turinici, Reliable real-time solution of parametrized partial differential equations: Reduced-basis output bound methods, *J. Fluids Eng.* **124**, 70–80, 2002.

[110] A. Quarteroni, A. Manzoni, and F. Negri, *Reduced basis methods for partial differential equations: an introduction*, Volume 92, Springer, 2015.

[111] S. Quicken, W. P. Donders, E. M. van Disseldorp, K. Gashi, B. M. Mees, F. N. van de Vosse, R. G. Lopata, T. Delhaas, and W. Huberts, Application of an adaptive polynomial chaos expansion on computationally expensive three-dimensional cardiovascular models for uncertainty quantification and sensitivity analysis, *Journal of biomechanical engineering* **138**, 121010, 2016.

[112] M. L. Raghavan, M. M. Hanaoka, J. A. Kratzberg, M. de Lourdes Higuchi, and E. S. Da Silva, Biomechanical failure properties and microstructural content of ruptured and unruptured abdominal aortic aneurysms, *Journal of biomechanics* **44**, 2501–2507, 2011.

[113] M. Rathinam and L. R. Petzold, A new look at proper orthogonal decomposition, *SIAM Journal on Numerical Analysis* **41**, 1893–1925, 2003.

[114] C. Reeps, A. Maier, J. Pelisek, F. Härtl, V. Grabher-Meier, W. Wall, M. Essler, H.-H. Eckstein, and M. Gee, Measuring and modeling patient-specific distributions of material properties in abdominal aortic aneurysm wall, *Biomechanics and modeling in mechanobiology* **12**, 717–733, 2013.

[115] T. Reis and T. Stykel, Balanced truncation model reduction of second-order systems, *Mathematical and Computer Modelling of Dynamical Systems* **14**, 391–406, 2008.

[116] S. I. H. Richardson, H. Gao, J. Cox, R. Janiczek, B. E. Griffith, C. Berry, and X. Luo, A poroelastic immersed finite element framework for modelling cardiac perfusion and fluid–structure interaction, *International journal for numerical methods in biomedical engineering* **37**, e3446, 2021.

[117] G. Rozza, D. B. P. Huynh, and A. T. Patera, Reduced basis approximation and a posteriori error estimation for affinely parametrized elliptic coercive partial differential equations, *Archives of Computational Methods in Engineering* **15**, 229–275, 2008.

[118] J. Rutzmoser, *Model order reduction for nonlinear structural dynamics*, PhD thesis, Technische Universität München, 2018.

[119] N. Sakalihasan, R. Limet, and O. D. Defawe, Abdominal aortic aneurysm, *The Lancet* **365**, 1577–1589, 2005.

[120] S. Sankaran and A. L. Marsden, A stochastic collocation method for uncertainty quantification and propagation in cardiovascular simulations, *Journal of biomechanical engineering* **133**, 031001, 2011.

[121] T. J. Santner, B. J. Williams, W. I. Notz, and B. J. Williams, *The design and analysis of computer experiments*, Volume 1, Springer, 2003.

[122] A. Schein and M. W. Gee, Greedy maximin distance sampling based model order reduction of prestressed and parametrized abdominal aortic aneurysms, *Advanced Modeling and Simulation in Engineering Sciences* **8**, 1–31, 2021.

[123] L. Sirovich, Turbulence and the dynamics of coherent structures. i. coherent structures, *Quarterly of applied mathematics* **45**, 561–571, 1987.

[124] J. Steffel and T. Luescher, *Herz-Kreislauf*, Springer-Verlag, 2014.

[125] N. Stergiopulos, B. E. Westerhof, and N. Westerhof, Total arterial inertance as the fourth element of the windkessel model, *American Journal of Physiology-Heart and Circulatory Physiology* **276**, H81–H88, 1999.

[126] J. Steuer, M. Lachat, F. J. Veith, and A. Wanhainen, Endovascular grafts for abdominal aortic aneurysm, *European heart journal* **37**, 145–151, 2016.

[127] G. W. Stewart, On the early history of the singular value decomposition, *SIAM review* **35**, 551–566, 1993.

[128] A. M. Stuart and A. Peplow, The dynamics of the theta method, *SIAM journal on scientific and statistical computing* **12**, 1351–1372, 1991.

[129] L. A. Taber, M. Yang, and W. W. Podszus, Mechanics of ventricular torsion, *Journal of biomechanics* **29**, 745–752, 1996.

[130] M. P. Thon, M. R. Myerscough, and M. W. Gee, A spatially resolved and quantitative model of early atherosclerosis, *Bulletin of mathematical biology* **81**, 4022–4068, 2019.

[131] P. Tiso and D. J. Rixen, Discrete empirical interpolation method for finite element structural dynamics, In *Topics in Nonlinear Dynamics, Volume 1*, pages 203–212, Springer, 2013.

[132] J. Van Der Herten, T. Van Steenkiste, I. Couckuyt, and T. Dhaene, Surrogate modelling with sequential design for expensive simulation applications, *Computer Simulation*, 173, 2017.

[133] M. C. Varona, B. Lohmann, and M. Nabi, Automatic adaptive sampling in parametric model order reduction by matrix interpolation, In *2017 IEEE International Conference on Advanced Intelligent Mechatronics (AIM)*, pages 472–477. IEEE, 2017.

[134] P. Virtanen, R. Gommers, T. E. Oliphant, et al., Scipy 1.0: Fundamental algorithms for scientific computing in python, *Nature Methods* **17**, 261–272, 2020.

[135] D. H. Wang, M. Makaroun, M. W. Webster, and D. A. Vorp, Mechanical properties and microstructure of intraluminal thrombus from abdominal aortic aneurysm, *J. Biomech. Eng.* **123**, 536–539, 2001.

[136] D. H. Wang, M. S. Makaroun, M. W. Webster, and D. A. Vorp, Effect of intraluminal thrombus on wall stress in patient-specific models of abdominal aortic aneurysm, *Journal of vascular surgery* **36**, 598–604, 2002.

[137] O. Weeger, U. Wever, and B. Simeon, On the use of modal derivatives for nonlinear model order reduction, *International Journal for Numerical Methods in Engineering* **108**, 1579–1602, 2016.

[138] N. Westerhof, J.-W. Lankhaar, and B. E. Westerhof, The arterial windkessel, *Medical & biological engineering & computing* **47**, 131–141, 2009.

[139] R. Wohlfarth, *A mixed-dimensional multi-physics model of a novel cardiac assist device coupled to patient-specific cardiovascular systems*, PhD thesis, Technische Universität München, 2021.

[140] C. Xi, C. Latnie, X. Zhao, J. L. Tan, S. T. Wall, M. Genet, L. Zhong, and L. C. Lee, Patient-specific computational analysis of ventricular mechanics in pulmonary arterial hypertension, *Journal of biomechanical engineering* **138**, 2016.

[141] R. Yondo, E. Andrés, and E. Valero, A review on design of experiments and surrogate models in aircraft real-time and many-query aerodynamic analyses, *Progress in Aerospace Sciences* **96**, 23–61, 2018.

[142] R. Yondo, K. Bobrowski, E. Andrés, and E. Valero, A review of surrogate modeling techniques for aerodynamic analysis and optimization: current limitations and future challenges in industry, In *Advances in Evolutionary and Deterministic Methods for Design, Optimization and Control in Engineering and Sciences*, pages 19–33, Springer, 2019.

[143] O. C. Zienkiewicz and R. L. Taylor, *The finite element method for solid and structural mechanics*, Elsevier, 2005.